MODIFIED POLYMERS AS ELECTROACTIVE BIOMATERIALS

Presented by

Brenda Guadalupe Molina García

Supervised by

Prof. Carlos Alemán

Dr. Elaine Armelin

Thesis submitted to obtain the degree Doctor of Philosophy in **Polymers and Biopolymers** at *Universitat Politècnica de Catalunya*

Barcelona, May 2020

Department of Chemical Engineering

Innovation in Materials and Molecular Engineering - Biomaterials for Regenerative Therapies

“Hay en el mundo un lenguaje que todos comprenden: es el lenguaje del entusiasmo, de las cosas hechas con amor y con voluntad, en busca de aquello que se desea o en lo que se cree.”

Paulo Coelho (El alquimista)

Abstract

Development of polymeric biomaterials with tailored properties is essential for expanding biotechnologies and, therefore, proposing novel solutions for diagnostic and treatments in modern medicine. In order to contribute with such expansion, this research suggests different strategies to modify intrinsically conducting polymers (ICPs) and overcome their few limitations. Three main engineering approaches were used to combine ICPs advantages with others from conventional insulating polymers and biopolymers, optimizing their performance as electrochemical biomaterials on tissues engineering, biomimetic platforms, actuators and specially on the biosensing field.

The first strategy evaluated in this Thesis was designed to take advantage of the "grafting-through" technique and prepare graft copolymers with ICPs backbones. The incorporation of well-known biocompatible polymers like polyethylene glycol (PEG) and polycaprolactone (PCL) into ICP backbones, increased the cell viability in presence of the synthetized copolymers. Such modifications and the ICPs electroactivity allowed to estimate the copolymers performance as electrochemical sensors of biomolecules.

The second approach was planned to prepare free-standing, flexible and electroactive films for the electrochemical detection of bacterial infections. The excellent mechanical properties of isotactic polypropylene (i-PP) plastic, combined with an ICP like poly(3,4-ethylenedioxythiophene) (PEDOT), enabled the obtained a novel composite with good dimensional stability to be applied as electrochemical platform for bacterial detection. This composite was able to perceive extracellular nicotinamide adenine dinucleotide

(NADH), generated from the respiration reactions of bacteria, and distinguishing prokaryotic microbes from eukaryotic cells. In addition, with a small adjustment, the generated films exhibited qualities as electroactive bioplatforms for tissue engineering.

Finally, the third strategy fashioned an electroactive multi-functional nanomembrane for applications of flexible biomedical implants. A layer-by-layer assembly (LbL) was used to integrate the PEDOT electroactivity to the poly(lactic acid) (PLA) biopolymer. The self-supported nanomembrane of 5 layers, showed benefits as biomimetic platforms for selective ion and ATP transport, as well as actuator/artificial muscles.

Overall, the characterization studies of the electroactive and biocompatible composites presented in this Thesis, offer a comprehensive view on how modifications in ICPs optimize its abilities as biomaterials and open a wide range of possible applications in biomedicine.

Acknowledgements

Muchas son las personas que desde mi primer viaje CUU-BCN a la fecha me han apoyado, y a quienes espero poder retribuir.

A mi familia a quienes tengo tantas cosas que agradecer, pero en especial gracias Papi y M^{a}-Lupe por ser estrictos pero complacientes, por darme todo pero mostrarme con su ejemplo que debo trabajar para ganarlo, por enseñarme que puedo decir lo que pienso con educación y respeto, por estar siempre cerca y darme la libertad de tomar mis decisiones aun cuando no están de acuerdo o sabes que me equivoco, por las tantas veces que me han dicho "tú puedes con esto y más" "no se me raje ni un pelo" y en especial "si tengo que llevarte de la mano hasta el avión para que regreses y termines lo que empezaste ¡Lo voy a hacer!". Rulo-Nanis poco puedo escribir para agradecerles que toda mi vida hayan cuidado de mí, me dejan formar parte de sus vidas y las de sus hijos y, además, ajustan sus vidas para que pueda estar presente en los momentos que de verdad importan. Tal-Ivan, Bodoque, Galleto, Mime y MaFe/Lucifer/Chachita gracias por sus llamadas a las 3 a.m, por hacerme reír tanto, pero sobre todo, por siempre tener ganas de jugar conmigo. Al resto de Molinitas y Garcias gracias por su cariño, apoyo y por toda la comida que me preparan cada vez que voy a casa.

Profesor Aleman, he sido tu alumna por varios años y todavía no lo entiendo, pero agradezco, que me aceptaras en tu grupo aun sin tener referencias mías, por permitirme hacer esta tesis a mi manera, por decir si a 10 de cada 10 peticiones que hacía y, porque cuando caminaba a tu oficina con noticias que le podían enfadar nunca fue así y hasta salía más tranquila, pero con más trabajo. Igual de agradecida debo mencionar a la Dra. Elaine Armelin, quien como tutora de tesis me aconsejo y apoyo para crecer a nivel profesional y personal.

Dr. Luis Javier del Valle, mi otro tutor dentro y fuera de la uní, gracias por todas las veces que se tomó el tiempo para ir a tomarnos un café, hablar

de experimentos o proyectos raros y por darme consejos que me permitieran madurar un poquito.

Niñas de "La miquinista" o Angie, Soni e Ina gracias por el montón de comidas, cafés, clases en el gym y reuniones que compartí con ustedes, por cuidarme, por invitarme a conocer a sus familias, por sus consejos y por simplemente estar.

Anna, Guillem, Güero, Vitor, Ludka y Philip, Max, Geo, Hamidreza, Ali, Mari Carmen, Alejandra, Katty, Maryam, Cindy, Lucas, mis hijos (Ari, Laura, Sergi y Eva), Fran, Mar, Didac, Manolo, Omid, Reza, Hamidreza, Amir, Amir A., Silvana, Jordi, Neudys, Mari Curz, Sofi, Adrian, Christian, Cinthia, Helena, Isma y Enric me considero afortunada por haber tenido la oportunidad de conocer excelentes personas y compartir, además de lo académico, risas, cafés, enojos, frustraciones, cantos, bailes, fiestas, trabajos, viajes, más cafés, cookies y galletas, fotos, seminarios, chismes, cumpleaños, … thanks!.

Con respeto y admiración agradezco a las personas de quienes, en más de una ocasión, recibí ayuda: María Teresa, Lourdes, Iren P., Francsesc, Jordi P., Nuria S., Trifon Trifonov, Margarita, Irene, José Luis, Irene, Nuria, Joan, Lourdes C., David, Guillem e Iñaki. De igual manera, reconozco a las personas que me dieron la oportunidad de compartir trabajos de investigación: Anca Bendrea, Luminita Cianga, Ioan Cianga, Hossein Besharatloo, Joan Josep Roa, Pau Turon, Roshan Vasani, Beatriz Prieto-Simon y Nicolas Voelcker.

A todas las personas que aun ajenas a la universidad me han apoyado durante esto años, espero algún día poder corresponderles con mis acciones.

Finalmente doy las gracias a CONACYT por financiar este proyecto.

Table of content

List of figures

List of schemes

List of tables

CHAPTER 1

INTRODUCTION

1.1 Motivation of the Thesis research

The scientific-technological progress has increased the quality of life form the human being in many areas, among the most important, the health. This improvement has been only possible with the development of devices for detection and treatment of diseases, where biomaterials play an essential role.

In 1986, Williams defined a biomaterial as *"a nonviable material used in a medical device, intended to interact with biological systems"*. [1] However, with the advances in medicine, chemistry, biology, physics and materials science the study of such materials has also increased, resulting in numerous applications in medicine not only as medical devices but also as part of clinical laboratory assays or diagnostic devices. Thus, a better definition could be the one introduced by the journal Biomaterials:

"A biomaterial is a substance that has been engineered to take a form which, alone or as part of a complex system, is used to direct, by control of interactions with components of living systems, the course of any therapeutic or diagnostic procedure". [2]

The interest of the scientific community in biomaterials has been increasing rapidly in the last years. Figure 1.1.1 shows the percentage of published research articles from 2010 to 2019, the amount of works in this area was multiplied by a factor of almost 3 times and, consequently, a huge number of applications where biomaterials have been developed or improved can be found. Among them are: joint replacements (hips and knee), dental and orthopaedic implants, pacemakers, screws, structure wires, bone plates and cement, blood vessels, artificial tendons, ligaments, hearts and kidneys, catheter, skin

repair template, contact lens, corneal bandage, biosensors, biochips, blood bag, surgical tools, gene arrays, assays for blood proteins, grow cell in culture, and many others. [3–6]

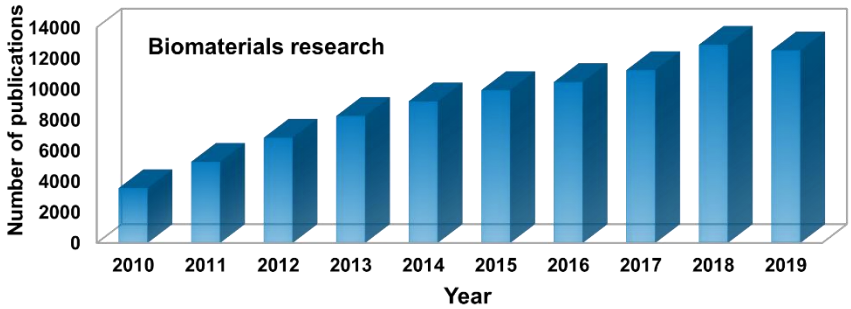

Figure 1.1.1 Biomaterials published research articles in the last ten years (total of 90113 documents). Database used for the bibliography analysis: Web of science (WOS).

Properties need for a specific product are an important part in the design of a biomaterial. Obviously, these depend on the material type: metals, ceramics, polymers or their combinations, *i.e.* composite or hybrid materials. Figure 1.1.2 classifies the published research articles, during the year 2019, about biomaterials according to its chemical nature. The ones from polymer base are highlighted with ~54%, of 12510 publications.

Nowadays, polymers are widely studied as biomaterials base due to its versatility that is unmatched by metals and/or ceramics materials. Their attractive properties and the possibility to tailor them, by structural or superficial modifications, build a new class of materials with good thermal and mechanical properties while, at the same time, can be bioactive, biomimetic, biodegradable, and most importantly, biocompatible. In the past year, ~ 27% of published scientific work on

polymeric biomaterials was dedicated to the study of modified polymers (composites or hybrids).

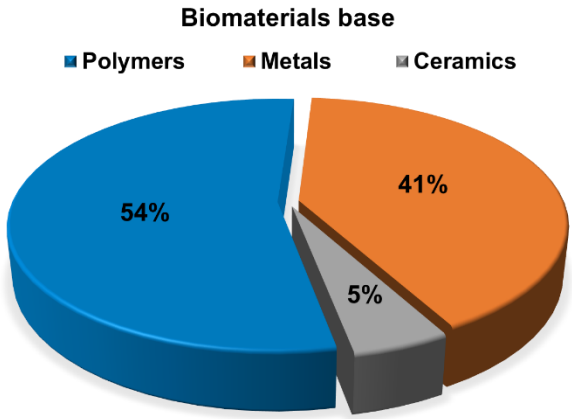

Figure 1.1.2 Published research articles in 2019, classified by material type (polymers, metals or ceramics), considering a total of 12510 scientific publications. Database used for the bibliography analysis: Web of science (WOS).

The advantage of polymers to be adapted, by synthesis or chemical modifications, makes them an indispensable component in the construction of modern sensory devices. A sensor receives and responds to a signal, which provides information about the physical, chemical or biological environment where they are located. In 2004, Adhikari and Majumdar mentioned that polymers have been the most commonly used material for the construction of sensors, participating as: (*i*) substrate for the immobilization of receptor agents responsible for sensing or (*ii*) as part of the sensing mechanisms, coating or encapsulating material on an electrode surface. [7] Hence, polymers can be found in sensors of: temperature, pH, gas, stress–strain, biological elements, ion transfer, induced movements and many others. [7,8]

Within the field of biomedicine, the combination of nanotechnology and polymers with specific properties (*e.g.*, biocompatibility or electroactivity) has expanded studies on polymer-based sensors. The tendencies in this materials indicates that, besides selectivity, precise and rapid measurements, a biomedical sensors also required to be biocompatible and, recently, to mimic natural sensing processes for the development of more lifelike devices.

Therefore, it is important to increase the efforts and funds in research and development of novel polymeric biomaterials, for their future use as implantable medical devices. In this sense, the present Thesis will focus on the study of electrochemical sensors of (*i*) neurotransmitters and a biomolecule produced by cells during its growth , (*ii*) efficient transport of ATP and NaCl and (*iii*) electrically-induced movements.

1.2 Polymers in medicine

Since the birth of polymer science, plastics have been used in numerous applications, being able to replace traditional materials like metals or ceramics. Their low cost, easy processability and manufacture, lightweight, corrosion resistances and exceptional physical properties have made possible its use in several areas, among them medicine, where synthetic, natural and hybrid polymers are commonly employed.

Natural polymers have been part of health care since the beginning of manhood, however, with the outbreak of the Second World War common polyesters, polyamides and synthetic plastics were used to address medical problems, ushering a new era of polymeric materials in medicine. At the beginning they were only part of experimental research, as was published in 1946 by Blaine, who summarized investigations where poly (methyl methacrylate) (PMMA) was successfully studied as bone surgery plastic, filling gaps in the cranial vault and facial bones of animals. [9] Just one year later, Ingraham *et al.* mentioned that PMMA was utilized by surgeons due to its biocompatibility with human body, similar conclusions were established for the Nylon and polyethylene (PE) prostheses. [10,11]

In the present time, there are a lot of plastics used in medicine, like poly(tetrafluoroethylene) (PTFE), poly(vinylchloride) (PVC), polyolefins, silicone, polyacrylates, polyethers, polyesters, polyamides and polyurethanes. All of them in different applications, not only outside the body (surgical tools, containers, haemodialysis membranes, and others) but also as temporary *in vivo* tools (wound dressing, vascular and urinary catheters, etc.) or even inside the body

for being used in tissue engineering or regenerative medicine (meshes, surgical sutures, bone grafting, etc.). [12] Therefore, it is important to know the concepts of biocompatibility and biodegradability in polymers.

Biocompatible and biodegradable polymers

Tissue engineering is the field that applies the principles of biology, chemistry and engineering to repair, restore, regenerate or develop functional substitutes of damaged organs or tissues using cells, growth factors, biomaterials and their combinations. [13,14] The biomaterials employed in this field play an important role for the patient recovery, thus, they should accomplish some crucial properties, such as: non-toxicity, non-mutagenic, non-immunogenic and also be able to provide mechanical integrity, biocompatibility and biodegradability (if required). [15]

The term biocompatibility was defined by IUPAC as *"the ability to be in contact with a living system without producing an adverse effect"* [16] while, in 2008 Balaji *et al.* classified biodegradable polymers as "*polymeric materials that break down into biologically acceptable molecules"*. [17]

Frequently, the polymers that present biocompatibility and/or biodegradability are classified according to its origin, as natural or synthetic. Natural polymers, also called biopolymers, are composed by repeating units connected by covalently bonded units produced from renewable or biological sources, such as plants, animals and microorganisms. The most studied biopolymers can be found in proteins like collagen, gluten and gelatin or in polysaccharides such as

chitin, chitosan, alginate, cellulose and starch; their similar origin to the host tissue is its principal advantages but, their difficult processability constitutes their main drawback. [15,17]

On the contrary, few synthetic polymers (produced from non-renewable petroleum resources) are widely used in tissue engineering science due its easy manufacture, controllable biodegradability and minimal immunological risks. Among the most promising polymers are the polyesters, like polycaprolactone (PCL), polyglycolic acid (PGA) and polylactic acid (PLA). Even if the last one can be obtained from natural sources (*e.g.*, corn starch or cassava roots), it is classified as synthetic because the large-scale production involves some chemical and enzymatic polymerizations. [18] Furthermore, PLA, PGA and the copolymer poly(lactic-*co*-glycolic acid) (PLGA) were approved by the U.S. Food and Drug Administration (FDA) for human clinical applications, confirming that they are a good option for medical solutions. [19]

Besides polyesters, other synthetic polymers that can be degraded by microorganism, hydrolytic, enzymatic, or intracellular mechanisms, include polyanhydrides, polyphosphazenes and polyurethane. [20] Currently, biodegradable polymers like poly(vinyl alcohol) (PVA), poly(glycerol-*co*-sebacate) (PGS), poly(ethylene glycol) (PEG), PLGA or polydimethylsiloxane (PDMS), have different applications in medicine, as for instance as components in electronic devices for detection and treatment of diseases, avoiding the need of secondary surgery. [21] However, due the lack of electrical properties in insulating polymers, it is necessary to combine them with semiconductors, conductive or dielectric materials using stainless

steel, platinum, titanium, cobalt-based alloys or conducting polymers for electron transport.

As was mentioned before, a biomaterial should be also resistant to corrosion and, unfortunately, it is the major handicap of metals in electronic devices. In contact with body fluids they release metal ions, that represent a risk for tissues and structural failures can occur, disabling the sensor device. In order to prevent it, several modifications in the metal surfaces, to enhance the corrosion resistance and biocompatibility, have been studied. [6,22–26] A successful example was reported by Sui-Sun *et.al*. in 2013. This consists on a titanium surface coated with an amorphous tantalum pentoxide (Ta_2O_5) layer, which improved the metal wettability, albumin adsorption, and cell adhesion. [27] Another alternative is to replace them with non-metallic materials, such as polypyrrole (PPy), polythiophene (PTh) and, its derivatives; which are biocompatible and also display conducting properties.

Conducting polymers

Intrinsically conducting polymers (ICPs) are carbon-based materials with a chemical structure covalently bonded by alternated single and double bonds, as a result, ICPs show electrical and optical properties similar to metals and semiconductors. [28] The electrical conductivity is due the delocalization of electrons along the conjugated backbones through the overlap of π-orbitals as well as π-π stacking between polymer chains. [21,29] Besides, this remarkable property, ICPs also exhibit benefits typically associated with conventional polymers, such as lightweight and corrosion resistant.

Since its discovery at the end of the 1970s by Heeger, MacDiarmid and Shirakawa, Nobel Prize in Chemistry 2000, numerous ICPs have been reported in the literature. [30,31] Among the most successful ICPs reported we can mention: polyaniline (PAni), polypyrrole (PPy), polythiophene (PTh) and, its derivative, poly(3,4-ethylenedioxythiophene) (PEDOT). [21,32,33] Figure 1.2.1 shows the chemical structure of such polymers.

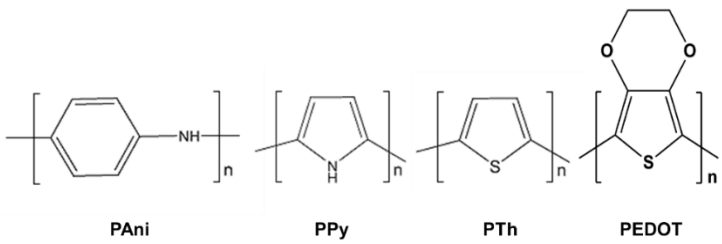

Figure 1.2.1 Chemical structures of the most studied ICPs.

The biocompatibility of ICPs has been widely questioned and toxicity tests have been studied through the *in vitro* adhesion and proliferation of a wide range of cell types. PPy and PEDOT polymers have been reported as biocompatible materials with a successful growth of cells during toxicity assays. [34,35] However, it has been also reported negative effects in the biological performance of conducting polymers due the presence of unreacted monomers, residual solvent and toxicity of dopant ions. [29,34,36] Despite of the inconvenient previously mentioned, when ICPs are synthetized with the necessary precautions, their null toxicity and the ability to induce electrical, electrochemical and electromechanical stimulation make them useful in several applications for modern biomedicine, including tissue engineering scaffolds, [29,37–39] drug delivery systems, [40–42] neural interfaces, [43] biomimetic platforms, [44–46] actuators [47–50] or biosensors. [51–54]

Inspired by biological systems, a biomimetic platform intent to imitate the structure and/or function of biological cells and tissues. These similarities allow less invasive biomaterials capable to emulate human body process with more efficient results. [55,56] An example of biomimicry can be found in biomaterials designed to act as artificial muscles, also named actuators. These materials or devices can behave as muscles through reversible contractions, expansions or rotations trigger by an external stimulus (such as voltage, current, pressure, temperature, light, etc.). [57,58]

Similar to an actuator, a biosensor responds to produced signals, in this case, biological reactions. The term was defined by Turner *et al.* as *"analytical devices incorporating a biological material, a biologically derived material or a biomimic intimately associated with or integrated within a physicochemical transducer or transducing microsystem, which may be optical, electrochemical, thermometric, piezoelectric, magnetic or micromechanical".* [59,60] Nowadays, the term is also used for sensing devices, that may or may not include a biological material, but with the ability to analyse substances and other parameters of biological interest. The latter, will be identified along this work as (bio)sensors.

This research work is mainly focused on different modifications strategies of ICPs through the combination with polymers or biopolymers, the aim of these variations is optimize their performance as electrochemical (bio)sensors of neurotransmitters and biomolecules produce by cell; biomimetic platforms for selective ion and ATP transport; and as actuators.

1.3 References

1 D. F. Williams, *The Williams Dictionary of Biomaterials*, Liverpool University Press, 1999.

2 Elsevier, Biomaterials international journal, https://www.journals.elsevier.com/biomaterials, (accessed 10 April 2020).

3 J. Park and R. S. Lakes, *Biomaterials An Introduction*, Springer New York, New York, NY, 3rd edn., 2007.

4 B. D. Ratner, A. S. Hoffman, F. J. Schoen and J. E. Lemons, *Biomaterials Science*, Elsevier, San Diego, CA, 2nd edn., 2013.

5 W. He and R. Benson, *Polymeric Biomaterials*, Elsevier Inc., Second Edi., 2017.

6 A. Hudecki, G. Kiryczyński and M. J. Łos, in *Stem Cells and Biomaterials for Regenerative Medicine*, Elsevier, 2019, pp. 85–98.

7 B. Adhikari and S. Majumdar, *Prog. Polym. Sci.*, 2004, **29**, 699–766.

8 S. Cichosz, A. Masek and M. Zaborski, *Polym. Test.*, 2018, **67**, 342–348.

9 G. Blaine, *Lancet*, 1944, 525–528.

10 F. D. Ingraham, E. Alexander and D. D. Matson, *N. Engl. J. Med.*, 1947, **236**, 362–368.

11 F. D. Ingraham, E. Alexander and D. D. Matson, *N. Engl. J. Med.*, 1947, **236**, 402–407.

12 M. F. Maitz, *Biosurface and Biotribology*, 2015, **1**, 161–176.

13 R. Langer and J. P. Vacanti, *Science (80-.).*, 1993, **260**, 920–926.

14 R. James, M. Deng, S. G. Kumbar and C. T. Laurencin, *Polyphosphazenes*, Elsevier Inc., 1st edn., 2014.

15 F. Asghari, M. Samiei, K. Adibkia, A. Akbarzadeh and S. Davaran, *Artif. Cells, Nanomedicine Biotechnol.*, 2017, **45**, 185–192.

16 M. Vert, Y. Doi, K. H. Hellwich, M. Hess, P. Hodge, P. Kubisa, M. Rinaudo and F. Schué, *Pure Appl. Chem.*, 2012, **84**, 377–410.

17 A. B. Balaji, H. Pakalapati, M. Khalid, R. Walvekar and H. Siddiqui, *Biodegrad. Biocompatible Polym. Compos. Process. Prop. Appl.*, 2017, 3–32.

18 B. Guo and P. X. Ma, *Sci. China Chem.*, 2014, **57**, 490–500.

19 T. J. Webster, *Nanotechnology for the Regeneration of Hard and Soft Tissues*, WORLD SCIENTIFIC, 2007.

20 I. Vroman and L. Tighzert, *Materials (Basel).*, 2009, **2**, 307–344.

21 Y. Cao and K. E. Uhrich, *J. Bioact. Compat. Polym.*, 2019, **34**, 3–15.

22 Y. Okazaki and E. Gotoh, *Biomaterials*, 2005, **26**, 11–21.

23 R. Singh and N. B. Dahotre, *J. Mater. Sci. Mater. Med.*, 2007, **18**, 725–751.

24 N. S. Manam, W. S. W. Harun, D. N. A. Shri, S. A. C. Ghani, T. Kurniawan, M. H. Ismail and M. H. I. Ibrahim, *J. Alloys Compd.*, 2017, **701**, 698–715.

25 F. Varíola, F. Vetrone, L. Richert, P. Jedrzejowski, J. H. Yi, S. Zalzal, S. Clair, A. Sarkissian, D. F. Perepichka, J. D. Wuest, F. Rosei and A. Nanci, *Small*, 2009, **5**, 996–1006.

26 J. H. Jo, B. G. Kang, K. S. Shin, H. E. Kim, B. D. Hahn, D. S. Park and Y. H. Koh, *J. Mater. Sci. Mater. Med.*, 2011, **22**, 2437–2447.

27 Y. S. Sun, J. H. Chang and H. H. Huang, *Thin Solid Films*, 2013, **528**, 130–135.

28 M. Geoghegan and G. Hadziioannou, *Polymer Electronics*, Oxford university press, 1st edn., 2013.

29 R. Balint, N. J. Cassidy and S. H. Cartmell, *Acta Biomater.*, 2014, **10**, 2341–2353.

30 H. Shirakawa, E. J. Louis, A. G. MacDiarmid, C. K. Chiang and A. J. Heeger, *J. Chem. Soc. Chem. Commun.*, 1977, 578.

31 Nobel prize organization, The Nobel Prize in Chemistry 2000, https://www.nobelprize.org/prizes/chemistry/2000/prize-announcement/, (accessed 10 April 2020).

32 V. R. Feig, H. Tran and Z. Bao, *ACS Cent. Sci.*, 2018, **4**, 337–348.

33 R. Cherrington and J. Liang, *Materials and Deposition Processes for Multifunctionality*, Elsevier Inc., 2016.

34 N. Ferraz, M. Straømme, B. Fellström, S. Pradhan, L. Nyholm and A. Mihranyan, *J. Biomed. Mater. Res. - Part A*, 2012, **100 A**, 2128–2138.

35 S.-C. Luo, E. Mohamed Ali, N. C. Tansil, H. Yu, S. Gao, E. A. B. Kantchev and J. Y. Ying, *Langmuir*, 2008, **24**, 8071–8077.

36 R. A. Green, N. H. Lovell, G. G. Wallace and L. A. Poole-Warren, *Biomaterials*, 2008, **29**, 3393–3399.

37 A. Dominguez-Alfaro, N. Alegret, B. Arnaiz, J. M. González-Domínguez, A. Martin-Pacheco, U. Cossío, L. Porcarelli, S. Bosi, E. Vázquez, D. Mecerreyes and M. Prato, *ACS Biomater. Sci. Eng.*, 2020, **6**, 1269–1278.

38 P. Baei, M. Hosseini, H. Baharvand and S. Pahlavan, *J. Biomed. Mater. Res. - Part A*, 2020, **108**, 1203–1213.

39 M. Solazzo, F. J. O'Brien, V. Nicolosi and M. G. Monaghan, *APL Bioeng.*, 2019, **3**, 041501.

40 A. Puiggalí-Jou, L. J. del Valle and C. Alemán, *ACS Biomater. Sci. Eng.*, 2020, acsbiomaterials.9b01794.

41 N. Hosseini-Nassab, D. Samanta, Y. Abdolazimi, J. P. Annes and R. N. Zare, *Nanoscale*, 2017, **9**, 143–149.

42 J. Ge, E. Neofytou, T. J. Cahill, R. E. Beygui and R. N. Zare, *ACS Nano*, 2012, **6**, 227–233.

43 G. Kang, R. Ben Borgens and Y. Cho, *Langmuir*, 2011, **27**, 6179–6184.

44 W. Zhao, Y. Ni, Q. Zhu, R. Fu, X. Huang and J. Shen, *Biosens. Bioelectron.*, 2013, **44**, 1–5.

45 J. G. Hardy, R. C. Cornelison, R. C. Sukhavasi, R. J. Saballos, P. Vu,

D. L. Kaplan and C. E. Schmidt, *Bioengineering*, 2015, **2**, 15–34.
46 S. Ramírez-García and D. Diamond, *Sensors Actuators, A Phys.*, 2007, **135**, 229–235.
47 B. Kwak and J. Bae, *IEEE Robot. Autom. Lett.*, 2020, **5**, 3758–3765.
48 H. Okuzaki, H. Suzuki and T. Ito, *Synth. Met.*, 2009, **159**, 2233–2236.
49 D. Guo, L. Wang, X. Wang, Y. Xiao, C. Wang, L. Chen and Y. Ding, *Sensors Actuators B Chem.*, 2020, **305**, 127488.
50 L. Wang, Y. Wu, T. Hu, B. Guo and P. X. Ma, *Acta Biomater.*, 2017, **59**, 68–81.
51 M. I. Prodromidis and M. I. Karayannis, *Electroanalysis*, 2002, **14**, 241–261.
52 S. Nambiar and J. T. W. Yeow, *Biosens. Bioelectron.*, 2011, **26**, 1825–1832.
53 G. G. Wallace, M. Smyth and H. Zhao, *TrAC Trends Anal. Chem.*, 1999, **18**, 245–251.
54 D. Zhai, B. Liu, Y. Shi, L. Pan, Y. Wang, W. Li, R. Zhang and G. Yu, *ACS Nano*, 2013, **7**, 3540–3546.
55 M. Sarikaya, C. Tamerler, A. K. Y. Jen, K. Schulten and F. Baneyx, *Nat. Mater.*, 2003, **2**, 577–585.
56 F. Taraballi, M. Sushnitha, C. Tsao, G. Bauza, C. Liverani, A. Shi and E. Tasciotti, *Adv. Healthc. Mater.*, 2018, **7**, 1–13.
57 T. Driver and X. Shen, *J. Bionic Eng.*, 2013, **10**, 222–230.
58 S. M. Mirvakili and I. W. Hunter, *Adv. Mater.*, 2018, **30**, 1–28.
59 A. P. F. Turner, I. Karube, G. S. Wilson and P. J. Worsfold, *Biosensors: fundamentals and applications*, 1987, vol. 201.
60 A. P. F. Turner, *Sensors and Actuators*, 1989, **17**, 433–450.

1

2

CHAPTER

OBJECTIVES

The main aim of the present Thesis is to improve ICPs properties by engineering strategic modifications that combine the benefits of conventional insulating polymers and biopolymers with the electrochemical and electrical behaviour of ICPs. Applications of the systems resulting from such modifications have been mainly focused on the biosensing field. The efficiency and performance of such systems, as electrochemical sensors and biosensors, have been established.

2.1 Specific objectives

In order to fulfil the main aim of this Thesis, specific objectives have been designed for the next chapters. The specific objective of **Chapter 3** is to present the state-of-the-art of polymeric electrochemical sensors. For this purpose, a critical literature review of engineered polymeric electrochemical (bio)sensors employ in medicine has been conducted.

After this, in **Chapter 4**, the characterization techniques used for the analyses of the studied biomaterials are presented. Within the context of the Thesis, three main engineering strategies developed in this work are presented. These consist on: (*i*) the utilization of the "grafting-through" approach to prepare graft copolymers with ICP backbones, which could be considered as "molecular hybrids" or "molecular composites"; (*ii*) the design of free-standing, flexible and electroactive films prepared using PEDOT and its derivative PHMeEDOT; and (*iii*) the design of an electroactive multi-functional coating for flexible biomedical implants.

The specific objectives of **Chapter 5** are: (*i*) to modify ICPs by grafting conventional polymers as side chains using the "grafting-

through" technique; and (*ii*) to evaluate the performance of the resulting graft copolymers as electrochemical sensors of biomolecules. For this purpose, the following items have been analysed:

- Examine the effect of reaction time in the electrocopolymerization of macromonomers prepared using the "grafting-through" approach.
- Analyse the antibacterial activity, protein adhesion and biocompatibility of the pyrrole-containing copolymers.
- Examine the applicability as serotonin sensors of graft copolymers having pyrrole in the backbone and PEG as side chains. Quantification of the detection sensitivity against such neurotransmitter.
- Evaluate the effects of side chains' density in the properties of graft copolymers having ICP-backbone. This study, which was conducted using PCL as side chains, includes a comparison with homopolymer ICPs (*i.e.* without grafted side chains).
- Examine the applicability of the graft copolymers, having thiophene in the backbone and PCL as side chains, as selective and biocompatible dopamine sensors.
- Adapt the "grafting-through" strategy to produce graft copolymers having two different types of side chains. In order to reach this objective, a copolymer having a PTh backbone and both PEG and PCL side chains have been designed, prepared and characterized.

Following the specific objectives of the present Thesis, the main aims of **Chapter 6** are to develop an electrochemical biosensor able to distinguish between eukaryotic and prokaryotic cells and to integrate

it in biomedical implants. For this purpose, a two-step strategy has been followed. In the first step, efforts have been focused on the development of a sensor to distinguish between bacteria and prokaryotic cells, which has been integrated on isotactic polypropylene (i-PP) using a very simple mechanical approach. In the second step, the sensor has been incorporated on the surface of biomedical i-PP using a smart combination of different polymerization techniques. In order to achieve these goals, the following items have been studied:

- Synthetize PEDOT nanoparticles an improve its mechanical handling through its incorporation into a i-PP matrix.
- Examine the applicability of the composite as highly sensitive and selective electrochemical (bio)sensor of bacterial infections, based on the oxidation of nicotinamide adenine dinucleotide (NADH), which has been proved to be related with the bacterial metabolism.
- Design a layer-by-layer system to integrate a PEDOT onto the surface of a biomedical i-PP, employing plasma treatment, oxidative polymerization and electrodeposition of ICPs.
- Evaluate the layered assembly as intelligent implants with the ability to detect bacterial infections through the recognition of low concentrations of NADH.
- Engineer a strategy to improve the biocompatibility of the composite, integrating a graft copolymer having PEDOT as backbone and PCL as side chain.
- Examine the effects of the grafted PCL chains during the cell adhesion and proliferation onto the composite.

The main objectives in **Chapter 7** are: (*i*) to engineer a free-standing nanomembrane through a superficial modification of a biopolymer to incorporate an electroactive material; and (*ii*) to test several biomedical applications for the developed nanomembrane. More specifically, the following items have been examined:

- Design a layer-by-layer procedure to produce a biocompatible, electroactive and self-supported nanomembrane, combining the mechanical advantages of PLA and the electrochemical response of anodically polymerized PEDOT.
- Test the biocompatibility of the engineered system using protein adhesion and cell viability assays.
- Optimize the design of the nanomembrane for its utilization as a sensor for the transport of metabolites. In order to fulfil this optimization, some modifications have been introduced in the engineered nanomembrane: (*i*) it has been functionalized with a membrane protein (*i.e.* a porin); and (*ii*) PEDOT has been replaced by a graft copolymer having a PEDOT backbone and a lipophilic side chain.
- Evaluate the utilization of the free-standing nanomebrane as a Faradaic motor (actuator), taking into account the mechanical integrity and the electrochemical properties of the whole system, and quantifying the soft-robot ability to move under electrical charge-discharge cycles.

Finally, **Chapter 8** summarizes the principal conclusions obtained from this research work.

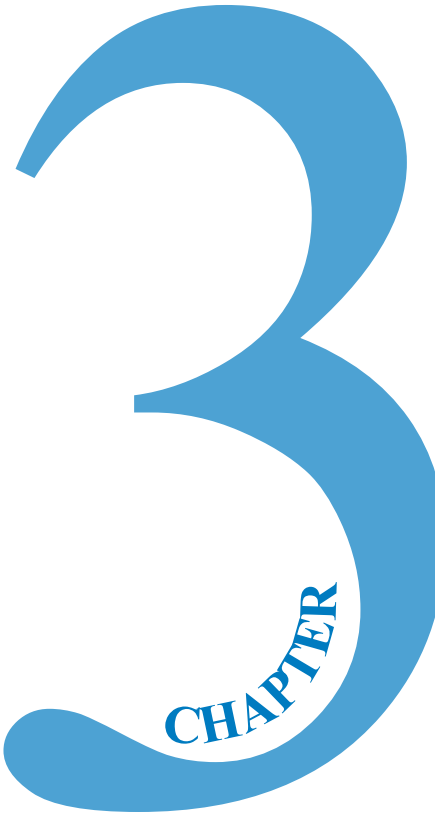

MODIFIED CONDUCTING POLYMERS AS ELECTROCHEMICAL SENSORS IN MEDICINE

State of the art

A single material hardly offers all the requirements of a biomaterial; however, polymer modifications have become a major route to fashion them with specific properties, achieving versatile materials that can fulfill specific needs. Since the first polymer modification in 1846 by Christian Schonbein, [1,2] several adjustments had been developed and classified in two main groups: structural and superficial modifications. Figure 3.1 illustrates with more detail the mentioned classification. In the former, two or more materials are mix while in the second, the surface is transformed without altering the bulk polymer. For more detailed descriptions of the fundamental aspects of each method, excellent books and reviews are available and suggested for further reading. [3–12]

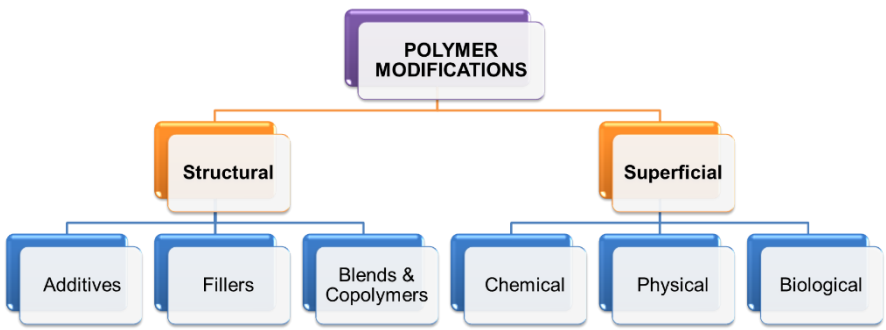

Figure 3.1 Classification of polymer modifications.

The present Chapter, reviews the literature about electrochemical sensors fabricated by modified polymers with potential applications in medicine, focusing the attention on modified conducting polymers to improve its sensitivity, selectivity and/or biocompatibility.

3.1 Introduction

A report published by IDTechEx, predicts a gradual growth in the future of biomedical diagnostics expecting to reach $43 billion by 2029, the forecast is based on the growing and aging global population increasing health expenditure and more prevalent sicknesses such as obesity, cancer and cardiovascular diseases. [13] This report also presents a list of new technologies and devices which may be highly disruptive to the *in vitro* diagnostics market, including microfluidic lab-on-a-chip, lateral flow assays, molecular diagnostics, DNA sequencing and electrochemical sensor strips. [13]

Electrochemical sensors in medicine might represent an economic, fast and precise option for the measurements of extracellular bio-species. The combination of a recognition agent with a transducer, converts a chemical response into a signal that provides qualitative and quantitative information. [14] In the health area, two types of electrochemical sensors have been studied for the detection of biomolecules, (*i*) (bio)sensors, which only involve abiotic elements and, (*ii*) biosensors, that include a biological recognition agent like enzymes, antibodies, oligonucleotides or aptamers. [15]

Different materials can be used for the fabrication of these devices, interestingly, in the last decades a great attention has been addressed to polymers based sensors. [16,17] Polymeric materials have several intriguing advantages when are considered sensing agents or support platforms for sensors in medicine: they are lightweight, ultra-conformable (bendable, stretchable, foldable), portable, disposable, inexpensive [18] and, specially, easy to modify. This quality, enables to improve key requirements to fulfill the most important parameters for

an efficient sensing performance: sensitivity, selectivity, response/recovery time and reversibility/reproducibility of response, which are strongly dependent on the chemical structure and size of the polymers. From both an engineering point of view and a sensor development point of view, we consider that is very useful to make a review related to the emerging field of medical sensors, based on electrochemical methods and produced from polymeric materials subjected to surface and/or structural modification.

This review focuses on significant works over the last 10 years that could potentially determine future trends in medical sensors. Figure 3.1.1 presents the evolution in the number of papers published, showing an increased attention of the research community in the last 10 years. The graph in Figure 3.1.1a compares the related works with sensors based on electrochemical detection, those produced with polymeric materials and the ones employed in the biomedical field. From this research study, it is possible to realize that over 22860 papers were published about electrochemical sensors since 2010, from them, ~ 63% (2429) are composed by polymers and ~14% (536 works found) are related to electrochemical sensor based on polymers with future application in medicine, which are almost equally divided into modified (59%) and unmodified (41%) polymers, as shown in Figure 3.1.1b. The number of scientific investigations dedicated to this specific field is elevated and project an exponential growth, supporting the prediction reported by IDTechEx about the continuous growing of diagnostics technologies and its relevance in the future. [13]

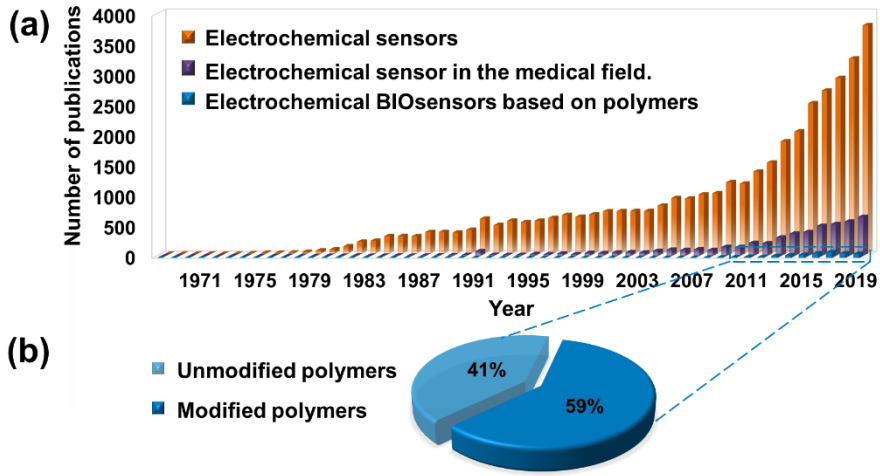

Figure 3.1.1 (a) Comparison between the evolution of electrochemical sensors published research papers per year, those employed in the biomedical field and the ones based on polymeric materials (b) Percentage of BIOsensors based on electrochemical detection composed by unmodified or modified polymers. Source: Web of Science (WOS).

Prompted by the noteworthy and growing interest registered in the last decade, and by the need to explore the potential utilization of polymers as electrochemical sensors in medicine, this review compiles and discusses selected highlighted papers, that discusses sensors employing electrochemical methods for the detection of bio-species based on conducting polymers, where the modifications were carried out to improve the sensing mechanisms, altering both the surface and/or the entire structure of polymeric material.

3.2 Electrochemical sensors based on modified conducting polymers

This section will expose selected works in which intrinsically conducting polymers (ICPs) were modified to improve their properties with the aim to maximize their performance as electrochemical sensors in medicine.

The unique structure of this class of polymers (*i.e.* their π-orbital system, which allows electrons mobility through the polymer chain) is the responsible of the electrical conductivity that resemble metals, the low ionization potentials and the high electron affinity. Therefore, ICPs permit a direct route of electron-transfer between the environment and the electrodes surface, acting as an electron promoter and avoiding the need of an electronic mediator. [19–21] Besides, ICPs are highly sensitive to oxidation/reduction reactions thus, in the presence of a redox analytes, their electronic structure manifest changes that activate a sensing mechanism detected by electrochemical methods, [20,22] such as chronoamperometry (CA), cyclic voltammetry (CV), differential pulse voltammetry (DPV), electrochemical impedance spectroscopy (EIS), etc.

Among ICPs those that have been employed as materials for sensing devices are polypyrrole (PPy), polyaniline (PAni) and poly(3,4-ethylenedioxythiophene) (PEDOT). Their biocompatibility, *i.e.* ability to interact with biological systems without any adverse response, and the possibility to be tailored with inorganic and/or organic elements, such as metals, metal oxide nanoparticles, graphene, graphene oxide, carbon nanotubes, biotargets and others polymers, make them ideal biomaterials for several biomolecules recognition,

[19,22] including dopamine, serotonin and acetylcholine neurotransmitters, nicotinamide adenine dinucleotide (NADH), glucose, drugs, flavonoids, bioproducts, biomarkers, among others.

ICPs modified with metals

Metal and metal oxide nanoparticles offer unique characteristics that can be used to modify polymers and develop high-performance hybrids. Particularly, metal nanoparticles (NPs) show exceptional optoelectrical properties, fast kinetics and easy absorption, behaviors associated to their high ratio between surface area and volume. [23–25] However, NPs have the tendency to aggregate, reducing their surface area to volume ratio and with that their effectiveness. [25] In order to overcome this limitation, polymeric materials have been used as supporting matrix leading to a new class of polymer/metal hybrids which exhibit benefits that cannot be obtained by the materials separately.

Metal NPs in electrochemical (bio)sensors have been used to modify conducting polymers, employing structural or surface methods that amplify ICPs' sensitivity toward a specific analyte. Poletti Papi and coworkers, merged silver nanoparticles (AgNPs) and PPy through a reversed microemulsion. [26] The structural changes in the conducting matrix ascribed to the metal NPs incorporation, allowed to successfully use this hybrid for a simple and direct electrochemical determination of glucose, reporting a limit of detection (LOD) of 3.6 μM (signal-to-noise ratio of 3), which permitted an accuracy of 99 to 105% in studies with human saliva samples, proposing a new tool for the treatment of diabetes through a glucose levels control.

Sangamithirai *et al.* reported a different method for the structural reinforcement of an ICP matrix, by means of an *in situ* chemical oxidative polymerization of o-anisidine monomer in the presence of silver nanoparticles. [27] Poly(o-anisidine) (POA), which is a PAni derivative, modified with AgNPs exhibited good electrocatalytic activity due the synergistic effects of both materials. The POA-AgNPs hybrid was able to distinguish between nicotinamide adenine dinucleotide and 3,4-dihydroxyphenethylamine (dopamine, DA) with a LOD = 6.0 nM and 52 nM for NADH and DA, respectively. The precise recognitions of DA neurotransmitter, known to be responsible of several neurological diseases, [28] and NADH, metabolic coenzyme involved in cellular energy production, [29] play an important role for the early diagnosis of diseases and is essential their detection in water samples, human urine or pharmaceutical injections, as was proposed by the authors. Figure 3.2.1a shows the AgNPs dispersed in POA matrix, while, Figure 3.2.1b demonstrates the simultaneously detection of NADH and DA by the hybrid.

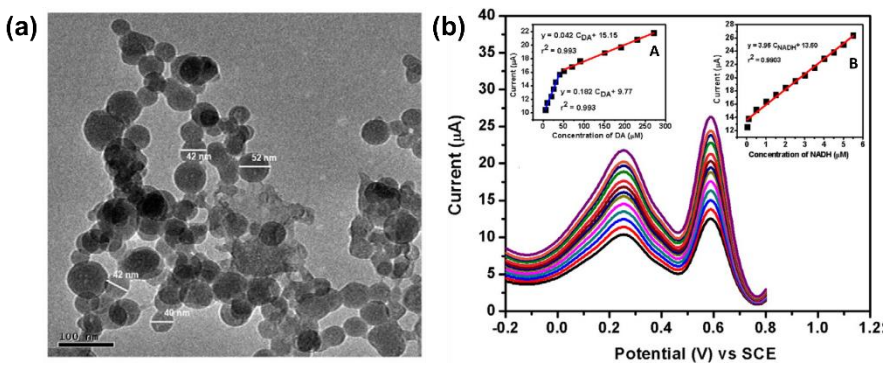

Figure 3.2.1 (a) TEM micrographs of POA-AgNPs hybrid (ratio 3:1). (b) Differential pulse voltammograms of POA-AgNPs in 0.1 M PBS (pH 7.0) containing different concentrations of DA and NADH (from inner to outer). Inset calibration plot of (A) DA and (B) NADH. Adapted with permission from Reference 27. Copyright © 2017 Elsevier B.V.

Gold nanoparticles (AuNPs), represent another metallic nanomaterials of great scientific interest due to their high catalytic activity and stability. [30–32] In fact, it has been reported that AuNPs exhibit a relevant stability for non-enzymatic oxidation of glucose. [33–35] Ansari *et al.* modified poly(aniline blue) (PAB), using it as surface for the seed-mediated growth of AuNPs. [36] As was expected, PAB/AuNPs displayed a good sensitivity detection of glucose (LOD = 0.4 μM) associated to the improvement of electron transport properties induced by the synergistic effect of AuNPs and PAB.

Fabregat and coworkers studied the sensing abilities of two PPy derivatives, also modified superficially with AuNPs. [37] Poly[N-(2-cyanoethyl)pyrrole] (PNCPy) and poly(N-methylpyrrole) (PNMPy) were electropolymerized on a glassy carbon electrode (GC) and coated with a drop of AuNPs colloidal solution. Their results indicated that AuNPs enhance the electronic transference and the charge migration processes of the DA oxidation. Although, was only a slight improvement because of the powerful sensing abilities showed by both conducting polymers without NPs. This behavior can be perceived comparing Figure 3.2.2a and 3.2.2b, which present cyclic voltammograms of PNMPy without (Figure 3.2.2a) and with (Figure 3.2.2b) gold nanoparticles, at different concentrations of DA. Following the same research line, the same authors reported the combination of two different conducting polymers and gold nanoparticles. [38] A three-layered sensor was obtained from an electrochemical polymerization, layer by layer, of PEDOT and PNMPy, followed by AuNPs colloidal solution dropping onto the external layer of the film. Similar to their previous results, the

sensitivity of PEDOT/PNMPy/PEDOT film only increased from 5.3 to 6.1 μA/mM DA after the coating with AuNPs (Figure 3.2.2c). Nevertheless, Figure 3.2.2d exhibits differences in the current response of the sensor, with and without metals NPs, against different concentration of DA, proving that AuNPs not only increase the (bio)sensor sensitivity but, also, the selectivity toward the neurotransmitter in presence of common interferents agents, *i.e.* ascorbic (AA) and uric acid (UA).

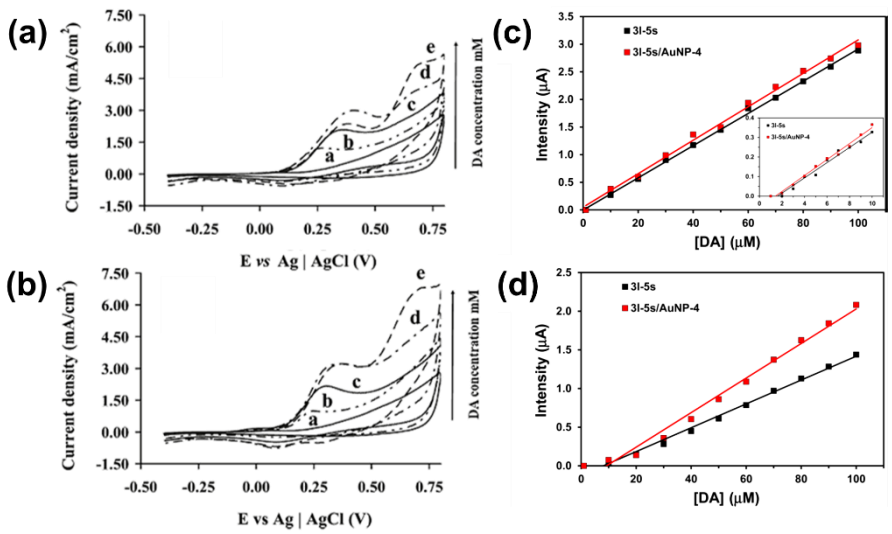

Figure 3.2.2 Cyclic voltammograms for the oxidation of (a) PNMPy- and (b) PNMPy/AuNP-modified GCs in the absence and presence of different DA concentrations (from 1 to 10 mM). (c) Calibration curve for DA concentrations ranging from 1 to 100 μM (inset: from 1 to 10 μM) in 0.1 M PBS and (d) calibration curve for DA concentrations ranging from 1 to 100 μM in 0.1 M PBS with 200 μM AA and 100 μM UA, acting as interferents at PEDOT/PNMPy/PEDOT (3l-5s) and PEDOT/PNMPy/PEDOT/AuNPS (3l-5s/AuNP-4) electrodes. (a-b) Adapted with permission from Reference 37, Copyright © 2011 American Chemical Society, and (c-d) from Reference 38, Copyright © 2014 American Chemical Society.

A good interaction between the ICP matrix and metal NPs is essential for an optimum modification. Within this context, the study of Mao *et al.* evaluated poly(ionic liquids) (PILs) as linkers between AuNPs and PPy nanotubes (PPyNTs), the main steps of the procedure are presented in Scheme 3.2.1. [39] The PPyNTs modified surface, displayed excellent electrocatalytic activity towards the human hormone epinephrine (EP). Hormone not only involved in cardiac activity also used as medication for the treatment of hypersensitivity reactions including anaphylaxis, and hypotension derived from a septic shock. [40] The EP electrochemical (bio)sensor reported a linear response in a range from 35 to 960 μM and a LOD of 298.9 nM; this behavior was attributed to the PILs which promoted a high-density and uniform distribution of AuNPs on the polymer surface.

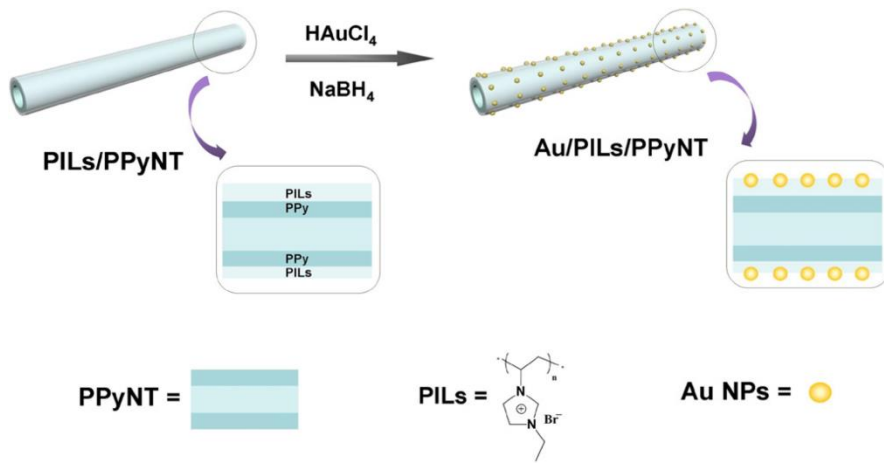

Scheme 3.2.1 The reaction procedure for the preparation of PPyNTs/PILs/AuNPs. High-density and well-dispersed AuNPs could be deposited on the surface of PPyNTs/PILs by anion-exchange of PILs with Au precursor and the *in situ* reduction of the metal ions, due to the presence of PILs. Reprinted with permission from Reference 39. Copyright © 2017 Elsevier B.V.

Other metals employed to increase PPy sensitive properties as electrochemical (bio)sensors are nickel and cobalt. Yang and coworkers, modified the surface of over-oxidized PPy nanowires (oPPyNW) with nickel hydroxide nanoflakes $Ni(OH)_2$NF. [41] The electrodeposited oPPyNW on graphite electrode, were used as platform for the growth of $Ni(OH)_2$NF by chemical bath method. As consequence, the hybrid oPPyNW/$Ni(OH)_2$NF demonstrated an excellent performance for non-enzymatic glucose detection (LOD = 0.3 µM), associated with the efficient electrocatalytic activity and stability of both materials. Whit the same goal, Özcan *et al.* also fashioned a non-enzymatic glucose (bio)sensor based on an overoxidized PPy nanofibers (oPPyNFs). The ICP surface was modified with cobalt(II) phthalocyanine tetrasulfonate (CoPcTS). [42] oPPyNFs/ CoPcTS limit of detection was 0.1mM, within the likely glucose level in a diabetic person.

ICPs modified with carbon

Carbonaceous materials like graphene (Gr), reduced graphene oxide (rGO), graphene oxide (GO) and carbon nanotubes (CNTs) have been widely studied in the past, as result, several review papers have been published reporting different methodologies for the synthesis, processing and applications. [43–47] The combination of their unique characteristics with other materials, has been also explored in the sensing field due their promising role to enhance structural and functional properties with low manufacturing cost.

Awarded with the Nobel Prize in Physics 2010, Andre Geim and Konstantin Novoselov were the pioneers to isolate graphene. [48,49] Since then, the two-dimensional carbon allotrope, has attracted

tremendous attention due to its extraordinary electrical, chemical, optical and mechanical properties, which make it a perfect candidate for the reinforcement of high-performance hybrids.

In the field of electrochemical (bio)sensors, graphene has been employed to increase the detection signal. More specifically, in 2014, Li *et al.* modified the structure of PPy by the incorporation of Gr, expecting a higher sensitivity in the detection of the neurotransmitter dopamine (DA). [50] The hybrid PPy/graphene (PPy-Gr) was obtained *via* electrodeposition onto platinum (Pt) micro-electrodes, components of a planar microelectrode array (pMEA) fabricated by a standard micromachining process. The current response of the modified hybrid PPy-Gr compared with the bare Pt in DA solution is displayed in Figure 3.2.3a. If compared with PPy-Gr, the bare Pt did not present obvious changes during the addition of DA, while the ICP hybrid recorded a well-defined stepwise curve, permitting the detection of ten times lower concentrations of DA. The LOD collected for PPy-Gr was 0.3 µM against 3 µM of DA for Pt. Figure 3.2.3b exposes the electrochemical response in different concentrations of DA (from 0.3 to 61.71 µM), showing a linear behaviour recorded in both cases with correlation coefficients of 0.997 and 0.963 for PPy-Gr and Pt, respectively.

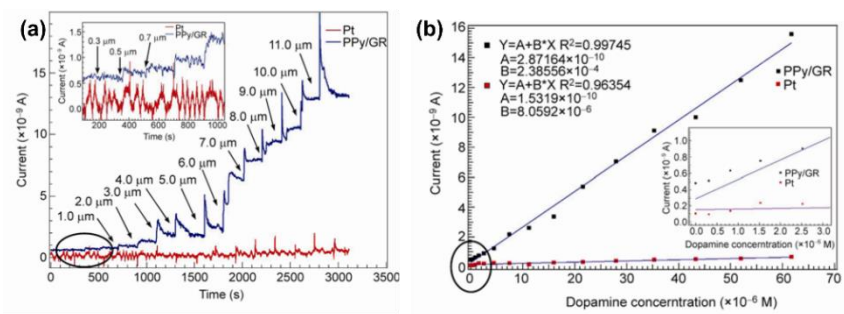

Figure 3.2.3 (a) Current response of Pt and PPy-Gr for DA (stepwise changes of 0.3 to 11 μM). Working potential, 600 mV *vs* Ag|AgCl. (b) Linear relationship between the current and DA concentration in the range of 0.30 to 61.71 μM. Adapted with permission from Reference 50. Copyright © Science China Press and Springer-Verlag Berlin Heidelberg 2014.

Similar results were reported by Sha and coworkers who, through the surface modification of PAni with Gr, designed a non-enzymatic electrochemical (bio)sensor of urea. [51] This bioproduct is excreted by the kidneys in urine, so, kidney diseases are associated with a reduction or increase of urea concentrations in urine and in blood, respectively. The urea sensor PAni/Gr was synthesized by electrodeposition of PAni on the surface of a GC, which was previously coated with Gr *via* drop casting. The optimized sensor reported a LOD of 5.88 μM of urea, confirming that the modification with a carbonaceous material improved the current response of the electrochemical (bio)sensor ~ 4.74 folds, if compared with the unmodified PAni sensor.

A promising method for the graphene production is represented by the chemical oxidation of graphite, followed by an exfoliation and reduction processes. Taking into account that graphite is a layered material, as result of the exfoliation are obtained graphene oxide sheets with oxygen functional groups on their basal planes and edges. [44] Then, as final step, GO product is dedoped and, therefore, reconvert to its reduce state graphene, named reduced graphene oxide. A work published by Wang *et al.* [52] proposed to convert GO to rGO by an electrochemical reduction process. For that, PEDOT was doped with graphene oxide during the ICP electrochemical polymerization, then

the new hybrid was exposed to an electrochemical reduction applying a negative potential (-0.9 V for 600 s). The obtained PEDOT-rGO was used as dopamine electrochemical (bio)sensor. As was expected, the modification of PEDOT with rGO improved the electron transfer kinetics in the hybrid, leading to a highly sensitive detection of DA, with a LOD of 39 nM, even in the presence of common interferences such as uric acid and ascorbic acid. Although rGO shows better conductivity than its unreduced state, GO, some authors have taken advantages from the benefits associated to the oxidative form of graphene; for example, it can be easily dispersed in aqueous solution and the negatively charged carboxyl group in its structure act as an excellent dopant for the polymerization of conducting polymers. [52,53] In 2014, Weaver and coworkers altered a PEDOT matrix with unreduced GO, employing a electrodeposition on a GC. [54] Results demonstrated that the electrostatic interactions between DA molecules and PEDOT-GO surface, selectively amplified the DA oxidation signal, however the LOD achieved was higher than the reported for a PEDOT-rGO hybrid, 83 and 39 nM respectively.

The structural modification of PEDOT with GO was also employed by Huang *et al.* to develop a paper-based analytical device, capable of detect uric acid in real human saliva, without any dilution or adjustment of the samples. [53] The modification of PEDOT was carried out during an electrochemical deposition of a mixture containing the ICP monomer and GO dispersion. A piece of paper was used as a solid electrolyte to connect the three electrodes (*i.e.* working, counter and reference electrode), either during the PEDOT-GO synthesis or in the UA measurements. Figure 3.2.4a reports the mentioned procedure.

The benefits of the PEDOT tailored with GO and the clever idea to combine it with a paper-based analytical device, were applied for the salivary UA analysis. Figure 3.2.4b-c show the response signal of UA oxidation in human saliva, while, the additions of UA standard solution to undiluted saliva samples in Figure 3.2.4c, confirm a linear response of the peak currents as a function of concentrations.

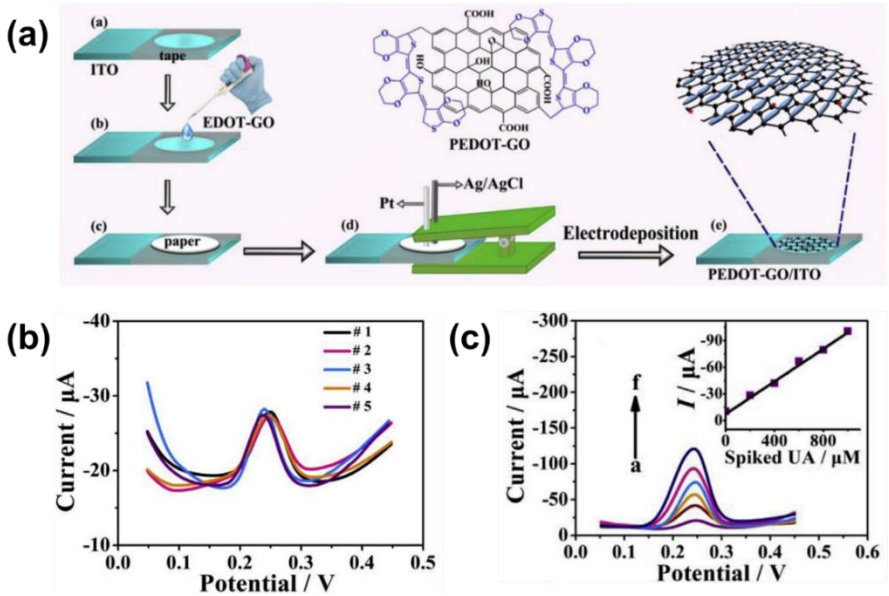

Figure 3.2.4 (a) Schematic route for the preparation of the integrated paper-based analytical device, (b) DPV response of the saliva sample using 5 disposable electrodes fabricated independently and (c) electrochemical response of saliva samples spiked with increasing concentrations of UA in 200 mM increments (inset calibration plot). Adapted with permission from Reference 53. Copyright © 2019 Elsevier B.V.

In order to design a material that gathers all characteristics required for an electrochemical (bio)sensor, several authors explored more than one material or modification technique at the same time. Kalloor *et al.* combined reduced graphene oxide and silver to modify PEDOT

nanotubes (PEDOTNTs). [55] The improved ICP showed better charge transfer properties, sensitivity with a LOD of 0.1 nM and selectivity to serotonin oxidation, even in the presence of interferences like ascorbic acid, uric acid and tyrosine.

Another method employed to enhance an electrochemical (bio)sensor is the molecular imprinting technique (MIT), a system for the preparation of polymers with selective receptor sites, resulting in platforms with predetermined attraction to a specific target. For this technology, the selected monomers are polymerized around a template molecule. Then, the molecule is removed from the polymer matrix, leaving a stereochemical image that is used by the resulting polymer for the template selective recognition. [56–59] Sun and coworkers utilized MIT combined with the structural modification of PPy by graphene oxide and molecularly printed quercetin. [58] The double modification in the molecularly imprinted polymer (MIP) PPy-Gr was designed to improve its behavior as electrochemical (bio)sensor of quercetin, a flavonoid capable of modulate enzymes activity. On one side, the GO enhanced its electrochemical sensitivity until a LOD of 4.8×10^{-8} M of quercetin and, on the other side, the imprinted template increased the (bio)sensor selectivity to quercetin, even in the presence of other similar flavonoids (rutin and morin). MIT technology was also used by Qian *et al.*, but, in this case, carbon nanotubes were selected to increase PPy sensitivity to DA, which was imprinted in the ICP matrix for a better selectivity (Scheme 3.2.2). [59] The modified polymer was proposed for *in vivo* detection of dopamine due its remarkable selectivity and sensitivity, achieving a LOD of 1×10^{-11} M.

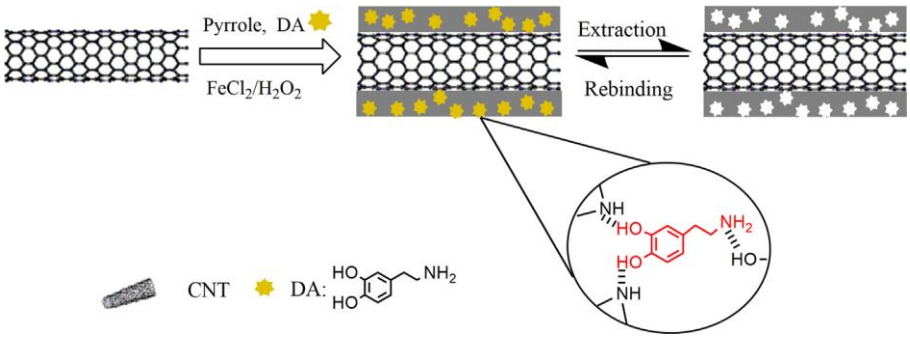

Scheme 3.2.2 Chemical route for the preparation of MIP PPy/CNTs. Reprinted with permission from Reference 59. Copyright © 2014 Elsevier B.V.

ICPs biomodified

The modification of a material by bioactive agents, such as DNA, antibodies, enzymes or microorganism, is a biomimetic approach that has been studied to enhance the biochemistry of an electrochemical sensor and, consequently, improve its detection selectivity.

This kind of modification is produced by common methods like physical or chemical adsorption, covalent bonding, cross-linking or entrapment of bioagents on a transducer. [60,61] Several authors have reported biomodifications in conducting polymers, which act as abiotic electroactive materials, to increase their selectivity toward bio-species.

According to Wei and coworkers, a protein can denature when is directly immobilized on a metal surface, decreasing its activity and signal, while the ICPs biocompatibility can prevent this problem. [62] In fact, they reported a PPy biosensor superficially modified with the attachment of DNA-dendrimer (DDPPy). The amperometric biosensor not only reduced the denaturation of three salivary bio-markers for oral cancer, IL-8 protein, IL-1β protein and IL-8 mRNA, but achieved a

salivary limit of detection (LOD = 100-200 fg/ml) three orders of magnitude better than PPy without the DNA-dendrimer.

In the same way, Avelino *et al.* utilized DNA to develop a selective biosensor of leukemia trough the recognition of the philadelphia chromosome. [63] PAni was structurally modified with gold nanoparticles entrapped in its matrix for a better sensitivity. A single strand DNA (ssDNA) was captured on the PAni-AuNPs surface through electrostatic interactions. Figure 3.2.5a illustrates the biosensor synthesis route and the recognition sites by BRC/ABL fusion gene in leukemia (philadelphia chromosome) as a result of their hybridization with DNA. The hybridization process leads to a gradual reduction of the amperometric response when the sensor was exposed to different concentrations of plasmodial ssDNA containing the BCR/ABL fusion gene, while opposite effect was collected for non-complementary plasmodial DNA. The LOD achieved was 69.4 fM of BCR/ABL fusion gene in leukemia patient samples (Figure 3.2.5b). Similarly, Radhakrishnan and coworkers took advantage of the hybridization process as well, but this time, for the electrochemical recognition of DNA. [64] A PPy nanostructure was coated with PAni through an oxidative polymerization, followed by a second coating of gluteraldehyde (GA) for the immobilization of 5'-amine modified ssDNA. Detection performance was evaluated after a hybridization reaction of PPy/PANi/GA/ssDNA in the presence of the redox indicator methylene blue (MB), which responded to hybridized and unhybridized surfaces. The biomodified composite exhibited sensitivity and selectivity attributed to the nanostructure of PPy/PAni,

a conductivity 472 times greater than conventional PPy/PAni composite and a LOD of 50 fM.

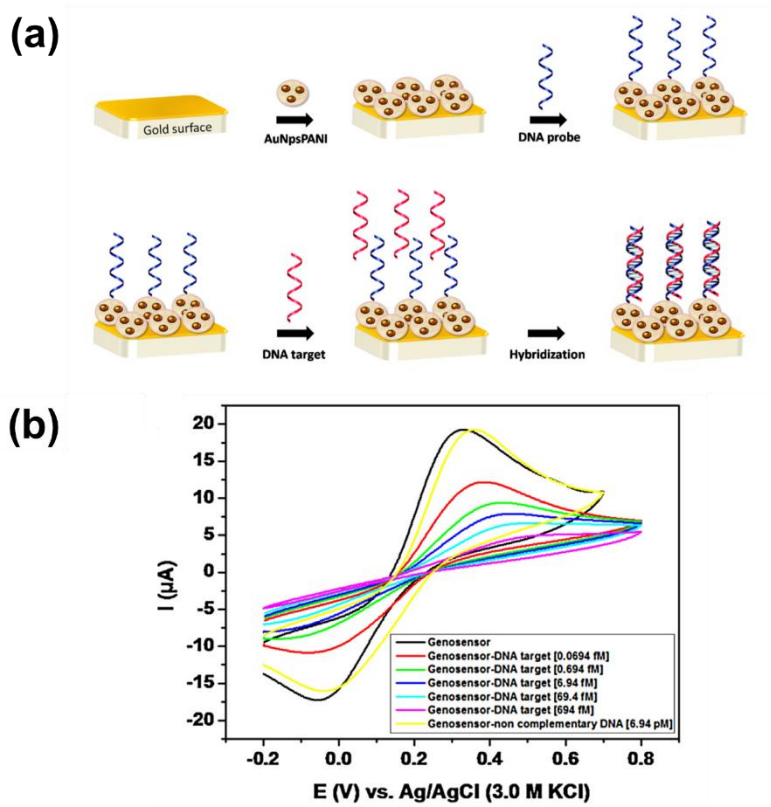

Figure 3.2.5 (a) Schematic representation of the PAni-AuNPs/DNA construction and (b) cyclic voltammograms or the biosensor exposed to different concentrations of recombinant plasmid containing the BCR/ABL fusion gene (DNA target – 0.0694, 0.694, 6.94, 69.4, 694 fM) and nonspecific plasmid (negative control). Adapted with permission from Reference 63. Copyright © 2016 Elsevier B.V.

A biosensor for the electrochemical detection of acetylcholine (Ach) neuromodulator was developed by Chauhan *et al.*[65] The design included a dual modification of PEDOT by a structural reinforcement with electrochemical reduced graphene oxide and the adhesion of immobilized enzymes, acetylcholinesterase (ACh) and cholineoxidase

(ChO), on the surface of iron oxide nanoparticles (Fe_2O_3NPs). The hybrid sensor PEDOT-rGO/ACh-Fe_2O_3NPs exhibited a LOD and sensitivity of 4.0 nM and 0.39 μA/μM, respectively, while the average detection of ACh concentrations in the serum of healthy volunteers (n =10) was 9.26 ± 2.19 nM (within the normal levels of a healthy person (*i.e.* 8.66 ± 1.02 nM). A similar approach was used by Bayram and Akyilmaz, [61] who modified an ICP with a carbonaceous material and a bioagent. The aim of this work was the development of a microbial biosensor for the sensitive determination of paracetamol. The PAni structure was first modified by carboxylated multiwalled carbon nanotubes (cMWCNTs) during their electrodeposition on a gold working electrode, subsequently, the microorganism *Bacillus subtilis* was adhered on the PAni-cMWCNTs surface. In order to efficiently transform the biochemical response into a physical signal, GA was used as cross-linking agent between the recognition element (*Bacillus sp.*) and the abiotic electroactive surface, PAni-cMWCNTs. Paracetamol detection assays by PAni-cMWCNTs/ *Bacillus sp./*GA were carried out with amperometric experiments, that displayed a LOD of 2.9 μM and an efficient selectivity toward paracetamol in a medium containing epinephrine, L-dopa, L-ascorbic acid, uric acid, and D-glucose.

ICPs modified with other polymers

In previous sub-sections, different modification strategies to maximize the sensitivity and selectivity of conducting polymers as electrochemical sensors were described. However, other properties of interest can be enhanced through the combination of ICPs with other polymers or biopolymers. An example is the work reported by

Adeosun and coworkers, where the biocompatibility and conductivity of polydopamine (PDA) where complemented with PPy. [66] The outstanding biocompatibility of PDA homopolymer [67,68] and PPy-PDA copolymer [69] was previously proved, while, for the first time, was studied its electrochemical response towards uric acid. The biocompatibility, high conductivity and electrochemical capacitive behavior of the copolymer PPy-PDA allowed the recognition of low concentrations of UA, with 0.1 μM as limit of detection (LOD). In addition, the biocompatible composite was used to detect UA in human serum and urine, demonstrating its potential in the analysis of human samples.

Piro *et al.* modified the surface of the electropolymerized PEDOT with carboxylic acid PEG, employing the non-conducting polymer as a cross-linker between the PEDOT and the enzyme glucose oxidase (GOD). [70] The enzyme was attached to carboxylic acid PEG forming peptide bonds between the amine groups of GOD and the carboxylic acid groups of PEG, afterwards PEG-GOD was entrapped within PEDOT films electrogenerated on glassy carbon electrode. Amperometric assay in the presence of glucose and ferrocene as mediator, indicated that the biosensor PEDOT/PEG-GOD possessed good sensitivity up to 22 mM, quite similar to the unmodified GOD electrode (*i.e.* PEDOT/GOD). However, opposites results were obtained from stability assays indicating that the PEG incorporation in PEDOT surface increased the biosensor stability against time.

Another example of the benefits associated to the combination of PEDOT and PEG is represented by the work published by Cui and coworkers in 2016. [71] In this case, PEDOT matrix was structurally

modified with a PEG derivative, 4-arm PEG terminated with thiol groups. A second modification was carried out with AuNPs introduced to the copolymer surface through their interaction with the thiol groups. AuNPs provided support for the immobilization of α-fetoprotein (AFP) antibody, a vital tumor biomarker for liver cancer. The synthesis route of PEDOT-PEG/AuNPs-AFP is displayed in Figure 3.2.6a. Electrochemical impedance spectroscopy was employed to examine hybrid's biosensing performance after its incubation in target AFP antigen solution at different times, as can be observed in Figure 3.2.6b. EIS experiments proved that PEDOT electroactivity in the hybrid, provided high sensitivity to AFP antigen. Higher the antigen concentration, lower the charger transfer resistance, with a LOD of 0.0003 fg/mL (S/N = 3). On the other hand, antibody immobilization on AuNPs permitted an excellent selectivity toward AFP antigen, results displayed in Figure 3.2.6c compare the signal response of the hybrid in solutions containing bovine serum albumin (BSA), human serum albumin (HSA), hemoglobin (HGB) or single strand DNA sequence. As can be observed, the hybrid showed a negligible signal response in all cases with the exception of solution containing the target AFP antigen, either separated or combined with the other substances. Besides cross-linked PEDOT and AnNPs-AFP, 4-arm PEG apported hydrophilicity to the hybrid and, therefore, it exhibited good anti-fouling ability which allowed the detection of target AFP in 10% (v/v) human serum samples.

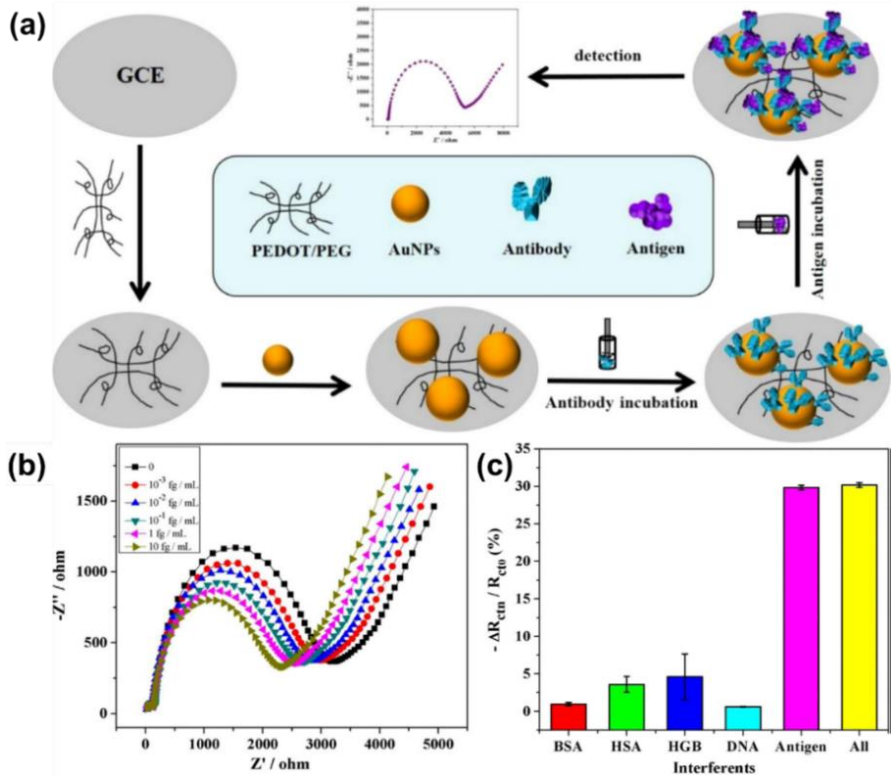

Figure 3.2.6 (a) Schematic illustration of AFP biosensor synthesis. (b)Impedance spectra corresponding to the biosensor with different antigen concentrations (0.01M PBS, pH7.4), curves from inner to outer represent 10fg/mL, 1fg/mL, 10-1 fg/mL, 10-2fg/mL, 10-3fg/mL AFP antigen, respectively. (**c**) Responses of the AFP biosensor to BSA (1.0 nM), HAS (1.0 nM), HGB (1.0 nM), DNA sequence (1.0 nM), AFP antigen (1.0 fg/mL) and a mixture of all the above substances, respectively. Adapted with permission from Reference 71. Copyright © 2016 Elsevier B.V.

3.3 Conclusions and future outlooks

A meticulous study about the different routes to optimize ICPs capacities for the electrochemical recognition of a wide range of biomolecules has been performed. The collected information revealed that structural or superficial modifications with other materials, like metallic nanoparticles, graphene or its derivatives, improved the sensitivity of ICPs, achieving the ability to detect biomolecules with an important role in the diagnostics or treatments of diseases. Similarly, biomodifications also contribute to enhance the ICPs sensibility, in addition to the selectivity of the material toward specific bio-species, such as oncogenes or tumour markers. On the other hand, assemblies between ICPs and non-conducting polymers or biopolymers have been employed to enhance other important qualities in a medical sensor, biocompatibility and hydrophilicity. However, these modifications are not limited to its individual use, in fact, several authors have been proved that more than one material or modification techniques could be merged to maximize the ICP behaviour as electrochemical sensors in medicine.

Based in the collected information and with the aim to improve ICPs properties, we proposed engineering strategic modifications that combine the benefits of ICPs and conventional insulating polymers or biopolymers for their use in the biosensing field.

3.4 References

1 J. Meister, Ed., *Polymer Modification: Principles, Techniques, and Applications*, Marcel Dekker, Inc., 2000.

2 F. Schonbein, *Pogg. Ann*, 1846, **70**, 220.

3 M. Senna, *Powder Technol. Fundam. Part. Powder Beds, Part. Gener.*, 2006, **454**, 485–491.

4 C. F. Jasso-Gastinel, J. F. A. Soltero-Martínez and E. Mendizábal, *Modif. Polym. Prop.*, 2017, 1–21.

5 R. Petrucci and L. Torre, *Filled Polymer Composites*, Elsevier Inc., 2017.

6 V. Ambrogi, C. Carfagna, P. Cerruti and V. Marturano, *Additives in Polymers*, Elsevier Inc., 2017.

7 M. Pracella, *Blends and Alloys*, Elsevier Inc., 2017.

8 R. V. Kulkarni, S. Z. Inamdar, K. K. Das and M. S. Biradar, *Polysaccharide-based stimuli-sensitive graft copolymers for drug delivery*, Elsevier Ltd., 2019.

9 W. He and R. Benson, *Polymeric Biomaterials*, Elsevier Inc., Second Edi., 2017.

10 P. Fabbri and M. Messori, *Surface Modification of Polymers: Chemical, Physical, and Biological Routes*, Elsevier Inc., 2017.

11 A. Sionkowska, *Prog. Polym. Sci.*, 2011, **36**, 1254–1276.

12 D. Katti, R. Vasita and K. Shanmugam, *Curr. Top. Med. Chem.*, 2008, **8**, 341–353.

13 L. Jiang, Biomed. Diagnostics Point-of-Care 2019-2029 Technol. Appl. Forecast., https://www.idtechex.com/de/research-report/biomedical-diagnostics-at-point-of-care-2019-2029-technologies-applications-forecasts/622, (accessed 8 May 2020).

14 F. Faridbod, V. K. Gupta and H. A. Zamani, *Int. J. Electrochem.*, 2011, **2011**, 1–2.

15 F. Arduini, S. Cinti, V. Scognamiglio, D. Moscone and G. Palleschi, *Anal. Chim. Acta*, 2017, **959**, 15–42.

16 Y. Khan, A. E. Ostfeld, C. M. Lochner, A. Pierre and A. C. Arias, *Adv. Mater.*, 2016, **28**, 4373–4395.

17 S. T. Han, H. Peng, Q. Sun, S. Venkatesh, K. S. Chung, S. C. Lau, Y. Zhou and V. A. L. Roy, *Adv. Mater.*, 2017, **29**, 1–22.

18 K. M. Lee, K. H. Kim, H. Yoon and H. Kim, *Chemical design of functional polymer structures for biosensors: From nanoscale to macroscale*, 2018, vol. 10.

19 M. Rahman, P. Kumar, D.-S. Park and Y.-B. Shim, *Sensors*, 2008, **8**, 118–141.

20 H. Peng, L. Zhang, C. Soeller and J. Travas-Sejdic, *Biomaterials*, 2009, **30**, 2132–2148.

21 F. Ghorbani Zamani, H. Moulahoum, M. Ak, D. Odaci Demirkol and S. Timur, *TrAC - Trends Anal. Chem.*, 2019, **118**, 264–276.

22 V. Tsakova and R. Seeber, *Anal. Bioanal. Chem.*, 2016, **408**, 7231–7241.

23 B. C. Sih and M. O. Wolf, *Chem. Commun.*, 2005, 3375–3384.

24 I. Khan, K. Saeed and I. Khan, *Arab. J. Chem.*, 2019, **12**, 908–931.

25 S. Sarkar, E. Guibal, F. Quignard and A. K. SenGupta, *J. Nanoparticle Res.*, , DOI:10.1007/s11051-011-0715-2.

26 M. A. Poletti Papi, F. R. Caetano, M. F. Bergamini and L. H. Marcolino-Junior, *Mater. Sci. Eng. C*, 2017, **75**, 88–94.

27 D. Sangamithirai, S. Munusamy, V. Narayanan and A. Stephen, *Mater. Sci. Eng. C*, 2017, **80**, 425–437.

28 D.-S. Kim, E.-S. Kang, S. Baek, S.-S. Choo, Y.-H. Chung, D. Lee, J. Min and T.-H. Kim, *Sci. Rep.*, 2018, **8**, 14049.

29 W. Li and A. A. Sauve, 2015, pp. 39–48.

30 H. Jia, X. Gao, Z. Chen, G. Liu, X. Zhang, H. Yan, H. Zhou and L. Zheng, *CrystEngComm*, 2012, **14**, 7600–7606.

31 G. M. Veith, A. R. Lupini, S. Rashkeev, S. J. Pennycook, D. R. Mullins, V. Schwartz, C. A. Bridges and N. J. Dudney, *J. Catal.*, 2009, **262**, 92–101.

32 M. Signoretto, F. Menegazzo, V. Trevisan, F. Pinna, M. Manzoli and F. Boccuzzi, *Catalysts*, 2013, **3**, 656–670.

33 S. Fu, G. Fan, L. Yang and F. Li, *Electrochim. Acta*, 2015, **152**, 146–154.

34 R. Sedghi and Z. Pezeshkian, *Sensors Actuators, B Chem.*, 2015, **219**, 119–124.

35 Y. Xianyu, J. Sun, Y. Li, Y. Tian, Z. Wang and X. Jiang, *Nanoscale*, 2013, **5**, 6303–6306.

36 S. A. Ansari, A. Ahmed, F. K. Ferdousi, M. A. Salam, A. A. Shaikh, H. R. Barai, N. S. Lopa and M. M. Rahman, *J. Electroanal. Chem.*, 2019, **850**, 113394.

37 G. Fabregat, E. Córdova-Mateo, E. Armelin, O. Bertran and C. Alemán, *J. Phys. Chem. C*, 2011, **115**, 14933–14941.

38 G. Fabregat, E. Armelin and C. Alemán, *J. Phys. Chem. B*, 2014, **118**, 4669–4682.

39 H. Mao, H. Zhang, W. Jiang, J. Liang, Y. Sun, Y. Zhang, Q. Wu, G. Zhang and X. M. Song, *Mater. Sci. Eng. C*, 2017, **75**, 495–502.

40 G. L. Sacha, S. R. Bauer and I. Lat, *Pharmacother. J. Hum. Pharmacol. Drug Ther.*, 2019, **39**, 369–381.

41 J. Yang, M. Cho, C. Pang and Y. Lee, *Sensors Actuators, B Chem.*, 2015, **211**, 93–101.

42 L. Özcan, Y. Şahin and H. Türk, *Biosens. Bioelectron.*, 2008, **24**, 512–517.

43 S. Priyadarsini, S. Mohanty, S. Mukherjee, S. Basu and M. Mishra, *J. Nanostructure Chem.*, 2018, **8**, 123–137.

44 Y. Wang, Z. Li, J. Wang, J. Li and Y. Lin, *Trends Biotechnol.*, 2011, **29**, 205–212.

45 G. Mittal, V. Dhand, K. Y. Rhee, S. J. Park and W. R. Lee, *J. Ind. Eng. Chem.*, 2015, **21**, 11–25.

46 L. Tang, L. Zhao and L. Guan, in *Advanced Composite Materials: Properties and Applications*, De Gruyter Open, Warsaw, Poland, 2017.

47 D. G. Papageorgiou, Z. Li, M. Liu, I. A. Kinloch and R. J. Young, *Nanoscale*, 2020, **12**, 2228–2267.

48 K. S. Novoselov, A. K. Geim, S. V. Morozov, D. Jiang, Y. Zhang, S. V. Dubonos, I. V. Grigorieva and A. A. Firsov, *Science*, 2004, **306**, 666–669.

49 Nobel Prize organisation, The Nobel Prize in Physics 2010, https://www.nobelprize.org/prizes/physics/2010/prize-announcement/, (accessed 26 April 2020).

50 L. Wang, T. Jiang, Y. Song, W. Shi and X. Cai, *Sci. China Technol. Sci.*, 2014, **57**, 288–292.

51 R. Sha, K. Komori and S. Badhulika, *Electrochim. Acta*, 2017, **233**, 44–51.

52 W. Wang, G. Xu, X. T. Cui, G. Sheng and X. Luo, *Biosens. Bioelectron.*, 2014, **58**, 153–156.

53 X. Huang, W. Shi, J. Li, N. Bao, C. Yu and H. Gu, *Anal. Chim. Acta*, 2020, **1103**, 75–83.

54 C. L. Weaver, H. Li, X. Luo and X. T. Cui, *J. Mater. Chem. B*, 2014, **2**, 5209–5219.

55 N. K. Sadanandhan, M. Cheriyathuchenaaramvalli, S. J. Devaki and A. R. Ravindranatha Menon, *J. Electroanal. Chem.*, 2017, **794**, 244–253.

56 M. Kempe, in *Encyclopedia of Separation Science*, Elsevier, 2000, pp. 2387–2397.

57 D. Bitas and V. Samanidou, in *Fullerens, Graphenes and Nanotubes*, Elsevier, 2018, pp. 135–168.

58 S. Sun, M. Zhang, Y. Li and X. He, *Sensors (Switzerland)*, 2013, **13**, 5493–5506.

59 T. Qian, C. Yu, X. Zhou, P. Ma, S. Wu, L. Xu and J. Shen, *Biosens. Bioelectron.*, 2014, **58**, 237–241.

60 C. Y. Lee, D. Y. Hsu, A. Prasannan, R. Kalaivani and P. Da Hong, *Appl. Surf. Sci.*, 2016, **363**, 451–458.

61 E. Bayram and E. Akyilmaz, *Sensors Actuators, B Chem.*, 2016, **233**, 409–418.

62 F. Wei, W. Liao, Z. Xu, Y. Yang, D. T. Wong and C.-M. Ho, *Small*, 2009, **5**, 1784–1790.

63 K. Y. P. S. Avelino, I. A. M. Frias, N. Lucena-Silva, R. G. Gomes, C. P. de Melo, M. D. L. Oliveira and C. A. S. Andrade, *Colloids Surfaces B Biointerfaces*, 2016, **148**, 576–584.

64 S. Radhakrishnan, C. Sumathi, V. Dharuman and J. Wilson, *Anal. Methods*, 2013, **5**, 1010–1015.

65 N. Chauhan, S. Chawla, C. S. Pundir and U. Jain, *Biosens. Bioelectron.*, 2017, **89**, 377–383.

66 W. A. Adeosun, A. M. Asiri, H. M. Marwani and M. M. Rahman, *ChemistrySelect*, 2020, **5**, 156–164.

67 P. Zhang, Q. Xu, J. Du and Y. Wang, *RSC Adv.*, 2018, **8**, 34596–34602.

68 S. Zavareh, M. Mahdi, S. Erfanian and H. Hashemi-Moghaddam, *Cancer Chemother. Pharmacol.*, 2016, **78**, 1073–1084.

69 S. Kim, L. K. Jang, M. Jang, S. Lee, J. G. Hardy and J. Y. Lee, *ACS Appl. Mater. Interfaces*, 2018, **10**, 33032–33042.

70 B. Piro, L. A. Dang, M. C. Pham, S. Fabiano and C. Tran-Minh, *J. Electroanal. Chem.*, 2001, **512**, 101–109.

71 M. Cui, Z. Song, Y. Wu, B. Guo, X. Fan and X. Luo, *Biosens. Bioelectron.*, 2016, **79**, 736–741.

CHAPTER 4

CHARACTERIZATION TECHNIQUES

This chapter, briefly describes the characterization techniques employed during the research of the three main engineering strategies developed in this work.

Macromonomers

The macromonomers used in this thesis, specifically in Chapter 5 and in Section 6.4, were synthetized and characterized in the laboratory of Prof. Ioan Cianga, from the Institute of Macromolecular Chemistry "Petru Poni" Iasi, Romania.

Macromonomers were characterized by ^{1}H-NMR, ^{13}C-NMR and FTIR spectroscopies. ^{1}H-NMR and ^{13}C-NMR spectra were recorded at room temperature on a Bruker Avance DRX-400 spectrometer at 400 MHz and 100. 61 MHz, respectively. Chemical shifts are reported in ppm and referenced to TMS as internal standard. The FTIR spectra were recorded on a Bruker Vertex 70 FTIR spectrometer equipped with a diamond ATR device (Golden Gate, Bruker) in transmission mode, by using KBr pellets.

The relative molecular weight of the side chain was determined by gel permeation chromatography (GPC) using a PL-EMD instrument, polystyrene standards for the calibration plot, and tetrahydrofuran (THF) as elution solvent; or a WGE SEC-3010 multidetection system, consisting of a pump, two PL gel columns (PLgel 5micro Mixed C Agilent and PLgel 5micro Mixed D Agilent), dual detector RI/VI (Refractometer/Viscometer) WGE SEC-3010, using chloroform ($CHCl_3$), at a flow rate of 1.0 mL/min at 30ºC. The RI/VI detector was calibrated with polystyrene standards (580-467,000 Da) having narrow molecular weight distribution.

Differential scanning calorimetry (DSC) was performed on a Mettler Toledo DSC822e. Approximately 2-3 mg of samples were tested by applying a heating/cooling rate of 10 ºC/min or 2 ºC/min from 20 ºC to 210 ºC, under nitrogen atmosphere (50 mL/min).

Thermal stability was analysed by means of a Mettler Toledo TGA-SDTA851e derivatograph. Thermogravimetry and differential thermogravimetry curves were recorded under nitrogen atmosphere, in a temperature interval of 25 ºC – 700 ºC, with a heating rate of 10 ºC/min. Constant operational parameters were preserved for all the samples, which had the mass ranging between 1.8 and 5.3 mg, so as to obtain comparable data and, moreover, the recordings were repeated for the same heating rate, so as to verify their reproducibility. The curves were processed using the STAR software from Mettler Toledo in order to obtain the thermal and kinetic characteristics.

Profilometry

Film thickness measurements and roughness were carried out using a Dektak 150 stylus profilometer (Veeco, Plainview, NY). Different scratches were intentionally caused on the films and measured to allow statistical analysis of data. For each studied system, three independent samples were analyzed and at least eighteen independent measurements were performed for each sample. Imaging of the films was conducted using the following optimized settings: tip radius = 12.5 μm; stylus force = 3.0 mg; scan length = 1 mm; and speed = 33 or 100 μm/s (depending on the sample).

For some of the studied systems, the thickness was measured using two different items: (*i*) the vertical distance (VD), which corresponds

to the difference between the height polymer and the height of the steel substrate without any average; and (*ii*) the average step height (ASH), which measures the difference between the average height of the polymer and the average height of the steel substrate.

Water contact angle

Water contact angle (WCA) measurements were carried out with the sessile drop method at room temperature. Images of milli-Q water drops (0.5 µL) were recorded after stabilization (5-10 s) with an OCA 15EC instrument (Data-Physics Instruments GmbH, Filderstadt) and analyzed using the SCA20 software SCA20. For each sample, the average WCA value and the corresponding standard deviation was derived from ten independent measures at least.

Scanning electron microscopy (SEM)

Detailed inspection of films and layers was conducted by scanning electron microscopy. Micrographs were acquired in a Focused Ion Beam Zeiss Neon 40 instrument (Carl Zeiss, Germany) equipped with an energy dispersive X-ray (EDX) spectroscopy system, operating at 2 or 5 kV, depending on the sensitivity to beam degradation of the studied systems.

Atomic force microscopy (AFM)

The surface topography of films supported onto steel sheets was studied by AFM. Images were obtained with a Molecular Imaging PicoSPM using a NanoScope IV controller under ambient conditions. The tapping mode AFM was operated at constant deflection (*i.e.* vertical constant force with triangular shaped gold-coated silicon

nitride). The row scanning frequency was set to 0.87 or 0.68 Hz, depending on the sample response, and the physical tip sample motion speed was 10 mm/s.

RMS roughness (Rq) and profile sections of the images were determined using the statistics application and tools of the NanoScope Analysis software version 1.20 (Bruker), which calculates the average considering all the values recorded in the topographic image with exception of the maximum and the minimum. The scan window sizes were $5 \times 5\ \mu m^2$.

The AFM scratching technique was used to measure the thickness of the films. Specifically, contact mode AFM was used to intentionally scratch the film deposited on the steel substrate. Thus, the force was set to completely remove the layer in a scratch area of $0.5 \times 0.5\ \mu m^2$. A line profile determined across the scratch with tapping mode AFM was used to determine the film thickness from the depth of the scratch. It should be noted that such topographic image was taken of a region bigger than the scratch area so as to accurately measure the step between the coated and the uncoated surface.

Transmission electron microscopy (TEM)

TEM images were taken from a Philips TECNAI 10 electron microscope operated at 100 kV. Copolymers were observed with and without uranyl acetate coating. In the former case, a solution of 0.5% v/v in distilled water was dripped onto the sample previously deposited in a copper grid and dried at room temperature.

FTIR spectroscopy

FTIR spectra were recorded on a FTIR Jasco 4100 spectrophotometer or a Nicolet 6700 spectrophotometer by transmittance. The powder and films were deposited on an attenuated total reflection accessory (Top-plate) with a diamond crystal (Specac model MKII Golden Gate Heated Single Reflection Diamond ATR). Samples were evaluated using the spectra manager software and, for each sample, 64 scans were performed between 4000 and 600 cm^{-1} with a resolution of 4 cm^{-1}.

Raman spectroscopy

Samples were characterized by Raman spectroscopy using a commercial Renishaw inVia Qontor confocal Raman microscope. The Raman setup consisted of a laser (at 785 or 532 nm, with a nominal 300 mW output power) directed through a microscope (specially adapted Leica DM2700 M microscope) to the sample, after which the scattered light is collected and directed to a spectrometer with a 1200 lines·mm^{-1} grating. The exposure time ranged from 1 to 10 s, depending on the sample, the laser power was adjusted between 0.1% from to 1% of its nominal output power (according to the exposure time), and each spectrum was collected with three accumulations.

UV-vis spectroscopy

UV-vis spectra were obtained using an UV-vis-NIR Shimadzu 3600 spectrophotometer equipped with a tungsten halogen visible source, a deuterium arc UV source, a photomultiplier tube UV-vis detector, and an InGaAs photodiode and cooled PbS photocell NIR

detectors. Spectra were recorded in the absorbance mode using the integrating sphere accessory (model ISR-3100), the wavelength range was 300-800 nm. Single-scan spectra were recorded at a scan speed of 60 nm/min. Measurements, data collection and data evaluation were controlled by the software UV Probe version 2.31.

Films in Chapter 5 were deposited onto ITO glass slides for measurements and other uncoated ITO glass sheet was used as reference, while samples in Section 6.3 were evaluated directly and employing i-PP as reference.

X-ray photoelectron spectroscopy (XPS)

XPS analyses were performed in a SPECS system equipped with a high-intensity twin-anode X-ray source XR50 of Mg/Al (1253 eV/1487 eV) operating at 150 W, placed perpendicular to the analyzer axis, and using a Phoibos 150 MCD-9 XP detector. The X-ray spot size was 650 mm. The pass energy was set to 25 and 0.1 eV for the survey and the narrow scans, respectively. Charge compensation was achieved with a combination of electron and argon ion flood guns. The energy and emission currents of the electrons were 4 eV and 0.35 mA, respectively. For the argon gun, the energy and the emission currents were 0 eV and 0.1 mA, respectively. The spectra were recorded with a pass energy of 25 eV in 0.1 eV steps at a pressure below $6 \cdot 10^{-9}$ mbar. These standard conditions of charge compensation resulted in a negative but perfectly uniform static charge. The C1s peak was used as an internal reference with a binding energy of 284.8 eV. High-resolution XPS spectra were acquired by Gaussian/Lorentzian curve fitting after S-shape background

subtraction. The surface composition was determined using the manufacturer's sensitivity factors.

Dynamic light scattering (DLS)

Particle size and aggregation studies were performed using NanoBrook Omni Zeta Potential Analyzer from Brookheaven Instruments. Each measurement consisted of 3 runs of 120 s duration each, which were averaged to obtain the effective diameter. Samples were analysed at 25 ºC using a scattering angle of 90º.

Cyclic voltammetry (CV)

Electrochemical characterization by CV was performed using the Autolab PGSTAT302N. Experiments were conducted in 0.1 M PBS (pH 7.4) or acetonitrile with 0.1 M $LiClO_4$ at room temperature. The initial, final and reversal potentials, as well as the scan rates, were fixed depending on the system and the studied application. In Chapter 6 and 7, the free-standing films hold by an alligator pinch or the film directly prepared onto the steel AISI 316L sheet were used as working electrode, an Ag|AgCl 3 M KCl as reference electrode, and a steel AISI 316L sheets or a platinum wire as counter-electrode. The electrochemical activity was determined through direct measurement of the anodic and cathodic areas in the control voltammograms using Nova software.

The loss of electroactivity (LEA, in %) was expressed as:

$$LEA = \frac{\Delta Q}{Q_i} * 100 \qquad \textbf{Eqn. 4.1}$$

where ΔQ is the difference in voltammetric charges (in C) between the second and the last cycle, and Q_i is the voltammetric charge corresponding to the second cycle.

Galvanostatic charge/discharge (GCD)

GCD assays were performed using the Autolab PGSTAT302N. These assays were used to evaluate the durability of the membranes when submitted to electrochemical stress. More specifically, 1500 GCD cycles were applied at a current density of 1.05 mA/g with a cell voltage comprised between −0.20 V and +0.6 V.

Electrochemical impedance spectroscopy (EIS)

EIS measurements were performed using a conventional three-electrode cell and an AUTOLAB-302N potentiostat/galvanostat operating between the frequency range of 10^5 Hz and 10^{-2} Hz and 10 mV of amplitude for the sinusoidal voltage. All experiments were performed at room temperature. For the EIS assays with 5-layered free-standing membranes hold by an alligator pinch (working electrode), the electrolyte solutions were: 0.5 M NaCl, 0.05 M ATP and 0.1 M ATP. Platinum wire was used as counter-electrode, whereas Ag|AgCl saturated (KCl 3M) was employed as reference electrode.

Thermal characterization

Calorimetric data were obtained by differential scanning calorimetry (DSC) using a TA Instruments Q100 series (New Castle, DE, USA) equipped with a refrigerated cooling system (RCS) and TA-Universal Analysis software. The experiments were conducted under a flow of dry nitrogen with a sample weight of approximately

5 mg sealed in an aluminium pan for the measurements. The samples were heated from 20 to 200°C at a rate of 10°C/min, held at 200°C for 1 min, then quenched to -50°C and finally, the samples were re-heated to 200°C.

The degree of crystallinity (X_c) of the films was calculated from the melting thermograms using the following equation:

$$X_c = \frac{\Delta H_m}{\Delta H_m^0} * 100 \qquad \textbf{Eqn. 4.2}$$

where ΔH_m is the heat of fusion of the measured sample, ΔH_m^0 is the heat of fusion for 100% crystalline i-PP taken as 209 J/g.

Thermal degradation was determined by Q50 thermogravimetric analyzer of TA Instruments under a flow of dry nitrogen from 30 °C to 600 °C, using a heating rate of 10 °C/min and around 5 mg per sample.

Degradation

Degradation studies were carried for polymeric films deposited on steel electrodes. Films were placed in PBS (pH= 7.4) and incubated at 37 ºC in a shaking incubator at 100 rpm for a total of five weeks. Samples were analysed after 7 days, 14 days and 35 days. After each immersion time, samples were removed from the solution and gently washed with distilled water. After drying under vacuum for several days at room temperature, films were weighted to monitor the weight loss.

Tensile testing

Uniaxial elongation tests on rectangular samples with an area of 30 mm x 3 mm and a thickness of about 0.3 mm were performed using a Zwick Z2.5/TM1S testing machine. Once samples were secured in the frame, tensile testing was conducted at room temperature and samples were strained at a constant deformation rate of 10 mm/min until breakage. Mechanical parameters (*i.e.* Young's modulus, tensile strength and elongation at break) were obtained from the recorded stress-strain curves. The value provided in this work for each system corresponds to the average ± standard deviation testing 10 independent samples.

Nanoindentation

The mechanical response (hardness and elastic modulus) of the nanomembranes at the micro- and submicrometric length scale was studied by means of the nanoindentation technique. Nanoindentation tests were performed by using a Nanoindenter XP (MTS) with a Berkovich diamond indenter. This equipment worked with continuous stiffness measurement mode (CSM), allowing a dynamic determination of the mechanical properties during the indentation process. It was used a homogeneous array of sixteen imprints (four by four) working under displacement control mode. The tests were conducted at 100 nm of maximum displacement into surface to determine the coating mechanical properties in terms of hardness and elastic modulus. The distance between imprints was held constant and equal to 5 μm in order to avoid any overlapping effect. Such conditions guarantee that each individual test could be treated as an independent

statistical event. The strain rate was held constant at 0.05 s^{-1} and the shape of the indenter tip was carefully calibrated by indenting a fused silica standard of well-known Young's modulus (72 GPa).

Electro-mechanical assays

The electro-mechanical response of nanomembranes prepared in Chapter 7 was measured applying a square signal of 0.6, 1, 2, 3 or 4 V for a time comprised between 2 and 10 s. The first half of the time (*e.g.* first 5 s in the case of 10 s) were with a positive voltage to oxidize the sample while the last 5 s were with negative voltage to reduce it. The movement with increasing weights was examined. For this purpose, the weight of the outer pPLA layer was increased by decreasing the spin coating rate to 900, 600, 300 and 100 rpm during 60 s.

Images were captured with the digital microscope Dino-Lite AM7013MZT previously calibrated. The area of each sample before and after stimulus was measured by the software Image J. All the experiments were repeated three times.

Cell adhesion and proliferation

The behaviour of eukaryotic cells in presence of a specific material, was observed by cellular assays performed with COS-1 and Vero cell lines in Chapter 5, Section 6.2 and Section 7.2, while experiments in Section 6.4 were studied employing HeLa and IMR-90 cells. In both cases, the cellular lines were selected due to their fast growth.

Selected cells were cultured in DMEM high glucose supplemented with 10% FBS, penicillin (100 units/mL), and streptomycin (100

μg/mL). The cultures were maintained in a humidified incubator with an atmosphere of 5% CO_2 and 95% O_2 at 37ºC. Culture media were changed every two days. When the cells reached 80-90% confluence, they were detached using 2 mL of trypsin (0.25% trypsin/EDTA) for 5 min at 37°C. Finally, cells were re-suspended in 5 mL of fresh medium and their concentration was determined by counting with a Neubauer camera using 0.4% trypan blue as a vital dye.

Tested films were placed in plates of 24 wells and sterilized using UV irradiation for 15 min in a laminar flux cabinet. Controls were simultaneously performed by culturing cells on the empty well and the corresponding reference material. For adhesion and proliferation assays an aliquot containing 2×10^4 cells and 5×10^4 cells, respectively, were deposited on the film of each well. Then, attachment of cells to the film surface was promoted by incubating under culture conditions for 30 min. Finally, 2 mL of the culture medium were added to each well. After 24 h, cellular adhesion was determined by quantifying the cells attached to the films or the control. Cellular proliferation was evaluated by quantifying the viable cells onto the evaluated materials after 3, 5 or 7 days of culture.

Cellular viability was evaluated by the colorimetric MTT [3-(4,5-dimethylthiazol-2-yl)-2,5-diphenyltetrazolium bromide] assay. This assay measures the ability of the mitochondrial dehydrogenase enzyme of viable cells to cleave the tetrazolium rings of the MTT and form formazan crystals, which are impermeable to cell membranes and, therefore, are accumulated in healthy cells. This process is detected by a color change: the characteristic pale yellow of MTT transforms into the dark-blue of formazan crystals. [55] Specifically, 50

µL of MTT solution (5 mg/mL in PBS) were added to each well. After 3 h of incubation, samples were washed twice with PBS and stored in clean wells. In order to dissolve formazan crystals, 1 mL of DMSO was added. Finally, the absorbance was measured in a microplate reader at 570 nm. The viability results, derived from the average of three replicates (n = 3) for each independent experiment, were normalized to the control, for relative percentages.

The absorbance was measured in a microplate reader (EZ Read 400– Biochrom, UK) with ADAP 2.0 Plus Data Analysis Software and the statistical analyses were performed with a confidence level of 95% ($p < 0.05$) by Student's T-test.

Protein adsorption

The studies to examine the adsorption of proteins onto the surface of polymer in study were performed using bovine serum albumin (BSA) and lysozyme (Lyz) from chicken egg white.

In Section 5.2 three replicates of each sample, *i.e.* steel sheets covered by P(Py-*co*-AzbPy-*g*-PEG) (τ = 1000 s), PPy (τ = 300 s) and steel sheets as bare substrates, were immersed in 500 µL of BSA and Lyz aqueous solutions (c = of 1%), at 37 °C with moderate stirring. After 48 hours of immersion, samples were washed with deionized water and dried at room conditions. Once every electrode was completely dry, 300 µL of extraction buffer (Tris 0.625M, SDS 2%, BME 5%) were added and incubated for one hour. Then, the protein concentrations were determined by the colorimetric Ninhydrin reaction [57] For this procedure, 300 µL of extraction buffer form each sample and standards were mixed with Ninhydrin reagent and heated

at 95°C for 10 min then, the absorbance at 570 nm was measured in a microplate reader.

On the other hand, three replicates of each sample (0.5 cm^2) in Section 7.2 were immersed in 1 mL of BSA or Lyz aqueous solutions (0.5 mg/mL) during 24 h at room temperature, after immersion the samples were washed three times with milli-Q water. The adsorbed protein, BSA or Lyz, was removed from the surface by adding 0.4 mL of 0.1 M PBS with Triton X-100 surfactant (0.1% v/v) during 30 min at room temperature. In order to avoid interferences between the surfactant and the Bradford reagent, the former was eliminated by precipitating the proteins with 20 µL of trichloroacetic acid. Then, the solution was centrifuged for 15 min at 12000 rpm and the solid obtained was washed with cold acetone and maintained at 4 ºC for 1 hour. After this, the solid was centrifuged again during 15 min at 12000 rpm. The protein was dried under vacuum and, finally, dissolved in 0.1 M PBS. Then, another fast and precise method to measure the concentration of protein, the Bradford assay, was employed. Protein standards and samples were re-suspend in 0.1 M PBS, from that solutions 10 µL of each were added to a 96-well plate, subsequently, 200 µL of diluted dye reagent, with a proportion 1:4 Bradford reagent:milli-Q water, were add to each well. After 5 min incubation at 38°C and 80 rpm, the absorbance was measured at 595 nm.

The electrophoresis polyacrylamide gel used in this work was prepared at 12% resolving and 6% stacking. Lyophilized samples were prepared adding gel loading buffer, as a tracking dye, to the extracted proteins in a 1:4 v/v buffer: protein ratio. Reference bands of BSA and

Lyz solutions were loaded using the same tracking dye. All the samples were exposed to an electric field of 90 V for 2 h. After that time, the gel was coloured using a Coomassie blue–methanol-acetic acid (0.1% - 40% - 10%) solution and, subsequently, washed-out with a solution of 40% of methanol and 10% of acetic acid.

Antibacterial activity

The antimicrobial effect was evaluated using Gram-negative and Gram-positive bacteria, *Escherichia coli* (*E. coli*) and *Staphylococcus aureus* (*S. aureus*) respectively. Five hundred colony forming units (CFU) were seeded in 12 mL of broth culture and then 0.5 mL were added to each Eppendorf tube that contains steel sheets and polymer films. For the macromonomer and grafted copolymers, 1.5 mg was solubilized in 150 µL of water and then an aliquot of 30 µL of the solution was seed with the bacteria. All the samples and the control were vortexed for 1 min, and incubated at 37ºC with agitation at 80 rpm for 24 hours. UV absorbance was measured at λ = 595 nm to starting and finishing the experiment. The bacteria number was the results of the second reading minus the first one.

Statistical analyses were performed with a confidence level of 95% (p<0.05) using Student's T-test.

Electrochemical detection of dopamine neurotransmitter

The efficient detection of dopamine was evaluated by CV assays with an Autolab PGSTAT302N and NOVA software. The experiments were collected in a tree-electrode cell using a glassy carbon substrate as working electrode (3.14×10^{-2} cm^2 of surface area),

Ag|AgCl 3 M KCl and a Pt-wire were used as reference electrode and counter electrode, respectively.

The initial and final potentials were −0.40 V while the reversal potential was +0.80 V. A scan rate of 50 mV s^{-1} was applied for electrochemical oxidation of dopamine recorded in PBS (pH 7.4) solutions with different concentrations ranging from 0 μM to 50 μM.

Electrochemical detection of serotonin neurotransmitter

Due to its high sensitivity for quantitative analysis, differential pulse voltammetry (DPV) was applied as a methodology for the electrochemical detection of serotonin. The assays were carried out in a tree electrode cell using a glassy carbon substrate in the working electrode (3.14×10^{-2} cm^2 of surface area). The potential range applied was from -0.3 V to +0.7 V, with 80 mV as modulation amplitude and a scan increment of 2 mV. The modulation and interval time were 0.05 and 40 s, respectively. The DPV signal corresponding to electrochemical oxidation of serotonin was recorded in PBS (pH 7.4) solutions with serotonin concentrations ranging from 0 μM to 20 μM.

Electrochemical detection of NADH

CV assays were conducted using the experimental conditions previously described but in a 10 mM NADH as electrolyte solution. DPV assays were carried out also in a three-electrode cell. The applied potential range was from +0.5V to +0.8 V with 80 mV as modulation amplitude and a scan increment of 2 mV. The modulation and interval time were 0.05 and 40 s, respectively. The DPV signal corresponding to electrochemical oxidation of NADH was recorded in PBS (pH 7.4)

solutions with concentrations ranging from 2 mM to 10 mM. Chronoamperometric measurements were performed using a steady current of +0.65 V and increasing the concentrations of NADH from 0.2 to 2 mM each 50 s. In order to prove the sensitivity of PTh-*g*-(PEG-*r*-PCL) as sensor, CV and DPV assays were also carried out in presence of ascorbic acid (AA), which was used as interfering substance.

The electrochemical detection of NADH in Chapter 6 was also studied by cyclic voltammetry (CV) using a three-electrode cell. The modified i-PP film and platinum wire were employed as working and counter electrodes, respectively, while the reference electrode was an Ag|AgCl electrode containing a KCl saturated aqueous solution (E^0 = 0.222 V at 25 °C). The initial and final potentials were −0.20 V, and the reversal potential was +0.80 V. Measurements were performed by adding different concentrations of NADH to the electrolytic medium, which was a Dulbecco's modified Eagle medium (DMEM) high glucose supplemented with 2% fetal bovine serum (FBS; pH 8.1) and 0.2% $NaHCO_3$.

Electrochemical detection of prokaryotic vs. eukaryotic cells.

The electrochemical detection of prokaryotic *vs.* eukaryotic cells was performed by CV using the Autolab PGSTAT302N. Experiments were conducted in the cell culture media at room temperature. The initial and final potentials were −0.20 V while the reversal potential was +0.60 V. A scan rate of 100 mV s^{-1} was applied in all cases. An Ag|AgCl 3 M KCl and a Pt-wire were used as reference electrode and counter electrode, respectively. The working electrode consisted on a carbon screen-printed electrode (SPE) from Dropsens (DRP-150)

coated with a gelatin layer, which was used to adhere the i-PP and i-PP/PEDOT films. Such adhesive layer was prepared by dissolving 50 mg of gelatin from porcine skin in 1 mL of milli-Q water, which was placed in an ultrasonic bath at 40 °C for 15 minutes until a clear solution was acquired. A solution drop (10 μL) was deposited onto the SPE surface and, subsequently, a round film of i-PP or i-PP/PEDOT (4 mm in diameter) was placed onto the resulting gelatine-modified SPE. All experiments were replicated three times.

Identification of NADH from bacteria respiration reactions

The absorption peak of NADH was identified at λ= 340 nm by recording the UV-vis spectrum in the absorbance mode (250-800 nm) of a 0.25 mM NADH solution in DMEM high glucose supplemented with 2% FBS (pH 8.1) and 0.2% $NaHCO_3$. The spectrum was acquired on a quart cell (1 mL) using a UV-vis Cary 100 Bio (Varian) spectrophotometer. Then, a calibration curve was determined by measuring the absorbance at λ= 340 nm with a Synergy HXT multi-mode reader using 0-2 mM NADH solutions in DMEM high glucose supplemented with 2% FBS (pH 8.1) and 0.2% $NaHCO_3$.

In order to prove that bacteria cellular membranes are permeable to NADH, bacteria *Escherichia coli (E. coli*) colony forming units (CFU, $2 \cdot 10^8$ colony) per mL were seeded in DMEM high glucose supplemented with 2% FBS (pH 8.1) and 0.2% $NaHCO_3$. After 24 h, 150 μL were added to 5 mL of the same supplemented medium in sterile vials. The bacteria used for this purpose were ATCC 25922, a biofilm-positive strain (B+), and CECT 101 a biofilm-negative strain (B–). Samples were vortexed for 1 min and incubated at 37 ºC with

agitation at 80 rpm for 24 h and 48 h for bacteria growth. The UV absorbance was measured at λ = 340 nm in flat-bottomed 96-well plates with aliquots of culture media (200 μL) using a Synergy HXT multi-mode reader. Results displayed correspond to the average of three replicates (*n* =3) for each independent experiment.

CHAPTER 5

GRAFT COPOLYMERS USED AS ELECTROCHEMICAL (BIO)SENSORS

Polym. Chem., **2018**, 9, 4218

Polym. Chem., **2017**, 8, 6112

Polym. Chem., **2019**, 10, 5010

The fifth chapter of this Thesis studies three different ICP-based graft copolymers that have been prepared using the "grafting-through" technique. Besides, the performance of these materials as biocompatible and electrochemical platforms for sensing devices is evaluated.

5.1 Introduction

Hybrid organic materials composed of a biobased polymer and a synthetic polymer (natural–synthetic hybrids) or two synthetic polymers with very different chemical characteristics and properties (synthetic–synthetic hybrids) are gaining interest for a variety of biomedical applications, [1–5] among them, electrochemical sensors based on intrinsically conducting polymers (ICPs).

The high conductivity, good capacitive behaviour and unique electromechanical and electrochromic characteristics [6–10] of ICPs make them an ideal biomimetic candidate for the development of sensing devices. [11–15] However, an important requirement for sensors in medicine is that they should be implantable for a continuous monitoring and, therefore, ICPs have been tailored to accomplish specific needs by the incorporation of other elements. [16–19]

A route to obtain such change is the preparation of graft-copolymers using the "grafting-through" or macromonomer method. In this technique, macromonomers are copolymerized with conventional monomers producing graft copolymers, the density of side groups being roughly controlled by the comonomer: monomer ratio. [20,21] ICPs-based graft copolymers, in which π-conjugated backbones are connected with flexible, hydrophilic or hydrophobic side chains, have emerged as a new class of useful hybrid materials in

medicine because the interactions between the synthetic material and biologicals systems are improved.

ICPs like polypyrrole (PPy), polythiophene (PTh) and its derivatives poly(3,4-ethylenedioxythiophene) (PEDOT) and poly(hydroxymethyl-3,4-ethylenedioxythiophene) (PHMeEDOT) are particularly important due to their high stability, controllable electrochemical behaviour and easy chemical and structural modification.[22–24] PPy and PTh based graft copolymers have been previously reported.[25] For example, the pH responsive PTh-*g*-poly(N,N-dimethylaminoethylmethacrylate) (PTh-*g*-PDMA) was proposed as an aqueous sensor for biological applications [26] and the PPy-*g*-poly(styrenesulfonic acid) (PPy-*g*-PSSA) was used for the electrocatalytic biosensing of hypoxanthine. [27]

On the other hand, biodegradable and biocompatible graft copolymers based on polycaprolactone (PCL) and polyethylene glycol (PEG) units, which were approved by the FDA, represent interesting platforms for tissue engineering. For example, the copolymers PPy-*g*-PCL reported by Mecerreyes *et. al.* in 2002 exhibit an electrical conductivity between 10^{-6} and 10 S/cm, depending on the composition, [28] and the hybrid materials consisting of an all conjugate PTh backbone and well-defined PEG grafted chains are successfully used as active surfaces for the selective adsorption of proteins and substrates to promote the electrocommunication with cells. [29–31]

The following sections (5.2-5.4) are mainly focused on study the optimal conditions (*e.g.* polymerization time, comonomers molar ratio and polymerization technique) to synthetize graft copolymers that combine the benefits associated with ICPs (PPy and PTh) and

biopolymers (PEG and/or PCL), for its use as biocompatible electrochemical sensors of biomolecules (dopamine, serotonin and nicotinamide adenine dinucleotide).

The macromonomers used in this chapter and in Section 6.4 were synthetized and characterized in the laboratory of Prof. Ioan Cianga, from the Institute of Macromolecular Chemistry "Petru Poni" Iasi, Romania. Information of equipment and other parameters are provided in Chapter 4.

5.2 Amphiphilic polypyrrole-poly(Schiff base) copolymers with poly(ethylene glycol) side chains: Synthesis, properties and applications

Abstract

Amphiphilic, poly(ethylene glycol) (PEG)-grafted, random, intrinsically conducting copolymers, which combine three different functionalities, have been engineered, prepared and characterized. Specifically, these copolymers bear conducting polypyrrole (PPy) and poly(Schiff base) (PSB) sequences randomly distributed in the backbone; while hydrophilic grafted side chains, consisting of well-defined PEG chains, are attached on the PSB units. Basically, the copolymers synthesis has been conducted sequentially, by employing the "macromonomer" technique, *via* electrochemical copolymerization of a bis (pyrrole) benzoic Schiff base-containing PEG macromonomer with pyrrole monomers.

After investigation of the chemical and electrochemical properties of synthesized copolymers, the advantages of their multi-functionality, in terms of biomedical applications, have been demonstrated. More specifically, the conjugated PPy and PSB sequences allowed the grafted copolymers to exhibit great ability to catalyse the oxidation of serotonin, an important neurotransmitter found in the blood platelets and in the central nervous system of animals and humans. On the other hand, enhanced biocompatibility in comparison with bare PPy is due to the presence of PEG side chains, while bacteriostatic activity against both Gram-negative and Gram-positive bacteria is imparted by the synergistic combination of the polycationic character of PPy main

chain with the benzoic Schiff base functional groups presence and with bent-shaped architecture of facially amphiphilic PSB sequences, respectively. Consequently, these grafted copolymers are promising materials for develop of implantable electrodes for serotonin detection, which are expected to present the above-mentioned characteristics.

Materials and methods

Materials. Pyrrole (Py; from Aldrich, 98%) was used freshly distilled, 2-pyrrole-carboxaldehyde (from Fluka, 97%) was recrystallized from petroleum ether before use. *p*-Toluene sulfonic acid (PTSA; from Aldrich, 99%) and 3,5-diaminobenzoic acid (DABA; from Aldrich, 98%), poly(ethylene glycol) methyl ether with M_w=2000 $g \cdot mol^{-1}$ (PEG_{2000}; from Aldrich), *N*,*N'*-dicyclohexylcarbodiimide (DCCI; from Merk), 4-dimethylamino pyridine (DMAP; from Aldrich) and acetonitrile (ACN, from Panreac S.A.) were used as received. Meanwhile, anhydrous lithium perchlorate (from Sigma-Aldrich, 95%) was stored in an oven at 70°C before its use in the electrochemical trials.

Synthesis of AzbPyBA precursor. The azomethine-containing bis-pyrrole monomer: 3,5-bis(((E)-(1H-pyrrol-2-yl) methylene) amino) benzoic acid (AzbPyBA) was synthetized in a 250 mL three necks round bottom flask equipped with a condenser, a Dean-Stark trap, nitrogen inlet-outlet and magnetic stirrer was charged with 2-pyrrole-carboxaldehyde (5.89 g; 0.062 mol), DABA (4.56 g, 0.03 mol), PTSA (0.015 g) and toluene (150 mL). Nitrogen was purged through the reaction mixture for 15 minutes (Scheme 5.2.1).

The mixture was heated to reflux with stirring for 20 hours, continuously removing the toluene-water azeotrope. After cooling the reaction mixture, the formed solid product was filtered and purified by column chromatography (aluminum oxide-Fluka Type 507c) first with dichloromethane as eluent and after that with tetrahydrofuran (THF). The second fraction was concentrated by evaporation under reduced pressure, and the resulting dark-brown solid was dried. A dark-brownish solid was obtained. Yield: 62%.

Synthesis of AzbPy-g-PEG macromonomer. Pyrrole-*g*-polyethylene glycol macromonomer functionalized with azomethine-containig bis-pyrrole moieties (AzbPy-*g*-PEG) was obtained from 2 g (0.001 mol) of PEG_{2000} and 0.46 g (0.0015 mol) of AzbPyBA placed into a three-neck round-bottom flask equipped with a dropping funnel, under nitrogen. 17 mL of THF and 0.01815 g (0.00015 mol) of DMAP were added to the flask. 0.3078 g (0.0015 mol) of DCCI in 1.5 mL THF were placed in the dropping funnel and added in about 15 min. The mixture was stirred at room temperature for three days (Scheme 5.2.1). The resulting solution was filtered and precipitated in cold diethyl ether to remove the catalyst and the unreacted reagents. After filtration and drying a white solid was obtained. The product was passed through a silica gel filled column and re-precipitated in cold diethyl ether using CH_2Cl_2 as solvent.

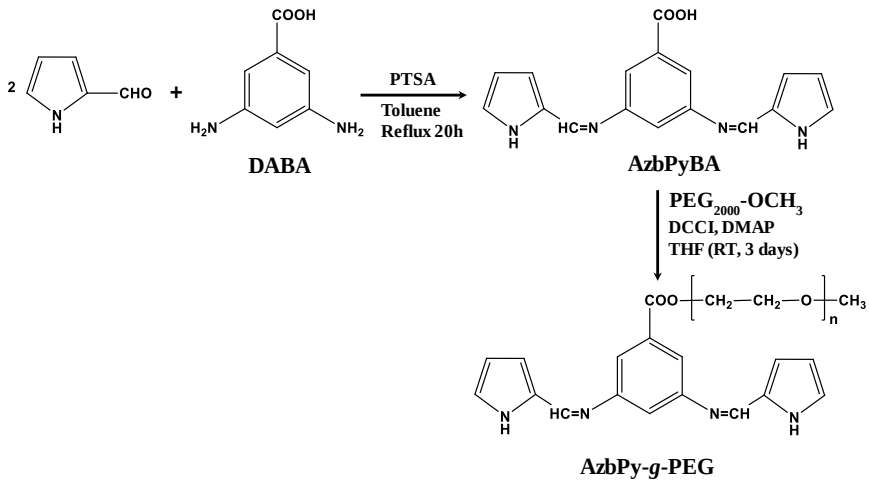

Scheme 5.2.1 Synthesis of AzbPy-*g*-PEG macromonomer.

Synthesis of P(Py-co-AzbPy-g-PEG) copolymers. Anodic polymerizations were carried out in a standard three-electrode cell of 50 mL under nitrogen atmosphere (99.995% in purity) at room temperature. The anodic compartment was filled with 10 mL of a 1 mM 1:1 Py:AzbPy-*g*-PEG in ACN solution with 0.1 M $LiClO_4$, as supporting electrolyte; while the cathodic compartment was filled with 10 mL of the same electrolyte solution. Stainless steel AISI 316 sheets of 0.5 cm^2 area were employed as working (WE) and counter electrodes (CE). The reference electrode (RE) was an Ag|AgCl electrode containing a KCl saturated aqueous solution (E^0 = 0.222 V at 25ºC), which was connected to the working compartment through a salt bridge containing the electrolyte solution. P(Py-*co*-AzbPy-*g*-PEG) polymeric films were prepared by chronoamperometry (CA) using a constant potential of +1.60 V and considering three different polymerization times (τ = 300, 500 and 1000 s).

PPy homopolymer, (PPy), was also prepared and characterized as a standard for copolymers' properties comparison. The generation

medium was 1 mM of Py in acetonitrile solvent, with 0.1 M $LiClO_4$ solution, as supporting electrolyte, and the anodic polymerization was performed using a constant potential of +1.70 V for τ = 300 s.

Characterization of the macromonomer and prepared copolymers. The AzbPy-*g*-PEG macromonomer was characterized by ^{1}HNMR and FTIR through KBr pellets, specific details are described in Chapter 4.

On the other hand, graft copolymers were evaluated by different characterization techniques, FTIR (with KBr pellets), Raman spectroscopy, SEM (operated a 5 kV), AFM, UV-vis of solid films deposited onto ITO-glass substrate, WCA and, thickness and roughness, by profilometry. More information is described in Chapter 4.

To evaluate its potential use as sensing devices in medicine, electrochemical and biological assays were also carried out. The electroactivity and electrostability were studied by CV using an acetonitrile solution containing 0.1 M of $LiClO_4$. The initial and final potentials were - 0.5 V, and the reversal potential was + 2.0 V. A scan rate of 50 mV/s was used in all cases. The electroactivity and electrostability were determined through direct measure of the anodic and cathodic areas in the control voltammograms, using the GPES software. To understand the ability of the P(Py-*co*-AzbPy-*g*-PEG) to interact with different proteins, adsorption assays were conducted using albumin (BSA) and Lysozyme (Lyz) proteins. While the cytotoxicity was evaluated by the proliferation of COS-1 and Vero cell lines and, the antimicrobial properties of AzbPy-*g*-PEG macromonomer, PPy and P(Py-*co*-AzbPy-*g*-PEG) were investigated using *Escherichia coli* (*E. coli*) and *Staphylococcus aureus* (*S.*

aureus), which are Gram-negative and Gram-positive bacteria, respectively. The complete experimental procedures of biological assays were described in Chapter 4.

Finally, DPV was applied for the electrochemical detection of serotonin, according to the procedure described in Chapter 4. The assays were carried out with a glassy carbon electrode (3.14×10^{-2} cm^2 of surface area) as WE in PBS (pH 7.4) solutions containing different concentrations of serotonin (between 0 μM to 20 μM), employing a potential range from - 0.3V to + 0.7 V.

Results and discussion

Macromonomer characterization. A multifunctional macromonomer was designed combining three elements (Scheme 5.2.1): (*i*) electroactive PPy which, in its oxidized form, is a biocompatible polycation with recognized antibacterial activity in all forms (powder, particles, nanotubes or thin film surfaces); [32,33] (*ii*) benzoic Schiff base bonds with potential antibacterial activity, stability at normal physiological pH (7.4) and capable of hydrolysis under very mild acidic conditions (6.5-6.8); [34] and (*iii*) non-ionic PEG, well known for improving the biocompatibility of polycations without a significant loss of antimicrobial activity. The presence of free carboxyl group in AzbPyBA allowed the attachment of the third element by esterification in the second step of synthesis.

In addition, the resulting new macromonomer, amphiphilic AzbPy-*g*-PEG, have a bent-shaped geometry imposed by the 3,5-substituted phenyl ring from DABA moiety, as well as the attachment of PEG side chain in the position one of this phenyl ring. Due to these structural

peculiarities, the new macromonomer has a facially amphiphilic structure (FA), very common in nature by antimicrobial peptides like magainin, cecropin or defensins. It has been reported that the architecture is imperative for antibacterial activity, thus, a synthetic polymer, mimicking such essential physicochemical features could provide fast access to less expensive materials for medical coatings, antimicrobial tubing, and other applications. [35]

After the synthesis, the structures of the new compounds were unambiguously elucidated by combining FTIR spectroscopy and ^{1}H-NMR.

Figure 5.2.1 compares the FTIR spectra of DABA, AzbPyBA and AzbPy-*g*-PEG. The spectrum of DABA presents the characteristic absorption bands of the primary aromatic amine functionality at 3427 cm^{-1} (ν_{asim} NH_2), 3339 cm^{-1} (ν_{sim} NH_2), and 1289 cm^{-1} and 1267 cm^{-1} (ν C-N of NH_2), which are missing in the spectrum of AzbPyBA. The successful synthesis of the latter is corroborated by the new band at 1669 cm^{-1} (ν C=N), which is associate to the formation of the azomethine bonds, as well by the presence of bands typically associated to the pyrrole ring. These are the broad band centred at 3344 cm^{-1} (ν NH), the shoulder at 3124 cm^{-1} (ν =C-H), and other bands at 1089 cm^{-1} (β NH), 1042 cm^{-1}, and 960 cm^{-1} (β C-H).

On the other hand, the FTIR spectra of DABA and AzbPyBA reveal that both aromatic acids are in dimerized form. Thus, the absorption bands due to carbonyl of carboxylic functionalities are centred at values (1686 cm^{-1} and 1701 cm^{-1} for DABA and AzbPyBA, respectively) lower than that typically found for the monomeric form (~1760 cm^{-1}). These bands are accompanied by others at 3212 cm^{-1}

(DABA) and 3221 cm^{-1} (AzbPyBA), which are also specific for aromatic acids dimeric form. Going further with the analysis, it can be observed that in the FTIR spectrum of AzbPy-*g*-PEG the absorption band at 3221 cm^{-1} disappeared concomitantly with the appearance of a broad band centred at approximately 1715 cm^{-1} due to the formation of the ester group. The band at 1632 cm^{-1} in this spectrum was attributed to azomethine bond. The presence of the PEG in the structure of AzbPy-*g*-PEG is confirmed by the additional bands at 1360, 1278 and 1059 cm^{-1} (common vibrations to crystallized PEG in a 7/2 helical structure) besides to those attributed to the *trans zig-zag* conformation at 1241 and 963 cm^{-1}, supporting the assumption that PEG in AzbPy-*g*-PEG is in the crystallized form. [36]

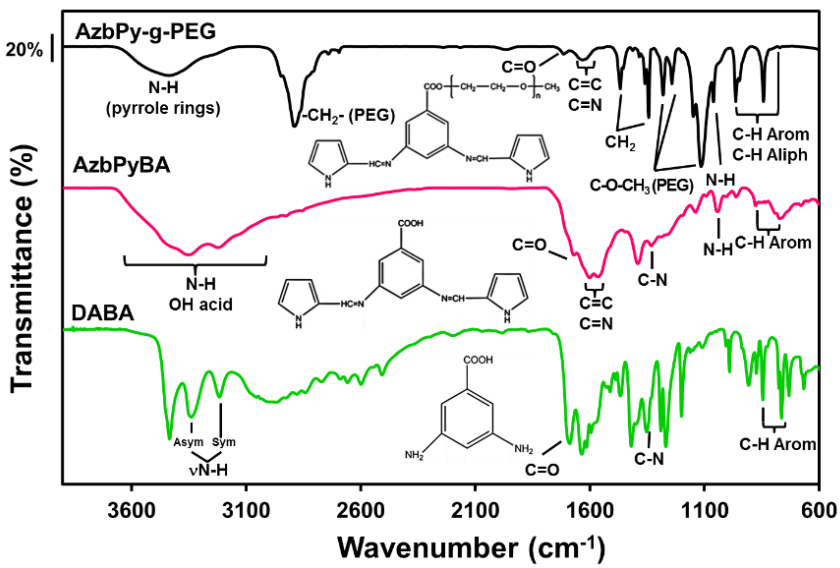

Figure 5.2.1 FTIR spectra of AzbPy-*g*-PEG, AzbPyBA and DABA. The latter two compounds are the precursors used for the synthesis of the AzbPy-*g*-PEG macromonomer.

The expected structures were also confirmed by ^{1}H-NMR spectroscopy, however, the solvent used for the spectra registration must be carefully choosen, taking into consideration structural peculiarities of the compounds, its possible interactions during the solution preparation and interference with the investigated compounds signals. In consequence, the spectrum of the precursor AzbPyBA, containing highly polar functional groups (carboxyl, imine, pyrrole ring), was registered in polar DMSO-d_6, due to solubility reasons, in spite of an appreciable amount of water that can be associated to DMSO due to its hygroscopic nature. Water remnant could act in a negative manner on the Schiff base linkages as was previously reported.[37] In the case of AzbPy-*g*-PEG macromonomer, the propensity to self-assembling (SA) of PEG in selective solvents like DMSO (ε = 47, δ_t = 26.7 MPa$^{1/2}$) can be anticipated, driven by the synergetic combination of hydrophobic and π-π stacking interactions. [38] Thus, a less polar acetone-d_6 (ε = 21, δ_t = 19.9 MPa$^{1/2}$) was employed for the NMR registration, decreasing as much as possible the solvent selectivity toward PEG (δ_t = 24 MPa$^{1/2}$). In this way, was eluded the appearance of the peaks for the hydrophobic and aromatic moieties that decreased the intensity of the peak due to the SA. [39] However, an amount of water was still present in acetone as well and, consequently, the values of the integrals are weakly affected for both hydrophobic (slightly decreased) and hydrophilic moieties (slightly increased), as can be seen in the spectra in Figure 5.2.2, which displays the ^{1}H-NMR spectra of AzbPy-*g*-PEG and AzbPyBA.

It is well known that polar solvents induce a downfield shifting of the signals. As the spectrum of the AzbPy-*g*-PEG macromonomer was

registered in acetone-d_6 (Figure 5.2.2a), an up field shifting for the peaks is expected in comparison with the spectrum of AzbPyBA for which the more polar DMSO-d_6 solvent was used (Figure 5.2.2b). In this case, such shifting was only appreciated for the N–H proton of the Py ring (**h** type in ^{1}H-NMR spectrum in Figure 5.2.2a). The phenomenon has been attributed to the higher sensitivity of the N–H moiety towards the solvent polarity in comparison with the other aromatic protons and to the enhanced electron density in the structure of AzbPy-*g*-PEG due to the PEG presence. On the other hand, the ^{1}H-NMR spectra of both compounds indicates that the azomethine functionality is stable in the registered conditions and exist in *syn* and *anti*-isomeric forms. [37] The increased amount of *syn*-conformer in the case of AzbPy-*g*-PEG compared to AzbPyBA organic molecule has been associated to the effect of the PEG chain grafted at the phenylene ring, which can modify its positions with respect to the azomethine linkage. [40] Therefore, the presence of the hydrophilic molecules of PEG increases the deviation from planarity about the azomethine bond due to steric interactions. [41]

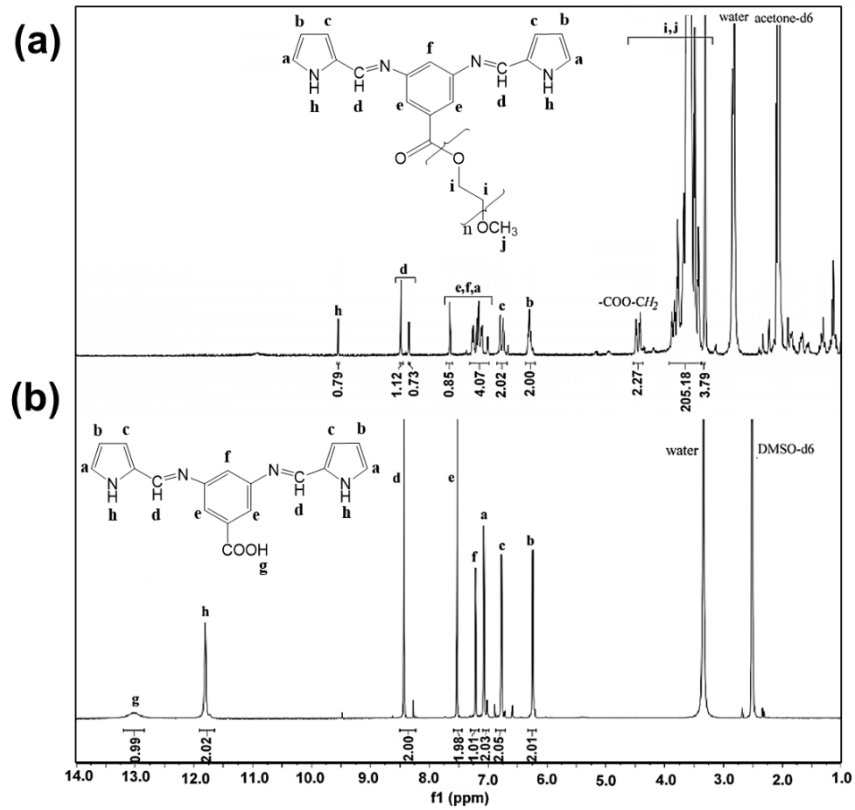

Figure 5.2.2 ^{1}H-NMR spectra of (a) AzbPy-*g*-PEG in acetone-d_6 and (b) AzbPyBA solid compound in DMSO-d_6.

Copolymers characterization. It is widely known that the oxidative chemical polymerization of PPy is limited by the tendency of this ICP to over-oxidize under oxygen-rich environments and the very low yield is usually obtained. Therefore, electrochemical synthesis becomes the most versatile method for the generation of Py-containing polymers and copolymers, [42–47] this procedure is also employed for the synthesis of other heterocyclic ICPs. [12,48] However, the success of the anodic polymerization processes, like those used in this work, largely depends on the mobility of monomers that must reach the electrode surface, *i.e.* lightweight and small size monomers are faster than the

heavy and bulky macromonomers. This is one of the reasons that could explain the unsuccessful homopolymerization of the AzbPy-*g*-PEG macromonomer, which due to its large size presents reduced mobility in organic solutions. This assumption is sustained also by the fact that other bis-pyrrole Schiff bases, similar in structure but with lower molecular weight, were able to be homo electropolymerized.[43]

In order to overcome the limitations associated to the low mobility of the macromomer, P(Py-*co*-AzbPy-*g*-PEG) copolymers were prepared, Scheme 5.2.2.

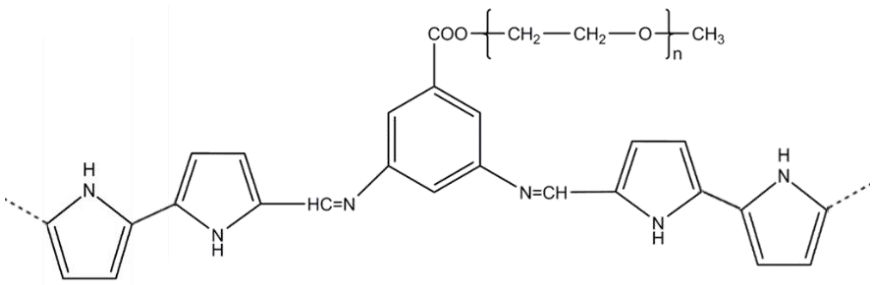

Scheme 5.2.2 Chemical structure of P(Py-*co*-AzbPy-*g*-PEG).

The presence of both PEG and AzbPy groups in the copolymers was assessed by comparing the FTIR spectra of the monomers with those of the final copolymers. Py monomer shows remarkable bands centred at 3125 and 720 cm^{-1}, which correspond to the C^{α}–H stretching and out-of-plane vibration modes, respectively (Figure 5.2.3a). The absence of these two absorption bands in the PPy homopolymer spectrum indicates that the hydrogen atoms at the C^{α}-position were removed during the polymerization process. The characteristic absorption bands of the PPy samples were the fundamental vibrations of the Py rings at 1525 and 1596 cm^{-1}, the =C–N stretching vibrations

at 1464 and 1413 cm^{-1}, the =C–H in-plane vibration at 1072 and 1040 cm^{-1}, and the N–H in plane vibration at 1010 cm^{-1}.[49] Despite the Py monomer was distilled before use, the appearance of the C=O band at 1714 cm^{-1} indicates some overoxidation after the electropolymerization in acetonitrile.[46]

After copolymerization, the most relevant bands from PPy homopolymer remained unaltered and new absorption bands from PEG side chains appeared (Figure 5.2.3b). The absorption band at 2921 cm^{-1} is usually attributed to the large methylene units (-CH_2-) from PEG chains, the bands at 1395 and 1446 cm^{-1} (not present in PPy) corroborating this assignment. The incorporation of AzbPy-*g*-PEG macromonomer to the copolymer formulations was particularly evidenced when the time of electropolymerization increased from 300 s to 1000 s, due to the appearance of the sharp peak at 1727 cm^{-1}, characteristic of ester linkages.

Even when the studied copolymers were synthetized in solutions containing the same amount of monomers, 1:1 Py:AzbPy-*g*-PEG, electropolymerization time influenced the final ratios, which were determined by FTIR absorption bands of the N–H stretching in Py units (at 3430 cm^{-1}) and the ether deformation (at 1108 cm^{-1}) in PEG units. For calculations, the Py:PEG molar ratio (1:1) and the molecular weight of the macromonomer (2313.4 g/mol) were taken into account. The final comonomers proportion in the generated films at 300, 500 and 1000 s was at about 521:1; 208:1; and 125:1 (Py:macromonomer), respectively. According to previous discussion, the inferior amount of macromonomer units in the copolymer films is probably due to the

lower mobility of the AzbPy-*g*-PEG macromonomer opposite to the higher mobility of Py molecules.

The structure of P(Py-*co*-AzbPy-*g*-PEG) was also corroborated by Raman spectroscopy, as is reflected in Figure 5.2.3c. The spectrum of PPy presents peaks at 1574 cm^{-1} and 1367 cm^{-1}, which arise from the conjugated polymer backbone (C=C stretching mode) and Py ring, respectively, and three bands at around 1090 cm^{-1}, 971 cm^{-1} and 935 cm^{-1} that are related to the in-plane and out-of-plane deformations of N–H and C–H groups.[50,51] Graft copolymers generated using τ = 500 and 1000 s also present a broad band at around 2890-2940 cm^{-1}, which has been attributed to the symmetric stretching vibrations of methylene groups of PEG chains.[29,52]

SEM micrographs and AFM images displayed in Figures 5.2.4, reveal a cauliflower-like morphology for P(Py-*co*-AzbPy-*g*-PEG) films, independently of τ, which is similar to what was found for PPy.[53,54] However, the films thickness (L) of P(Py-*co*-AzbPy-*g*-PEG) increases with τ, as was evidenced by profilometry measurements. Thus, values of L = 1.4 ± 0.4 µm, 2.6 ± 0.5µ, and 4.1 ± 0.5 µm were obtained for films generated using τ = 300, 500, and 1000 s, respectively. It can be assumed that the bent-shaped geometry and the presence of long PEG side chains in AzbPy-*g*-PEG comonomer hinder the copolymers intermolecular chains packing, having as the result the increasing of film thickness.

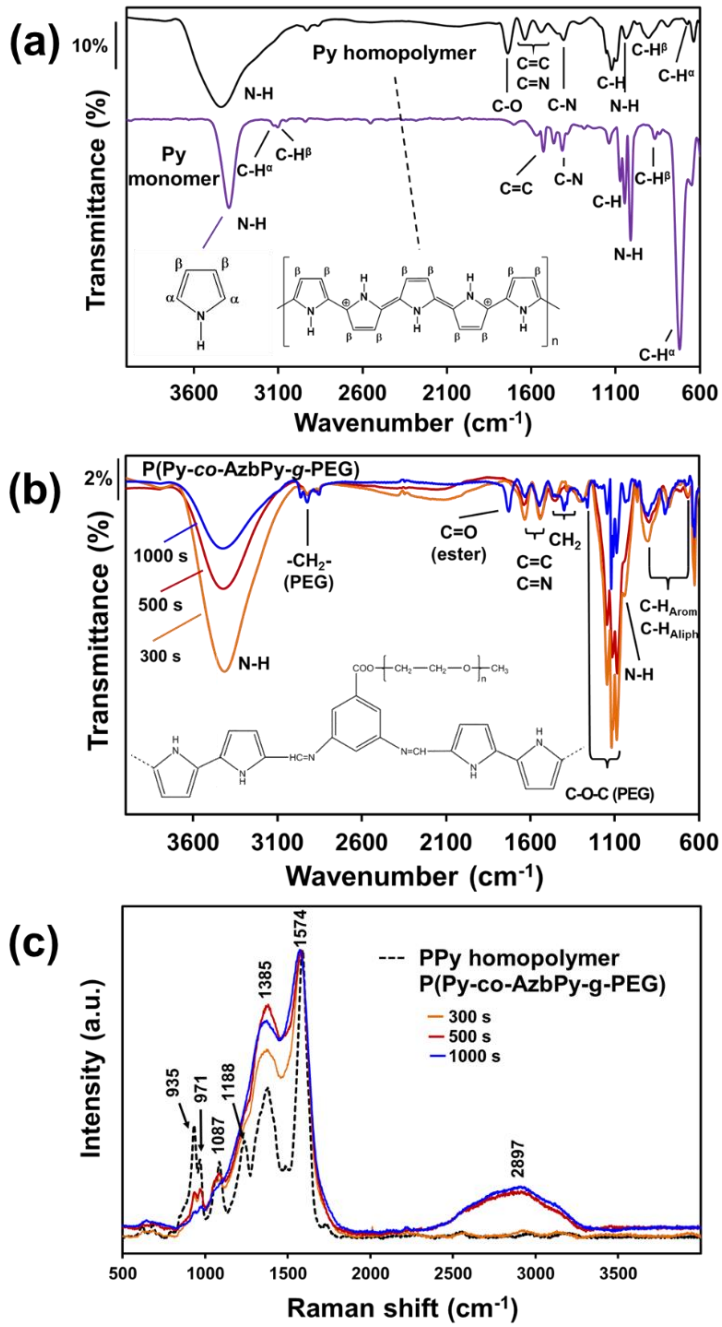

Figure 5.2.3 FTIR spectra of: (a) Py monomer and PPy prepared by CA using τ = 300 s; and (b) P(Py-*co*-AzbPy-*g*-PEG) synthesized by CA using τ = 300, 500 and 1000 s. (c) Raman spectra of P(Py-*co*-AzbPy-*g*-PEG) synthesized by CA using τ = 300, 500 and 1000 s. All films were generated on stainless steel electrodes as working electrodes.

Root mean square roughness (R_q), which was determined by AFM using a scan window size was 5×5 μm^2, increased from 91 ± 5 nm to 123 ± 11 nm when τ increase from 300 s to 1000 s. *L* and R_q values of PPy films prepared using τ = 300 s (2.2 ± 0.1 nm and 112 ± 9.9 nm, respectively) are higher than those of the graft copolymer obtained using the same τ value. A possible explanation for these experimental findings is that the anodic polymerization of PPy is dominated by the crosslinks in the β- and β'- ring positions, [55] allowing for a non-regular growth of polymer chains. The formation of multidirectional branches results in an increment of both *L* and R_q compared to other ICPs. [54]

As a part of the surface characterization, the copolymer wettability was determined by measuring the water contact angle (WCA), the reported values are the average of 10 measures for each condition. As was expected, the wettability of the copolymer increases with the film roughness and the content of hydrophilic grafted PEG chains. Thus, the values of WCA determined for P(Py-*co*-AzbPy-*g*-PEG) films obtained at τ = 300, 500 and 1000 s were 71.0º ± 0.4º, 62.6º ± 0.3º, 48.5º ± 0.3º, respectively, evidencing that the hydrophilicity increases with τ. The WCA exhibited by PPy, (58.9º ± 0.1º), was intermediate between those obtained for the copolymers prepared using τ = 300 and 1000 s, which is fully consistent with previous evidences about the influence of R_q on the wettability of PPy. [56]

The increased wettability observed for P(Py-*co*-AzbPy-*g*-PEG) films synthesized at the largest τ value can also be associated to a potential higher content of PEG on copolymer film surface.

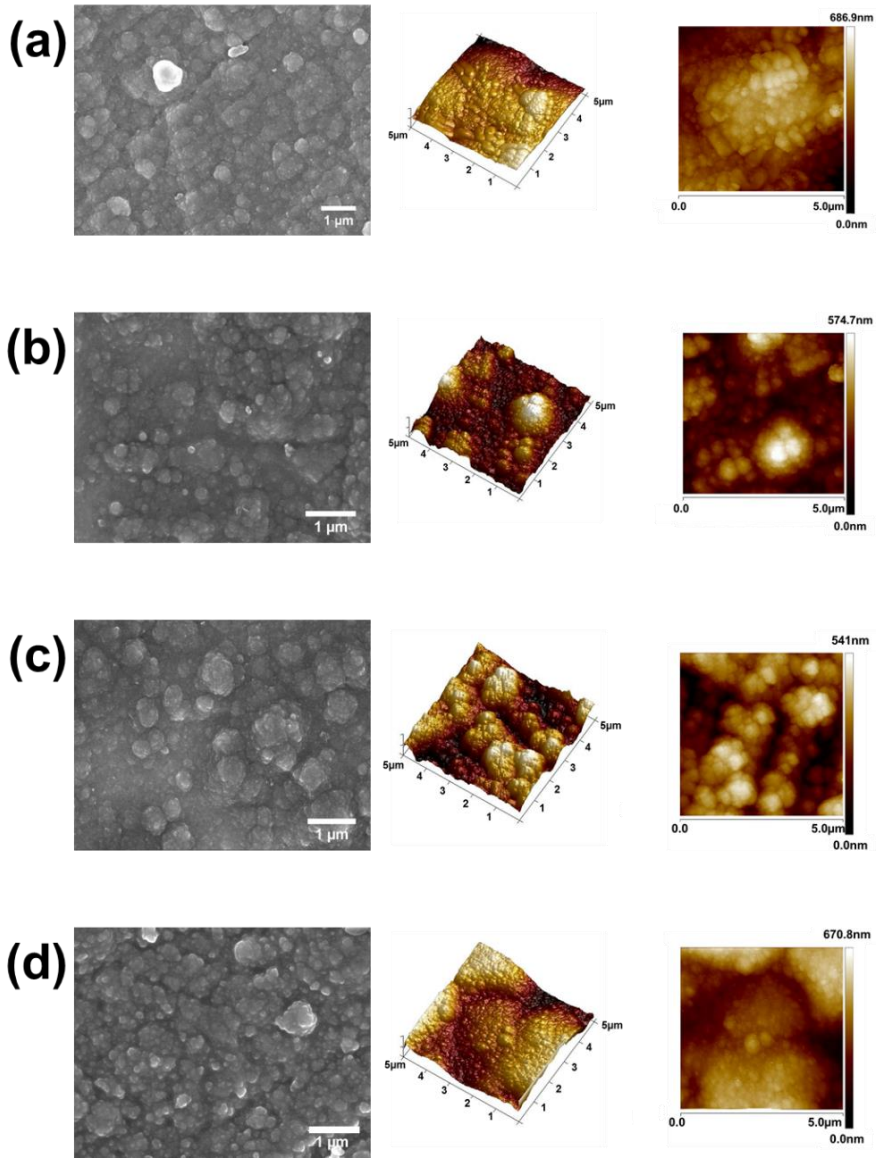

Figure 5.2.4 SEM micrographs (left), 3D topographic (centre) and 2D height AFM images (5×5 µm^2) (right) of PPy (a) and P(Py-*co*-AzbPy-*g*-PEG) prepared by CA during τ = 300, 500 and 1000 s (b, c and d, respectively). All samples for AFM analyses were supported on stainless steel electrodes.

The grafting of hydrophilic, polar PEG chains to the conjugated polymer backbone is expected to affect the electrochemical activity and the doping level. Control cyclic voltammograms of PPy deposited onto stainless steel showed the highest electroactivity with a voltammetric charge of 5.2×10^{-2} C (Figure 5.2.5a). Nevertheless, the control homopolymer displayed the highest loss of electrochemical activity (LEA = 48%) after 50 consecutive cycles, which has been attributed to the dense network of chemical crosslinks formed during the anodic polymerization process. [55] Thus, the formation of cross-links, which is also promoted by oxidation-reduction cycles, favours the organization of polymer chains in compact structures, precluding the diffusion of the dopant ions through the polymer/electrolyte interface.

On the other hand, the electroactivity of P(Py-*co*-AzbPy-*g*-PEG) copolymers was less than half of the one determined for PPy homopolymer, even when τ = 1000 s. More specifically, the electrochemical activity experiences a reduction of 54-65% ($2.8\text{-}3.4 \times 10^{-2}$ C) upon the incorporation of AzbPy-*g*-PEG macromonomer. This is consistent with the well-known detrimental effect caused in the heterocyclic ring conjugation by electron-donating substituents.[57] However, the LEA was significantly lower for the grafted copolymers than for the homopolymer after fifty oxidation-reduction cycles, evidencing that the new semiconducting copolymers present good electrochemical stability when consecutive redox processes are applied.

UV-vis spectra displayed in Figure 5.2.5b indicate that the electronic properties of P(Py-*co*-AzbPy-*g*-PEG) and PPy are quite

similar, no disturbing effect due to the presence of the electron-donating groups being detected. The UV-vis spectra show an absorption band at the visible region (~ 300 nm), which has been attributed to the π–π transition in the tri-substituted benzene ring of AzbPy units. On the other hand, PPy and P(Py-*co*-AzbPy-*g*-PEG) copolymers present two broad absorption transitions starting at 320 nm and finishing at ~ 500 nm, which have been associated to the polaron and bipolaron bands of the conductive quinoid and aromatic forms from heterocycle conjugated rings and Schiff base linkages.[45] Additionally, another high absorption band starts at 600 nm, extending to values higher than 800 nm. This corresponds to the dopant molecules interacting with the polymer chains, reflecting the complete oxidation of the latter. [58] This latter transition is practically identical for all copolymers, with exception of P(Py-*co*-AzbPy-*g*-PEG) generated at τ = 300 s that shows a slight reduction, evidencing that the doping level is quite similar for all systems.

The band gap energy (ε_g) was calculated for each sample from the intersection of the dotted line showed in Figure 5.2.5b, which corresponds to the tangent to the absorption band, and the absorption wavelength edge. The absorption maxima (λ_{max}) and the ε_g of grafted copolymers and PPy are listed in Table 5.2.1. The band gaps obtained for our systems are comprised between 2.25 (PPy) and 2.30 eV (P(Py-*co*-AzbPy-*g*-PEG) at τ = 300 s). These values are in accordance with that reported by Brooke *et al.* [59] for films of PPy with PEG-PP-PEG triblock copolymers, which were prepared by vapour phase deposition.

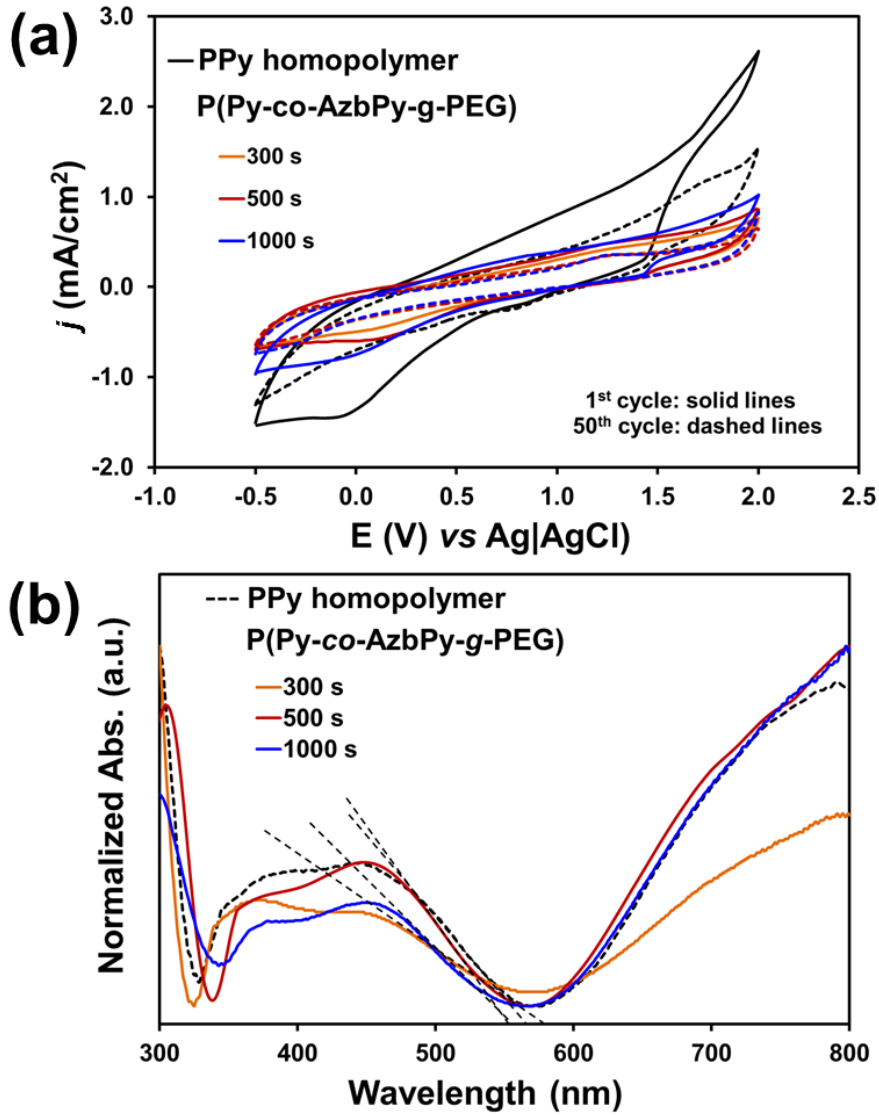

Figure 5.2.5 (a) Cyclic voltammograms (scan rate: 50 mV s^{-1}) recorded in a 0.1 M $LiClO_4$ acetonitrile solution for PPy and P(Py-*co*-AzbPy-*g*-PEG) copolymers obtained using τ = 300, 500 and 1000 s: 2nd cycle (solid lines) and 50th cycle (dashed lines). (b) UV-vis spectra of the homopolymer and the copolymers freshly generated by CA onto ITO glass working electrodes. The dotted straight lines represent the best fit for the tangent of the band used to determine the E_g for each system.

Table 5.2.1 Maximum absorption and optical band gap for PPy and P(Py-*co*-AzbPy-*g*-PEG).

Sample	Polymerization time (s)	λ_{max} ♦ (nm)	λ_{min} ♣ (nm)	E_g ♠ (eV)
PPy homopolymer	300	381, 451	551	2.25
P(Py-*co*-AzbPy-*g*-PEG)	300	369, 450	539	2.30
P(Py-*co*-AzbPy-*g*-PEG)	500	370, 449	547	2.27
P(Py-*co*-AzbPy-*g*-PEG)	1000	369, 451	544	2.28

♦Maximum absorption bands obtained by UV-visible, in solid state. ♣ Minima absorption band obtained by the intersection of the line of best fit to the lower absorption band and the tangent to the minimum absorption wavelength showed at Figure 5.2.5b. ♠*Eg* calculated as: $Eg = 1.24 \times 103/\lambda min$.

Antimicrobial activity, protein adsorption and cytotoxicity of P(Py-co-AzbPy-g-PEG). It has been reported that materials with azomethine exhibit antimicrobial activity. [60,61] Thus, antimicrobial response of PPy, P(Py-*co*-AzbPy-*g*-PEG) and AzbPy-*g*-PEG are compared in Figure 5.2.6a. As it can be seen, both the macromonomer and the graft copolymer exhibit an antibacterial response against *Escherichia coli* and *Staphylococcus aureus*, while the antimicrobial activity of steel and PPy is null. Previous studies indicated that the response of PPy against bacteria strongly depends on the dopant and redox state of the ICP and the characteristics of the bacterial strain. [33,62,63]

Although this effect could be due to the action of Schiff base moiety, other explanations are also possible since the concentration at which the antibacterial test was performed (4.3 mM) is approximately in the same range with those (6 mM) for which "T-shaped" septithiophene oligomers grafted with PEG_{2000} formed the self-assembled "core-shell" type micellar structure. [64] In that case, the access to the Schiff base groups was hindered by the PEG shell of the micelles and, therefore, the observed inhibitory effect could be due to

the PEG ability for complexing metal cations, in particular Ca^{2+}. [65] Thus, a displacement of Ca^{2+} ions from the outer membrane of bacterial cells toward AzbPy-*g*-PEG self-assembled micelles can disrupt its integrity, [66] having as a result the bacterial cells growth inhibition.

Besides antibacterial response, bovine serum albumin (BSA) and lysozyme (Lyz) proteins adsorption was also considered. These proteins, which contain free cysteine residues, (that can be exploited in conjugation studies or chemical adsorption with other substances), have considerably different molecular weight (66.5 kDa for BSA and 14.3 kDa for Lyz). Furthermore, Lyz exhibits an ellipsoidal shape as quaternary structure, in which both ordered (30% α-helix, 27% β-turn and 13% β-sheet secondary structures) and unordered (30%) regions coexist,[67] while "heart"-shaped[68] BSA's secondary structure is predominantly α-helical, with the remaining polypeptide occurring in turns and extended or flexible regions (*i.e.* with no β-sheets).[69]

Adsorption of BSA and Lyz onto the surface of steel, PPy and P(Py-*co*-AzbPy-*g*-PEG) generated at τ = 1000 s is shown in Figure 5.2.6b. As it can be seen, the adsorption of both BSA and Lyz is significantly higher onto the graft copolymer film than onto the PPy homopolymer. This has been attributed to the presence of PEG groups, which facilitates the interaction with the hydrophilic residues of the proteins.

In contrast, the N–H groups of the PPy are expected to be sterically hindered, making difficult their interaction with the polar residues of the proteins. Indeed, the adsorption of proteins onto PPy is even lower than that observed for the steel substrate. These results are fully

consistent with hydrophilicity ranking determined by WCA measurements (*i.e.* 48.5 ± 0.3 and 58.9º ± 0.1º for P(Py-*co*-AzbPy-*g*-PEG) and PPy, respectively). Also, the low protein adsorption observed for PPy in comparison with P(Py-*co*-AzbPy-*g*-PEG) indicates that, in the latter, PEG groups play the most important role in the interactions with Lyz and BSA.

On the other hand, P(Py-*co*-AzbPy-*g*-PEG) exhibits higher affinity for Lyz than for BSA, even though the amount of charged residues is significantly higher in the latter than in the former. This result indicates the preference of the copolymer towards small ellipsoid proteins with respect to bulky proteins organized in helical bundle domains, in which the attractive electrostatic interactions induced by many charged residues are shielded by residues located at neighboring secondary motifs.

The potential cytotoxicity of the P(Py-*co*-AzbPy-*g*-PEG), PPy and steel was evaluated using the MTT assay for cell viability determination, which was conducted after 72 h culturing Vero and COS-1 cells. No evidence of cytotoxicity was found for the PPy and P(Py-*co*-AzbPy-*g*-PEG). Nevertheless, differences in the number of cell growth in the films were detected (Figure 5.2.6c), the cell viabilities are 10-20% higher for P(Py-*co*-AzbPy-*g*-PEG) than for PPy. This behaviour has been attributed to the well-known biocompatibility of PEG grafted chains, which improves the behaviour for cellular proliferation of the semiconducting polymer backbone. The influence of steel, PPy and P(Py-*co*-AzbPy-*g*-PEG) films on the Cos-1 cell morphology was qualitatively evaluated by SEM (Figure 5.2.6d).

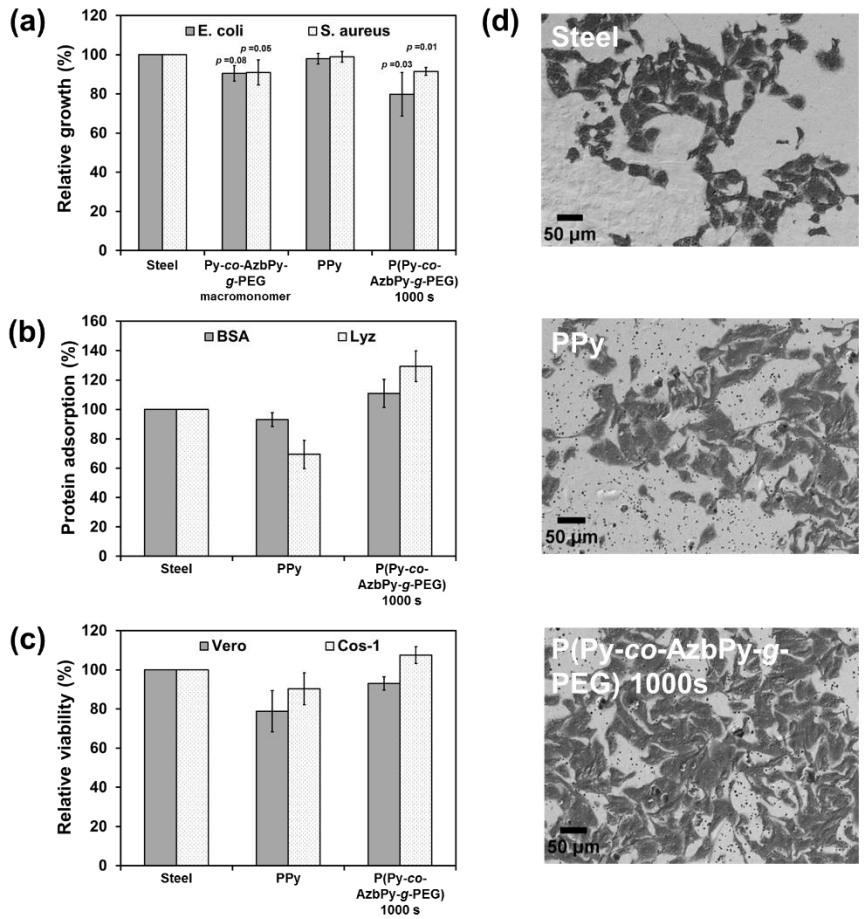

Figure 5.2.6 (a) Antimicrobial response of Steel (control), AzbPy-*g*-PEG macromonomer, PPy and P(Py-*co*-AzbPy-*g*-PEG) τ = 1000 s against *Escherichia coli (E. coli)* and *Staphylococcus aureus (S. aureus)*. Statistical analyses were performed with a confidence level of 95% ($p \leq 0.08$) by Student's T-test. (b) BSA and Lyz protein adsorption, (c) proliferation of Vero and Cos-1 cultured cells and (d) SEM micrograph of Cos-1 cell after 3 days cultured in Steel (control), PPy and P(Py-*co*-AzbPy-*g*-PEG) τ = 1000 s.

These results suggest that P(Py-*co*-AzbPy-*g*-PEG) is a promising candidate for the development of biomedical applications, like implantable integrated devices for release of neurotransmitters under

real-time monitoring. In this context, we explored the potential of P(Py-*co*-AzbPy-*g*-PEG) for the sensitive detection of serotonin (5-hydroxytryptamine), which is a monoamine neurotransmitter biochemically derived from tryptophan and primarily found in the blood platelets and the central nervous system of animals and humans.

Selective detection of Serotonin using P(Py-co-AzbPy-g-PEG). Py is a well-known π-conjugated building block typically employed for engineering planar anionic receptors, acting as both metal-coordination ligand (N sites) and as hydrogen-bonding donor (N–H moiety). [70] Additionally, the complementarity between the electron-donor and electron-acceptor behaviour of the Py ring and the serotonin neurotransmitter, respectively, represents a benefit for the design of a sensitive sensor.

Figures 5.2.7a and 5.2.7b compare the differential pulse voltammograms recorded in solutions with different concentrations of serotonin (from 0 to 20 μM) in 0.1 M PBS (pH 7.4) for PPy (τ= 300 s) and P(Py-*co*-AzbPy-*g*-PEG) (τ = 1000 s), respectively. As it can be seen, both polymers are able to catalyse the oxidation of serotonin molecules in a low potential range. Although the anodic peak current decreases with the serotonin concentration decreasing, the position of the peak potential in the copolymer film remains almost constant at 0.29-0.31 V, for all the tested concentrations. In a very recent study, Cristea and co-workers [71] prepared detectors of serotonin using electrochemically generated PPy nanoparticles, which were decorated with catalytic gold nanoparticles. However, the P(Py-*co*-AzbPy-*g*-PEG) sensor presents important advantages with

respect to the latter one, as for example, the easy preparation of polymeric films without need of activation with metal nanoparticles.

The serotonin detection limit of PPy and P(Py-*co*-AzbPy-*g*-PEG) sensors was derived from the variation of the maximum of peak current density (*j*), as determined by DPV, against the serotonin concentration. The resulting calibration curves (Figures 5.2.7c and 5.2.7d) evidence a linear behaviour in the whole interval of examined serotonin concentrations. The detection limit expressed as 3.3 σ/*S*, where σ and *S* is the standard deviation of the response and the slope of the calibration curve for serotine concentrations ranging from 0.5 to 20 μM is 0.04 and 0.07 μM for PPy and P(Py-*co*-AzbPy-*g*-PEG), respectively.

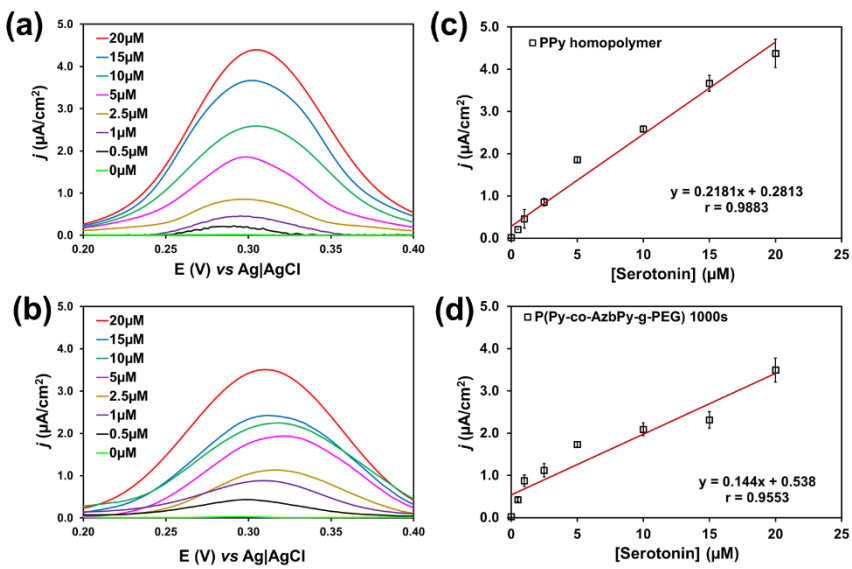

Figure 5.2.7 Differential pulse voltammograms in 0.1 M PBS (pH 7.2) with serotonin concentrations ranging from 0.5 to 20 μM for: (a) PPy and (b) P(Py-*co*-AzbPy-*g*-PEG) generated on glassy carbon electrode using τ = 300 and 1000 s, respectively. Calibration curves for serotonin detection

in a concentration range from 0 to 20 μM for (c) PPy and (d) P(Py-*co*-AzbPy-*g*-PEG).

In summary, the structural characteristics of P(Py-*co*-AzbPy-*g*-PEG) are suitable for complex biomedical applications in which several functions must be fulfilled simultaneously, as for example, implantable electrodes to monitor the level of serotonin. This kind of electrodes requires not only a high detection capacity, as the one imparted by the conjugated main chain of copolymer, but also must present the biocompatibility provided by the PEG grafted chains to facilitate its integration in the body, and antimicrobial activity induced by the synergistic combination of chemical and architectural peculiarities of copolymer to prevent infections after implantation. Additionally, the modified electrode obtained in this study is ease to prepare compared to other hybrid materials being developed, as for example, that would combine metallic nanoparticles and carbon nanotubes, [72] or complex electrodes. [73–75]

Conclusions

In this work, chemically and architecturally complex copolymers containing Py ring and Schiff base functionalities in the backbone and PEG as grafted chains have been engineered and characterized. The properties of the obtained P(Py-*co*-AzbPy-*g*-PEG) have been compared with those of bare PPy homopolymer. The antimicrobial activity of the novel graft copolymer was enhanced compared to the previously studied copolymers.

Our results show that the synthetic approach which combine, sequentially, the “macromonomer technique” with electrochemical

polymerization can be a useful alternative allowing for combination of incompatible building blocks to obtain multifunctional materials capable of encompassing diverse applications.

5.3 The biocompatible polythiophene-*g*-polycaprolactone copolymer as an efficient dopamine sensor platform

Abstract

Amphiphilic copolymers consisting of an all conjugated polythiophene backbone and sparsely attached oligo-ε-caprolactone side chains have been prepared by anodic electropolymerization of hydroxymethyl-3,4-ethylenedioxythiophene (HMeEDOT) with a thiophene-ended oligo-ε-caprolactone macromonomer (Th-PCL), obtained by ring opening polymerization of ε-caprolactone with thiophene methanol. The random copolymers, obtained starting from two different molar ratios of the comonomers in the feed (HMeEDOT:Th-PCL of 80:20 and 60:40), and the homopolymer (PHMeEDOT) were synthesized by using three different working electrodes. After structural characterization by FTIR, the electrochemical, morphological and surface properties of the obtained copolymers were examined, results evidencing a dependence on both the working electrode and the composition in the feed. In order to evaluate the opportunity of copolymers's further bioapplications, biodegradability, cell proliferation and biocompatibility investigations were carried out. By combining the results of electrochemical characterization with those of biocompatibility and dopamine sensing capability, it was concluded that comonomers feed ratio of 80:20 could be the optimal choice for the potential use of these amphiphilic copolymers in sensing devices.

Materials and methods

Materials. 3-thiophene-methanol (Th-MeOH) (Aldrich), ε-caprolactone (ε-CL; Aldrich), stannous octanoate (Sigma), hydroxymethyl-3,4-ethylenedioxythiophene (HMeEDOT; Sigma-Aldrich, 95%) and acetonitrile (Panreac S.A., PA) were used as received. Tetrabutylammonium tetrafluoroborate (TBATFB; Sigma-Aldrich, 95%) was stored in an oven at 80 °C before its use in the electrochemical trials. The other used solvents were purified and dried by usual methods.

Dulbecco's phosphate buffered saline solution (PBS) 0.1 M with pH 7.4, without calcium chloride and magnesium chloride, was prepared as electrolyte solution for electrochemical trials. DA hydrochloride (3-hydroxytyramine hydrochloride), ascorbic acid (AA; L-configuration, crystalline) and uric acid (UA; crystalline) of analytical reagent grade were purchased from Sigma-Aldrich (Spain).

For cell culture experiments, Cos-1 and Vero cells (kidney epithelial and fibroblast cells, respectively; obtained from African green monkey, *Cercopithecus aethiops*) were purchased from ATCC (USA). Dulbecco's modified Eagle's medium (DMEM, with 4500 mg of glucose/L, 110 mg of sodium pyruvate/L and (2 mM) L-glutamine), penicillin-streptomycin, 3-(4,5-dimethylthiazol-2-yl)-2,5-diphenyltetrazolium bromide (MTT, 97.5%) and trypsin-EDTA solution (0.05% trypsin, 0.02% EDTA) were all purchased from Sigma-Aldrich (USA). Fetal bovine serum (FBS) and trypan blue stain (0.4%) were purchased from Gibco, UK. Dimethyl sulfoxide (99.0%) was purchased from Panreac Quimica S.A.U. (Spain) and sodium azide (NaN_3, ≥ 99.5%) from Sigma-Aldrich (USA).

Synthesis of Th-PCL macromonomer. The oligo-ε-caprolactone based macromonomer, hereafter denoted Th-PCL, was prepared by ring opening polymerization (ROP) of ε-CL using Th-MeOH as initiator and stannous octanoate, $Sn(Oct)_2$, as catalyst (Scheme 5.3.1), following a slightly modified reported procedure. [76,77] In brief, appropriate amounts of ε-CL, initiator and catalyst were added under nitrogen in a previously flamed and nitrogen-purged two neck round-bottom flask equipped with a dropping funnel and magnetic stirrer. The ε-CL polymerization was carried out in bulk condition at 110 °C, and taking into account a concentration of 3-thiophene methanol (initiator monomer) of 0.61 mol/L, 0.030 mol/L of ε-CL and 3.0×10^{-3} mol/L of catalyst $(Sn(oct)_2)$. After 24 h, the mixture was diluted with CH_2Cl_2 and poured into a tenfold excess of cold methanol. The polymer was collected after filtration and dried at room temperature in vacuum for 3 days.

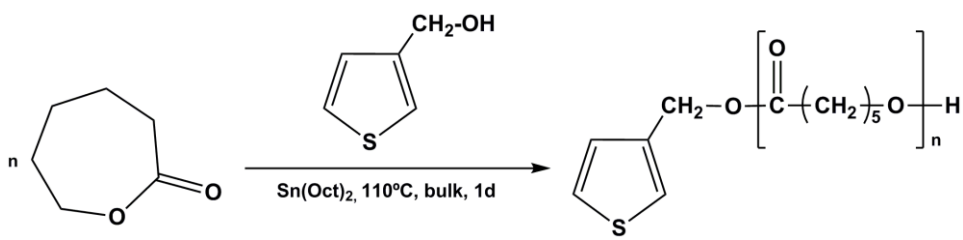

Scheme 5.3.1 Synthesis of the Th-PCL macromonomer.

Synthesis of PTh-g-PCL copolymers. The homopolymer and the copolymers were prepared by chronoamperometry (CA) with an Autolab PGSTAT302N equipped with the ECD module (Ecochimie, The Netherlands) using a three-electrode cell under a nitrogen atmosphere (99.995% in purity) at room temperature. Steel AISI 316L

and ITO sheets of 0.5 × 0.5 cm^2 area were employed as working electrode for characterization studies, while glassy carbon (GC) electrodes of 2 mm diameter were used for detection assays. The counter electrode was made of AISI 316L while the reference electrode was an Ag|AgCl electrode containing a KCl saturated aqueous solution (E^0 = 0.222 V at 25ºC), which was connected to the working compartment through a salt bridge containing the electrolyte solution.

For preparation of PHMeEDOT, the anodic compartment was filled with 5 mL of a 10 mM acetonitrile solution of HMeEDOT containing 0.1 M TBATFB as supporting electrolyte, while the cathodic compartment was filled with 10 mL of the same electrolytic solution. Polymerizations were carried out applying a constant potential of +1.50 V during a generation time (τ) of 500 seconds. On the other hand, PTh-*g*-PCL copolymers were prepared considering 80:20 and 60:40 HMeEDOT:Th-PCL molar ratios at the same total molar concentration in solution. Copolymers were also obtained applying a potential of +1.50 V, whereas the polymerization time was adjusted as a function of the monomers ratio: τ = 500 and 800 s for 80:20 and 60:40 HMeEDOT:Th-PCL ratios, respectively.

Characterization of the macromonomer and the prepared copolymers. A detailed description of the macromonomer and copolymers characterization was included in Chapter 4. The Th-PCL macromonomer was characterized by ^{1}H-NMR in $CDCl_3$, GPC, DSC and FTIR through KBr pellets. While, graft copolymers were evaluated by FTIR also with KBr pellets, SEM operated a 5 kV,

UV-vis of solids films deposited onto ITO-glass substrate, WCA, profilometry and degradability.

In order to evaluate its potential use as sensing devices in medicine, electrochemical and biological assays were carried out by CV and cellular proliferation, respectively. Electrochemical characterizations were conducted in a phosphate buffer solution (PBS) 0.1 M (pH= 7.4) at room temperature. The initial and final potentials were –0.4 V, and the reversal potential was +0.8 V. A scan rate of 50 mV/s was used.

Finally, CV was also applied for the electrochemical detection of dopamine, according to the procedure described in Chapter 4. The assays were carried out with a glassy carbon electrode (3.14×10^{-2} cm^2 of surface area) as WE in PBS (pH 7.4) solutions containing different concentrations of dopamine.

Results and discussion

Macromonomer characterization. Th-PCL experimental number average molecular weight (M_n) was determined using Equation 5.3.1, with the integral values of the characteristic peaks from ^{1}H-NMR (Figure 5.3.1a), while that M_n, theoretically expected, was calculated by molar concentrations of reactant and initiator in the feed (Equation 5.3.2).

$$M_{n,NMR} = \frac{(I_{4.067} + I_{3.64})}{I_{5.12}} \cdot M_{n,\varepsilon-CL} + M_{n,Th-MeOH} \qquad \textbf{Eqn. 5.3.1}$$

$$M_{n,theor} = \frac{[\varepsilon - CL]}{[Th - MeOH]} \cdot M_{n,\varepsilon-CL} + M_{n,Th-MeOH} \qquad \textbf{Eqn. 5.3.2}$$

where $I_{4.067}$, $I_{3.64}$ and $I_{5.12}$ are the intensities of the peaks at 4.067 ppm, 3.64 ppm and 5.12 ppm, respectively, $M_{n,\varepsilon\text{-}CL}$ is the molecular weight of ε-CL (114.15 g/mol), $M_{n,Th\text{-}MeOH}$ is the molecular weight of Th-MeOH (114.16 g/mol), and a ε-CL: Th-MeOH molar ratio of 20:1.

There resulting values, $M_{n,NMR}$ = 2511 g/mol and $M_{n,theor}$ = 2430 g/mol, exhibit a very good agreement and are consistent with a polymerization degree of oligo-ε-caprolactone of $n \approx 21$. The slight inaccuracy of M_n value obtained by GPC measurements, $M_{n,GPC}$ = 3120 g/mol, is probably due to the differences between the molecular characteristics of the polystyrene used as standards and the more polar oligo-ε-caprolactone, as observed in other cases. [76]

The thermal behaviour of the synthesized macromonomer was investigated by DSC (Figure 5.3.1b). The calorimetric plot evidences an exothermic peak due to the crystallization of oligo-ε-caprolactone, which has a maximum at T_c= 31ºC, and their melt at T_m= 55ºC, these values being fully consistent with those reported in the literature for the pristine polymer. [78] On the other hand, the crystallinity found for the macromonomer was very high, χ_c= 0.66, which is fully consistent with the fact that the degree of crystallinity of PCL largely increases with decreasing molecular weight. [79]

The FTIR spectrum of Th-PCL (Figure 5.3.2a) presents strong absorptions originating from both the PCL chain and the thienyl ring: 3441cm^{-1} OH from oligo-ε-caprolactone chains ends; 3102 cm^{-1} β(C–H) stretching vibration and α(C–H) stretching vibration of the thienyl ring; 1726 cm^{-1} C=O ester from oligo-ε-caprolactone in crystalline form; 1557, 1540 cm^{-1} symmetric stretching vibrations of

the thienyl ring; 1294 cm^{-1} (C–O and C–C) and 1189 cm^{-1} (ν O=C–O) PCL crystallization-sensitive bands; 706 cm^{-1} C–S; 581 cm^{-1} γ ring deformation; and 450 cm^{-1} C–S–C thienyl ring deformation.

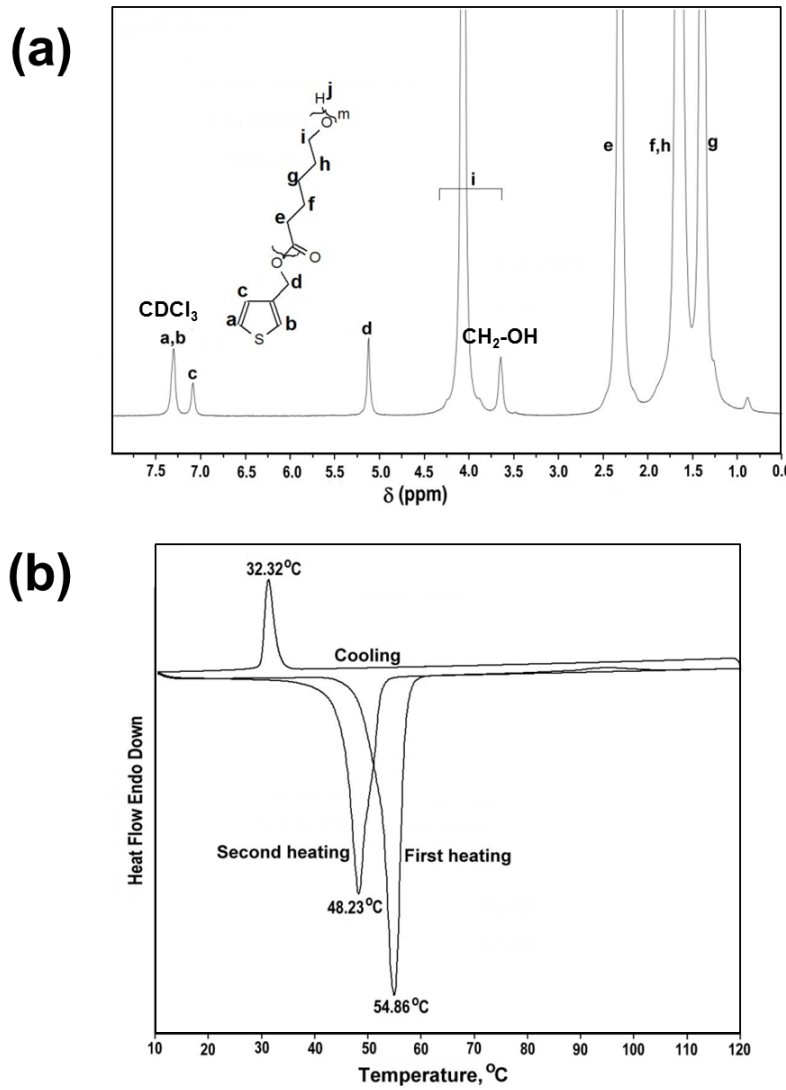

Figure 5.3.1 (a) ^{1}H-NMR spectrum of Th-PCL macromonomer in $CDCl_3$ and (b) DSC traces of Th-PCL macromonomer.

Copolymers characterization. Electropolymerization of Th-PCL macromonomer was unsuccessful, maybe due to the characteristics of its structure. The oligo-ε-caprolactone contains in its structural units electron-withdrawing ester groups, while the chain end shows a reactive hydroxyl function. As it was previously noticed,[37] such structural peculiarities could hinder electrochemical polymerization by a high oxidation potential. The ester group is a well-known moiety for increasing of oxidation potential.[80] Moreover, in some cases, the anodic polymerization of thiophenes with reactive functional groups (*e.g.* -NH_2, -OH and –COOH) has been reported to be difficult due to their substantial nucleophilicity, which allow the functional groups to attack on the radical cation intermediates formed during electropolymerization, hence inhibiting the polymerization process.[81] On the other hand, taking in account that the acetonitrile is a bad/non-solvent for polycaprolactone,[82] is very probable that it exists in the polymerization systems in a collapsed form, which sterically could hinder the reactive positions of the Th ring.

The polymerization degree achieved for the oligo-ε-caprolactone in Th-PCL, $n \approx 21$, is low enough to enable the copolymerization with other comonomers and large enough to preserve the most interesting property of PCL within the context of this study (*i.e.* biocompatibility). However, the incorporation of comonomers is expected to reduce rapidly the grafting density, as was observed for PTh-*g*-PEG[31] and PTh-*g*-PEO[83] (PEO= polyethylene oxide). As our final aim was to produce biocompatible grafted copolymers able to detect DA efficiently, HMeEDOT was selected as the most appropriated comonomer for the preparation of PTh-*g*-PCL (Scheme 5.3.2). Thus,

due to its exocyclic hydroxyl group, PHMeEDOT was found to be more sensitive and selective towards DA detection than PEDOT, which in turn exhibited higher performance than unsubstituted PTh.[84]

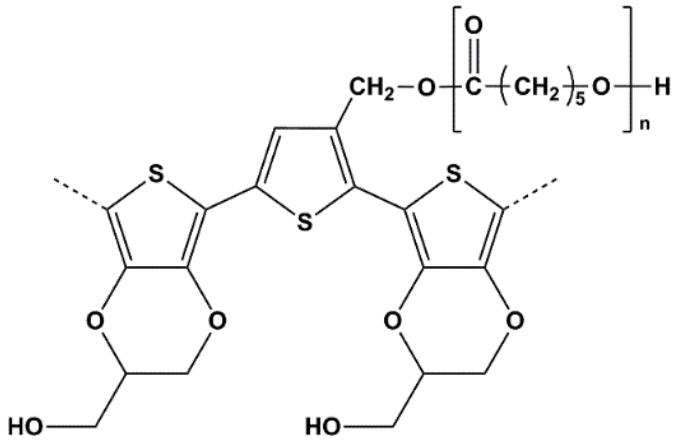

Scheme 5.3.2 Chemical structure of PHMeEDOT/PTh-*g*-PCL copolymer (hereafter coded as PTh-*g*-PCL for simplification).

PTh-*g*-PCL films were prepared by CA using 80:20 and 60:40 HMeEDOT:Th-PCL molar ratios, while PHMeEDOT films were obtained as control. TBATFB was used as supporting electrolyte due its already known ability to improve the electrochemical properties of PHMeEDOT. [84,85] CV of HMeEDOT and Th-PCL solutions in acetonitrile with 0.1 M TBATFB (not present), enabled us to choose the polymerization potential of +1.50 V, maximizing the rate of the polymerization process without oxidizing the reaction medium and, at the same time, avoiding the over oxidation of the generated materials. Considering the results in Section 5.2 and the difficulties for the polymerization of Th-PCL macromonomer discussed above, the polymerization times of 80:20 and 60:40 PTh-*g*-PCL were optimized separately to obtain homogeneous copolymer films that completely

covered the electrode. The optimized times were τ = 500 s PHMeEDOT and for 80:20 PTh-*g*-PCL, while τ was increased to 800 s for 60:40 PTh-*g*-PCL. The average thickness (10 samples) of the films generated onto was 27.3 ± 0.3, 31.1 ± 0.5 and 26.7 ± 0.4 μm for 80:20 PTh-*g*-PCL, 60:40 PTh-*g*-PCL and PHMeEDOT, respectively, increasing to 29.0 ± 1.5, 34.1 ± 2.8 and 30.3 ± 0.1 μm when the substrate was ITO.

Figure 5.3.2b which, in the insert, compares the FTIR spectra recorded for the HMeEDOT monomer and the prepared homopolymer, confirms the success of the anodic polymerization process. The monomer shows remarkable bands centered at 3099 and 752 cm^{-1}, which correspond to the C^{α}–H stretching and out of plane mode, respectively. The absence of these two absorption bands in the PHMeEDOT spectrum indicates that the hydrogen atoms at the C^{α}-position are removed during the polymerization process. Other relevant bands in the PHMeEDOT spectrum are observed at: 3450 cm^{-1} (O–H stretching), 2923 and 2850 cm^{-1} (–C–H aliphatic stretching); 1466 and 1413 cm^{-1} (stretching modes of the thiophene ring); and 1060 cm^{-1} (C–O stretching.). The absorption bands in the FTIR spectra of the two copolymers confirm the incorporation of the Th-PCL (Figure 5.3.2a) in the polymer chain. Thus, the presence of oligo-ε-caprolactone grafted chains is reflected by the bands at 1726 cm^{-1} (C=O ester) and 1047 cm^{-1} (C–O), the latter becoming broader and more intense than in the macromonomer because of the coexistence of both ester (from oligo-ε-caprolactone) and ether (from the dioxane ring of HMeEDOT) groups. On the other hand, the O–H

band at 3441 cm^{-1} (from both HMeEDOT and PCL chain ends) and other peaks associated to the thiophene ring are also clearly identified.

Although determination of the final composition of 80:20 and 60:40 PTh-*g*-PCL is a very difficult task because of the insolubility of the copolymers, differences in the intensities of the bands reflect that the amount of Th-PCL units in the latter are significantly higher than in the former. In order to obtain a rough estimation of the composition of the two prepared PTh-*g*-PCL copolymers, the ratios of the areas associated to the absorptions band at 1723 cm^{-1} (C=O ester) and 1633 cm^{-1} (C=C stretching vibration of the Th ring) were evaluated. Results indicate that the copolymers derived from 80:20 and 60:40 HMeEDOT:Th-PCL molar ratio present, respectively, ~ 450 and ~ 150 HMeEDOT units per Th-PCL unit.

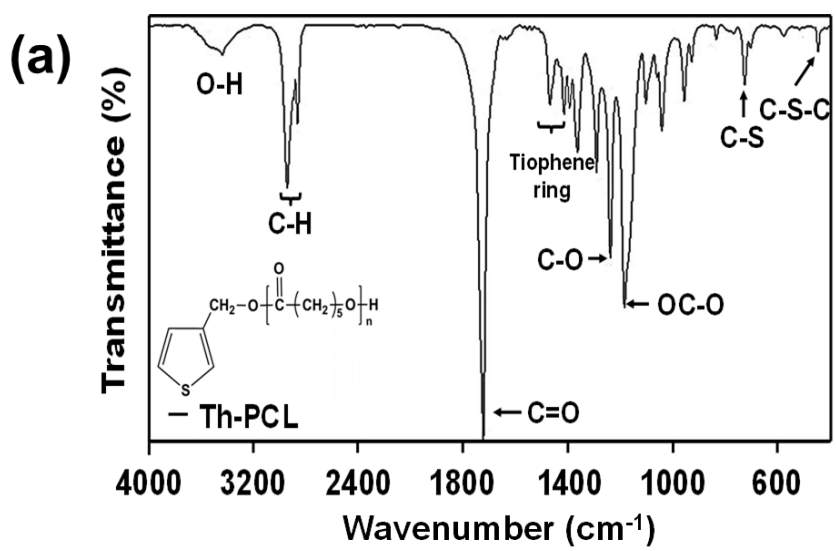

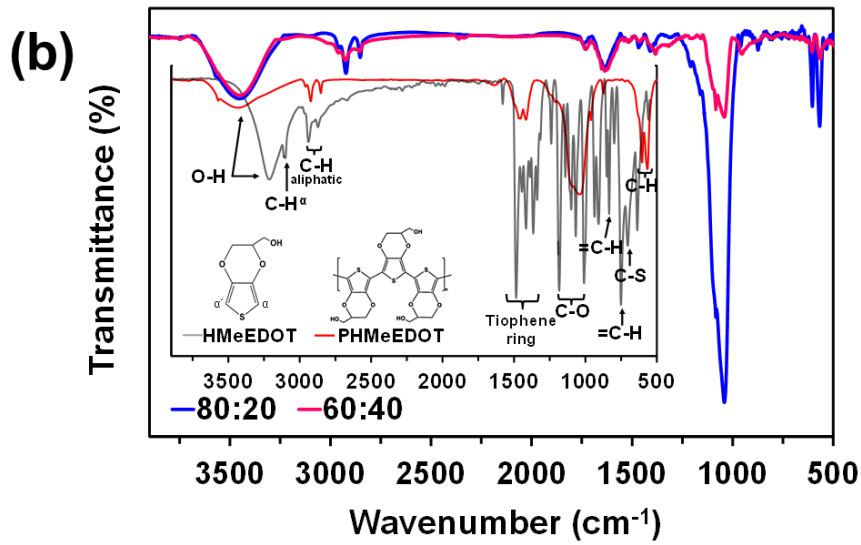

Figure 5.3.2 FTIR spectra of (a) Th-PCL macromonomer and (b) 80:20 and 60:40 PTh-*g*-PCL copolymers, synthesized using steel as working electrode. The spectrum of PHMeEDOT and its monomer have been included as inset.

SEM micrographs of PHMeEDOT and PTh-*g*-PCL homogeneously deposited onto steel electrodes are displayed in Figure 5.3.3. The granular surface morphology of PHMeEDOT, which resembles that of PEDOT, [86] seems to be affected by the incorporation of Th-PCL. However, a given amount of macromonomer is required for such change. Visual inspection of the micrograph suggests that the structure of 80:20 PTh-*g*-PCL is similar to that observed for PHMeEDOT, while the amount of granules apparently decreases for the 60:40 PTh-*g*-PCL. In any case, it should be highlighted that no empty zones, phase separation or cracking was observed in films of the two copolymers.

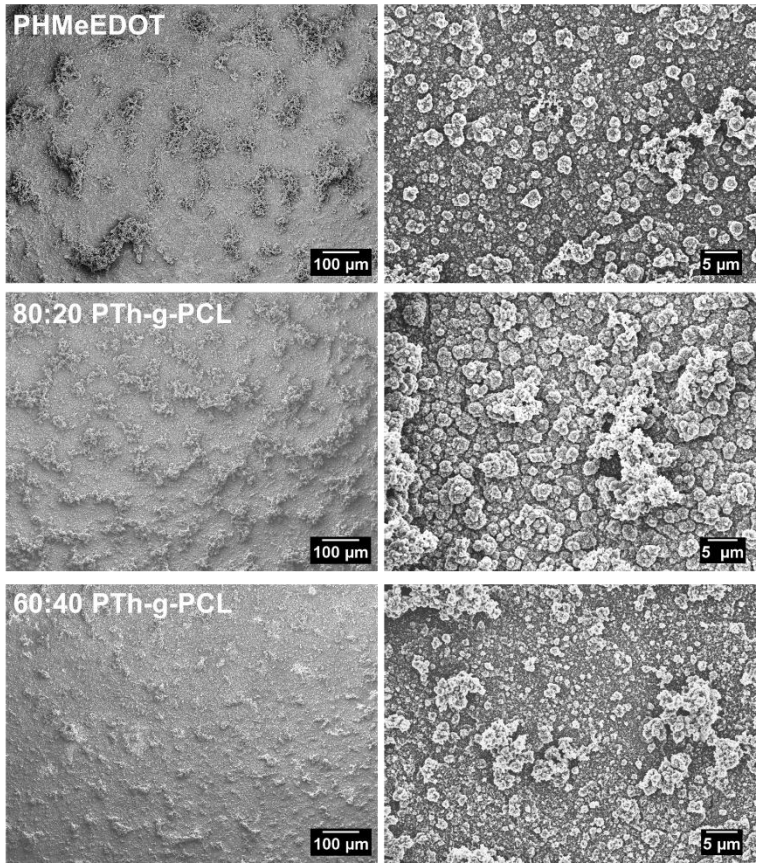

Figure 5.3.3 Low (left side) and high (right side) resolution SEM micrographs of PHMeEDOT, 80:20 PTh-*g*-PCL and 60:40 PTh-*g*-PCL films deposited onto steel as working electrode.

Figure 5.3.4a compares de UV-vis spectra of PHMeEDOT and PTh-*g*-PCL copolymers. All spectra display a broad absorption tail that starts at 480 nm, which is ascribed to the polaronic band of the conductive quinoid form. [87] As expected, the slope of such tail is more pronounced for the homopolymer than for the copolymers. Thus, the doping level of the copolymer chains decreases with the increasing amount of Th-PCL units. This doping level reduction could be due to the bulkiness of the Th-PCL units that can affect the overall planarity

and rigidity of the copolymer chains. More specifically, planarity and rigidity of PHMeEDOT chains are mainly due to the restrictions imposed by the fused dioxane ring and to the electron-donating effects provided by the oxygen atoms contained in such cyclic substituents.[88] By considering these experimental results, it seems that the incorporation of Th-PCL units locally perturbs the planarity of copolymers chains, producing a loss in aromaticity, and this adverse effect increased with the increasing number of Th-PCL units into the copolymers chains.

Control voltammograms of PHMeEDOT and PTh-*g*-PCL deposited onto steel sheets in PBS 0.1 M (Figure 5.3.4b) indicate that the anodic peak detected at +0.15 V in the homopolymer, which has been attributed to the formation of polarons in the PTh chain, shifts to higher potentials in the copolymers. Moreover, the charge stored in homopolymer films is around 2-9% higher than in the copolymer ones, which is fully consistent with loss in aromaticity in the HMeEDOT-chains induced by the incorporation of macromonomer units. Voltammograms registered after 25 consecutive oxidation-reduction cycles are included in Figure 5.3.4b. As it can be seen, the electrochemical activity decreases in all cases, especially for 60:40 PTh-*g*-PCL copolymer. Specifically, the LEA obtained for PHMeEDOT, 80:20 PTh-*g*-PCL and 60:40 PTh-*g*-PCL was 19%, 21% and 30%, respectively.

The homopolymer and copolymers were also deposited onto GC, which is the substrate typically used for the electrochemical detection of DA using PEDOT.[29,89] The shape of the registered control voltammograms (Figure 5.3.4c) was similar to those recorded for the

materials deposited onto steel. However, the amount of charge reversibly exchanged in 0.1 M PBS was significantly lower for the materials deposited onto GC than for those obtained using steel electrodes. Thus, the electroactivity of PHMeEDOT polymerized onto GC was ~86% lower than that of the homopolymer deposited onto steel, the differences determined for 80:20 and 60:40 PTh-*g*-PCL being of ~56% and ~87%, respectively. In spite of this drawback, it is worth noting that the electroactivity of 80:20 PTh-*g*-PCL generated onto GC is ~280% higher than that of PHMeEDOT prepared using same substrate. This behavior has been attributed to a combination of two features. On the one hand, the 80:20 copolymer deposited onto GC is more porous than PHMeEDOT, facilitating the access and escape of dopant ions during the oxidation and reduction processes, respectively. On the other hand, PCL chains tend to form separated phases when the 60:20 copolymer is generated onto GC, which obviously affects negatively the electroactivity of the film. The latter drawback is not observed for 80:20 PTh-*g*-PCL. These two features are clearly illustrated in the SEM images displayed in Figure 5.3.4d.

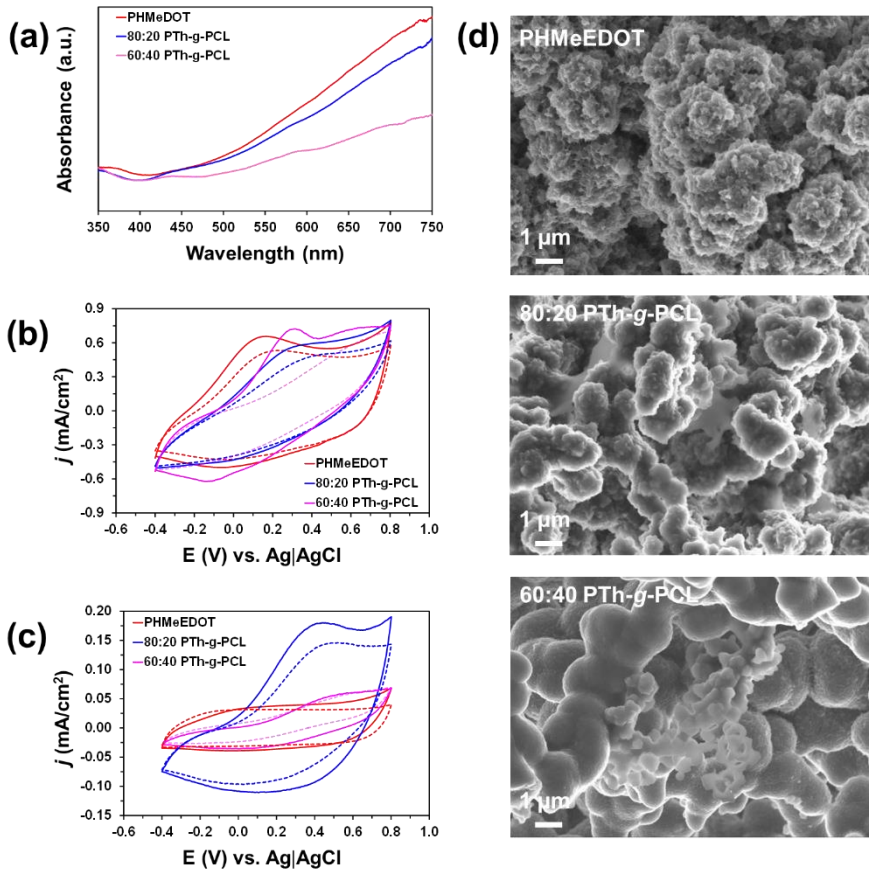

Figure 5.3.4 (a) UV-vis spectrum of PHMeEDOT, 80:20 PTh-*g*-PCL and 60:40 PTh-*g*-PCL deposited onto ITO. The spectra are normalized according the thickness of the film. First control voltammogram (solid lines) and voltammogram after 25 consecutive oxidation–reduction cycles (dashed lines) in PBS 0.1 M for PHMeEDOT, 80:20 PTh-*g*-PCL and 60:40 PTh-*g*-PCL deposited onto (b) stainless steel and (c) GC. (d) SEM images of PHMeEDOT, 80:20 PTh-*g*-PCL and 60:40 PTh-*g*-PCL deposited onto GC electrodes.

Biodegradability, wettability, cytotoxicity and biocompatibility of PTh-g-PCL copolymers. After 35 days of immersion in PBS solution, PHMeEDOT and PTh-*g*-PCL films retained both the adherence and the mechanical integrity of the films (Figure 5.3.5a). Although films showed some surface erosion, suggesting that water penetrates in the PCL domains of the copolymer chains, the weight loss (WL) was very

small (*i.e.* WL= 0.5 and 1.3% for 80:20 and 60:40 PTh-*g*-PCL, respectively, in Figure 5.3.5b). On the other hand, the average of at least eight independents measured by water contact angle (θ) determined values of < 10º and 86º ± 5º for PHMeEDOT and PCL, indicating that the former is very hydrophilic while the latter is just at the boundary between hydrophilic and lipophilic. The θ values of the 80:20 and 60:40 PTh-*g*-PCL (37º ± 2º and 41º ± 1º, respectively) are intermediate between those of the two homopolymers and increases with the content of Th-PCL. Considering that the RMS roughness (Rq) of PHMeEDOT, 80:20 PTh-*g*-PCL and 60:40 PTh-*g*-PCL are very similar (Rq = 5.1 ± 1.0, 5.9 ± 0.3 and 6.2 ± 0.2 μm, respectively), differences in the wettability of PHMeEDOT and the copolymer should be exclusively attributed to the chemistry of films surfaces, more specifically to the organization of oligo-ε-caprolactone chains. Although the content of Th-PCL is low in PTh-*g*-PCL, results suggest a biphasic organization similar to that reported for other grafted copolymers:[30] PTh and PCL segments are perpendicular and parallel to the surface, respectively. This explanation is also supported by the fact that acetonitrile is a bad solvent for oligo-ε-caprolactone chains and, during solvent evaporation, these moieties will be oriented to the film surface due to their natural tendency to exit from the solution earlier. This phenomenon could be enhanced by the formation of intra- and intermolecular hydrogen bonds between oligo-ε-caprolactone chains, the hydroxyl chain ends and the hydroxyl function of PHMeEDOT. Thus, oligo-ε-caprolactone chains expose their hydrophobic aliphatic parts towards the film surface. As acetonitrile is

an enough high boiling point solvent, these phenomena are most likely to take place.

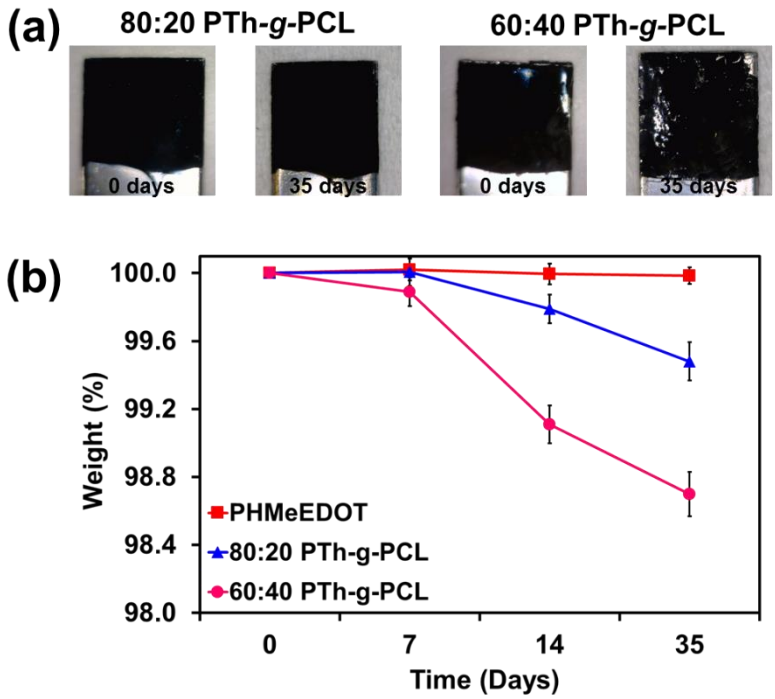

Figure 5.3.5 Photographs displaying 80:20 PTh-*g*-PCL and 60:40 PTh-*g*-PCL films before and after degradation assays (35 days in PBS, pH= 7.4, at 37 ºC); (b) Degradation curves (PBS, pH= 7.4, at 37 ºC) of PHMeDOT, copolymer 80HMeDOT:20Th-PCL and 60HMeDOT:40Th-PCL.

The effect of the grafted oligo-ε-caprolactone chains in proliferation and biocompatibility of PTh backbone chains was evaluated by considering epithelial (Vero) and fibroblast (Cos-1) cell lines derived from monkey kidney. For this purpose, the potential cytotoxicity of the PHMeEDOT and PTh-*g*-PCL was elucidated by culturing cells in plate wells containing steel sheets covered by these organic materials. Cell cultures on bare steel plates were used as controls.

Proliferation was determined after five days using the MTT assay and quantifying all viable cells contained in the wells, which allowed us to consider the toxic effects associated not only to the polymeric matrix but also to small molecules (*e.g.* acetonitrile, monomer, macromonomer and dopant molecules) or oligomers that could be eventually released to the medium. Results displayed in Figure 5.3.6a reflect the cytotoxic effects of PHMeEDOT, which reduce cells viability about 20-30% with respect to the steel control. These adverse effects are not observed for the 60:40 PTh-*g*-PCL, which show viabilities practically identical to the control, while they decrease significantly for the 80:20 copolymer (*i.e.* cell viability decreases 5-10% with respect to steel). This behaviour should be attributed to the benefits induced by the biocompatible oligo-ε-caprolactone chains that improve the biological response with respect to the homopolymer, even though another factor should be additionally considered. More specifically, the mass of TBATFB dopant, which is a toxic compound, decreases with the increased amount of grafted oligo-ε-caprolactone chains. Accordingly, the amount of TBATFB molecules that are leaching out from the polymeric films is lower for the copolymers than for the homopolymer.

On the other hand, the biocompatibility was examined by comparing the abilities of the polymeric matrices to enhance cellular proliferation. Thus, in this case the viability was determined considering the cells directly located onto PHMeEDOT and PTh-*g*-PCL films only. Results (Figure 5.3.6b) indicate that oligo-ε-caprolactone chains improve the bicompatibility of PTh chains, independently of the cell line. Although such improvement

increases with the increasing amount of Th-PCL units in copolymers, PTh-*g*-PCL are slightly less biocompatible than steel (control) due to the low ratio of oligo-ε-caprolactone chains. Overall, results reflect that the incorporation of a few Th-PCL macromonomers into PHMeEDOT chains may be an appropriate strategy to facilitate the integration in the organism of implanted biosensors, if no detriment in the detection efficiency (see next section).

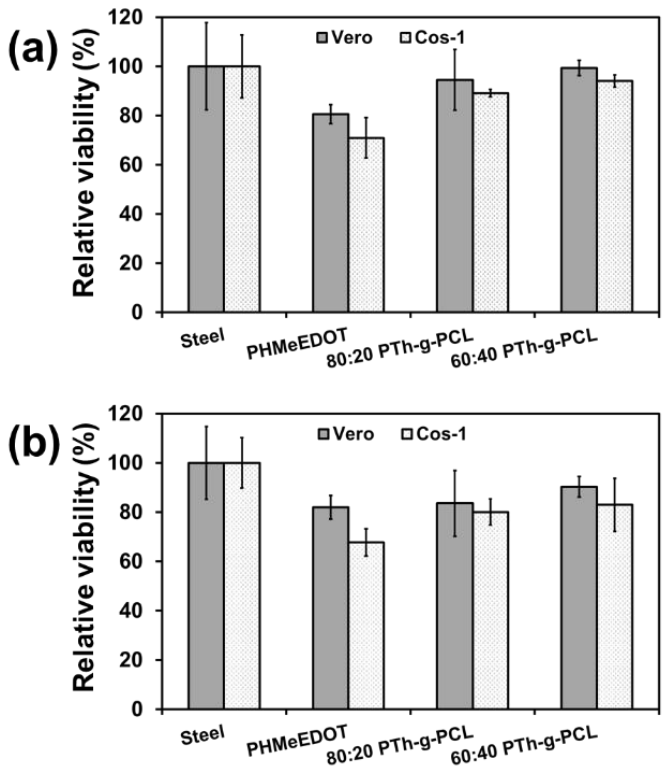

Figure 5.3.6 (a) Proliferation and (b) biocompatibility of PHMeEDOT, 80:20 PTh-*g*-PCL and 60 : 40 PTh-*g*-PCL deposited onto steel (four samples for each group). Bars represent the mean standard deviation. The relative viability of Vero and Cos-1 cells was established in relation to bare steel, which was considered as the control substrate.

Selective detection of DA using PTh-g-PCL. Dopamine (DA), ascorbic acid (AA) and uric acid (UA) coexist in extracellular fluids of the central nervous system and, therefore, the selective determination of these species is a major goal for the biosensors. Before comparing the performance of PHMeEDOT and PTh-*g*-PCL systems, the oxidation peaks of DA, AA and UA using steel and GC polymer-modified electrodes were examined by CV. Results obtained for a solution mixture with 100 µM DA, 200 µM AA and 100 µM UA in 0.1 M PBS are displayed in Figures 5.3.7a and 5.3.7b for the steel- and GC-modified electrodes, respectively. As it can be seen, the oxidation peaks of DA, AA and UA are much better defined for the electrodes deposited on GC than on steel, this feature being especially noticeable for the 80:20 PTh-*g*-PCL copolymer (Figure 5.3.7b). Furthermore, the oxidation peak potential of DA at the latter copolymer is clearly identified at 0.34 V, whereas the peak potential of oxidation of AA corresponds to -0.01 V and the one for UA exceeds the reversal potential. Accordingly, both the separation among the peak potentials and the high strength of the current signal for the oxidation of DA suggest that 80:20 PTh-*g*-PCL is an appropriated sensor for the latter neurotransmitter in terms of both resolution and sensitivity.

Figure 5.3.7c shows cyclic voltammograms of solution mixtures with different DA concentration (from 50 to 0.5 µM), 200 µM AA and 100 µM UA in 0.1 M PBS for the 80:20 PTh-*g*-PCL sensor. The grafted copolymer is able to catalyse the oxidation of DA molecules in a low potential range, which means that in cellular systems, the voltage applied would be the minimal to detect this kind of

biomolecule *in vivo*. The anodic peak current decreases with the decreasing concentration of DA, while the peak potential remains almost constant at 0.34-0.35 V for all concentrations, even when the response of DA is very weak at concentrations below 0.5 μM. However, this threshold is around the one that would be desirable (*i.e.* the synaptic DA concentration is 1.6 mM[90]).

The calibration curve (Figure 5.3.7d) shows a good rectilinear behaviour for low concentrations only (≤ 5 μM). The correlation coefficient for the first oxidation-reduction cycle is 0.9985, while the anodic peak currents determined for 0.5 and 5 μM DA are 128.2 and 270.0 μA, respectively. It is worth noting that profile linearity and sensitivity obtained for 80:20 PTh-*g*-PCL are higher than those obtained for PHMeEDOT (Figure 5.3.7e). The calibration curve obtained for the latter provides a correlation coefficient of 0.9349 only, while the anodic peak currents measured for 0.5 and 5 μM DA were 13.6 and 29.10 μA, respectively. Unfortunately, the response exhibited by the 60:40 PTh-*g*-PCL copolymer was not consistent, as is reflected in Figure 5.3.7f. Thus, the anodic peak current changed erratically when the DA concentration was increased or decreased.

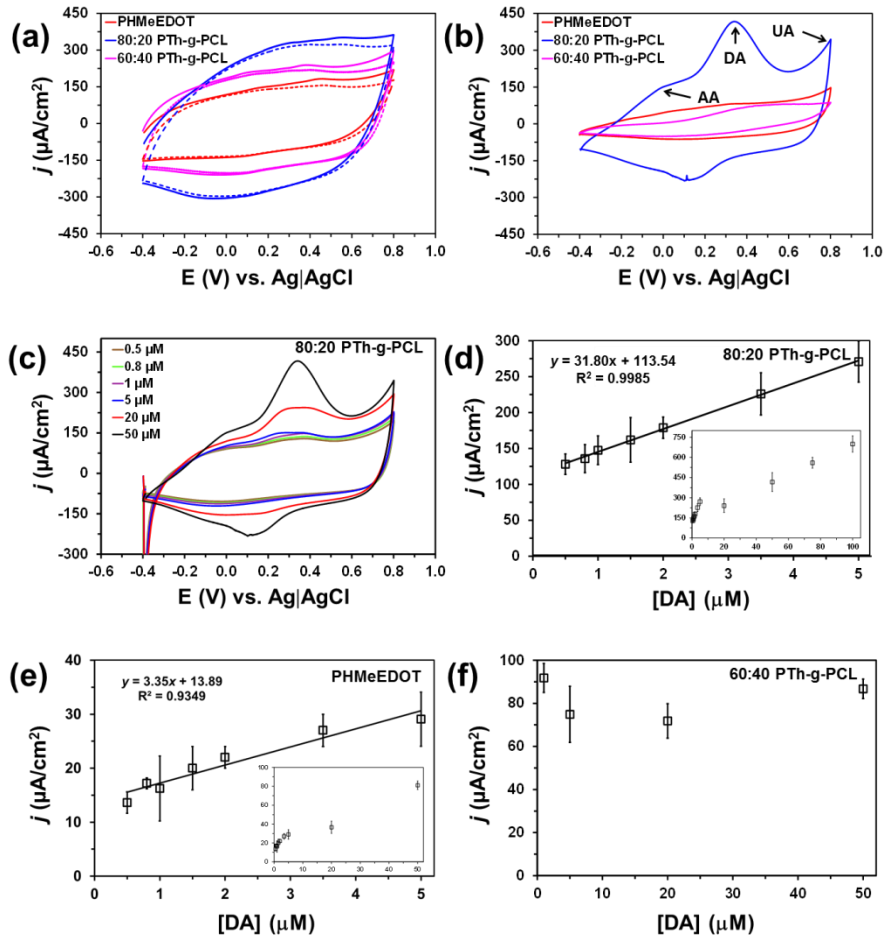

Figure 5.3.7 Cyclic voltammograms of electrodes consisting of PHMeEDOT and PTh-*g*-PCL deposited onto (a) steel and (b) GC in 0.1 M PBS with 100 μM DA, 200 μM AA and 200 μM UA. (c) Comparison of DA detection intensity from 0.5 to 50 μM in 0.1 M PBS with 200 μM AA and 200 μM UA. All voltammograms were obtained by scanning from −0.40 to 0.80 V at a scan rate of 50 mV s^{-1}. Calibration curves for DA detection in the concentration range from 0.5 to 5 μM (to 50 μM in inset) in 0.1 M PBS with 200 μM AA and 200 μM UA for (d) 80:20 PTh-*g*-PCL, (e) PHMeEDOT, and (f) 60:40 PTh-*g*-PCL deposited onto GC.

The PTh-*g*-PCL copolymers developed in this work represent a valuable alternative to previously reported PTh-*g*-PEG copolymers,[29–31] which were specifically designed to behave as active surfaces for the selective adsorption of proteins and substrates to promote the

electrocommunication will cells. Thus, PTh-*g*-PCL copolymers meet the conditions necessary to act as biocompatible and efficient dopamine detectors, while these conditions are poorly satisfied by PTh-*g*-PEG copolymers. Within this context, the advantages of PTh-*g*-PCL with respect to PTh-*g*-PEG can be summarized as follows: (*i)* PCL is more biodegradable and biocompatible than PEG, which is advantageous for implantable biosensors; (*ii)* PTh-*g*-PCL copolymers contain HMeEDOT units at the backbone, enhancing the sensitivity and selectivity for the determination of DA with respect to PTh-*g*-PCL copolymers, which involve simple thiophene units; and (*iii)* the electrochemical activity and stability of PTh-*g*-PCL copolymers are considerably higher than those reported for PTh-*g*-PEG.[29–31] The latter observations, which represent a benefit in terms of lifetime for the detector, have been attributed to the oxygen atoms attached at β,β' positions of the thiophene ring in HMeEDOT units, which induce strong electron-donating effects and prevent the formation of parasitic α-β linkages during the electropolymerization process.

Conclusions

In summary, Th-based graft copolymers, incorporating a few amounts of oligo-ε-caprolactone -containing electroactive macromonomer into PHMeEDOT chains, have been synthesized using the "*macromonomer technique*" *via* electrochemical polymerization. When comparing with PHMeEDOT homopolymer, the oligo-ε-caprolactone grafted chains onto copolymers main chains reduce considerably the cytotoxicity of the resulted films formed during polymerization on the electrode surface. Furthermore, the

80:20 PTh-*g*-PCL copolymer generated onto GC electrodes is more electroactive than PHMeEDOT since the former becomes more porous than the latter. As a consequence, sensing capability of 80:20 PTh-*g*-PCL for DA detection is demonstrated to be much higher, sensitive and selective than that of PHMeEDOT. Overall, the 80:20 PTh-*g*-PCL could be considered as an alternative, potential candidate for the fabrication of implantable DA sensors.

5.4 An amphiphilic, heterografted polythiophene copolymer containing biocompatible/ biodegradable side chains for use as an (electro) active surface in biomedical applications

Abstract

Given that the copolymers of complex topology and composition are at the forefront of multifunctional materials research, this work reports a novel amphiphilic random, heterografted copolymer of (A-*g*-B)$_m$-*ran*-(A-*g*-C)$_n$ type, which was designed to work as an efficient and biocompatible electronic interface. The copolymer (henceforth denoted as PTh-*g*-(PEG-*r*-PCL) for simplification) was synthesized in hierarchical fashion, having π-conjugated polythiophene (PTh) bearing polar side groups, as main chain and polar units, polyethylene glycol (PEG) and oligo-ε-caprolactone as side chains. The properties of the new copolymer, in solution and in solid state, were evaluated. The applied investigations showed that, due to its amphiphilic character and incompatibility of the side chains, PTh-*g*-(PEG-*r*-PCL) experiences microphase separation in solution and film states. By electronic microscopy techniques were evidenced two types of supramolecular structures: (*i*) porous spherical particles and (*ii*) rod-like structures. When deposited on carbon electrodes, the copolymer presented a good electroactivity and electrostability. Biological studies, performed using Cos-1 and Vero cell lines, demonstrated an excellent adhesion when comparing with bare steel electrode while a slight decrease of proliferation was registered, more pronounced for Vero cells, in spite of cells normal growth and morphology. Thanks to its excellent capability for electrochemically

interfacing with aqueous electrolytes, the voltammetric oxidation of NADH coenzyme at PTh-*g*-(PEG-*r*-PCL) film-modified carbon electrode revealed that it can be used as selective biosensor of this biomolecule, as well.

Materials and methods

Materials. Poly(ethylene glycol) methyl ether M_n = 2000 g/mol (hereafter denoted PEG2000), thiophene-3-carboxylic acid (98%), N,N'-dicyclohexylcarbodiimide (DCCI, 99%), 4-dimethylamino pyridine (DMAP, ≥ 98%), 3-thiophene-methanol (Th-MeOH, 98%), ε-caprolactone (ε-CL; 97%), stannous octoate ($Sn(Oct)_2$, 92.5-100%), anhydrous $FeCl_3$ (≥ 98%) and hydrazine monohydrate (98%) were used as received. Solvents were purified and dried by usual methods. The solvent used for the characterization of the copolymer was acetone (≥99.9% Sigma-Aldrich). For electrochemical trials, a Dulbecco's phosphate buffered saline solution (PBS) 0.1 M with pH 7.4, without calcium chloride and magnesium chloride, was used, meanwhile detection assays were carried out with NADH, reduced disodium salt hydrate (≥97%) and ascorbic acid (AA; L-configuration, crystalline) from Sigma-Aldrich.

Synthesis of Th-PEG macromonomer. First, 2 g (0.001 mol) of PEG_{2000} and 0.19 g (0.0015 mol) of thiophene-3-carboxylic acid were placed into a three-neck round-bottom flask equipped with a dropping funnel, under nitrogen. Then, 20 mL of CH_2Cl_2 and 0.0171 g of DMAP 0.14 mmol) were added to the flask, whereas 0.304 g (0.00147 mol) of DCCI in 1 mL CH_2Cl_2 were placed in the dropping funnel and added to the reaction flask in about 5 min. The mixture was stirred at room

temperature for three days. The resulting dicyclohexyl urea was removed by filtration and the resulting solution was precipitated in cold diethyl ether to remove the catalyst and the unreacted reagents. After filtration and drying, the macromonomer was obtained as a white solid.

Synthesis of Th-PCL macromonomer. Thiophene-ended oligo-ε-caprolactone (Th-PCL) macromonomer was synthesized similar to the reported in Section 5.3, with difference of the molar ratio between initiator and monomer ([I]/[M]), which has been changed from 1/20 to 1/18 in this work.

Synthesis of PTh-g-(PEG-r-PCL) copolymer. Chemical oxidative polymerization was carried out in a 25 mL round bottom flask equipped with magnetic stirrer and a lateral neck with a dropping funnel was used. The system was vacuumed and back-filled with dry nitrogen for several times. Then 2.1 mL $CHCl_3$, 0.360 g (0.17 mmol) Th-PEG and 0.392 g (0.17 mmol) Th-OCL were introduced under inert atmosphere. After the complete dissolution of the reactants, the mixture was cooled down at 0^oC and 0.211 g (1.3 mmol) of anhydrous $FeCl_3$ in 3.5 mL $CHCl_3$ was added dropwise during 25 min. The reaction mixture was stirred at room temperature for 4 days. After that time, the copolymer was separated by precipitation in diethylether, filtered and dried at room temperature under vacuum. Further purification was achieved by silica gel column chromatography, using CH_2Cl_2 as eluent. The resulted solution was concentrated in a rota evaporator and subsequently re-precipitated in diethyl ether. The obtained copolymer was dedoped by stirring its solution in CH_2Cl_2 with hydrazine hydrate for 30 minutes. After washing of organic layers

twice with water, the dedoped copolymer was obtained by precipitation with diethyl ether. The synthetic route is summarized in Scheme 5.4.1.

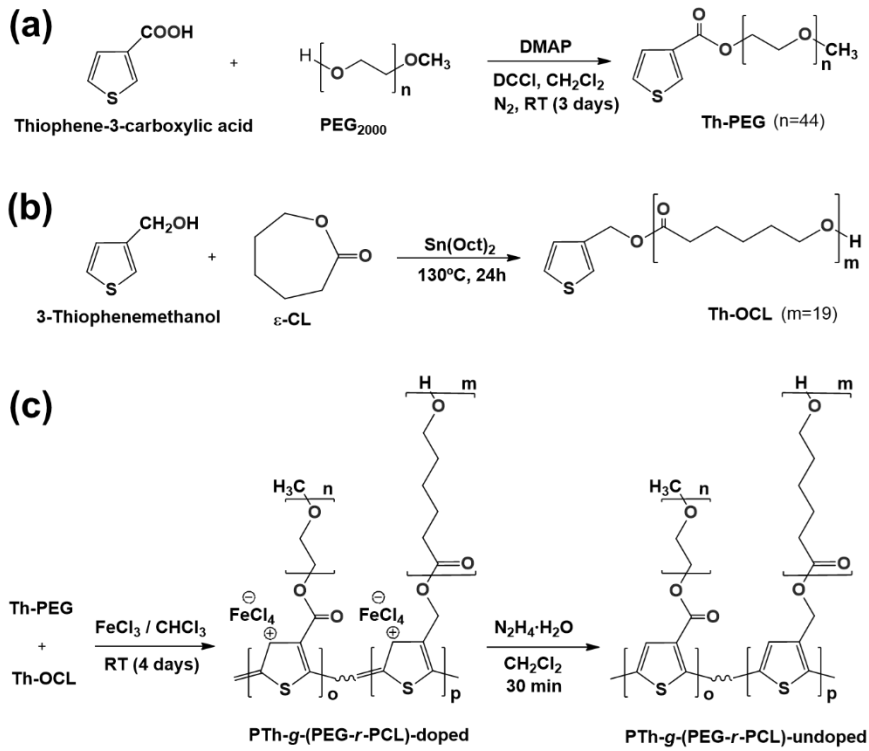

Scheme 5.4.1 Synthesis route of PTh-*g*-(PEG-*r*-PCL) copolymer: (a) esterification reaction of thiophene derivative and PEG_{2000}; (b) esterification reaction of thiophene derivative and oligo-ε-caprolactone; and (c) oxidative polymerization of macromonomers from (a) and (b) and dedoping reaction with hydrazine.

Characterization of macromonomers and prepared copolymer. A detailed description of the methods employed for the macromonomers and copolymer characterization is included in the supporting Chapter 4. The precursors and final product were characterized by NMR and FTIR spectroscopies, the molecular weight was approached with GPC

and the particle size was in acetone solution by DLS. Morphology of the microparticles obtained from PTh-*g*-(PEG-*r*-PCL) copolymer were evaluated by SEM and TEM while Cos-1 and Vero monkey kidney epithelial cells were employed for the adhesion and proliferation of cells. Small aliquots of 5 µL of a solution containing 100 mg of copolymer per mL of acetone, were dropped onto steel AISI 316L sheets with an area of 0.5 × 1 cm^2, after 3 days drying in vacuum, the coated steel sheets were studied for adhesion and proliferation of cells.

Electrochemical characterizations were carried out using a Screen-Printed Carbon Electrodes (SPCE, model C150, supplied by DropSens Co.) with carbon, as working electrode WE (4 mm diameter), Pt as counter electrode. A phosphate buffered saline (PBS) solution 0.1 M (pH = 7.4) at room temperature was used as electrolyte solution in all electrochemical assays. The initial and final potentials were −0.2 V, and the reversal potential was +0.6 V. Different scan rates were studied from 20 to 200 $mV \cdot s^{-1}$, considering the 50 $mV \cdot s^{-1}$ the best option for the successive assays. The small WE was covered with one aliquot of 5 µL of a 100 mg/mL, from the copolymer in acetone, and after careful sonication.

The electrochemical detection of NADH and NAD+ was studied by CV, differential DPV and CA as was described in Chapter 4.

Results and discussion

Macromonomers and copolymer characterization. The new amphiphilic heterografted copolymer was synthesized by combining "macromonomer" or "grafting through" technique with an oxidative

polycondensation reaction of an equimolecular mixture of two thiophene-ended macromonomers (Scheme 5.4.1), a classical method for ICPs chemical synthesis. The hydrophilic macromonomer, Th-PEG, was synthesized by chain-end functionalization method, through Steglich esterification of hydroxyl group of PEG_{2000} (Scheme 5.4.1a), being the first time it has been reported. The Th-PCL monomer, of hydrophobic nature, was obtained as previously reported method, using thiophene methanol for ring-opening polymerization (ROP) of oligo-ε-CL, (Scheme 5.4.1b). We should mention that the resulting compound is oligomeric in nature, despite we preferred use the acronym of PCL in the whole work, instead of OCL.

Meanwhile for the copolymer preparation, an equal molar amount of the macromonomers Th-PEG and Th-PCL was used, even when its nature was different. After the work-up of the resulted reaction mixture, including the de-doping stage with hydrazine, only water-insoluble part was kept to be purified (Scheme 5.4.1c).

The structures of the precursors and the final copolymer were evaluated by ^{1}H-NMR spectroscopy for which the solvents used were carefully choosen, as was explained in Section 5.2. Figure 5.4.1a shows the principal peaks of the macromonomer Th-PEG in acetone-d_6:

8.27- 7.52ppm (CH protons of the thiophene ring), 4.40ppm ($CO\text{-}OCH_2$), 3.81-3.57 ppm (CH_2O from PEG), and 3.30 ppm (OCH_3). While the signals of Th-PCL in $CDCl_3$ can be observe in Figure 5.4.1b: 7.33ppm, 7.09ppm (CH protons of the thiophene ring), 5.14 ppm (Th-CH_2), 4.10-4.06 ppm (CH_2-O),3.66 ppm (CH_2-OH),

2.37-3.31 ppm (CH_2COO),1.80-1.52 ppm (-*co*-CH_2-CH_2-CH_2-CH_2-CH_2-O-), 1.44-1.36 (-*co*-CH_2-CH_2-CH_2-CH_2-CH_2-O-).

The structural characterization of the grafted copolymer PTh-*g*-(PEG-*r*-PCL) was elucidated by NMR (acetone-d_6). Thus, in Figure 5.4.2a, all the observable signals in the ^{1}H-NMR spectrum were assigned to each type of protons belonging to PEG (**c, c', c", d**) and PCL (**f, g, i, j**) side chains, as well as those characteristic to the polythiophene conjugated main chain, (**a, b**), as a broadened peak placed in the range 6.9 ppm-8.12 ppm. Moreover, the signals attributable to protons of methylene group (**e**), in the PCL-substituted structural units, can be seen in the range of 5.05 ppm - 5.41 ppm. In general, for the 3-substituted polythiophenes the shape and positions of the three peaks (**a**, **b**, and **e**) can give information about the coupling of the monomers and about the regioregularity of the obtained polymer. Such shifts of each non-symmetric structural unit observed in the ^{1}H-NMR spectrum of PTh-*g*-(PEG-*r*-PCL) give one idea about the polymer regioregularity: head-tail (H-T), head-head (H-H) and tail- tail (T-T). Moreover, as α(1)-methylene protons and even β(2)-methylene protons in poly-3-alkylthiophenes, due to the difference in configuration, present split peaks associated to H-H and H-T dyads, from the intensities of these characteristic peaks the named dyads ratio can be evaluated.[91]

Interestingly, in the spectrum of PTh-*g*-(PEG-*r*-PCL), in the range 5.05 ppm - 5.41 ppm, two separated peaks are present at 5.05 -5.01 ppm and 5.39 -5.41 ppm, that could be attributed to both types of dyads, commented above, in the structural units of the new copolymer. However, due to the statistical distribution of the side chains, as well

as the presence of other possibilities for PTh main chain ends, it makes complicate the calculation of such H-H/H-T dyads ratio in the range of 5.05-5.41 ppm. Therefore, we used the information given by the ^{1}H-NMR technique for its evaluation. To this aim, the integral values of the peaks **j**, **c**, **c'**, **c"** and **d** (Figure 5.4.2a) were combined in order to obtain the values **o** (0.4) and **p** (0.6) (code of structural units showed in the Scheme 5.4.1c), determining that PTh-*g*-(PEG-*r*-PCL) contains 40% PEG side chains and 60% PCL side chains. Considering this composition of copolymer, its hydrophilic-lipophilic balance (HLB) was calculated as previously reported[92] and a value of 0.36 was obtained, which characterizes an amphiphilic, non-water-self dispersible material.

New interesting information was also obtained by analysing ^{13}C-NMR spectrum from Figure 5.4.2b in acetone due is better solvent for PEG and oligo-ε-CL units than for PTh units. The signals originating from PEG structural units appeared at 71.28 ppm (carbon atoms denoted **4** in Figure 5.4.2b), while those belonging to PCL, (**10-13**), are concentrated in the range of 24.2 ppm-34,71 ppm, excepting carbon atom **14**, placed in the neighbourhood of oxygen atom from ester; it can be seen at 64.4 ppm. The carbonyl groups of ester linkages, belonging to Th-PEG and PCL side chains, appeared at 173.58 ppm, as well. Besides, some of the signals attributable to the first and the last structural units of PEG (count starting from the thiophene ring) and to the structural unit of PCL, placed at its chain end, appeared separately in the spectrum of Figure 5.4.2b. Nevertheless, what is intriguing is the fact that from eight carbon atoms belonging to the two

types of thiophene rings in the main chain of copolymer, only two of them are hardly discernible.

For a more accurate assignment of the amphiphilic side chains present in PTh-*g*-(PEG-*r*-PCL) copolymer, a study with DEPT 135 ^{13}C-NMR registration was performed (Figure 5.4.2c). This technique is more sensitive than normal acquisition, so, allowed the differentiation of peaks corresponding to atom **13** from those of acetone used as registration solvent and for definitely assignment of the atoms **2**, **5**, **6** having particular positions in PEG side chains. A similar separate placement of peaks can be seen for carbon atoms **15** and **16** in oligo-ε-caprolactone final structural unit, that appeared separately from their homologues **13** and **14**. The carbon atoms **17** and **18** shown in Figure 5.4.2c, correspond to the hydrogen atoms connected to the β-position of thiophene heterocycle, that was not clearly discerned in the ^{13}C-NMR (Figure 5.4.2b). The explanation for the lack of C atoms in normal ^{13}C-NMR can be explained based on the combination of two factors: (*i*) the grafted side chains, both of them in extended configuration in a good solvent like acetone, restrict the mobility of the rigid, hydrophobic polythiophene main chain for which acetone is a bad solvent, leading to small peaks broadening in the ^{13}C-NMR, making them hard to discern; and (*ii*) the side chains at high grafting density can shield the polythiophene main chain carbon atoms resonance.

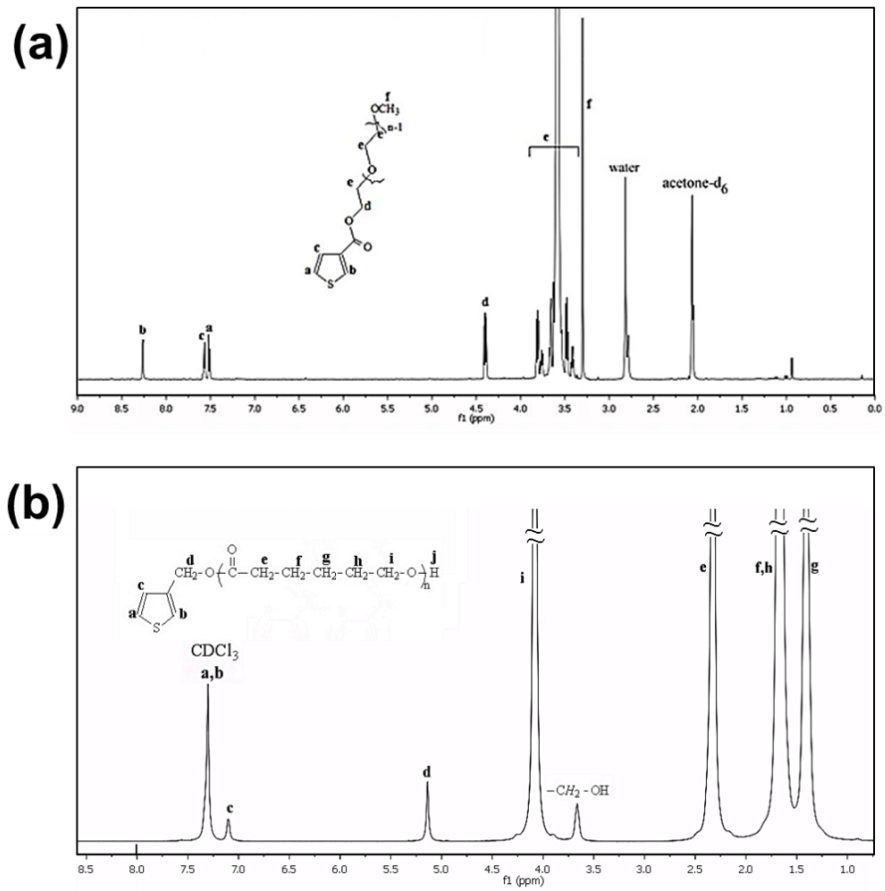

Figure 5.4.1 ^{1}H-NMR of macromonomers (a)Th-PEG$_{2000}$ and (b) Th-PCL and, precursors of PTh-*g*-(PEG-*r*-PCL) copolymer.

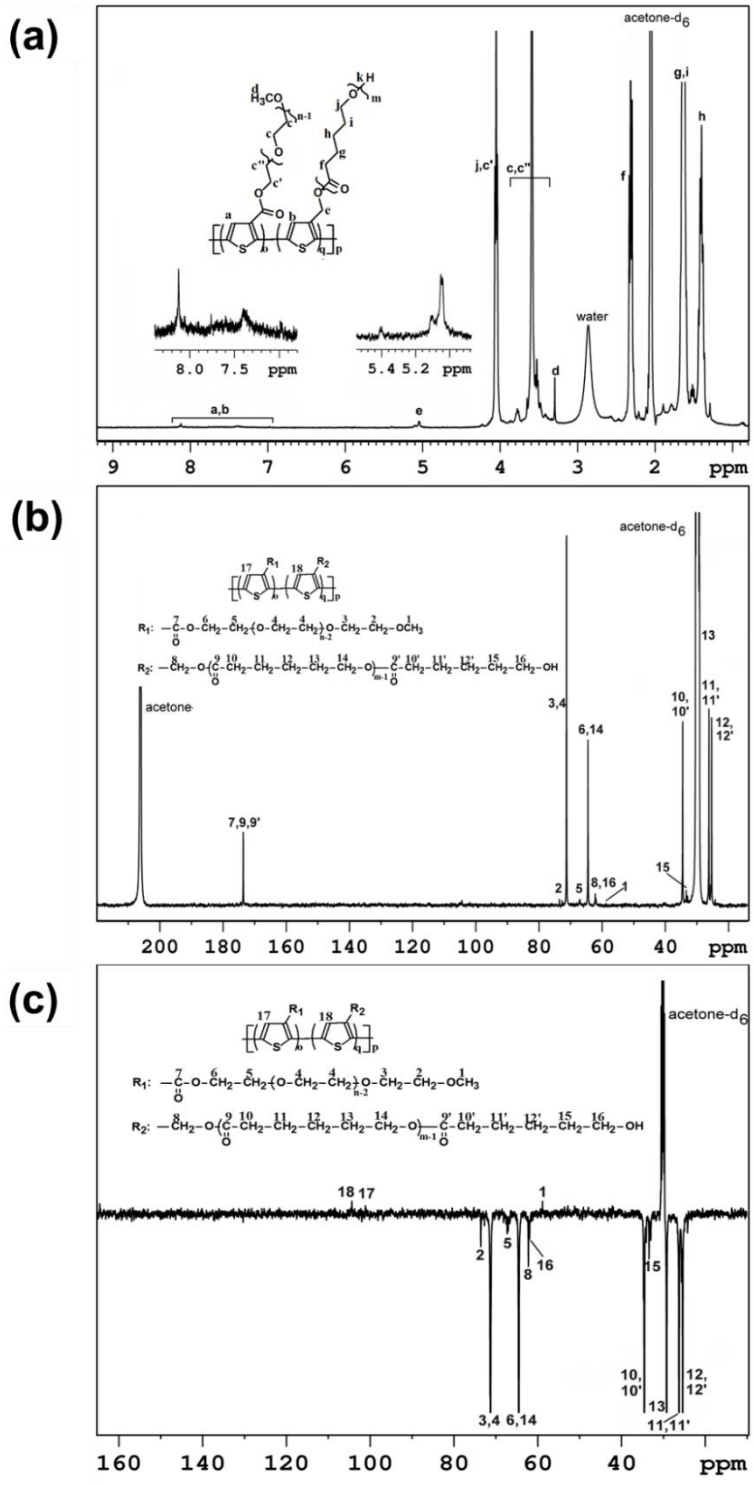
(a)
acetone-d6
water
a,b
e
d
f
g,i
h
j,c'
c,c''
8.0 7.5 ppm
5.4 5.2 ppm
9 8 7 6 5 4 3 2 ppm
(b)
acetone-d6
acetone
7,9,9'
3,4
6,14
10, 10'
11, 11'
12, 12'
13
15
2
5
8,16
1
200 180 160 140 120 100 80 60 40 ppm
(c)
acetone-d6
18 17
1
2
5
8
16
15
10, 10'
12, 12'
13
11, 11'
3,4
6,14
160 140 120 100 80 60 40 ppm

Figure 5.4.2 (a) ^{1}H-NMR, (b) ^{13}C-NMR and (c) DEPT 135 ^{13}C-NMR spectra of PTh-*g*-(PEG-*r*-PCL) copolymer, in acetone-d_6. R_1 and R_2 represent the PEG and PCL side groups.

The apparent molecular weight of the macromonomers and copolymer were determined by GPC measurements, which also provided the index of polydispersity (IPD) results are present in Table 5.4.1). The molecular weight of the macromonomers were higher than the calculated ones, attributed to the polarity difference between their chains and the polystyrene used as standard, the obtained values by GPC were taken in account for copolymer synthesis calculation.

Table 5.4.1 Molecular weight (M_n) and index of polydispersity (IPD) obtained by calculation and by GPC measurements.

Sample	$M_{n,\,^{1}H\text{-}NMR}$	$M_{n,\,GPC}$	IPD
Th-PEG	2110	2486	1.04
Th-PCL	2283	3070	1.47
PTh-*g*-(PEG-*r*-PCL)	-	5113	1.44

FTIR analyses of starting materials and the copolymer have been included in Figure 5.4.3. As PEG and PCL monomers are crystallisable substances, it is worthy to notice the presence of such absorption bands in the FTIR spectra. They can be summarized as follow: (*i*) triplet maxima of C-O-C stretching vibrations of PEG at 1148, 1114 and 1060 cm^{-1}, besides 1360 cm^{-1} and 1280 cm^{-1} (PEG 7/2 helix), while 10/3 helical conformation is proven by absorptions at 1242 and 963 cm^{-1},[93] for Th-PEG; (*ii*) crystallization-sensitive bands at 1726 cm^{-1} (ν C=O ester), at 1294 cm^{-1} (ν C–O and ν C–C), and at 1189 cm^{-1} (ν OC–O) for Th-OCL.

On the other hand, the PTh-*g*-(PEG-*r*-PCL) spectrum shows the typical signals originating from aliphatic CH_2 and CH_3 in the range of 2992-2818 cm^{-1} besides a shallow absorption centered approximately at 3066 cm^{-1} corresponding stretching vibration of thiophene rings in the main chain (β C-H aromatic). It is remarkable that relatively broad absorptions appeared. They are placed in the range of 3137-3072 cm^{-1}, for Th-PEG, and 3132-3080 cm^{-1} for Th-PCL; and they are attributable to both aromatic α(CH) and β(CH) stretching vibrations of thiophene rings. Those absorption bands, at 752 cm^{-1} and 782 cm^{-1} (characteristic to out-of-plane α C-H), of ring deformation[94] disappeared in the copolymer spectrum demonstrating that the polymerization took place through the α-positions of the thiophene rings. The carbonyl group from ester linkages, in both PEG and PCL side chains, appears centered at 1726 cm^{-1}, whereas the methylene moiety next to the carbonyl group in PCL units can be visualized at 1192 cm^{-1}.

Similar to previous sections, the copolymer composition was calculated using the ratio of the integrated area of the peak at 1726 cm^{-1} (belonging to both types of side chains) and the integrated area of the peak at 1192 cm^{-1} (typical to uniquely PCL side chains).[95,96] The resulted copolymer composition calculated in this way was 61.5% Th-PCL and 38.5% Th-PEG, that well agree with the composition values obtained by using NMR data.

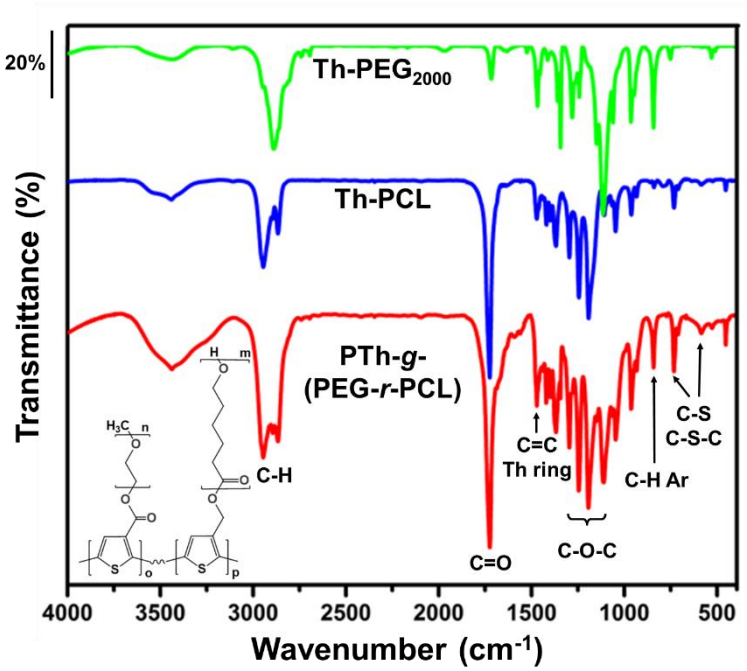

Figure 5.4.3 FTIR spectra of copolymer PTh-*g*-(PEG-*r*-PCL), Th-PCL and Th-PEG_{2000} macromonomers, obtained with KBr pellets.

The experimental results suggest that the polythiophene main chain forms a central solid-like hydrophobic core, while the side chains can function as a shell. However, the presence of the self-assembled structures in solution and their morphology characterization in solid state are both necessary.

In order to understand copolymer-solvent interaction and if its chains are intermolecular associated or not, due to non-covalent supramolecular interactions, a DLS study in acetone was performed. The results show the presence of three types of supramolecular aggregates, with size varying from 976 nm to 31 μm and to 146 μm.

Taking into account that, the acetone is a good solvent for both side chains and, the hydroxyl groups of the PCL chains-end could form

hydrogen bonds with this solvent, it can be supposed that PTh-*g*-(PEG-*r*-PCL) chains, in acetone solution, exist in molecularly well-dissolved state. The size of these chains with longer or shorter-π-conjugated main chains could be too small to be "sensed" by DLS technique. However, as acetone is a low hydrogen-bonding acceptor, besides these well-dissolved copolymer chains, it cannot be excluded the presence of micelles-like supramolecular aggregates, formed due to intermolecular interaction, as a result of the competition between polymer-polymer and polymer-solvent interaction. The multichains aggregation can be favored and enhanced by a synergistic combination of π-π stacking from thiophene units[97–99] and intermolecular PCL hydrogen bonding. As concluded from NMR investigation, the copolymer chains exist as core-lengthwise-segregated sheath structures that can form intermolecular π-π stacks because PEG side chains in the hydrophilic half-sheath may be too short and/or too loosely grafted to prevent the main chains interaction. All of these can explain the obtained results by DLS.

Generally, the changing from the solution to the dry state is a very complex phenomenon due to the many influencing factors that can act on the shape and size of such compounds, therefore, SEM and TEM analyses were indispensable.

The sample for SEM was prepared from a mother solution of the copolymer in acetone (100 mg/mL), previously sonicated in a bath ultrasound for 5 minutes, for complete dissolution. Afterwards, an aliquot of 5 µL from this mother solution was deposited on a silicon plate of 1 cm^2 and the solvent was evaporated with a vacuum system.

SEM micrographs (Figure 5.4.4a-c) evidenced the presence of spherical and porous particles, with very scattered sizes, and few amount of rod-like small structures. As it can be seen, such particles and agglomeration adopt an irregular spherical-like shape with high variability in diameter and porosity (Figure 5.4.4b). Thus, the heterogeneous morphology seen in Figure 5.4.4a-c can be attributed to several factors: (*i*) the fast evaporation of the solvent, which causes the appearance of aggregates; (*ii*) the backbone polydispersity (molecular weight); and (*iii*) the heterogeneous length of the conjugated main chain and the side chains.

Moreover, the EDX spectrum displayed in Figure 5.4.4d shows the presence of only C and O atoms, evidencing that the outer layer is constituted by the PEG/PCL branches. The sulphur atoms coming from the PTh backbone were hardly observed by EDX, confirming that the thiophene units are enclosed inside the spheres, as was deduced from NMR registration.

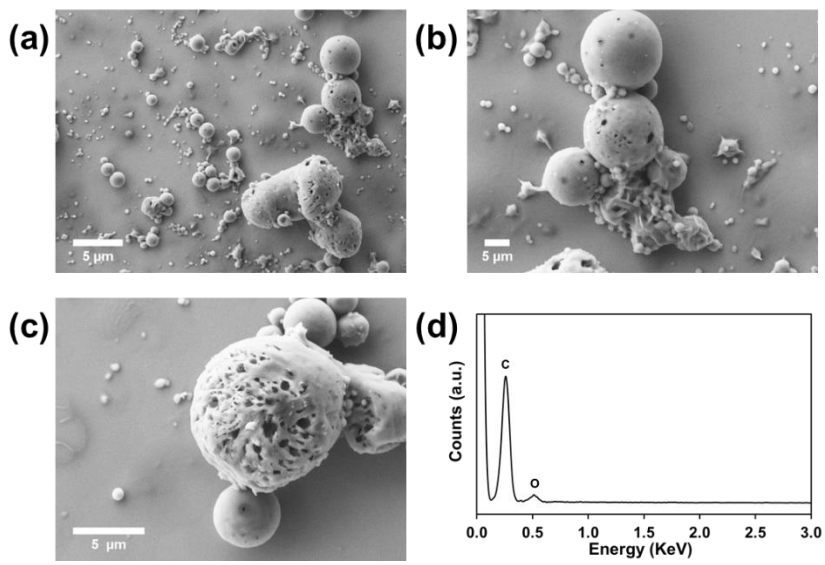

Figure 5.4.4 SEM micrographs of PTh-*g*-(PEG-*r*-PCL) microspheres (a-c); and EDX spectrum (d), from spherical particle showed in (c). The microscope was operated at 5 kV.

TEM analysis of two different concentrations (1 and 0.004 mg/mL) of copolymer in acetone where analysed. In the first scenario (1 mg/mL), the copolymer was observed with and without uranyl acetate coating. In the former case, a solution of 0.5% v/v in distilled water was dripped onto the sample previously deposited in a copper grid and dried at room temperature.

TEM micrographs displayed in Figure 5.4.5a-b show the round-like morphology of the copolymer with irregular sizes, corresponding to nano- and microparticles, as detected by DLS. After treatment with uranyl acetate, which is usually employed to observe non conducting materials in TEM, differentiation on material nature was revealed. Some spherical microparticles (black and without shell cover) were observed when the sample does not have the uranyl staining (Figure 5.4.5a) In contrast, a clear thin layer different from the core, which has been attributed to the PEG or PCL chains, is observed in TEM micrographs when the samples are treated with uranyl staining (Figure 5.4.5b). This proves that the core of those particles corresponds to the conjugated thiophene polymer backbone. Regarding the particle diameter (Figure 5.4.5c), a heterogeneous distribution with values ranging from 300 to 900 nm is observed, the average value being 569 ± 130 nm.

Rod-coil structures were also carefully observed by TEM, with further experiments carried out with very low concentration of the new copolymer in acetone solution (0.004 mg/mL). Therefore, in Figure

5.4.5d-e, the rod- and spherical-like morphologies were detected, among others. As for example, straight rods, horseshoe- and pseudospherical-like structures (formed for the longer or shorter PTh main chain, respectively) are also discernible due to the well-known phenomenon of spontaneous curvature which is taking place in the case of heterografted, statistical copolymers adsorbed at interfaces and during draying process.[100,101]

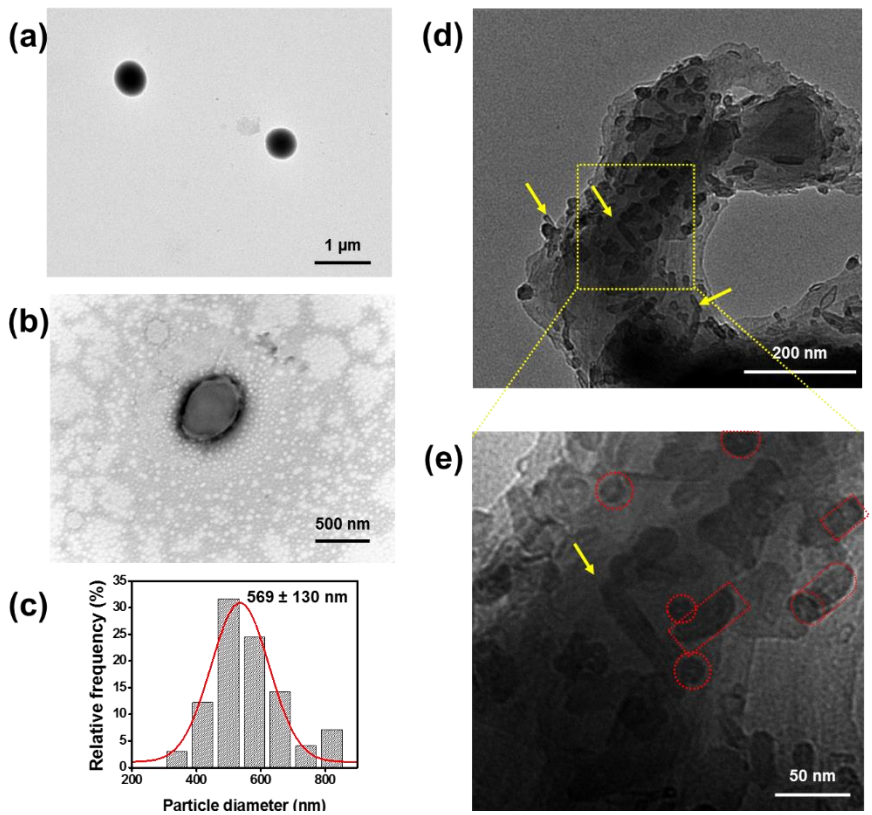

Figure 5.4.5 TEM micrograph of PTh-*g*-(PEG-*r*-PCL). Spherical particles detected (a) without and (b) with uranyl acetate staining; (c) size particle distribution. Rod like structures highlight with yellow arrows in (a) low magnification and (b) high magnifications images with straight rods, horseshoe- and pseudospherical-like structures highlighted with spherical and rectangular forms in red. The images were obtained from a solution in acetone with a concentration of 1 (a-b) and 0.004mg/mL (d-e).

In conclusion, the solvent and the concentration of the copolymer influenced the intra- and intermolecular forces on polymer chains, resulting in two different type of structures. These structures are illustrated in Scheme 5.4.2.

The rod-like structure can be the result of aggregates formed in solution by intermolecular multichains self-assembly (SA) (Scheme 5.4.2a), which even after solvent evaporation are able to keep their rod shape. The presence of the spherical particles can be due to the copolymer molecules having a shorter main chain and even shorter than the side chains (Scheme 5.4.2b). The transition from the linear-like shape to spherical shape starts from the collapse of the side chains onto copolymer main backbone causing the backbone to undergo the axial contraction under a limit value and the linear branched architecture will eventually transform into a spherical one, as reported elsewhere.[102]

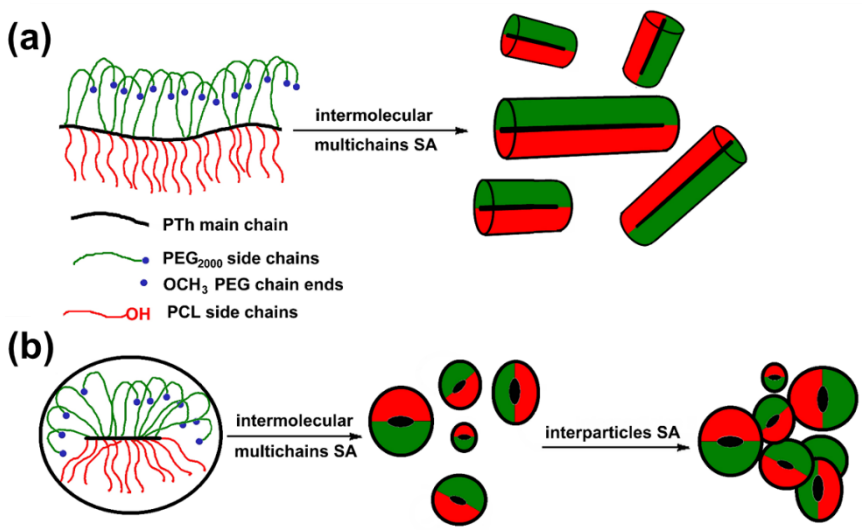

Scheme 5.4.2 Representation of PTh-*g*-(PEG-*r*-PCL) self-assembling in acetone with (a) long and (b) short PTh main chains.

The electroactivity and electrostability of the solid PTh-*g*-(PEG-*r*-PCL) copolymer, deposited by solvent casting onto carbon electrodes (DS 150), were evaluated with cyclic voltammetry. Experiments were conducted in 0.1M PBS solution, which mimicked a physiological electrolytic medium. Figure 5.4.6a compares the voltammetric curves of the bare electrode and the PTh-*g*-(PEG-*r*-PCL) copolymer at a scan rate of 50 $mV \cdot s^{-1}$. Although the current density of PTh-*g*-(PEG-*r*-PCL) is low, it is much higher than that of carbon electrode. This indicates that the charge storing capacity is significantly higher for the PTh-*g*-(PEG-*r*-PCL) graft copolymer than for the carbon electrode, even after 25 cycles (dashed line in Figure 5.4.6a).

Figure 5.4.6b represents the loss of electroactivity for PTh-*g*-(PEG-*r*-PCL) after several consecutive oxidation-reduction cycles. As it can be seen, the electroactivity decreased only 0.13% after 25 cycles, evidencing that the polymer is very stable to redox processes. In addition, voltammetry curves recorded at different scan rates (from 20 to 200 $mV \cdot s^{-1}$) were collected to check the response of the copolymer to the variable sweep rate (Figure 5.4.6c). The increase of peak current density with the scan rate evidences a good kinetics of the copolymer interfacial redox properties and the improvement of the ionic charge transport, even at high rates. Thus, these results reflect that the redox behaviour of PTh-*g*-(PEG-*r*-PCL) shows an excellent rate capability.[94]

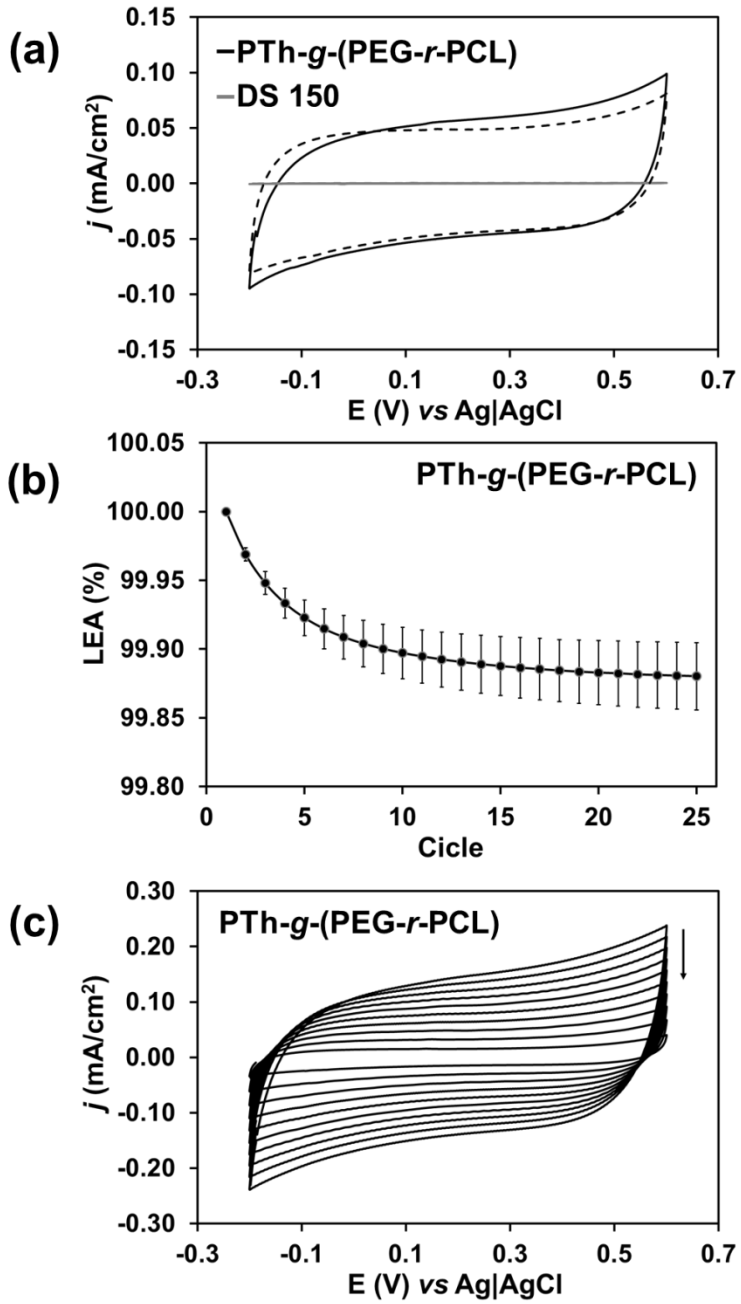

Figure 5.4.6 (a) Cyclic voltammograms of PTh-*g*-(PEG-*r*-PCL) in 0.1M PBS solution, the solid and dashed lines correspond to the 2st and the 25th oxidation-reduction cycle. (b) Loss of electroactivity (LEA, %) with the number of redox cycles. (c) cyclic voltammograms of PTh-*g*-(PEG-*r*-PCL) in PBS solution at different san rates (200, 180, 160, 140, 120, 100, 80, 60, 40 and 20 mV·s^{-1}).

Adhesion and proliferation of cells in PTh-g-(PEG-r-PCL). The biocompatibility of PTh-*g*-(PEG-*r*-PCL) copolymer was evaluated by cell adhesion (after one day) and proliferation (after 7 days) assays. Due to their fast growth, fibroblast (Cos-1) and epithelial (Vero) cell lines were selected. Figure 5.4.7a shows the quantitative results of cell viability, steel being used as control substrate. Quantification of cell adhesion onto copolymer surface reveals higher viabilities than those of the steel control substrates, for both types of cell lines (160%/cm^2 and 120%/cm^2 for Cos-1 and Vero cells, respectively). Thus, for short period of time (24 h) PTh-*g*-(PEG-*r*-PCL) copolymer does not show any cytotoxic effects acting as excellent supportive matrix, especially for the Cos-1. However, after seven days of culture, a slight reduction of the relative cell viability (12% for Cos-1 and 30% for Vero cells) on PTh-*g*-(PEG-*r*-PCL) in comparison to steel was recorded. A recent report [103] concluded that pure PCL significantly decreases the viability of Vero cells, which could explain the reduction of cells proliferation on PTh-*g*-(PEG-*r*-PCL) copolymer surface, found in the present work.

The SEM images (Figure 5.4.7b) demonstrate a normal growth and morphology of Cos-1 and Vero cells onto PTh-*g*-(PEG-*r*-PCL), after one week of incubation. It is well known that normal fibroblasts or epithelial cells, excepting adhesion, necessitate also an efficient spreading on the substrate for growth in vitro.[104] The obtained results induced the conclusion that PTh-*g*-(PEG-*r*-OCL) microspheres surface properties highly stimulate adhesion of cells but subsequently the cells are most probably inhibited from spreading, resulting in a lower proliferation observed after 7 days. However, as the cell morphology is a useful indicator of a material biocompatibility[105] and

the SEM micrographs displayed show an unaltered normal growth; it could be consider that probably, the reduction of cellular proliferation is a consequence of heterogeneous microscale surface topography combined with a certain surface chemistry of PTh-*g*-(PEG-*r*-PCL) copolymer.

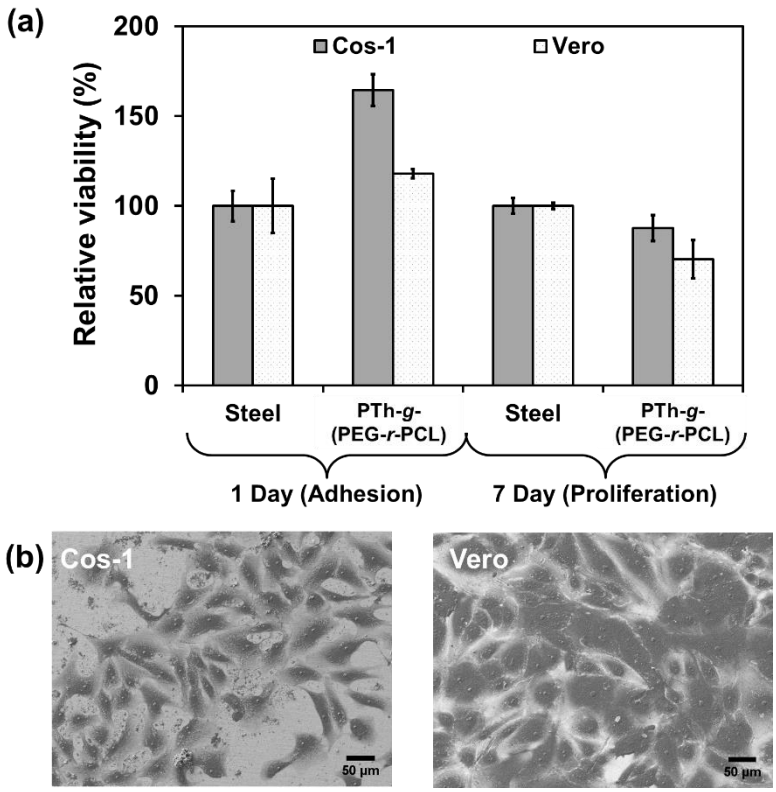

Figure 5.4.7 (a) Cellular adhesion and proliferation for PTh-*g*-(PEG-*r*-PCL) amphiphilic copolymer using Cos-1 and Vero cells; (b) Cos-1 and Vero cells observed with SEM microscope, after incubation for 7 days.

Selective detection of NADH using PTh-g-(PEG-r-PCL). NADH is a vital coenzyme for metabolic redox reactions. NADH loses two electrons and delivers a hydrogen ion, as it becomes oxidized to NAD+

(Figure 5.4.8a). As the main role of NADH and NAD^+ in the metabolism is the transfer of electrons from one molecule to another, the balance between such oxidized and reduced species is called the NAD^+/NADH ratio. This ratio is an important parameter to certify the correct metabolic activity and the health status of the cells, among other functions.

Figure 5.4.8b shows the voltammetric curve obtained for 10 mM of NADH solution at 50 $mV \cdot s^{-1}$. As it can be seen, the grafted copolymer is able to catalyse the oxidation of NADH molecules in PBS (pH=7.4) and the resulting oxidation potential is detected at ~ 0.6 V, which agrees with the value reported in the literature.[106] Figure 5.4.8c shows the differential pulse voltamogramms (DPV) in a PBS solution with different concentrations of NADH (from 2 to 10 mM). Results evidence that the copolymer catalyses the oxidation of NADH with good current density response in a low potential range. Even when the anodic peak current decreases with the concentration of NADH, the peak potential remains almost constant between 0.62-0.65 V, for all concentrations. Moreover, the calibration curve (Figure 5.4.8d) shows a good linear behaviour, the regression coefficient being 0.9801.

The performance of copolymer as amperometric sensor for the detection of very low NADH concentrations has been also evaluated. The amperometric current density-time response against the addition of NADH and the corresponding calibration plot are shown in Figure 5.4.8e-f. A linear relationship with a regression coefficient of 0.9873 was obtained for NADH concentration interval between 0.2 to 2 mM (Figure 5.4.8f). We attribute such sensor ability to the unusual topology of the copolymer, that is independent from the heterogeneous

microparticle size, but with a positive influence of the presence of porous, that could allow the permeation of NADH molecules to the thiophene inner units.

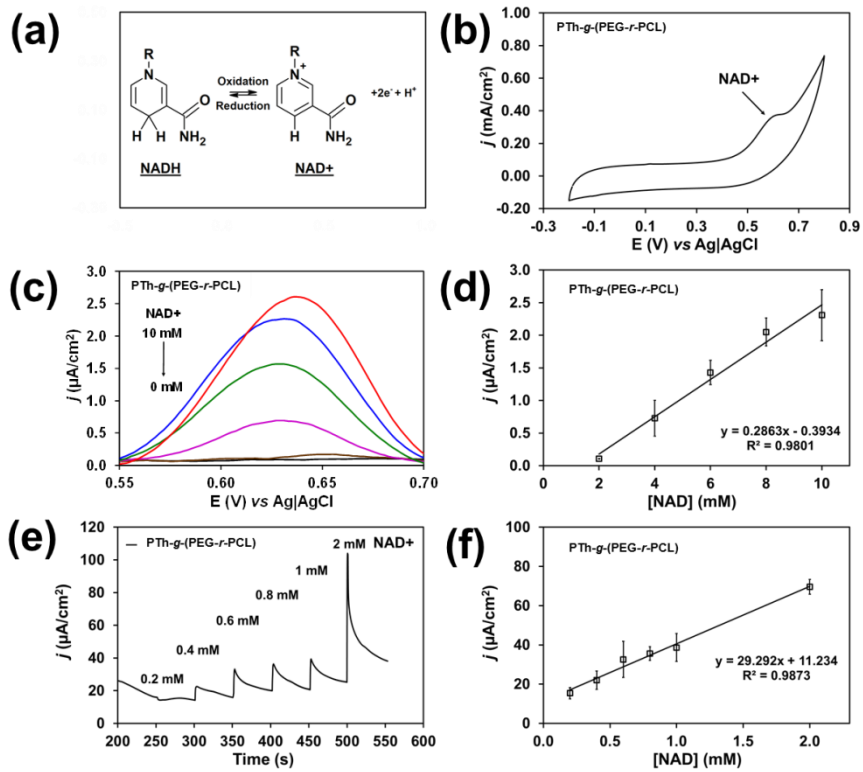

Figure 5.4.8 (a) Redox NADH/NAD^+ reaction. (b) Cyclic voltammogram of PTh-*g*-(PEG-*r*-PCL) in a 0.1M PBS solution containing 10 mM M NADH (scan rate= 50 $mV \cdot s^{-1}$). (c) DPV obtained for PBS solutions (pH=7.4) containing a NADH concentration comprised between 2 mM and 10 mM. (d) Calibration curve of the NADH detection in a concentration range from 2 to 10 mM using the PTh-*g*-(PEG-*r*-PCL) copolymer. (e) Current density-time responses of PTh-*g*-(PEG-*r*-PCL) upon successive injection of a given concentration of NADH into the PBS solution (pH=7.4). (f) Calibration curve for the NADH detection in a concentration range from 0.2 to 2 mM using PTh-*g*-(PEG-*r*-PCL).

In summary, the prepared amphiphilic heterografted polythiophene copolymer containing PEG and PCL side chains has been proved to detect NADH. This sensing capacity is simply achieved by depositing the copolymer microparticles onto a carbon electrode via drop-casting. After optimization of the sensor, the sensibility of PTh-*g*-(PEG-*r*-PCL) to low NADH concentrations can be used in future studies for the quantitative determination of NAD+/NADH ratio in living cells.

Having in mind the good sensitivity for low NADH concentrations, the sensibility of PTh-*g*-(PEG-*r*-PCL) particles to detect NADH oxidation was evaluated in the presence of interfering species. AA is the most common interfering compound in the electrochemical detection of NADH from biological samples.[107] Accordingly, the selective determination of NADH in a mixture with AA was conducted using both CV and DPV. Figure 5.4.9a shows the voltammetric curve recorded for PTh-*g*-(PEG-*r*-PCL) in a 0.1 M of PBS solution with of 5 mM of AA and 5 mM of NADH. Two main oxidation peaks, which have been attributed to the oxidation of AA (lower potential) and NAD+ process, are clearly detected. The differential pulse voltammogram, which is displayed in Figure 5.4.9b, presents two well defined oxidation peaks at 300 and 580 mV that correspond to AA and NADH, respectively. Moreover, the peak separation of 280 mV indicates that the amphiphilic PTh grafted copolymer can be successfully used for selective detection of NADH in the presence of AA.[107]

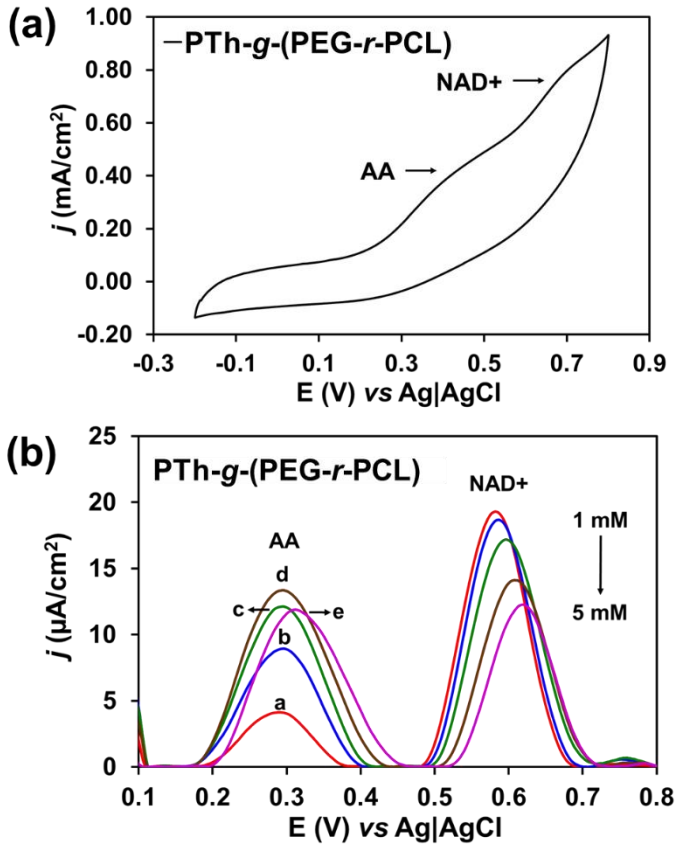

Figure 5.4.9 (a) Cyclic voltammogram obtained from PTh-*g*-(PEG-r-PCL) in a 0.1M PBS solution with 5mM NADH and 5 mM AA. Scan rate: 50 mV·s-1. (b) Differential pulse voltammogram obtained for PTh-*g*-(PEG-r-PCL) in a PBS solution with 5mM NADH and a variable concentration of AA (from the lowest, a = 1mM; to the highest concentration, e = 5 mM).

Conclusions

By oxidative polycondensation method of an equimolar mixture of PEG-containing thiophene macromonomer (Th-PEG) and OCL-containing thiophene macromonomer (Th-OCL), amphihilic PTh-*g*-(PEG-*r*-PCL) copolymer was synthesized. The resulting material, so-called prototype or Janus type copolymer, has a

hydrophilic-lipophilic balance (HLB) of 0.36 and a copolymer composition of 40% of Th-PEG and 60% of Th-OCL, as proved by NMR spectroscopy. DLS measurements and the morphology study of the copolymer in acetone, revealed rod-like and spherical microparticles with heterogeneous size and porosity. The deposition of such microspheres onto carbon electrodes evidenced the ability of the π-conjugated system to detect the oxidation reaction of NADH coenzyme molecules, with lineal response, dependent on the increase concentration of the coenzyme.

In conclusion, by intelligently combining the components of well-known polymeric biomaterials (PEG and PCL) with a multi-sensitive conjugated polymer (PTh), a biomimetic material was obtained. Its biomimicry is reflected in its amphiphilicity similitude and in its self-assembling ability. The presence of PCL side chains strengthened the electrochemical stability and increased the ionic conductivity, endowing the copolymer with high ability to work in aqueous electrolytes.

5.5 Conclusions

PPy and PTh ICPs were smartly modified by the "grafting-through" technique, via electrochemical or oxidative polymerization. The biocompatibility of the grafted biopolymers, PEG and/or PCL, are well known and, therefore, the cytotoxicity of the systems was reduced considerably as was demonstrated by biological assays.

In order to obtain the optimal conditions for the preparation of the mentioned copolymers, different polymerization times and comonomers ratios were evaluated. Previous results suggest that macromonomers have low mobility so, long electropolymerization times are required, particularly with similar comonomers ratio. However, even with low percentages of macromonomers in the feed solution, a positive impact in the biocompatibility of the final films was observed. Moreover, the effect of the polymerization methods was evaluated. While electrochemical polymerization produces films of controlled thickness, oxidative polycondensation turned out in self-assembling rod-like and spherical microparticles with heterogeneous size and porosity.

The electrochemical stability provided by prepared graft copolymers allowed to detect low concentrations of dopamine, serotonin or nicotinamide adenine dinucleotide, even in the presence of interfering substances. This capacity together with the good response of the prepared materials towards cells, prove that the proposed modification is a smart alternative for developing precise electrochemical sensors, which could be implanted in living systems.

5.6 References

1 R. L. Dimarco and S. C. Heilshorn, *Adv. Mater.*, 2012, **24**, 3923–3940.

2 J. Huang and A. Heise, *Chem. Soc. Rev.*, 2013, **42**, 7373–7390.

3 J. Wu, N. Kamaly, J. Shi, L. Zhao, Z. Xiao, G. Hollett, R. John, S. Ray, X. Xu, X. Zhang, P. W. Kantoff and O. C. Farokhzad, *Angew. Chemie - Int. Ed.*, 2014, **53**, 8975–8979.

4 C. L. McGann, E. A. Levenson and K. L. Kiick, *Macromol. Chem. Phys.*, 2013, **214**, 203–213.

5 R. Dong, X. Zhao, B. Guo and P. X. Ma, *ACS Appl. Mater. Interfaces*, 2016, **8**, 17138–17150.

6 T. F. Otero, *Electrochim. Acta*, 2016, **212**, 440–457.

7 M. E. Abdelhamid, A. P. O'Mullane and G. A. Snook, *RSC Adv.*, 2015, **5**, 11611–11626.

8 T. F. Otero and J. G. Martinez, *J. Mater. Chem. B*, 2016, **4**, 2069–2085.

9 Y. Z. Long, M. M. Li, C. Gu, M. Wan, J. L. Duvail, Z. Liu and Z. Fan, *Prog. Polym. Sci.*, 2011, **36**, 1415–1442.

10 T. H. Le, Y. Kim and H. Yoon, *Polymers (Basel).*, , DOI:10.3390/polym9040150.

11 S. Soylemez, S. O. Hacioglu, M. Kesik, H. Unay, A. Cirpan and L. Toppare, *ACS Appl. Mater. Interfaces*, 2014, **6**, 18290–18300.

12 G. Fabregat, E. Córdova-Mateo, E. Armelin, O. Bertran and C. Alemán, *J. Phys. Chem. C*, 2011, **115**, 14933–14941.

13 G. Fabregat, E. Armelin and C. Alemán, *J. Phys. Chem. B*, 2014, **118**, 4669–4682.

14 L. D. Sappia, E. Piccinini, W. Marmisollé, N. Santilli, E. Maza, S. Moya, F. Battaglini, R. E. Madrid and O. Azzaroni, *Adv. Mater. Interfaces*, 2017, **4**, 1–11.

15 N. Aydemir, J. Malmström and J. Travas-Sejdic, *Phys. Chem. Chem. Phys.*, 2016, **18**, 8264–8277.

16 M. M. Pérez-Madrigal, E. Armelin, J. Puiggalí and C. Alemán, *J. Mater. Chem. B*, 2015, **3**, 5904–5932.

17 R. Green and M. R. Abidian, *Adv. Mater.*, 2015, **27**, 7620–7637.

18 Z. Wang, P. Tammela, J. Huo, P. Zhang, M. Strømme and L. Nyholm, *J. Mater. Chem. A*, 2016, **4**, 1714–1722.

19 D. E. López-Pérez, D. Aradilla, L. J. Del Valle and C. Alemán, *J. Phys. Chem. C*, 2013, **117**, 6607–6619.

20 N. Hadjichristidis, M. Pitsikalis, H. Iatrou and S. Pispas, *Macromol. Rapid Commun.*, 2003, **24**, 979–1013.

21 D. MARGERISON and G. C. EAST, *Ionic Polymerization*, Elsevier Inc., 1967.

22 H. Kurosu, *Chapter 16 Electrically-Conducting Polymers*, Elsevier B.V., 1998, vol. 84.

23 N. Yi and M. R. Abidian, *Conducting polymers and their biomedical applications*, 2016.

24 T. P. Kaloni, P. K. Giesbrecht, G. Schreckenbach and M. S. Freund, *Chem. Mater.*, 2017, **29**, 10248–10283.

25 Y. Yagci and L. Toppare, *Polym. Int.*, 2003, **52**, 1573–1578.

26 M. Wang, S. Zou, G. Guerin, L. Shen, K. Deng, M. Jones, G. C. Walker, G. D. Scholes and M. A. Winnik, *Macromolecules*, 2008, **41**, 6993–7002.

27 J. Zhang, J. Lei, R. Pan, Y. Xue and H. Ju, *Biosens. Bioelectron.*, 2010, **26**, 371–376.

28 D. Mecerreyes, R. Stevens, C. Nguyen, J. A. Pomposo, M. Bengoetxea and H. Grande, *Synth. Met.*, 2002, **126**, 173–178.

29 A. D. Bendrea, G. Fabregat, L. Cianga, F. Estrany, L. J. Del Valle, I. Cianga and C. Alemán, *Polym. Chem.*, 2013, **4**, 2709–2723.

30 A. D. Bendrea, G. Fabregat, J. Torras, S. Maione, L. Cianga, L. J. Del Valle, I. Cianga and C. Alemán, *J. Mater. Chem. B*, 2013, **1**, 4135–4145.

31 S. Maione, G. Fabregat, L. J. Del Valle, A. D. Bendrea, L. Cianga, I. Cianga, F. Estrany and C. Alemán, *J. Polym. Sci. Part B Polym. Phys.*, 2015, **53**, 239–252.

32 F. A. G. Da Silva, J. C. Queiroz, E. R. Macedo, A. W. C. Fernandes, N. B. Freire, M. M. Da Costa and H. P. De Oliveira, *Mater. Sci. Eng. C*, 2016, **62**, 317–322.

33 M. Golabi, A. P. F. Turner and E. W. H. Jager, *Macromol. Chem. Phys.*, 2016, **217**, 1128–1135.

34 X. Qu and Z. Yang, *Chem. - An Asian J.*, 2016, **11**, 2633–2641.

35 L. Arnt, K. Nüsslein and G. N. Tew, *J. Polym. Sci. Part A Polym. Chem.*, 2004, **42**, 3860–3864.

36 D. G. Colak, I. Cianga, L. Cianga and Y. Yagci, *Des. Monomers Polym.*, 2016, **19**, 508–534.

37 M. M. Pérez-Madrigal, L. Cianga, L. J. Del Valle, I. Cianga and C. Alemán, *Polym. Chem.*, 2015, **6**, 4319–4335.

38 X. Zhao, B. Guo and P. X. Ma, *J. Mater. Chem. B*, 2015, **3**, 8459–

8468.

39 K. Adamska, A. Voelkel and A. Berlińska, *J. Pharm. Biomed. Anal.*, 2016, **127**, 202–206.

40 W. G. Herkstroeter, *J. Am. Chem. Soc.*, 1973, **95**, 8686–8691.

41 P. Douglas, C. Couture, D. Clarke, D. Reed, I. H. Sadler and T. Wear, *J. CHEM. SOC. PERKIN TRANS*, 1994, **2**, 1295–1298.

42 S. Tarkuc, E. Sahin, L. Toppare, D. Colak, I. Cianga and Y. Yagci, *Polymer (Guildf).*, 2006, **47**, 2001–2009.

43 C. I. Simionescu, M. Grovu-Ivanoiu, M. Grigoras and I. Cianga, *Die Angew. Makromol. Chemie*, 1994, **221**, 103–115.

44 C. I. Simionescu, I. Cianga, M. Ivanoiu, A. Airinei, M. Grigoras and I. Radu, *Eur. Polym. J.*, 1999, **35**, 1895–1905.

45 C. I. Simionescu, M. Grovu-Ivanoiu, I. Cianga, M. Grigoras, A. Duca and I. Cocarla, *Die Angew. Makrornolekulare Chemie*, 1996, **239**, 1–12.

46 B. Teixeira-Dias, C. Alemán, F. Estrany, D. S. Azambuja and E. Armelin, *Electrochim. Acta*, 2011, **56**, 5836–5843.

47 D. Aradilla, F. Estrany, E. Armelin, R. Oliver, J. I. Iribarren and C. Alemán, *Macromol. Chem. Phys.*, 2010, **211**, 1663–1672.

48 C. Ocampo, R. Oliver, E. Armelin, C. Alemán and F. Estrany, *J. Polym. Res.*, 2006, **13**, 193–200.

49 M. Omastová, M. Trchová, J. Kovářová and J. Stejskal, *Synth. Met.*, 2003, **138**, 447–455.

50 V. Chandra and K. S. Kim, *Chem. Commun.*, 2011, **47**, 3942–3944.

51 X. Fan, Z. Yang and N. He, *RSC Adv.*, 2015, **5**, 15096–15102.

52 L. Cianga, A. D. Bendrea, N. Fifere, L. E. Nita, F. Doroftei, D. Ag, M. Seleci, S. Timur and I. Cianga, *RSC Adv.*, 2014, **4**, 56385–56405.

53 F. Estrany, D. Aradilla, R. Oliver, E. Armelin and C. Alemán, *Eur. Polym. J.*, 2008, **44**, 1323–1330.

54 D. Aradilla, F. Estrany, E. Armelin and C. Alemán, *Thin Solid Films*, 2010, **518**, 4203–4210.

55 C. Alemán, J. Casanovas, J. Torras, O. Bertrán, E. Armelin, R. Oliver and F. Estrany, *Polymer (Guildf).*, 2008, **49**, 1066–1075.

56 K. S. Teh, Y. Takahashi, Z. Yao and Y. W. Lu, *Sensors Actuators, A Phys.*, 2009, **155**, 113–119.

57 A. R. Murphy, J. Liu, C. Luscombe, D. Kavulak, J. M. J. Fréchet, R. J. Kline and M. D. McGehee, *Chem. Mater.*, 2005, **17**, 4892–4899.

58 J. Arjomandi, A. U. H. A. Shah, S. Bilal, H. Van Hoang and R. Holze, *Spectrochim. Acta - Part A Mol. Biomol. Spectrosc.*, 2011, **78**, 1–6.

59 R. Brooke, D. Evans, P. Hojati-Talemi, P. Murphy and M. Fabretto, *Eur. Polym. J.*, 2014, **51**, 28–36.

60 N. Yılmaz Baran, M. Karakışla, H. Ö. Demir and M. Saçak, *J. Mol. Struct.*, 2016, **1123**, 153–161.

61 C. M. Da Silva, D. L. Da Silva, L. V. Modolo, R. B. Alves, M. A. De Resende, C. V. B. Martins and Â. De Fátima, *J. Adv. Res.*, 2011, **2**, 1–8.

62 M. Golabi, A. P. F. Turner and E. W. H. Jager, *Sensors Actuators, B Chem.*, 2016, **222**, 839–848.

63 W. Zhou, L. Lu, D. Chen, Z. Wang, J. Zhai, R. Wang, G. Tan, J. Mao, P. Yu and C. Ning, *J. Mater. Chem. B*, 2018, **6**, 3128–3135.

64 A. D. Bendrea, L. Cianga, E. G. Hitruc and I. Cianga, *Int. J. Polym. Anal. Charact.*, 2013, **18**, 189–198.

65 M. Pannuzzo, D. H. De Jong, A. Raudino and S. J. Marrink, *J. Chem. Phys.*, , DOI:10.1063/1.4869176.

66 L. A. Clifton, M. W. A. Skoda, A. P. Le Brun, F. Ciesielski, I. Kuzmenko, S. A. Holt and J. H. Lakey, *Langmuir*, 2015, **31**, 404–412.

67 M. S. Weiss, G. J. Palm and R. Hilgenfeld, *Acta Crystallogr. Sect. D Biol. Crystallogr.*, 2000, **56**, 952–958.

68 M. L. Ferrer, R. Duchowicz, B. Carrasco, J. G. De La Torre and A. U. Acuña, *Biophys. J.*, 2001, **80**, 2422–2430.

69 K. A. Majorek, P. J. Porebski, A. Dayal, M. D. Zimmerman, K. Jablonska, A. J. Stewart, M. Chruszcz and W. Minor, *Mol. Immunol.*, 2012, **52**, 174–182.

70 J. A. Pranzetti, Alice Preece and P. M. Mendes, *Intelligent stimuli-responsive materials: from welldefined nanostructures to applications*, John Wiley & Sons, Ltd, 2013.

71 M. Tertiș, A. Cernat, D. Lacatiș, A. Florea, D. Bogdan, M. Suciu, R. Săndulescu and C. Cristea, *Electrochem. commun.*, 2017, **75**, 43–47.

72 I. Cesarino, H. V. Galesco and S. A. S. Machado, *Mater. Sci. Eng. C*, 2014, **40**, 49–54.

73 X. Jiang and X. Lin, *Anal. Chim. Acta*, 2005, **537**, 145–151.

74 J. Li and X. Lin, *Sensors Actuators, B Chem.*, 2007, **124**, 486–493.

75 S. Sharma, N. Singh, V. Tomar and R. Chandra, *Biosens. Bioelectron.*, 2018, **107**, 76–93.

76 S. Yurteri, I. Cianga, M. Degirmenci and Y. Yagci, *Polym. Int.*, 2004, **53**, 1219–1225.

77 I. Kerman, L. Toppare, F. Yilmaz and Y. Yagci, *J. Macromol. Sci.* -

Pure Appl. Chem., 2005, **42 A**, 509–520.

78 L. G. M. Beekmans and G. J. Vancso, *Polymer (Guildf).*, 2000, **41**, 8975–8981.

79 M. J. Jenkins and K. L. Harrison, *Polym. Adv. Technol.*, 2006, **17**, 474–478.

80 B. X. Valderrama-García, E. Rodríguez-Alba, E. G. Morales-Espinoza, K. M. Chane-Ching, E. Rivera, S. Reed and M. Resendiz, *Molecules*, , DOI:10.3390/molecules21020172.

81 G. Li, G. Koj, H. Welzel, G. Engelmann and W. Hunnius, 1998, **533**, 525–533.

82 C. J. Luo, E. Stride and M. Edirisinghe, *Macromolecules*, 2012, **45**, 4669–4680.

83 L. Qi, M. Sun and S. Dong, *J. Appl. Polym. Sci.*, 2006, **102**, 1803–1808.

84 G. Fabregat, J. Casanovas, E. Redondo, E. Armelin and C. Alemán, *Phys. Chem. Chem. Phys.*, 2014, **16**, 7850–7861.

85 S. Akoudad and J. Roncali, *Electrochem. commun.*, 2000, **2**, 72–76.

86 S. Maione, A. M. Gil, G. Fabregat, L. J. Del Valle, J. Triguero, A. Laurent, D. Jacquemin, F. Estrany, A. I. Jiménez, D. Zanuy, C. Cativiela and C. Alemán, *Biomater. Sci.*, 2015, **3**, 1395–1405.

87 S. Garreau, G. Louarn, J. P. Buisson, G. Froyer and S. Lefrant, *Macromolecules*, 1999, **32**, 6807–6812.

88 J. Poater, J. Casanovas, M. Solà and C. Alemán, *J. Phys. Chem. A*, 2010, **114**, 1023–1028.

89 I. Cianga and Y. Yagci, *Prog. Polym. Sci.*, 2004, **29**, 387–399.

90 E. K. Richfield, J. B. Penney and A. B. Young, *Neuroscience*, 1989, **30**, 767–777.

91 L. Cianga, A. D. Bendrea, N. Fifere, L. E. Nita, F. Doroftei, D. Ag, M. Seleci, S. Timur and I. Cianga, *RSC Adv.*, 2014, **4**, 56385–56405.

92 H. Liu, A. Jiang, J. Guo and K. E. Uhrich, *J. Polym. Sci. Part A Polym. Chem.*, 1999, **37**, 703–711.

93 D. G. Colak, I. Cianga, L. Cianga and Y. Yagci, *Des. Monomers Polym.*, 2016, **19**, 508–534.

94 R. B. Ambade, S. B. Ambade, N. K. Shrestha, R. R. Salunkhe, W. Lee, S. S. Bagde, J. H. Kim, F. J. Stadler, Y. Yamauchi and S. H. Lee, *J. Mater. Chem. A*, 2017, **5**, 172–180.

95 A. D. Bendrea, G. Fabregat, L. Cianga, F. Estrany, L. J. Del Valle, I. Cianga and C. Alemán, *Polym. Chem.*, 2013, **4**, 2709–2723.

96 T. P. Tuyen Dao, T. H. Nguyen, V. V. To, T. H. Ho, T. A. Nguyen

and M. C. Dang, *A new formulation of curcumin using poly (lactic-co-glycolic acid) - Polyethylene glycol diblock copolymer as carrier material*, 2014, vol. 5.

97 F. Rodríguez-Ropero, J. Casanovas and C. Alemán, *J. Comput. Chem.*, 2008, **29**, 69–78.

98 E. Córdova-Mateo, O. Bertran, A. D. Schlüter, M. Kröger and C. Alemán, *Soft Matter*, 2015, **11**, 1116–1126.

99 J. Torras and C. Alemán, *J. Phys. Chem. C*, 2014, **118**, 9769–9779.

100 T. Stephan, S. A. Muth and M. Schmidt*, *Macromolecules*, 2002, **35**, 9857–9860.

101 I. I. Potemkin, A. R. Khokhlov, S. Prokhorova, S. S. Sheiko, M. Möller, K. L. and Beers and K. Matyjaszewsk, *Macromolecules*, 2004, **37**, 3918–3923.

102 D. M. Henn, J. A. Holmes, E. W. Kent and B. Zhao, *J. Phys. Chem. B*, 2018, **122**, 7015–7025.

103 C. Alvim Valente, P. Cesar Chagastelles, N. Fontana Nicoletti, G. Ramos Garcez, B. Sgarioni, F. Herrmann, G. Pesenatto, E. Goldani, M. L. Zanini, M. M. Campos, R. Meurer Papaléo, J. Braga da Silva and N. R. de Souza Basso, *J. Biomed. Mater. Res. Part A*, 2018, **106**, 1522–1534.

104 M. J. Dalby, S. Childs, M. O. Riehle, H. J. H. Johnstone, S. Affrossman and A. S. G. Curtis, *Biomaterials*, 2003, **24**, 927–35.

105 D. Ajami-Henriquez, M. Rodríguez, M. Sabino, R. V. Castillo, A. J. Müller, A. Boschetti-de-Fierro, C. Abetz, V. Abetz and P. Dubois, *J. Biomed. Mater. Res. Part A*, 2008, **87A**, 405–417.

106 L. Meng, A. P. F. Turner and W. C. Mak, *Biosens. Bioelectron.*, 2018, **120**, 115–121.

107 L. Rotariu, O. M. Istrate and C. Bala, *Sensors Actuators, B Chem.*, 2014, **191**, 491–497.

CHAPTER 6

BACTERIA SENSOR THROUGH NADH ELECTROCHEMICAL DETECTION

J. Phys. Chem. C, **2019**, 123, 22181

This Chapter present the functionalization of an insulating polymer that exhibits excellent mechanical properties, isotactic polypropylene, with a conducting polymer, poly(3,4-ethylenedioxythiophene). After characterization of the resulting composite, its performances as electrochemical (bio)sensor of bacteria and as an electroactive bioplatform for tissue engineering were evaluated.

6.1 Introduction

Rapid detection of bacterial pathogens is essential for an effective treatment of infections. Nowadays, the most classical technique for microbial detection involves bacteria culturing on agar plates, which takes at least 24 h. In the same time, the bacteria embed themselves in a hydrated extracellular matrix of polysaccharides and proteins, forming a slimy layer known as a biofilm. Biofilms, which are considered as an adaptation of microbes to hostile environments, [1] are generated after initial adhesion of bacteria onto any kind of living or inert surface, followed by their growth and reproduction. During the growth phase, bacteria produce extracellular biopolymers that create a complex matrix of molecular fibres with unique characteristics like its capacity to hinder the access of antimicrobials through it. [2–4] As a consequence, adhered microorganisms increase their antimicrobial resistance, becoming one thousand times more resistant to antibiotics and, in consequence, difficult to eradicated.

Electrochemical (bio)sensors are a promising solution for a rapid and accurate bacteria detection. Recently, electrochemical impedance spectroscopy (EIS) has been employed to detect variations in charge transfer resistance and capacitance corresponding to the growing stages of a biofilm. [5–10] However, the development of more precise

strategies for bacteria detection is highly desirable. With that in mind, we propose the use of cyclic voltammetry (CV) to detect the presence of bacteria by the electrochemical recognition of nicotinamide adenine dinucleotide (NADH). This biomolecule plays an important role not only as cofactor for numerous dehydrogenase enzymes but also in the electron transfer chain in living organisms. [11,12] In fact, NADH and its oxidized form (NAD+) mediate many redox reactions and provide the major source of ATP for aerobic organisms. [12]

Eukaryotic cells present two major NADH pools, the cytosolic and the mitochondrial pools. [13] Although aerobic respiration reactions in eukaryotic cells take place in mitochondria, the mitochondrial and cytosolic NADH ratio is cell-type specific. [14] However, a distinctive characteristic is that mitochondrial double-membrane is impermeable to NADH or NAD+ (*i.e.* the outer membrane is quite permeable but the inner membrane is highly folded into cristae), so, mitochondrial NADH levels are maintained even upon massive depletion of cytosolic NADH. [15,16] Contrary, prokaryotes do not have mitochondria thus, their respiration occurs in the cytosol or on the inner surfaces of the cell membrane. Therefore, as prokaryote cellular membranes are permeable to NADH and NAD+ and a gradient is expected, the extracellular detection of these species could be an appropriate target for monitoring growing bacterial infections or biofilms.

As was proved in the former Chapter, the electroactivity, electrostability and biocompatibility of ICPs make them an excellent option for the electrochemical recognition of low concentrations of NADH. Therefore, in this work we studied the sensing abilities of a polythiophene derivative, poly(3,4-ethylenedioxythiophene)

(PEDOT), combined with isotactic polypropylene (i-PP) a recognized biomaterial used for the fabrication of internal prostheses, to develop a smart electrochemical (bio)sensor capable to distinguish the bacterial growth from the growth of eukaryotic cells and the amount of NADH in a culture medium. In addition, the last section is dedicated to optimize the biocompatibility of the resulting i-PP_f/PEDOT composite, by grafting poly(ε-caprolactone) chains to the conjugated backbone, which has been achieved using the "grafting-through" or macromonomer synthetic approach.

6.2 Electrochemical sensor for bacterial metabolism based on the detection of NADH by polythiophene nanoparticles

Abstract

Composite i-PP/PEDOT films made of isotactic polypropylene (i-PP), which is frequently used for the fabrication of implantable medical devices for internal use, and chemically synthesized poly(3,4-ethylenedioxythiophene) (PEDOT) nanoparticles, which are electroactive and biocompatible, have been prepared and used to detect biofilm infection. After chemical and morphological characterization, the properties (interfacial, mechanical, thermal and electrochemical) and biocompatibility of i-PP/PEDOT have been examined. Besides, carbon screen-printed electrodes coated with i-PP/PEDOT have been found to detect the growth of Gram-positive and Gram-negative bacteria through the oxidation of nicotinamide adenine dinucleotide (NADH), which comes from the bacteria metabolism (*i.e.* the respiration). Thus, as outer bacterial membranes are permeable to cytosolic NADH, this metabolite has been found to be an appropriate target for the detection of growing bacterial infections (biofilms). In addition, the sensor does not respond towards eukaryotic cells. This is because the major NADH pool in eukaryotic cells is located at the mitochondria and, therefore, the concentration in the medium is not high enough to be detected since the inner mitochondrial membrane is impermeable to NADH or NAD+.

Materials and methods

Materials. 4-Dodecylbenzenesulfonic acid (DBSA), ammonium persulfate (APS), 3,4-ethylenedioxythiophene monomer (EDOT), isotactic polypropylene (i-PP) pellets and gelatine from porcine skin (gel strength 300, type A G2500) were purchased from Sigma Aldrich Chemical Company. Xylene, methanol and sodium chloride were purchased from Panreac Quimica S.A.U. (Spain). Sodium chloride was dried under vacuum at 70 ºC prior to blending.

For cell culture experiments, Cos-1 fibroblast-like cells and Vero epithelial-like cells from African green monkey *(Cercopithecus aethiops)* were acquired from ATCC (USA). Dulbecco's phosphate buffered saline solution (PBS) without calcium chloride and magnesium chloride, Dulbecco's modified Eagle's medium (DMEM, with 4500 mg of glucose/L, 110 mg of sodium pyruvate/L and 2 mM L-glutamine), penicillin-streptomycin, N-(2-hydroxyethyl)piperazine-N′-(2-ethanesulfonic acid) (HEPES) solution (1 M, pH 7.0-7.6), 3-(4,5-dimethylthiazol-2-yl)-2,5-diphenyltetrazolium bromide (MTT, 97.5%) and trypsin-EDTA solution (0.05% trypsin, 0.02% EDTA) were all purchased from Sigma-Aldrich (USA). Fetal bovine serum (FBS) and trypan blue stain (0.4%) were purchased from Gibco, UK. Dimethyl sulfoxide (99.0%) was purchased from Panreac Quimica S.A.U. (Spain) and sodium azide (NaN_3, ≥99.5%) from Sigma-Aldrich (USA).

The bacteria *Escherichia coli* (*E. coli*) and *Staphylococcus aureus* (*S. aureus*), which are Gram-negative and Gram-positive bacteria, respectively, were obtained from the Spanish Collection of Type Culture (Valencia, Spain).

Synthesis of PEDOT NPs. PEDOT NPs were prepared by chemical polymerization adapting a previously reported procedure. [17] In brief, an aqueous micellar solution was prepared by stirring (750 rpm) a solution of 0.07 g of 4-dodecylbenzenesulfonic acid (DBSA) in 20 mL of milli-Q water for 1 hour. This was followed by the addition of 11.8 mg of 3,4-ethylenedioxythiophene (EDOT) monomer and, again, was stirred (750 rpm) for 1 hour at room temperature. Finally, 0.45 g of ammonium persulfate (APS) dissolved in 5 mL of milli-Q water was added to the solution. Then, the reaction was maintained in agitation at 30 ºC for 24 hours protected from light with aluminium foil. In this process, the colour of the reaction mixture changed from light grey to dark blue.

No sedimentation was observed after the reaction, indicating a good colloidal stability. The resultant solution was centrifuged (11000 rpm) for 40 min at 4 °C. The supernatant solution was decanted and the sediment was re-dispersed in milli-Q water using an ultrasonic bath for 15 min at 30 °C. The centrifugation and re-dispersion process were conducted two more times to ensure the elimination of side products and unreacted chemicals, purifying the dispersion medium. Finally, the last pellet was kept under vacuum two days and, subsequently, was weighted and re-dispersed in the corresponding media at the desired concentration.

Preparation of compact i-PP films. In order to dissolve polymer pellets, 3 g of i-PP (M_n = 50000 g/mol, M_w = 190000 g/mol, and polydispersity index = 3.80) and 100 mL of xylene were loaded in a round bottom flask equipped with a magnetic stirrer. The solution was heated on an oil bath set at 130 ºC and continuously stirred (250 rpm)

until the pellets were completely dissolved. Then, the temperature was decreased to 120 ºC, maintained at such conditions for 20 min, and cooled to room temperature. After that, the polymer was precipitated by adding 400 mL of methanol. The polymer was separated by filtration, washed with methanol for three times, and put in a ventilation hood during 48 hours for solvent evaporation. The recovered product was dried at 50 ºC for 24 hours.

i-PP films were prepared in a hydraulic press of 15 tons equipment with Atlas series heated platens. For this purpose, 0.1 g of polymer powder were placed in the press, heated until 180 ºC and, after 5 min, the pressure was increased from 0 to 5 tons. After 2.5 min, the pressure was increased to 7 tons and maintained for 2.5 min more. Finally, the film was removed from the press and cooled to room temperature.

Preparation of porous i-PP films. i-PP powder was mixed with 10% w/w NaCl by mechanical stirring at 1000 rpm for 12 hours. Films were obtained by pressing the powder mixture following the procedure previously explained. Porous films were obtained by dissolving the NaCl particles, immersing the samples in deionized water for periods of 12 hours, after time, the films were dry on a vacuumed chamber for 12 hours and weighed. The procedure was repeated until the weight of the dry sample was stable (water was changed every period). Hereafter, the porous films resulting from such process have been denoted i-PP(p) to differentiate them from compact i-PP films.

Preparation of i-PP/PEDOT films. i-PP/PEDOT films were prepared by incorporating PEDOT NPs powder to the initial mixture, as described for i-PP(p). PEDOT NPs were added considering 40 or 60 % w/w with respect to the i-PP weight, the films were store in a dry

condition under vacuum. The films resulting from such concentrations were denoted i-PP/PEDOT(40%) and i-PP/PEDOT(60%), respectively.

Characterization of prepared films. A detail description of the characterization methods employed to evaluate the films, which involved dynamic light scattering (DLS), scanning electron microscopy (SEM, operating at 5 kV), FTIR and micro-Raman spectroscopies, wettability, stress-strain, calorimetric, thermogravimetric and biological assays, *i.e.* antibacterial activity and cell adhesion and proliferation were provided in the Chapter 4. The thickness of i-PP, i-PP(p), i-PP/PEDOT(40%) and i-PP/PEDOT(60%) films was measured using a LIST-MAGNETIK MEGA-CHECK Pocket thickness meter. Average values and standard deviations were obtained using ten independent replicas for each film composition.

Electrochemical detection of prokaryotic vs. eukaryotic cells. All the electrochemical assays and the electrochemical detection of cells were performed by cyclic voltammetry (procedure described in Chapter 4), the experiments were collected with an initial and final potentials of −0.20 V while the reversal potential was +0.60 V. A scan rate of 100 mV s^{-1} was applied in all cases. An Ag|AgCl 3 M KCl and a Pt-wire were used as reference electrode and counter electrode, respectively. The working electrode consisted on a carbon screen-printed electrode (SPE) from Dropsens (DRP-150) coated with a gelatine layer, which was used to adhere the i-PP and i-PP/PEDOT films. Such adhesive layer was prepared by dissolving 50 mg of gelatine from porcine skin in 1 mL of milli-Q water, which was placed in an ultrasonic bath at 40 °C for 15 minutes until a clear solution was

acquired. A solution drop (10 μL) was deposited onto the SPE surface, subsequently, a round film of i-PP or i-PP/PEDOT (4 mm in diameter) was placed onto the resulting gelatine-modified SPE and refrigerated overnight before use. All experiments were replicated three times.

Growth curves of *E. coli* and *S. aureous* were obtained seeding 5 mL of culture medium containing 1 x 10^3 colony forming units in 15 mL polystyrene tubes. The cultures were incubated at 37 ºC and agitated at 100 rpm. Aliquots of 100 μL were taken at pre-defined time intervals for absorbance measurement at 650 nm in a plate reader. Thus, turbidity was directly related to bacterial growth. The bacterial growth in broth culture alone (in absence of any film) was considered as the maximum growth (control) and it was used to calculate the relative growth of the bacteria in presence of the samples. All assays were conducted in triplicate and the values averaged.

Results and discussion

Preparation and characterization of the prepared films. Figure 6.2.1a displays a micrograph of the prepared PEDOT NPs, which present a coral-like morphology and exhibit an effective diameter of 48 ± 9 and 91 ± 1 nm as determined by SEM and DLS, respectively. The FTIR spectra of EDOT monomer and PEDOT NPs doped with DBSA are compared in Figure 6.2.1b. The monomer shows bands at 3109 and 772 cm^{-1} which correspond to the C^{α}–H stretching and out-of-plane vibration modes, respectively. The disappearance of these two absorption bands in the polymer spectrum proves the success of the polymerization process, reflecting that the hydrogen atoms at the C^{α}-position were removed during the formation of PEDOT NPs.

Some characteristic bands from PEDOT correspond to the stretching modes of C=C in the thiophene ring at 1557 cm^{-1}, the C–O–C vibrations at 1223 and 1053 cm^{-1}, the stretch of the C–S bond in the thiophene ring at 834 and 681 cm^{-1}. The absorption band at 1646 cm^{-1} is assigned to the C=C stretching vibration band of phenyl side group from DBSA. [17–20] The presence of the peak at 1719 cm^{-1} deserves consideration. It corresponds to the carbonyl group formed by the irreversible overoxidation of the thiophene ring and indicates that PEDOT NPs are overoxidized. Interestingly, overoxidized PEDOT was reported to exhibit unique sensitivity for the detection of biomolecules, such as dopamine and uric acid.[21,22]

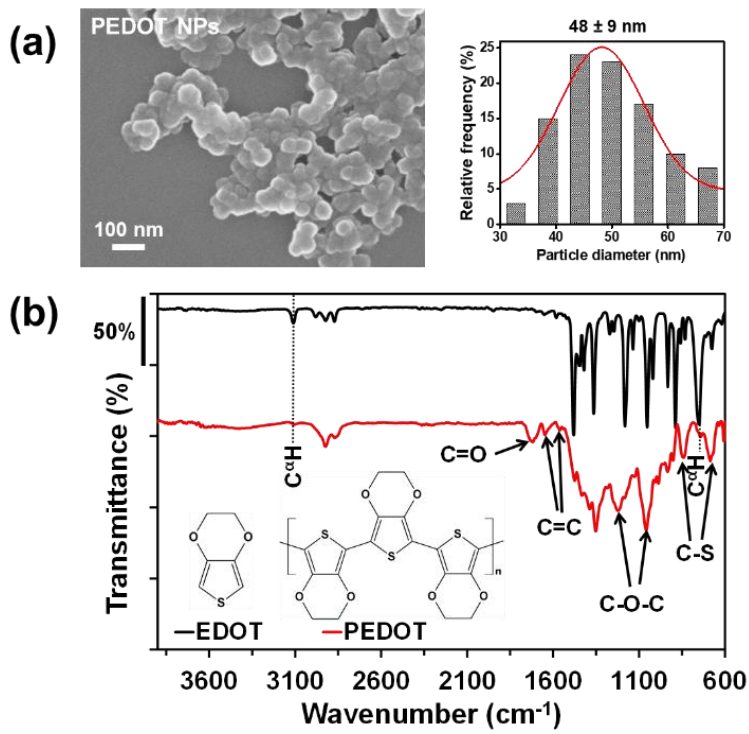

Figure 6.2.1 (a) SEM micrograph of PEDOT NPs (left) and effective diameter histogram derived from SEM measurements (right). (b) FTIR spectra of EDOT monomer and PEDOT NPs.

FTIR spectra of i-PP, i-PP(p), i-PP/PEDOT(40%) and i-PP/PEDOT(60%) films (Figure 6.2.2a), which display an average thickness of 47 ± 5, 74 ± 5, 81 ± 4 and 76 ± 4 μm, respectively, are completely dominated by the polyolefin absorption bands in 2953, 2879, 1377, 1156 and 968 cm^{-1} (stretching, deformation and rocking vibration of $–CH_3$), 2915 and 2840 cm^{-1} (stretching vibration of $–CH_2$), and 1449 cm^{-1} (bending vibration of $–CH_2$). [23,24]

The bands identified in the Raman spectrum of i-PP (Figure 6.2.2b) are: 809 (CH_2 rocking and C–C stretching), 843 (CH_2 rocking) 973 (CH_3 rocking and C–C stretching), 998 (CH_3 rocking), 1151 (C–C stretching, C–H bending), 1120 (CH_2 twisting, CH wagging and C–C stretching), and 1436 cm^{-1} (CH_2 deformation). [25–27] Moreover, the CH_3 vibrations at 973 cm^{-1} are attributed to the 3_1 helical conformation of crystalline i-PP chains, while the CH_3 rocking at 998 cm^{-1} involves segments with such helical structure. [26] The normalized integral intensity of the bands at 809 and 843 cm^{-1} was proposed to be an estimation of the crystallinity (χ_c) of i-PP. [25] The former band is related with chains in regular helical conformations, while the latter is associated with conformational defects and chains with non-helical conformations. The χ_c value derived from the 809 and 843 cm^{-1} bands is 51% and 40%, respectively, the average value (46%) being fully consistent with that derived from melting thermograms (see below).

Figure 6.2.2b also includes the Raman spectra of PEDOT NPs, i-PP/PEDOT(40%) and i-PP/PEDOT(60%). The Raman fingerprints of PEDOT were reported in previous studies: 1424 cm^{-1} (symmetric $C_\alpha=C_\beta$ stretching), 1490 cm^{-1} (asymmetric $C_\alpha=C_\beta$ stretching), 1368 cm^{-1} ($C_\alpha–C_\alpha$, inter-ring stretching), 708 cm^{-1}

(symmetric C–S–C deformation), 856 cm^{-1} (asymmetric C–S–C deformation) and 991 cm^{-1} (O–C–C–O ring deformation). [28–30] The bands of PEDOT NPs are clearly identified in the Raman spectra of i-PP/PEDOT films, which look very different from the spectrum of the neat i-PP. The complementary information provided by the FTIR and Raman spectra confirms the integration of PEDOT NPs into the polyolefin matrix of i-PP/PEDOT films.

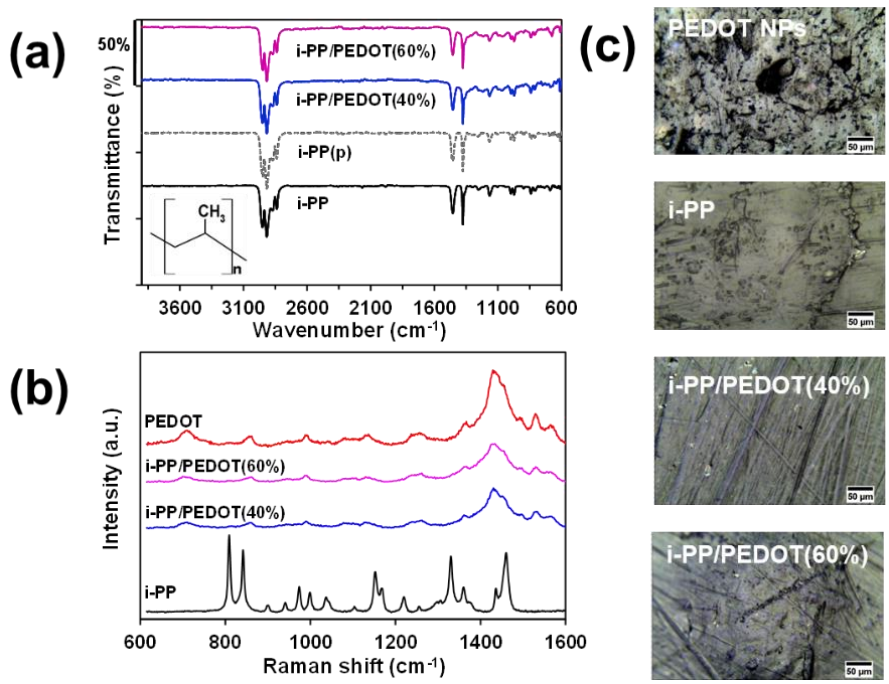

Figure 6.2.2 (a) FTIR spectra of neat i-PP, i-PP(p), i-PP/PEDOT(40%) and i-PP/PEDOT(60%) films. (b) Raman spectra and (c) optical micrographs recorded with the Raman microscope of PEDOT NPs and i-PP, i-PP/PEDOT(40%), and i-PP/PEDOT (60%) films.

Figure 6.2.3a displays SEM micrographs of the different films prepared in this work. i-PP exhibits a homogeneous and compact surface morphology, whereas a distribution of closed and non-

interconnected micropores are clearly distinguished on the surface of i-PP(p) films. Thus, the concentration of NaCl is too low to create contact between particles, precluding the formation of networks of interconnected pores crossing the entire film thickness. i-PP/PEDOT micrographs present light spots distributed on the surface, which correspond to micro-aggregates of PEDOT NPs, as was proved by the signal of sulfur in the energy dispersive X-ray (EDX) spectra (Figure 6.2.3b). As it was expected, size and number of spots, which are responsible for the change of color of i-PP film, increase with the concentration of PEDOT NPs. More specifically, the average diameter of the micro-aggregates is 4.0 ± 1.1 μm and 5.1 ± 2.4 μm for i-PP/PEDOT(40%) and i-PP/PEDOT(60%), respectively.

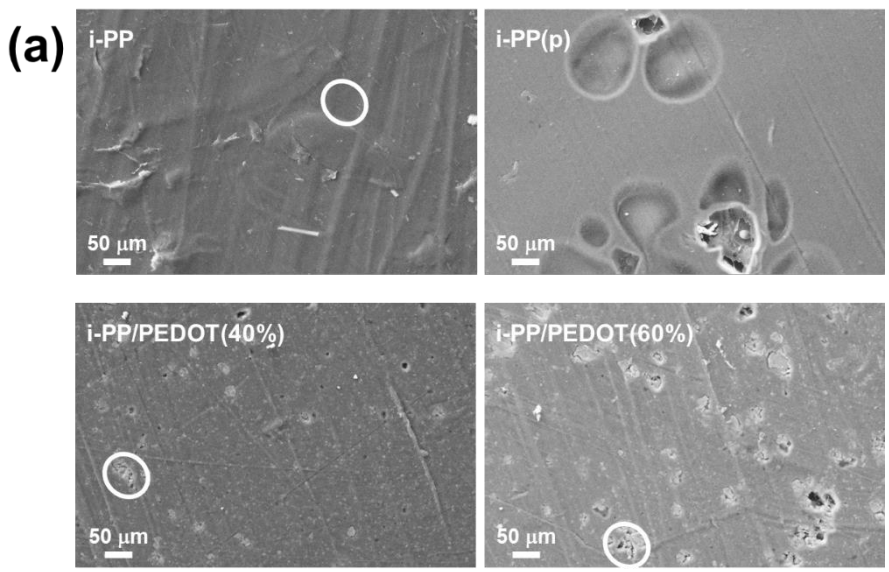

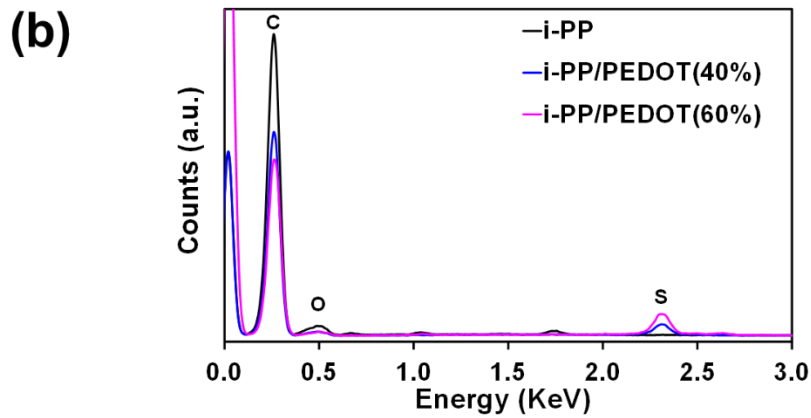

Figure 6.2.3 (a) SEM micrographs of i-PP, i-PP(p), i-PP/PEDOT(40%), and i-PP/PEDOT (60%) films. The light spots observed in i-PP/PEDOT films correspond to microaggregates of PEDOT NPs, as was evidenced by EDX spectroscopy (b) The EDX analyses of such films correspond to the regions marked by white circles in SEM micrographs.

Another change attributed to PEDOT NPs in the i-PP matrix is the film appearance, camera photographs displayed in Figure 6.2.4a show that the whitish color of neat i-PP films turns into very dark blue when the PEDOT NPs are incorporated.

On the other hand, it has been reported that wettability affects the cellular response of materials, [31] so, WCA was measured to study the NPs effect. The water contact angle (WCA) of PEDOT films was reported to be ~ 80º, [32] reflecting a poor hydrophilic behaviour. Comparison of the WCA values measured for the different films prepared in this work (Figure 6.2.4b), indicates that PEDOT NPs do not cause significant changes in the hydrophobic response of i-PP (*i.e.* WCA > 90º in all cases). The alteration of the surface topography by forming non-interconnected pores and by introducing PEDOT NPs only reduced the WCA of neat i-PP (108º ± 1º) by 9-13º.

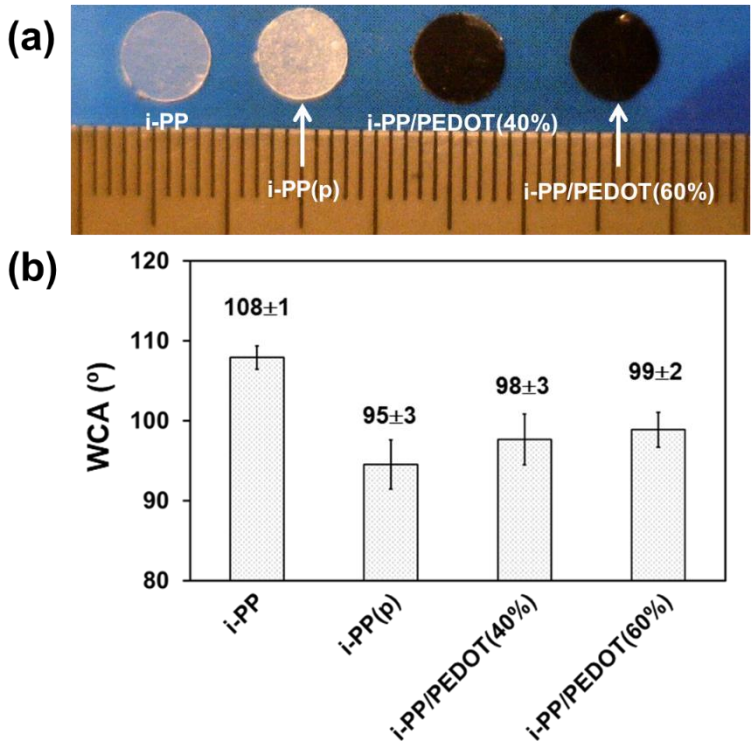

Figure 6.2.4 (a) Photographs of i-PP, i-PP(p), i-PP/PEDOT (40%), and i-PP/PEDOT (60%) films. (b) Comparison of the water contact angle (WCA) measured for i-PP, i-PP(p), i-PP/PEDOT(40%) and i-PP/PEDOT(60%) films.

The incorporation of pores and, especially, PEDOT NPs was in detriment of the mechanical properties of i-PP (Figure 6.2.5). The addition of PEDOT drastically reduced the Young modulus (~ 50%), the tensile strength (~ 70%) and the elongation at break (~ 50%) of compact i-PP films due to the aggregation of the NPs. Thus, aggregates behaved as fracture sites participating in the initiation and/or propagation of the mechanical failure. These effects are more pronounced with the increasing NPs concentration since the interfacial adhesion between the i-PP matrix and the PEDOT aggregates become weaker, facilitating the detachment of the latter from the matrix. Also,

the incorporation of PEDOT NPs drastically reduces the ductility of i-PP matrix, which undergoes a stiffening effect that drastically decreases the elongation at break.

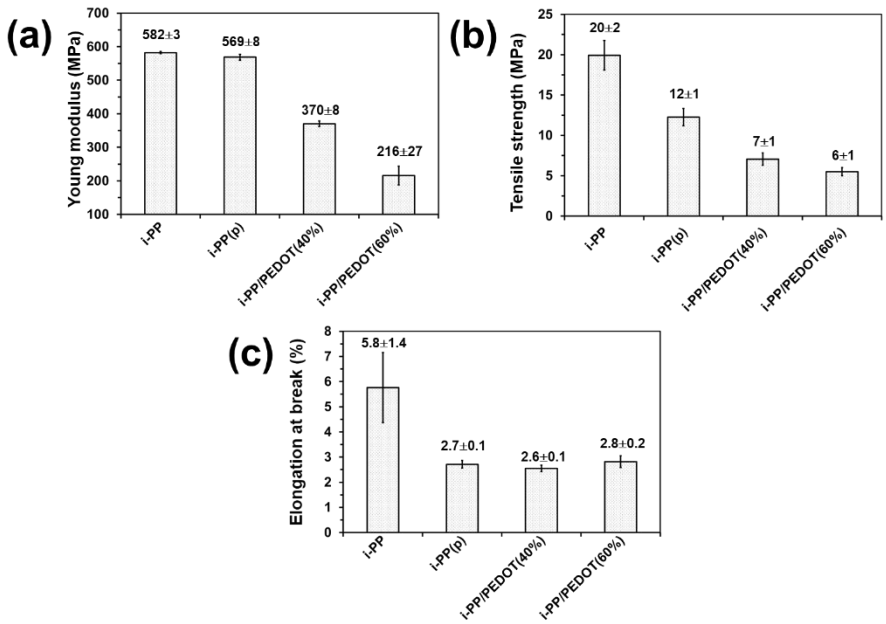

Figure 6.2.5 Comparison of the (a) Young modulus, (b) tensile strength and (c) elongation at break of i-PP, i-PP(p), i-PP/PEDOT(40%) and i-PP/PEDOT(60%) films.

Calorimetric data were obtained by differential scanning calorimetry (DSC) and thermogravimetric analyses (TGA). DSC melting and crystallization curves of neat i-PP and i-PP/PEDOT composites are shown in Figure 6.2.6a-b, while the characteristics from those runs are summarized in Table 6.2.1. Neat i-PP displays two melting peak temperatures at T_{m1} = 155 ºC and T_{m2} = 162 ºC, which correspond to the melting of β- and α-type crystals, respectively. Incorporation of PEDOT NPs results in small shifts of the T_m values

(*e.g.* T_{m1} = 158 ºC and T_{m2} = 164 ºC for i-PP/PEDOT(40%)), which have been attributed to small increments of the crystal sizes, and in an enhancement of the heat flow at the T_{m2} peak, which illustrates that PEDOT NPs favour the formation of α-type i-PP. Besides, when cooled at 10 ºC/min, the crystallization temperature of neat i-PP (T_c = 122 ºC) increases 3-4 ºC upon the incorporation of PEDOT NPs, suggesting that the latter act as nucleating agents. However, the χ_c values calculated from the melting thermograms (Eqn. 4.2 in Chapter 4) indicate that size of the crystals decreases upon the incorporation of PEDOT NPs (*i.e.* χ_c = 33-36% for i-PP/PEDOT and χ_c = 44% for neat i-PP). This could be attributed to the poor interfacial adhesion between i-PP crystals and PEDOT NPs.

Table 6.2.1 Characteristic thermal parameters for neat i-PP and i-PP/PEDOT composites: Melting temperatures (T_{m1} and T_{m2}), heat of fusion (ΔH_m), crystallization temperature (T_c), heat of crystallization (ΔH_c) and degree of crystallinity (χ_c).

Sample	T_{m1} / T_{m2} (ºC)	ΔH_m (J/g)	T_c (ºC)	ΔH_c (J/g)	χ_c (%)♣
i-PP	155 / 162	81	122	91	44
i-PP/PEDOT(40%)	158 / 164	70	125	76	36
i-PP/PEDOT(60%)	160 / 163	70	127	68	33

♣Heat of fusion for 100% of crystalline i-PP: 209 J/g

TGA curves (Figure 6.2.6c) show that the ICP NPs affect the thermal stability and the decomposition mechanism of the i-PP matrix. Although the decomposition starts at a lower temperature for the composites than for the neat polymer, the temperature of 70% of weight loss ($T_{0.7}$) is lower for i-PP ($T_{0.7}$ = 450 ºC) than for the i-PP/PEDOT ($T_{0.7}$ = 462 and 459 ºC for 40% and 60% composites, respectively). Furthermore, the derivative of the TGA curves (DTGA)

reveals that i-PP follows a one-step decomposition pattern with a maximum at T_{max} = 448 ºC, whereas the two i-PP/PEDOT composites present a more complex mechanism that depends on the concentration of CP NPs. Thus, the DGTA curve obtained for i-PP/PEDOT(40%) displays a maximum at $T_{max,1}$ = 457 ºC and a shoulder at $T_{max,2}$ = 370 ºC, while i-PP/PEDOT(60%) shows a peak centred at $T_{max,1}$ = 446 ºC and two shoulders at $T_{max,2}$ = 424 ºC and $T_{max,3}$ = 355 ºC. Such shoulders have been related to concentration-dependent degradation steps of PEDOT NPs. [33]

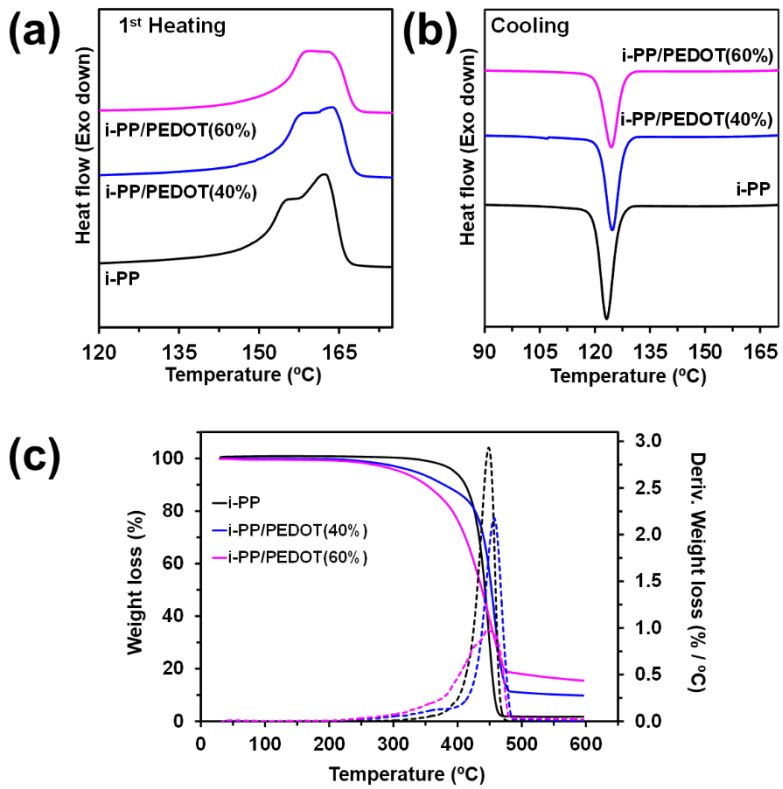

Figure 6.2.6 Selected regions of the DSC thermograms showing (a) melting and (b) crystallization for neat i-PP and both i-PP/PEDOT (40%) and i-PP/PEDOT (60%) composites. (c) TGA and DGTA curves obtained at a heating rate of 10 ºC/min for neat i-PP and both i-PP/PEDOT(40%) and i-PP/PEDOT(60%) composites.

Control voltammograms for bare and film-modified electrodes in 0.1 M PBS (pH 7.4), are displayed in Figure 6.2.7a. The lack of anodic and cathodic peaks in the voltammograms recorded for i-PP(p) indicates that oxidation and reduction processes do not occur at specific positions of polymer chains. However, the shape of the voltammogram changes with increasing number of oxidation-reduction cycles (Figure 6.2.7b), becoming similar to that of the bare electrode. Moreover, the voltammetric charge (|Q|) increases from 7 ± 3 μC (first control voltammogram) to 19 ± 2 μC after 500 redox cycles (Figure 6.2.7e), reflecting an increment of electroactivity (Figure 6.2.7f). Both, the variation in the shape and the increment of electroactivity, suggest that i-PP(p) films undergo chemical or structural degradation during the electrochemically induced redox processes (see below).

On the other hand, the control voltammograms of the two i-PP/PEDOT composites (Figure 6.2.7a, c and d) resemble those reported for neat PEDOT films, [32,34] with an anodic peak at approximately –0.1 V and a cathodic peak at a potential slightly lower than the reversal potential. As observed for i-PP(p), |Q| increases with the number of consecutive redox cycles for both i-PP/PEDOT(40%) and i-PP/PEDOT(60%) (Figure 6.2.7e). This infrequent "*self-electrostabilizing*" effect is much more pronounced for latter composite than for the former one. Thus, after 500 consecutive redox cycles |Q| increases from 17 ± 3 to 32 ± 2 μC and from 13 ± 3 to 56 ± 4 μC for i-PP/PEDOT(40%) and i-PP/PEDOT(60%) (Figure 6.2.7e), respectively, which represents an increment in the electroactivity of ~ 190% and ~ 330% (Figure 6.2.7f), respectively.

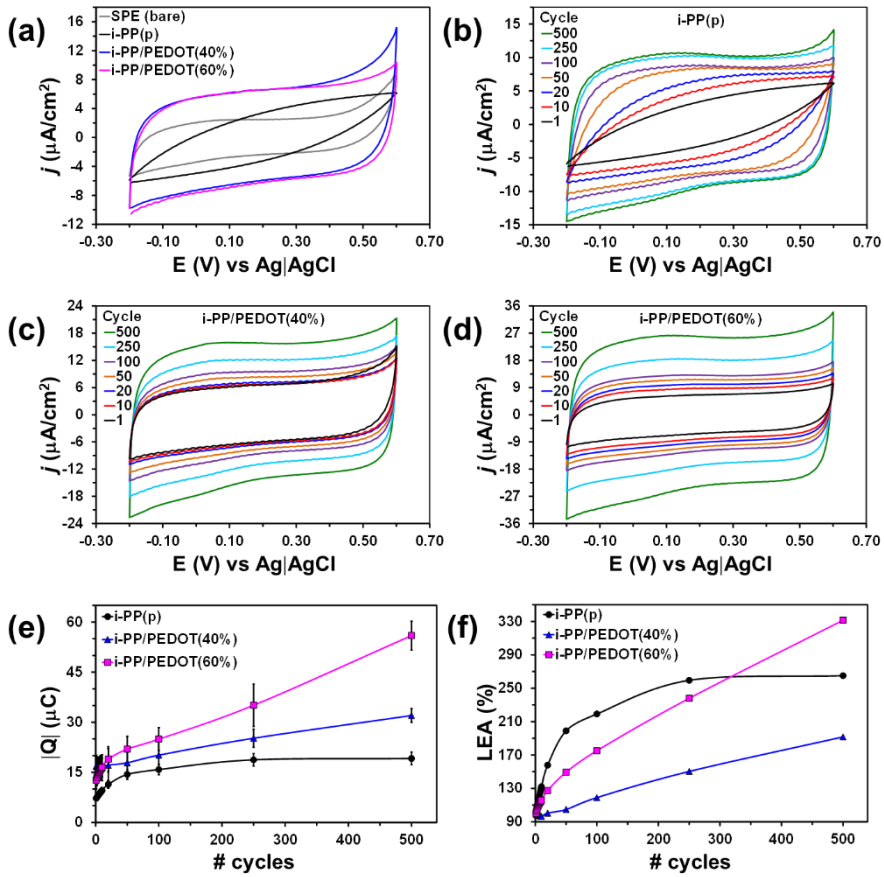

Figure 6.2.7 (a) Control voltammograms of bare and modified SPEs. The latter were obtained by assembling i-PP(p), i-PP/PEDOT(40%) or i-PP/PEDOT(60%) films onto the surface of the SPEs using gelatine as intermediate layer. Cyclic voltammograms recorded after a variable number of consecutive oxidation-reduction cycles: (b) i-PP(p), (c) i-PP/PEDOT(40%) and (d) i-PP/PEDOT(60%). Variation of (e) the measured voltammetric charge (|Q|) and (f) the loss of electrochemical activity (LEA) against the number of consecutive redox cycles for i-PP(p), i-PP/PEDOT(40%) and i-PP/PEDOT(60%).

The FTIR spectra recorded before and after 500 consecutive redox cycles are very similar for i-PP(p) and i-PP/PEDOT (Figure 6.2.8), indicating that i-PP does not undergo significant chemical changes. Therefore, the "*self-electrostabilizing"* effect observed in Figure 6.2.7 cannot be attributed to the chemical degradation of the i-PP matrix. In

contrast, SEM images of i-PP(p) and i-PP/PEDOT after 500 redox cycles, which are displayed in Figure 6.2.8, indicate important structural changes in the films. After 500 cycles, microfractures appeared on the surface of i-PP(p) films (Figure 6.2.9a) due to the stress induced by the potential scans. In the case of i-PP/PEDOT(40%) and i-PP/PEDOT(60%) (Figure 6.2.9b-c), the structural stress is adsorbed by some PEDOT aggregates that end up detaching. The shape and size of the resulting pores are defined by the characteristics of detached PEDOT particles, which are very varied. The increment of the surface porosity facilitates the access and escape of ions during the oxidation and reduction processes, respectively, explaining the unusually observed "*self-electrostabilizing"* behaviour.

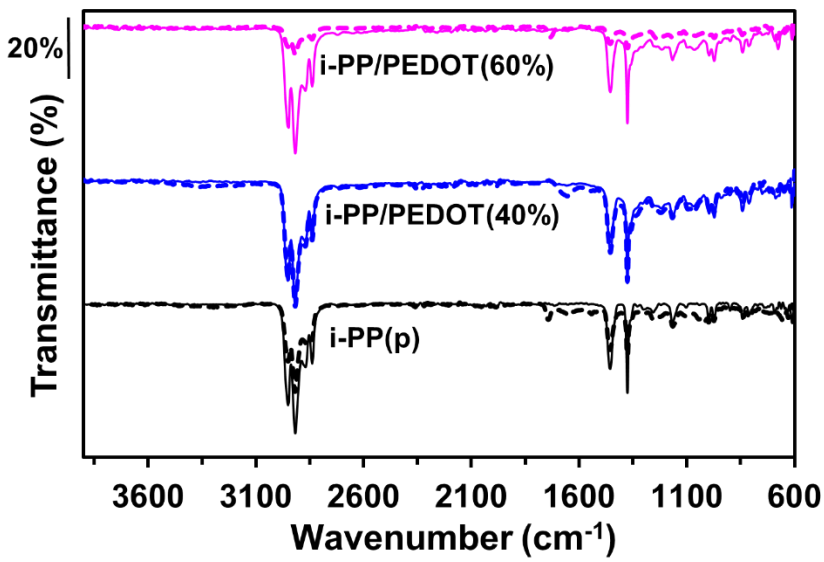

Figure 6.2.8 FTIR spectra of i-PP(p), i-PP/PEDOT(40%) and i-PP/PEDOT(60%) films before (thin solid lines) and after 500 consecutive redox cycles (thick dashed lines).

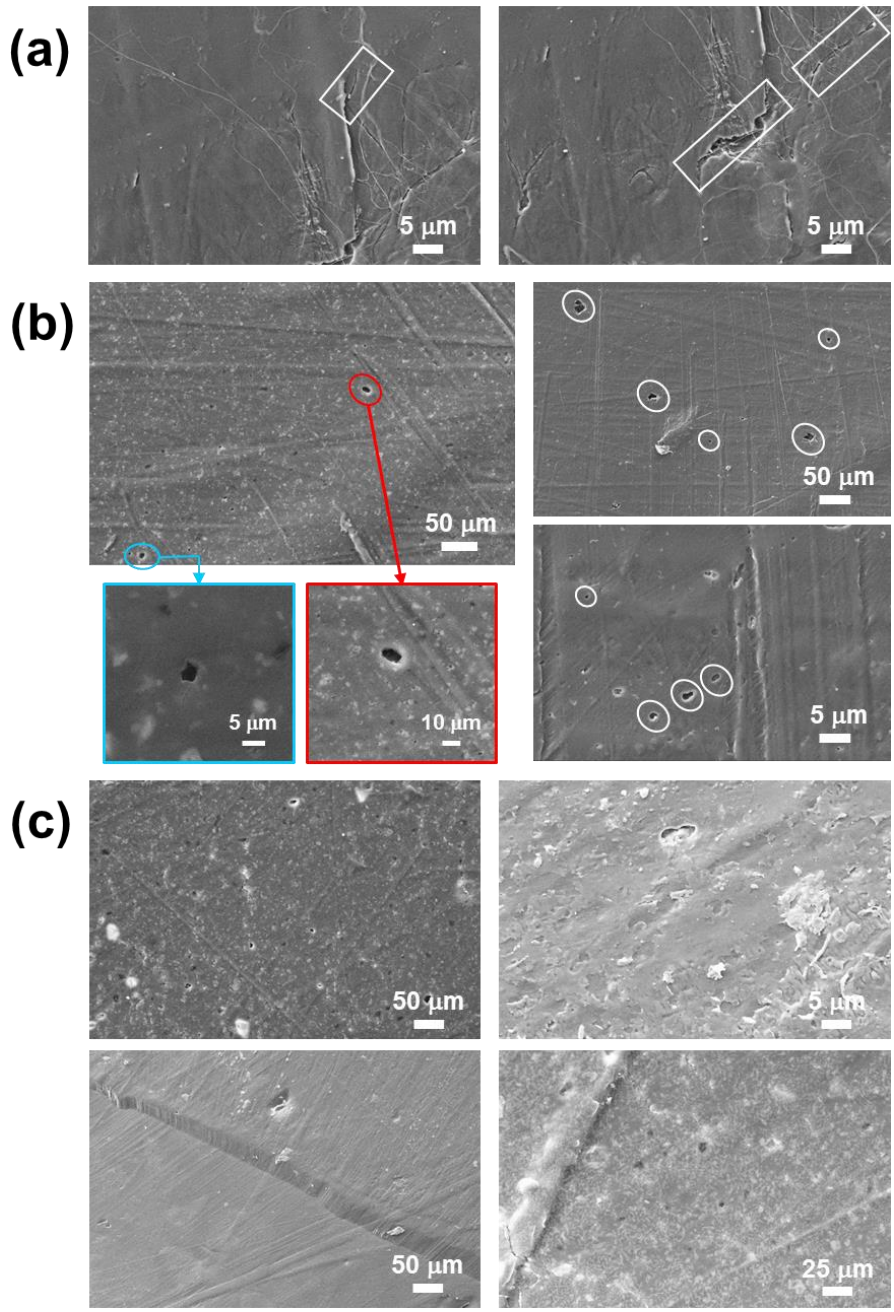

Figure 6.2.9 SEM micrographs of (a) i-PP(p), (b) i-PP/PEDOT(40%) and (c) i-PP/PEDOT(60%) after 500 consecutive redox cycles. Microfractures in i-PP(p) films (marked with rectangles) and pores in i-PP/PEDOT(40%) (marked with circles) are induced by the stress associated to consecutive potential scans. The shape and size of the pores in i-PP/PEDOT(60%) are similar to those of the pores marked in (b).

Antibacterial activity, adhesion and proliferation of eukaryotic cells. The growth of prokaryotic cells, the adhesion (24 hours) and long-term proliferation (7 days) of eukaryotic cells onto i-PP, i-PP(p) and i-PP/PEDOT were evaluated considering different bacteria and eukaryotic cell lines. Regarding to prokaryotic cells, *E. coli* and *S. aureus*, which are Gram-negative and Gram-positive bacteria, respectively, were incubated onto such films. The antimicrobial activity (*i.e.* bacterial growth) was quantified measuring the turbidity of the incubated bacteria cultures after 24 hours by UV-vis spectroscopy at λ= 450 nm. The relative viabilities after 24 hours (Figure 6.2.10a) are very similar to that of the control, indicating that bacteria do not exhibit a specific attraction towards i-PP, i-PP(p) and i-PP/PEDOT.

The ability of i-PP, i-PP(p), i-PP/PEDOT(40%) and i-PP/PEDOT(60%) films to enhance the adhesion and proliferation of eukaryotic cells are compared also in Figure 6.2.10. As it can be seen in Figure 6.2.10b, the cellular adhesion onto the composite films is conditioned by the i-PP matrix, which presents the lowest relative viability for Vero and, especially, Cos-1 cells. Specifically, after 24 h, Cos-1 viability is ~ 40% lower for i-PP and i-PP(p) than for the control, while the incorporation of ICP results in an increment of the viability that depends on the NPs concentration. The number of cells on the surface of all films increases after 7 days (Figure 6.2.10c). Results confirm that cell adhesion onto the composite films is easier than onto the i-PP ones, this tendency increasing with the concentration of PEDOT NPs. Although the viabilities obtained for the Vero cell line are higher for all prepared films than for the control, Cos-1 cells clearly

prefer the composite films than the i-PP and i-PP(p) films. This behaviour has been attributed to the ion exchange ability of the electroactive ICP, which favours the exchange of electrolytes with cell at the interface defined by the surface of the film and the cell membrane.

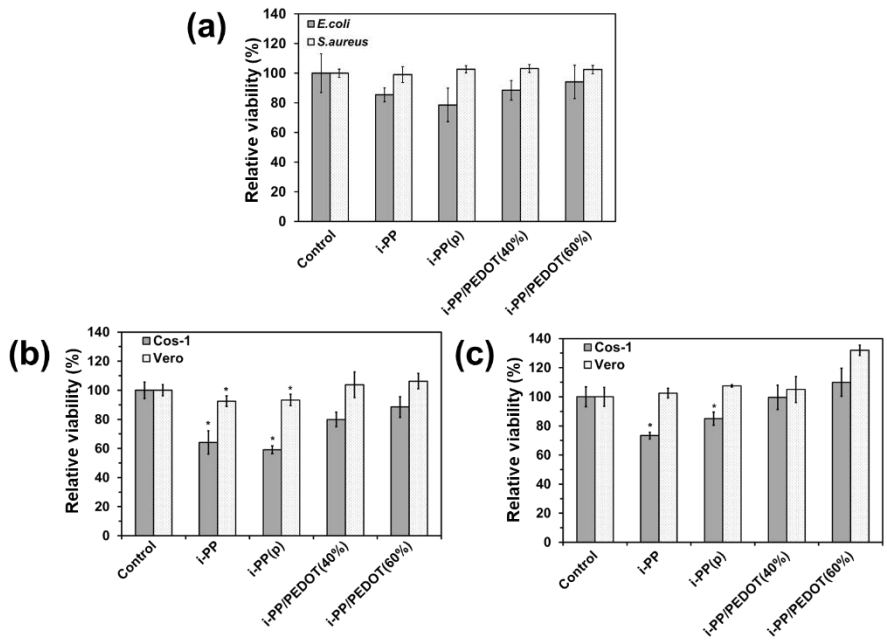

Figure 6.2.10 (a) Antibacterial activity of i-PP, i-PP(p), i-PP/PEDOT(40%), i-PP/PEDOT(60%) films with two representative bacteria (*E. coli* and *S. aureus*). Cellular adhesion (b) and cellular proliferation (c) on i-PP, i-PP(p), i-PP/PEDOT(40%), i-PP/PEDOT(60%) films. Assays were performed using two representative eukaryotic cells (Cos-1 and Vero). In all the experiments three samples were analysed for each group, bars represent the mean standard deviation and the relative viability was established in relation to the control (100%). The asterisk (*) indicates a significant difference with the control, Tukey's test ($p < 0.03$).

Detection of bacterial cells while fingerprints of eukaryotic cells remain undetected. The performance of the i-PP/PEDOT composite for the *in situ* electrochemical detection of biofilm contamination is examined through the oxidation of NADH to NAD+. With the aim of orienting this sensor towards clinical applications, the fingerprints of eukaryotic and prokaryotic cells colonizing a medical device should be differentiated. Therefore, we focused on monitoring the metabolism of prokaryotic and eukaryotic cells using carbon SPEs coated with i-PP/PEDOT(40%) since the load of PEDOT NPs is smaller and display properties similar to i-PP/PEDOT(60%). The growth of bacteria and eukaryotic cells was following by examining the electrochemical response of the medium at different times, which ranged from 0 (just when the cells are introduced in the culture medium) to 24 hours.

Figure 6.2.11a displays the response of the sensor to the culture medium without cells at different incubation times. As it can be seen, cyclic voltammograms are similar to those displayed in Figure 6.2.7, independently of the incubation time, indicating that the response coming from the oxidation of species contained in the $NaHCO_3$ supplemented DMEM is practically null. Accordingly, the anodic current at the reversal potential ($j_{0.6}$), 0.60 V, only decreases from 13 to 11 $\mu A/cm^2$ after 24 hours. In opposition, i-PP/PEDOT(40%) is remarkably affected by the presence of cultured bacteria, even though the response of the sensor against *E. coli* and *S. aureus* are different and change with the incubation time (Figure 6.2.11b-c). Thus, an oxidation peak at 0.60 V is clearly observed in both cases. This has been attributed to the oxidation of NADH to NAD+. Previous studies on PEDOT-based electrodes reported that the oxidation peak of

NADH in a solution without the presence of bacteria can be found between 0.5 V (*i.e.* processable PEDOT colloidal microparticles) [35] and 0.70 V (*i.e.* electrochemically synthesized graphene-PEDOT:PSS). [36] Thus, the detection of the of NADH to NAD+ is indicative of bacterial activity. [37,38] Moreover, the current density at 0.60 V varies with the incubation time (Figure 6.2.11d), reflecting that i-PP/PEDOT(40%) detects that the bacteria growth is very fast at the first stages of incubation. For *E. coli*, $j_{0.6}$ increases from 8 to 171 μA/cm^2 after 2 hours, decreasing to 161 μA/cm^2 after 24 hours. For *S. aureus*, the $j_{0.6}$ value is 298 μA/cm^2 after 24 hours of culture, which is consistent with the cell viability measurements displayed in Figure 6.2.10a (*i.e.* adhesion was higher for the Gram-positive bacterium than for the Gram-negative one). However, analysis of the temporal evolution of $j_{0.6}$ displayed in Figure 6.2.11d allows monitoring that in the first stages the growing of *E. coli* is faster than of *S. aureus*, besides, can be observed that $j_{0.6}$ reaches a plateau before biofilm formation, which is expected to occur after ~ 24 h. This feature is especially striking for *E. coli* since the plateau is reached very fast. In a first assumption this observation could be attributed to the saturation of PEDOT NPs in the electrode and/or to limitations in the linear dynamic range. More specifically, the adsorption of oxidized analytes onto the electroactive materials used as electrodes and their subsequent saturation is a well-known limitation of some electrochemical biosensors. Besides, the huge number of bacteria involved in biofilms requires that a very high interval of CFU/mL over which the sensor response is linear. The plateaus reached in Figure 6.2.11d could be interpreted as the loss of the linear regime, which eventually could

limit the quantitative utilization of the sensor. However, comparison of the profiles displayed in Figure 6.2.11d with Figure 6.2.11e, which shows to the growth of *E. coli* and *S. aureus* in the culture medium against the incubation time as determined UV-vis spectroscopy, suggest that the limitations discussed above are less decisive than expected. Thus, the variation of the absorbance at 450 nm with the incubation time agrees with the profiles electrochemically obtained for the two bacteria (Figure 6.2.11d), evidencing the capacity of the sensor for detecting the presence of growing bacteria. The calibration curve (Figure 6.2.11f), which was approximated using the McFarland standard, indicates that the amount of *E. coli* and *S. aureus* bacteria grow from 1.6 x 10^8 CFU/mL (first measure for both types) to 1.7 x 10^8 and 2.4 x10^8 CFU/mL, respectively, after 24 h. These results are fully consistent with the electrochemical sensing displayed in Figure 6.2.11b-c.

The selectivity with respect eukaryotic cells is crucial for the performance and practical application of the sensor in medical devices. Figure 6.2.12 proves that the electrochemical response of i-PP/PEDOT(40%) against the growth of eukaryotic cells is completely different to that displayed for bacteria. Cyclic voltammograms recorded just after the addition of Cos-1 and Vero cells are practically identical to those obtained after 24 hours of cell culture (not shown) and very similar to those achieved after 7 days of cell proliferation (Figure 6.2.12). Moreover, after such long time, $j_{0.6}$ only increases from 7 to 10 μA/cm^2 and from 9 to 11 μA/cm^2 for Cos-1 and Vero cells, respectively, evidencing that the concentration

of NADH induced by such eukaryotic cells is not high enough to be detected by the i-PP/PEDOT sensor.

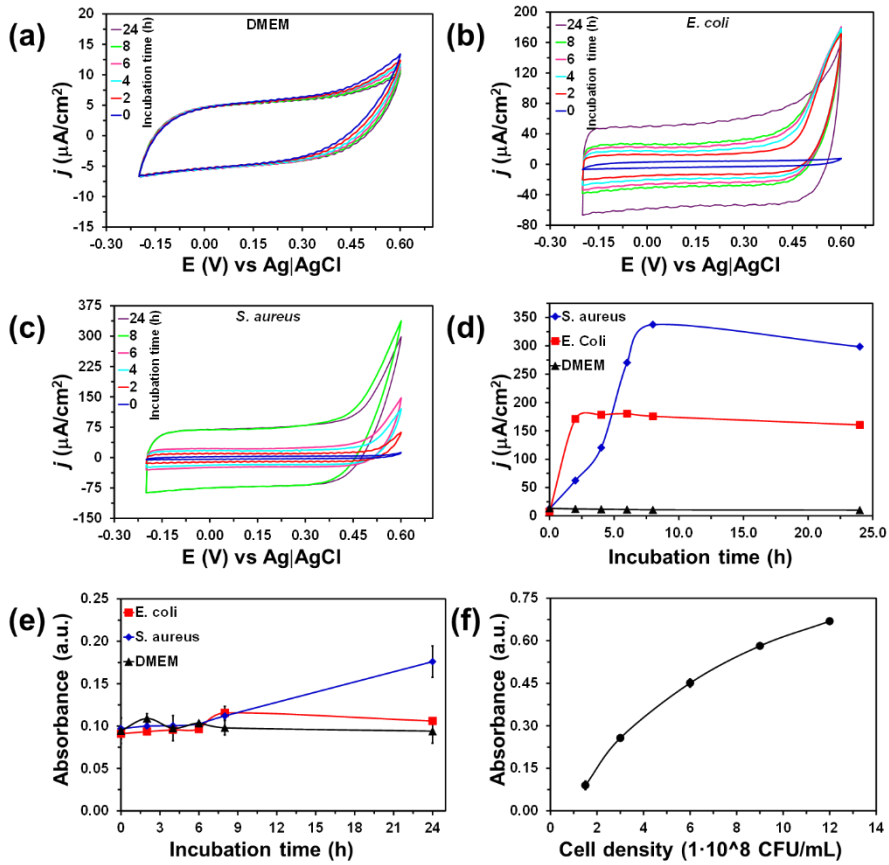

Figure 6.2.11 Cyclic voltammograms for i-PP/PEDOT(40%) in the culture medium ($NaHCO_3$ supplemented DMEM) recorded at different incubation times: (a) in absence of bacteria; (b) in presence of *E. coli*; and (c) in presence of *S. aureus*. Initial and final potentials: -0.20 V; reversal potential: 0.60 V; and scan rate: 100 mV/s. (d) Variation of the current density at 0.60 V ($j_{0.6}$) with the incubation time for (a), (b) and (c). (e) Variation of the absorbance at 450 nm with the incubation time as determined in the culture medium ($NaHCO_3$ supplemented DMEM) in absence of bacteria and in presence of *E. coli* and *S. aureus*. (f) Calibration curve obtained using the McFarland standard to approximate the number of bacteria as a function of the absorbance.

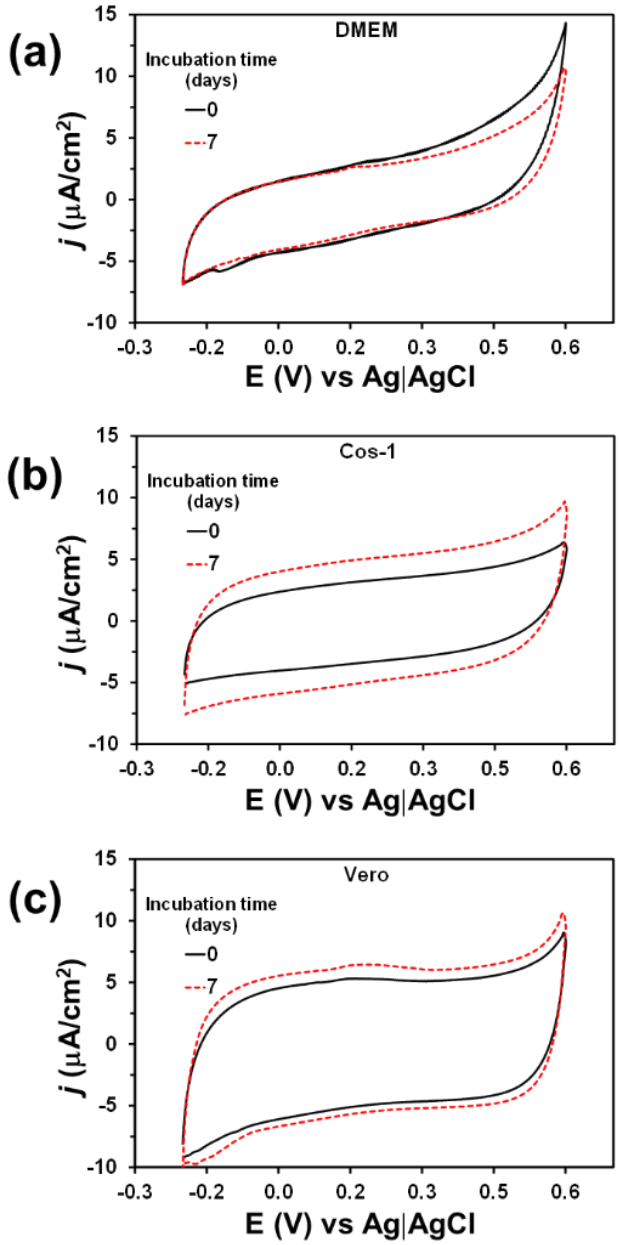

Figure 6.2.12 Cyclic voltammograms for i-PP/PEDOT(40%) in the culture medium recorded just after the addition of the cells and after seven days of incubation: (a) in absence of cells; (b) in presence of Cos-1 cells; and (c) in presence of Vero cells.

Results displayed in Figure 6.2.11 and 6.2.12 clearly indicate that the i-PP/PEDOT(40%) sensor distinguishes bacteria while eukaryotic cells remain undetected. This behaviour originates from the sensitivity of the i-PP/PEDOT composite towards the oxidation of NADH, which is high enough to detect the metabolism of bacteria but too low for the respiration of eukaryotic cells. In addition, the oxidation of NADH towards NAD+ probably causes an electrochemically-induced concentration gradient, favouring the exit of cytosolic NADH to the medium through the outer bacterial membrane and, consequently, facilitating the detection of the bacterial metabolism.

Conclusions

In this study, simple and highly sensitive (bio)sensors have successfully developed for the detection of bacteria growth through the oxidation of NADH. In a first stage the sensors, which are based on PEDOT NPs supported into an i-PP matrix, have been characterized by FTIR and Raman spectroscopies, SEM, contact angle measurements, mechanical tests, differential scanning calorimetry and thermogravimetry analyses. Although the mechanical and thermal properties of i-PP/PEDOT composites are affected by the interfacial adhesion between their components, the combination of i-PP and PEDOT NPs is very attractive in terms of electrochemical properties. Thus, the electrochemical processes observed for i-PP/PEDOT are similar to those described for neat PEDOT films and, in addition, the composite exhibits "*self-electrostabilizing"* behaviour. This unusual characteristic, which consists in the increase of electrochemical activity as the number of consecutive redox cycles grow, is due to an increment in the surface porosity of the films.

The i-PP/PEDOT sensor detects the growth of Gram-negative and Gram-positive bacteria through the oxidation of the NADH, which comes from bacterial metabolism and permeates through the outer membrane to the extracellular culture medium. In contrast, the NADH produced by the respiration of eukaryotic cells remains in the mitochondria pool and, therefore, the presence of those cells does not interfere with the readings of the bacterial sensor. The prepared sensor, which can be produced at low cost, is deemed to be of high clinical interest as it might be the first line of defence against biofilm formation benefit in a number of scenarios where bacteria colonize the implanted medical devices competing with healthy eukaryotic cells.

6.3 Plasma functionalized isotactic polypropylene assembled with conducting polymers for bacterial quantification by NADH sensing

Abstract

Rapid detection of prosthetic infection is essential to prevent biofilm formation, which consists of densely packed communities of bacteria able to withstand antibiotic-mediated killing. In this work we present a smart approach to integrate an electrochemical (bio)sensor for bacterial infections in isotactic polypropylene (i-PP) films, used for the fabrication of biomedical implants. The electrochemical detection is based on the capacity of intrinsically conducting polymers (ICPs) to detect extracellular nicotinamide adenine dinucleotide (NADH) from the respiration reactions of bacteria, which allows distinguishing prokaryotic microbes from eukaryotic cells. An oxygen plasma functionalized free-standing i-PP film coated with a first layer (~1.1 μm in thickness) of ICP nanoparticles, obtained by oxidative polymerization, has been used as working electrode for the anodic polymerization of a second and thicker ICP layer (~8.2 μm in thickness). This chemical assembly strategy provides very high electrochemical activity and stability to the iPP insulating material. The resulting layered compound, i-PP_f/PEDOT, detects the electro-oxidation of NADH in physiological media with a sensitivity of 417 $\mu A/cm^2$ and a detection limit of 0.14 mM, which is above the concentration of extracellular NADH found for bacterial cultures of biofilm-positive and biofilm-negative strains (*i.e.* 0.3-0.4 mM after 24-48 h).

Materials and methods

Materials. Isotactic polypropylene (i-PP) films, which were used as a base substrate, were kindly supplied by B Braun Surgical S.A. (Rubí, Barcelona, Spain). Hydroxymethyl-3,4-ethylenedioxythiophene (HMeDOT; 95%), 3,4-ethylenedioxythiophene (EDOT; 97%), lithium perchlorate ($LiClO_4$), β-Nicotinamide adenine dinucleotide reduced disodium salt hydrate (NADH; 97%), acetonitrile (99.8%) and phosphate buffered saline (PBS) solution were purchased from Sigma-Aldrich (USA). $LiClO_4$ was stored in an oven at 80 °C before its use in the anodic polymerization. Ammonium persulfate (APS; 98%), hydrochloric acid (37%) and sodium hydroxide were used as received from Panreac Quimica S.A.U. (Spain).

Plasma treatment of i-PP. For its surface functionalization, i-PP films were previously washed in 30% ethanol aqueous solution. The functionalization was carried out by employing the cold-plasma equipment and conditions reported elsewhere, [39] with low pressure radio-frequency (RF) plasma (80 MHz), using an LFG generator 1000 W (Diener Electronic GmbH Co., Germany), and a chamber of 25 dm^3. i-PP films of 6×5 cm^2 size were placed inside the chamber, the system was purged up to 0.07 mbar of vacuum pressure and, subsequently, filled with oxygen plasma pressure of 0.30 mbar using a gas flow fixed during 180 seconds. The power discharge was of 250 W. After the plasma treatment, all functionalized i-PP films (hereafter named i-PP_f) were stored under vacuum.

Electroactivation of i-PP_f surfaces via oxidative polymerization. A layer of poly(hydroxymethyl-3,4-ethylenedioxythiophene) (PHMeEDOT) nanoparticles was adhered to i-PP_f films by chemical

oxidative polymerization. More specifically, i-PP_f films were cut in 0.5 × 1.5 cm^2 samples and immersed in 5 mL of a 0.2 M HCl solution with 50 mM HMeEDOT (monomer) during 30 min at room temperature and under stirring (250 rpm). After this time, 1 mL of a 0.2 M HCl solution with 60 mM APS was slowly dropped to the solution containing the functionalized film. The reaction was maintained for 24 h at 37 ºC under agitation (80 rpm). After such time, the film was removed, washed three times with milli-Q water, one with acetone and dry at room temperature. Hereafter, the i-PP_f samples with superficial PHMeEDOT NPs layer are denoted i-PP_f/NPs.

Anodic polymerization on i-PP_f/NPs flat films. A second layer of intrinsically conducting polymer (ICP) was provided by *in situ* polymerization of EDOT onto the surface of i-PP_f/NPs samples, which were previously washed with 0.2 M NaOH to balance the charge of over oxidized PHMeEDOT NPs. EDOT was polymerized by chronoamperometry (CA) under a constant potential of +1.40 V and adjusting the polymerization charge to 1.0 C. Anodic polymerizations were performed using a VersaStat II potenciostat-galvanostat connected to a computer controlled through a Power Suite Princenton Applied Research program. Experiments were conducted in a three-electrode cell at 25°C, which was filled with 20 mL of a 10 mM EDOT solution in acetonitrile containing 0.1 M $LiClO_4$ as supporting electrolyte. The i-PP_f/NPs films (0.5 × 1.5 cm^2) were employed as working electrode, while a platinum wire was used as counter electrode. The reference electrode was an Ag|AgCl electrode containing a KCl saturated aqueous solution (E^o = 0.222 V at 25 °C). Films made of i-PP_f coated with a thin layer of PHMeEDOT and an external thicker layer of PEDOT are identified as i-PP_f/PEDOT.

Characterization of the macromonomer and the prepared (bio)sensor. Chapter 4 presented a detailed description of the characterization methods employed to evaluate the electrochemical (bio)sensors. The characterization technique used in this work include UV-vis, FTIR and micro-Raman spectroscopy, scanning electron microscopy (SEM), atomic force microscopy (AFM), contact angle, profilometry, electrochemical characterization carried out by cyclic voltammetry (CV). The procedures for the electrochemical detection of NADH and its identification from bacteria respiration reactions are also explained in Chapter 4.

Results and discussion

Construction of the Sensor: Chemical Assembly of ICPs on functionalized i-PP. A sketch of the three steps used to prepare the sensor integrated in an i-PP film typically used for the fabrication of biomedical implants, which was kindly supplied by Braun Surgical S.A. (Rubí, Barcelona, Spain), is shown in Figure 6.3.1a. The surface of the i-PP films was functionalized with low pressure radio-frequency (RF) oxygen plasma using the conditions described in the methods section. After plasma treatment, which took 180 s, functionalized films were stored under vacuum.

The aspect of the resulting electroactive i-PP_f/PEDOT film with respect to the other previous substrates, is compared in Figure 6.3.1b. As is shown, the translucent aspect of pristine i-PP changes to whitish (i-PP_f), blueish (i-PP_f/NPs) and dark blue (i-PP_f/PEDOT), suggesting the success of the steps associated to the plasma functionalization, the integration of the PHMeEDOT layer by oxidative polymerization, and

the incorporation of the external PEDOT layer by anodic polymerization, respectively.

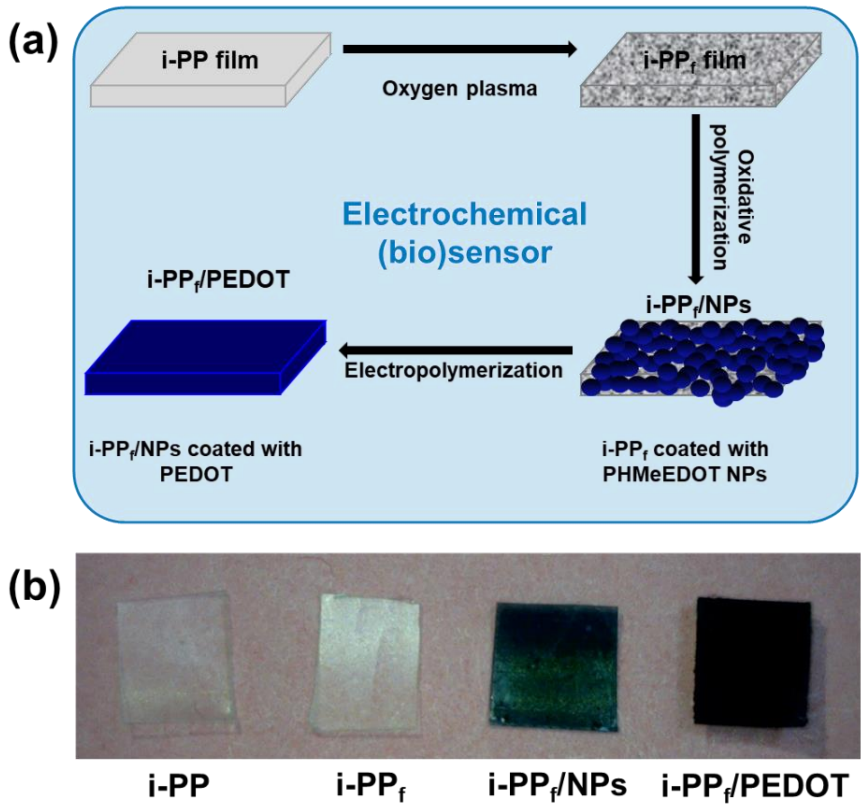

Figure 6.3.1 (a) Sketch representing the three steps used to transform i-PP into i-PP$_f$/PEDOT, an electroactive i-PP with sensing properties. (b) Photographs of pristine i-PP, i-PP$_f$, i-PP$_f$/NPs and i-PP$_f$/PEDOT films.

Chemical characterization. The effects of the plasma functionalization and the successful incorporation of PHMeEDOT (1st) and PEDOT (2nd) layers on i-PP$_f$ were investigated by UV-vis, FTIR and Raman spectroscopies. The UV-vis spectra recorded for i-PP, i-PP$_f$, i-PP$_f$/NPs and i-PP$_f$/PEDOT are compared in Figure 6.3.2a. As was expected, no absorption band was detected by UV-vis spectroscopy for i-PP and i-PP$_f$. Opposite than i-PP$_f$/NPs, its

absorption in the range of 300-400 nm decreased due to the π-π electronic transition of aromatic rings, which is typically observed at ~250 nm, while in the range of 400-750 nm increased, as corresponds to the polaron absorption of the doped PHMeEDOT layer. [40] This effect becomes more pronounced for i-PP_f/PEDOT, suggesting that the doping level by the electrochemically polymerized PEDOT layer is higher than that of the internal PHMeEDOT layer.

The FTIR spectrum of i-PP (Figure 6.3.2b) shows the characteristic absorption peaks with the broad and intense bands associated to the C–H stretch vibrations (*ca.* 2920 cm^{-1}), the moderate absorption peaks associated to deformation vibration of the CH_2 group (1455 cm^{-1}), the methyl group vibrations (1376 cm^{-1}), and the characteristic vibration of unsaturated CH_2 groups (841, 999 and 1167 cm^{-1}). The FTIR spectrum of i-PP_f (Figure 6.3.2b) shows new signals appearing at 1534 and 1686 cm^{-1}, which are attributed to C=O stretching, and a band at 1088 cm^{-1} associated to C–O stretching. Detailed discussion of i-PP_f spectrum was reported in recent work. [39] PHMeEDOT and PEDOT are revealed in the spectra of i-PP_f/NPs and i-PP_f/PEDOT (Figure 6.3.2b) by the characteristic bands of the C–S and C–S–C vibrations in the thiophene ring (869, 757 and 614 cm^{-1}). However, many fingerprints of the ICPs are hidden by the predominant bands of i-PP, which is the main component of the composite. To overcome this issue and better visualize the presence of PHMeEDOT and PEDOT, the Raman spectra of i-PP, i-PP_f, i-PP_f/NPs and i-PP_f/PEDOT were recorded (Figure 6.3.2c-d).

Raman spectra of i-PP and i-PP_f, which are compared in Figure 6.3.2c, show that the peaks associated to crystalline i-PP (809 and

973 cm^{-1}) becomes enhanced after plasma treatment. [39] In addition, plasma treatment induces a change in the shape and intensity of the band at 2962 cm^{-1}, which corresponds to the C–H stretching vibrations from methyl groups, [41] as well as a reduction of the CH_3 rocking band at 841 cm^{-1}. These features suggest that the CH_3 groups are modified by the plasma, becoming the favourite site for the formation of oxidized groups, which is in agreement with previous work. [39]

Figure 6.3.2d, which compares the Raman spectra of i-PP_f/NPs and i-PP_f/PEDOT, shows the predominance of ICPs bands with respect to the i-PP and i-PP_f ones. This has been attributed to the resonance Raman effect that increases the intensity of the bands of the material when the laser energy coincides with the frequency of the electronic transition of the sample. [42] However, the i-PP_f band at 2962 cm^{-1} is still detectable after the incorporation of the PHMeEDOT layer, while it completely disappears after the anodic polymerization of PEDOT. This feature suggests that the thickness of second ICP layer in i-PP_f/PEDOT is much higher than the PHMeEDOT in i-PP_f/NPs, as confirmed by profilometry measurements (see below). Furthermore, the spectra reported in Figure 6.3.2d exhibit the main characteristics peaks of PHMeEDOT and PEDOT: C=C symmetrical stretching (1430 and 1420 cm^{-1}, respectively) and C=C asymmetrical stretching (1500 cm^{-1}).

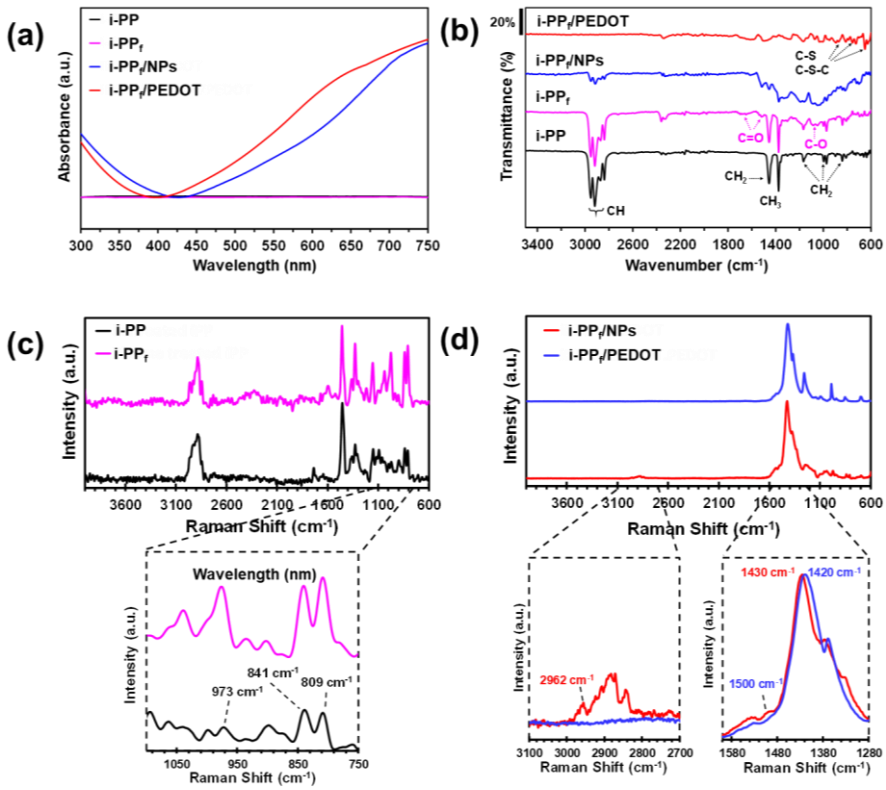

Figure 6.3.2 (a) UV-vis, (b) FTIR and (c, d) micro-Raman spectra i-PP, i-PP_f, i-PP_f/NPs and i-PP_f/PEDOT.

Surface characterization. Representative scanning electron microscopy (SEM) micrographs and 3D atomic force microscopy (AFM) images of i-PP, i-PP_f, i-PP_f/NPs and i-PP_f/PEDOT are shown in Figure 6.3.3. The i-PP surface film shows a flat and smooth morphology (Figure 6.3.3a), which is modified after exposure to the oxygen plasma. Thus, i-PP_f exhibits a nano-patterning that extends through the whole surface (Figure 6.3.3b). This morphological change affects significantly the topography increasing the surface roughness (R_q), as is evidenced by comparing the 3D height AFM images of i-PP and i-PP_f (R_q = 27 ± 5 and 41 ± 7 nm, respectively).

The morphology of PHMeEDOT in i-PP_f/NPs is shown in Figure 6.3.3c. SEM micrographs evidence that the oxidative polymerization of HMeEDOT resulted in the formation of abundant and irregular PHMeEDOT NPs between 100 and 200 nm in size. These NPs are randomly distributed in a layer with a thickness of ~ 1 μm, leaving empty spaces between them. The lack of a continuous contact among them affects the formation of conduction paths, explaining the poor electrochemical activity of i-PP_f/NPs (see below). Besides, the oxidative polymerization step affects the surface topography of i-PP_f, which becomes much more abrupt (R_q = 334 ± 19 nm).

Finally, PHMeEDOT NPs were used as polymerization nuclei of PEDOT chains, which was electrochemically generated at a constant potential of +1.40 V. The morphology and topography of i-PP_f/PEDOT (Figure 6.3.3d) are very similar to those reported for PEDOT films. [43,44] Thus, anodically polymerized PEDOT organizes in the clusters of aggregated molecules that are located at different levels. The roughness, R_q= 603 ± 36 nm, is almost twice than i-PP_f/NPs, indicating that PEDOT chains grow not only filling the empty spaces between neighbouring PHMeEDOT NPs (Figure 6.3.3c) but also on the top of the layer. Indeed, PEDOT completely covers the PHMeEDOT NPs, integrating them into a single conducting layer with continuous and well-defined conduction paths. The heterogeneous and porous topography of i-PP_f/PEDOT, which is clearly reflected in the 3D height AFM image (Figure 6.3.3d), practically matches the organization found for PEDOT films. [44,45] Consistently, the thickness of the conducting layer increases from ~ 1 μm for i-PP_f/NPs to ~ 8 μm for i-PP_f/PEDOT.

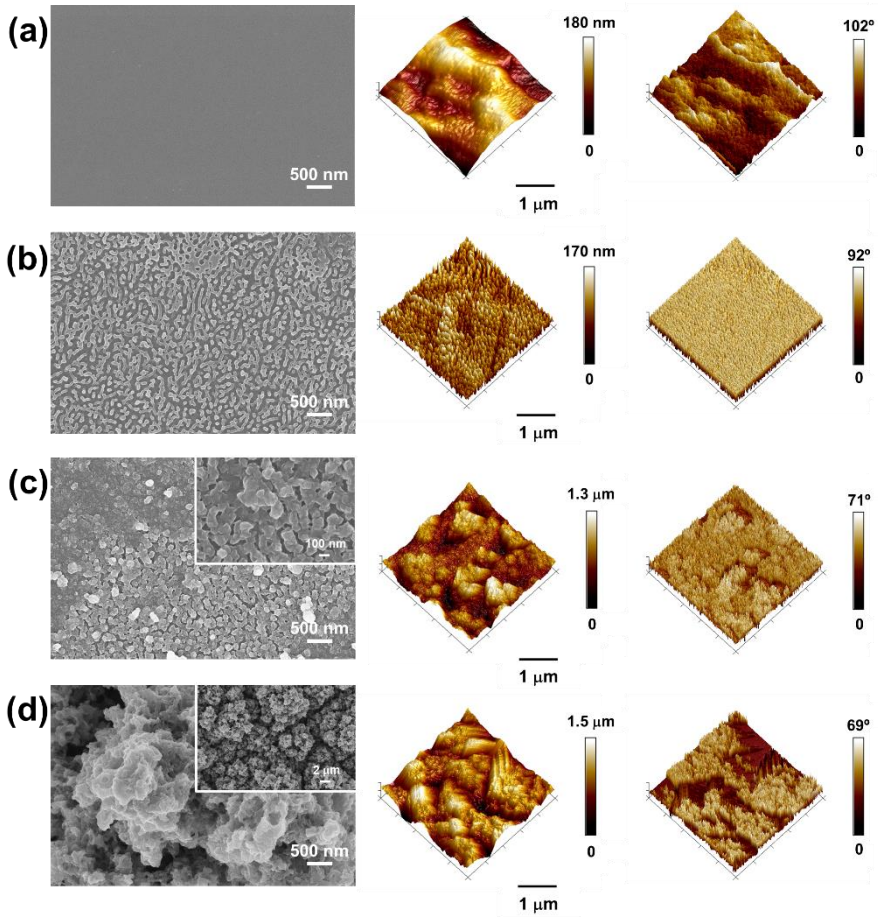

Figure 6.3.3 Representative high resolution SEM micrograph (left) and both 3D height and phase AFM images (center and right, respectively) of (a) i-PP, (b) i-PP_f, (c) i-PP_f/NPs and (d) i-PP_f/PEDOT.

Electrochemical characterization. The electrochemical activity of the systems under study was investigated by cyclic voltammetry (CV) using phosphate buffer saline (PBS) solution, pH 7.4, as supporting electrolyte. Control voltammograms recorded for i-PP, i-PP_f and i-PP_f/NPs in PBS are compared in Figure 6.3.4a. As expected, no electrochemical activity was detected for i-PP and i-PP_f (*i.e.* the areas of the voltammograms are negligible). However, the formation of

PHMeEDOT NPs on the surface of i-PP_f results in an increment of electroactivity, even though the voltammograms recorded for i-PP_f/NPs do not show clear oxidation nor reduction processes. This observation, which is consistent with the poor contact between the ICP NPs (Figure 6.3.3c), indicates that formation of redox species in the potential range from −0.20 to +0.80 V is blocked by the i-PP_f matrix.

The incorporation of a PEDOT layer using the PHMeEDOT NPs as polymerization nuclei results in a huge increase of the electrochemical activity. The transformation associated to the formation of a dense and compact network of PEDOT chains filling the spaces between the NPs and coating them, as observed by SEM (Figure 6.3.3d), is visually detected when the film progressively changes from blueish to dark blue with increasing polymerization charge (Figure 6.3.4b). Inspection to the control voltammograms displayed in Figure 6.4.4c shows that electroactivity of i-PP_f/PEDOT is higher than that of i-PP_f/NPs by several orders of magnitude. More specifically, the voltammetric charge (Q) and the current density at the reversal potential ($j_{0.8}$) determined for i-PP_f/NPs are $Q = 1.3 \times 10^{-5}$ C and $j_{0.8} = 3 \times 10^{-3}$ mA/cm^2, while these parameters increase to $Q = 0.020$ C and $j_{0.8} = 3.28$ mA/cm^2 for i-PP_f/PEDOT. This observation confirms that i-PP_f/NPs can be described as a network of PEDOT-based conduction paths coating the plasma treated i-PP film.

On the other hand, i-PP_f/PEDOT exhibits a very high electrochemical stability in PBS. Figure 6.3.4c compares the first control voltammogram with that recorded after 50 consecutive oxidation-reduction cycles in the potential range from −0.20 to 0.80 V, both showing very similar anodic and cathodic areas. Indeed,

the electrochemical activity of i-PP$_f$/PEDOT decreases by only 1.5% after 50 cycles. This is a very interesting observation since the electrochemical stability of PEDOT in PBS is known to be relatively poor when the scanned potential interval is slightly wider than that used in this work. For example, the electrochemical activity of PEDOT films was reported to decrease by 17% and 39% when 10 and 50 redox cycles were applied in PBS using a potential range from −0.40 to 0.90 V. [46] This is consistent with the fact that the anodic limit for PEDOT polarization occurs at +0.80 V, as reported by Marzocchi *et al.*, [47] while higher potential values lead to a strong overoxidation of the ICP.

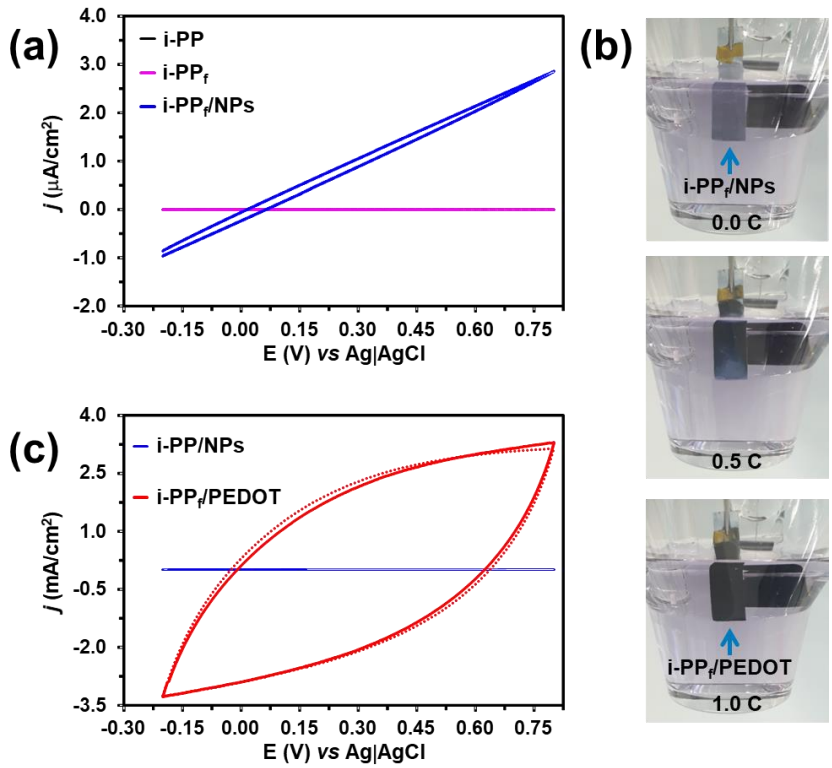

Figure 6.3.4 (a) Control voltammograms of i-PP, i-PP$_f$ and i-PP$_f$/NPs in PBS. (b) Photographs displaying the progressive variation of the colour when i-PP$_f$/NPs transforms into i-PP$_f$/PEDOT by the electrodeposition of

PEDOT layer. (c) Control voltammograms of i-PP_f/NPs and i-PP_f/PEDOT in PBS. The voltammogram recorded for i-PP_f/PEDOT after 50 consecutive oxidation-reduction cycles is also displayed (dotted red curve). For (a) and (c): initial and final potentials, −0.20 V; reversal potential, +0.80 V; scan rate: 50 mV/s.

Electrochemical detection of NADH by i-PP_f/PEDOT flexible films.

The electrochemical performance of the free-standing i-PP_f/PEDOT sensor towards the electrocatalytic oxidation of NADH was examined by CV in Dulbecco's modified Eagle's medium (DMEM) supplemented with 2% fetal bovine serum (FBS; pH 8.1) and 0.2% $NaHCO_3$. As shown in Figure 6.3.5a and 6.3.5b, which compare the voltammograms recorded for increasing NADH concentrations (*i.e.* from 0 to 2 mM and from 2 to 16 mM, respectively), the oxidation of NADH to NAD+ is evidenced by oxidation peak at around 0.6 V.

The potential peak for NADH electro-oxidation shifted positively 170 mV when the NADH concentration increased from 0.25 mM to 16 mM (*i.e.* from 0.52 V to 0.69 V), while the peak current density increased 1.88 mA/cm^2 (*i.e.* from 4.17 to 6.05 mA/cm^2). Furthermore, a change in the slope is observed when peak current density (y; in mA/cm^2) is plotted versus the amount of NADH (x; in mM). More specifically, the linear dynamic interval observed from 0 to 2 mM (Figure 6.3.5a, right) with linear regression equation $y = 0.4174x + 4.1056$ ($R^2 = 0.9559$) changes to $y = 0.0759x + 4.9028$ ($R^2 = 0.9282$) in the interval from 2 to 16 mM (Figure 6.3.5b, right). The slope of the equation corresponds to the linear sensitivity, which is 417 and 75.9 μA/cm^2 for the 0-2 and 2-16 linear dynamic range, respectively.

The limit of detection (LOD) of the i-PP_f/PEDOT sensor, which is defined as $(3 \cdot \sigma)/b$, where σ is the standard deviation of the blank and

b is the slope of the calibration curve in the lowest dynamic range, is found to be 0.14 mM. This LOD value, which was obtained using self-supported i-PP_f/PEDOT films as working electrode, is lower than that reported for electropolymerized PEDOT films supported onto glassy carbon electrodes (LOD= 0.50 mM) [48] and close to that found in our previous work for PTh-*g*-(PEG-*r*-PCL) composite films adhered on carbon screen-printed electrodes (LOD= 0.2 mM).

As a first approach, the change in the slope for NADH concentrations higher than 2 mM has been attributed to changes in the aggregation state of NADH molecules. More specifically, NADH has been supposed to be solubilized or forming small molecular cluster for concentrations ≤ 2 mM, whereas NADH aggregates with itself or with other components of the medium for concentrations > 2 mM. This aggregation behavior, which is hypothesized to increase with the concentration of NADH, would explain the anomalies observed not only in the electrochemical detection but also in the optical one (see below).

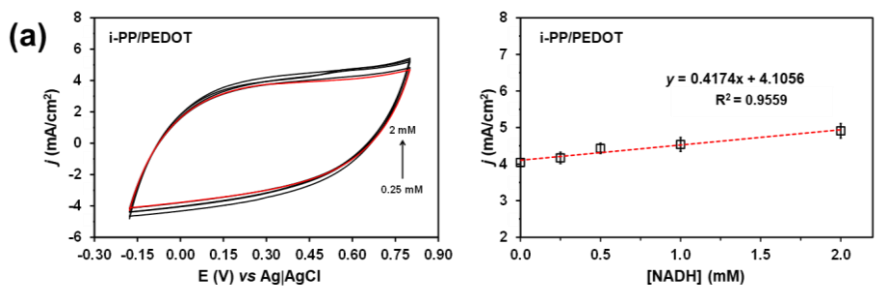

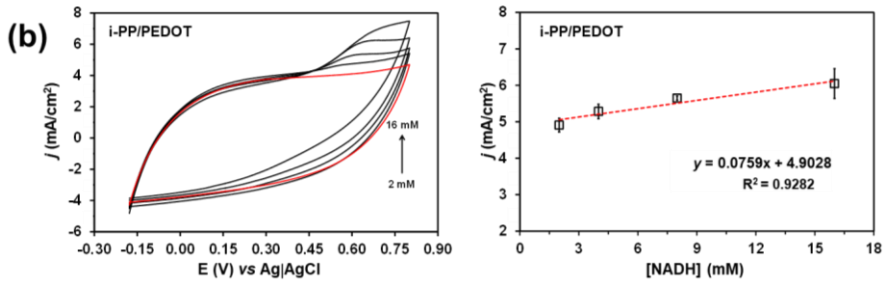

Figure 6.3.5 Control voltammograms (left) for i-PP_f/PEDOT in DMEM solutions with NADH concentrations from (a) 0.25 to 2 mM and (b) from 2 to 16 mM. The corresponding calibration curves (*i.e.* peak current vs. NADH concentration) are also depicted (right). The red curves correspond to the blanks (*i.e.* DMEM solutions without NADH).

Characterizing extracellular NADH from aerobic bacterial metabolism. In this sub-section, we determine the concentration of NADH in extracellular media coming from the aerobic respiration reactions of bacteria. For this purpose, the confidence in the spectroscopic detection of NADH as a function of its concentration has been studied first. Figure 6.3.6a shows the UV-vis spectrum recorded for a 0.25 mM NADH solution in DMEM supplemented with FBS and $NaHCO_3$. Although the most intense peak at 340 nm confirms that NADH is the predominant specie, the presence of the peak at 250 nm evidences the partial oxidation to NAD+ in the used medium. On the other hand, Figure 6.3.6b displays the calibration curve obtained using the absorbance at λ = 340 nm for the interval of NADH concentrations from 0 to 2 mM. A linear regression equation, $y = 1.5916x + 0.1883$ ($R^2 = 0.9972$), with a LOD of 0.01 mM was obtained for this NADH concentration interval. However, both a drastic change in the slope and a loss of linearity is observed for the interval of NADH concentrations higher than 2 mM (inset in Figure 6.3.6b). These observations, which are fully consistent with the results

obtained for the electrochemical detection of NADH in supplemented DMEM using i-PP_f/PEDOT (Figure 6.3.5), confirms the difficulty in detecting high concentrations of this analyte.

In order to ascertain if the concentration of NADH in media with high contents of bacteria is within the linear interval of detection with linear response, *Escherichia coli (E. coli*) colony forming units (CFU, 2×10^8 colony) were seeded in DMEM supplemented with FBS and $NaHCO_3$. The bacteria used for this purpose were ATCC 25922, a biofilm-positive strain (B+), and CECT 101 a biofilm-negative strain (B–). Colonies were incubated at 37 ºC and 150 rpm for 24 h and 48 h maintaining conditions. After such periods of time, the concentrations of NADH in the culture media were determined by measuring the absorbance at λ = 340 nm and applying the calibration curve displayed in Figure 6.3.6b.

Figure 6.3.6c represents the absorbance at λ = 340 nm obtained for B+ and B– cultures after 24 and 48 h as well as the NADH concentrations calculated by applying the corresponding calibration curve (Figure 6.3.6d). The NADH concentration, which was null after seeding the bacteria in the medium, grows with time, independently of the ability to form biofilm. Thus, after 24 h the NADH concentration is 0.25 and 0.34 mM for B+ and B–, respectively, increasing 36% and 8%, respectively, after 48 h. Furthermore, the NADH concentration is higher for B– than for B+. This expected behaviour has been attributed to compactness of the biofilm structure, which comprises a self-produced matrix of extracellular polymeric substances and restricts the release of NADH to the medium. Overall, these results confirm that cellular membranes are permeable to NADH produced by bacteria

respiration reactions. Moreover, the NADH concentration in the culture media is above the LOD found for i-PP$_f$/PEDOT and below 2 mM, and, therefore, detectable by both CV and UV-vis spectroscopy.

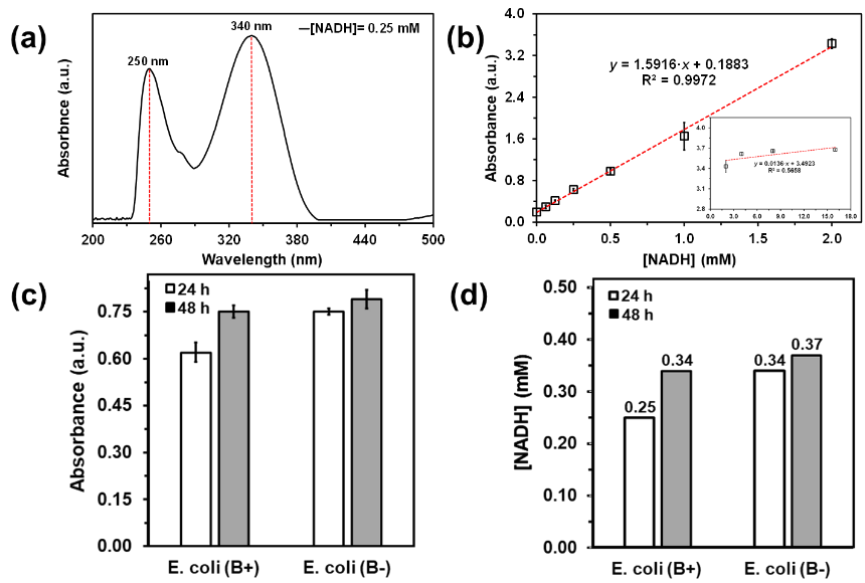

Figure 6.3.6 (a) UV-vis spectrum of a DMEM solution with 0.025 mM NADH and (b) calibration curve obtained by representing the absorbance at λ= 340 nm *vs* the concentration of NADH (from 0 to 2 mM) added to a supplemented DMEM solution. (c) Absorbance at λ= 340 nm and (d) concentration of extracellular NADH in *E. coli* B+ and B– cultures after 24 and 48 h.

Conclusions

An ICP-based biosensor for the detection of bacterial microorganisms have been incorporated to free-standing and flexible i-PP films for future applications as biomedical implants. For this purpose, the following three step approach has been applied: (*i)* functionalization of the i-PP surface using an oxygen plasma treatment (i-PP$_f$); (*ii)* deposition on the surface of the plasma treated film of an

ICP layer (~ 1.1 μm), which consisted of PHMeEDOT NPs prepared by oxidative polymerization (i-PP_f/NPs); and *(iii)* electrochemical deposition of a PEDOT layer (~ 8.2 μm) covering the PHMeEDOT NPs and filling the spaces among them to improve the electrochemical properties (i-PP_f/PEDOT). Indeed, the electrochemical response of i-PP_f/PEDOT was several orders of magnitude higher than that of i-PP_f/NPs because of the effective conduction paths formed during the electropolymerization of PEDOT. In addition, the i-PP_f/PEDOT platform detects NADH with a linear sensitivity of 417 μA/cm^2 and the limit of detection is 0.14 mM, which is below the concentration of extracellular NADH from aerobic bacterial metabolism.

In summary, results indicate that i-PP_f/PEDOT is highly promising for bacteria detection on flexible medical implants and can be also extrapolated to rigid prostheses. In the next Section, the improvement of the biocompatibility of this two-layered ICP-based technology will be explained, on basis of a new strategy of its chemical assembly, by the “grafting through” technique described in the previous Chapter 5.

6.4 Smart engineering of flexible and electroactive platforms for tissue engineering

Abstract

Development of smart functionalized materials for tissue engineering has attracted significant attention in recent years. In this work we have functionalized isotactic polypropylene (i-PP), which is typically employed for biomedical applications (*e.g.* fabrication of sutures and surgical meshes for hernia repair), for engineering a 3D all-polymer flexible interface that enhances cell proliferation by a factor of *ca.* three. For this purpose, a hierarchical construction process consisting of three steps: (*i*) functionalization of i-PP by applying a plasma treatment; (*ii*) electroactivation of the functionalized i-PP by polymerizing conducting polymer nanoparticles on the surface; and (*iii*) deposition of a graft copolymer, having poly(3,4-ethylenedioxythiophene) (PEDOT) backbone, and randomly distributed short poly(caprolactone) (PCL) side chains (PEDOT-*g*-PCL), as a coating layer of micrometric thickness (~ 9 μm). The deposition of the PEDOT-*g*-PCL layer has been conducted using the *grafting through* approach according to which a new synthesized 3,4-ethylenedioxythiophene (EDOT)-containing macromonomer has been anodically copolymerized with EDOT. The properties of the resulting bioplatform, which can be defined as a macroscopic composite coated with a "molecular composite", has been characterized and both cell adhesion and cell proliferation have been evaluated. Results obtained for two human cell lines demonstrate that the incorporation of the PEDOT-*g*-PCL layer significantly

improves cell attachment and cell growth not only compared to i-PP but also with respect to the same platform coated with PEDOT (*i.e.* without PCL side groups).

Materials and methods

Materials. Isotactic polypropylene (i-PP) films, which were used as a base substrate, were kindly supplied by B Braun Surgical S.A. (Rubí, Barcelona, Spain). Hydroxymethyl-3,4-ethylenedioxythiophene (HMeEDOT; 95%), ε-caprolactone (ε-CL), stannous octanoate ($Sn(Oct)_2$), 3,4-ethylenedioxythiophene (EDOT; 97%), lithium perchlorate ($LiClO_4$), acetonitrile (99.8%) and phosphate buffered saline (PBS) solution were purchased from Sigma-Aldrich (USA). $LiClO_4$ was stored in an oven at 80 °C before its use in the anodic polymerization. Ammonium persulfate (APS; 98%), hydrochloric acid (37%) and sodium hydroxide were used as received from Panreac Quimica S.A.U. (Spain).

Synthesis of EDOT-PCL macromonomer. The EDOT-PCL macromonomer was obtained by ring-opening polymerization of ε-CL using HMeEDOT as initiator and $Sn(Oct)_2$ as catalyst. Briefly, 1.45 mmol HMeEDOT, 14.5 mmol ε-CL and 0.0072 mmol $Sn(Oct)_2$ were added under nitrogen, in previously flamed and nitrogen-purged two neck round-bottom flask equipped with a dropping funnel and magnetic stirrer. The ε-CL polymerization was carried out in bulk at 130°C. After 24h the mixture was diluted with $CHCl_3$ and poured into a tenfold excess of cold methanol. The polymer was collected after filtration and dried at room temperature in vacuum for 3 days.

Synthesis of i-PP$_f$/PEDOT-g-PCL bioplatform. The flexible bioplatforms were synthetized trough three steps. The first one, functionalization of i-PP by plasma treatment, and the second, electroactivation of the functionalized i-PP by polymerizing conducting polymer nanoparticles on the surface (i-PP$_f$/NPs), both procedures were described in Section 6.3. For the third step, deposition of a graft copolymer, EDOT-PCL and EDOT were electro-copolymerized on i-PP$_f$/NPs by chronoamperometry (CA) using a three-electrode cell with 20 mL acetonitrile solution, 0.1 M $LiClO_4$ as supporting electrolyte, 7 mM EDOT and 3mM EDOT-PCL. The resulting bioplatform was denoted i-PP$_f$/PEDOT-*g*-PCL. On the other hand, bioplatforms coated with PEDOT homopolymer were synthetized as reference. For the electropolymerization of EDOT, the cell was filled with 20 mL acetonitrile containing 0.1 M $LiClO_4$ and 10 mM of EDOT, the resulting bioplatform was denoted i-PP$_f$/PEDOT. In all cases a constant potential of +1.40 V was applied until the polymerization charge achieved 1.0 C.

Previous to the polymerization of both, copolymer or homopolymer, i-PP$_f$/NPs films were washed with 0.2 M NaOH to balance charge of over oxidized PHMeEDOT NPs. Then, electroactivated films (i-PP$_f$/NPs) were employed as working electrodes while a platinum sheet and an Ag|AgCl electrode, containing a KCl saturated aqueous solution (E^o = 0.222 V at 25 °C), were used as counter and reference electrode, respectively.

Characterization of the macromonomer and the prepared bioplatforms. The macromonomer was evaluated by ^{1}H-NMR in $CDCl_3$, FTIR through KBr pellets, GPC, DSC and TGA. While the

bioplatforms were characterized by FTIR and Raman spectroscopy, WCA, DSC, TGA, SEM operated a 5 kV, AFM and stylus profilometry.

Electrochemical characterization was carried out by cyclic voltammetry (CV) in a three-electrode cell using the studied bioplatforms as working electrode and a platinum wire as counter electrode. The reference electrode was an Ag|AgCl electrode containing a KCl saturated aqueous solution (E^0 = 0.222 V at 25 °C). All electrochemical assays were performed using a 0.1 M phosphate buffer saline (PBS) solution (pH = 7.4) at room temperature. The initial and final potentials were − 0.20 V, while the reversal potential was + 0.80 V.

The biocompatibility of the samples was tested by adhesion and proliferation of HeLa and IMR-90 cells, cultured in the presence of the films during 24 h (adhesion) and 7 days (proliferation). A detailed description of all methods employed for the macromonomers and copolymer characterization was included in Chapter 4.

Results and discussion

Macromonomer characterization. The EDOT-PCL macromonomer (Scheme 6.4.1) is one of the only few reported to date. [49–53] EDOT-PCL was obtained by ring-opening polymerization of ε-caprolactone (ε-CL) using HMeEDOT as initiator and stannous octanoate, $Sn(Oct)_2$, as catalyst. The chemical structure of EDOT-PCL macromonomer was evaluated by ^{1}H NMR and FTIR spectroscopy.

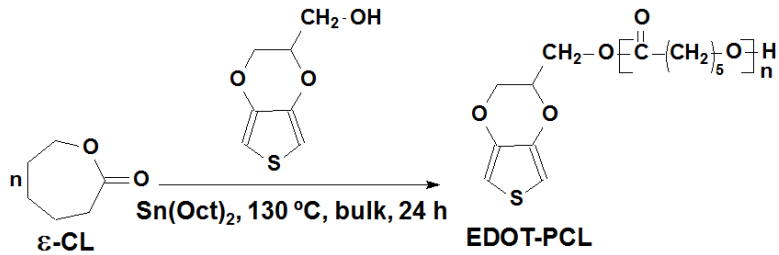

Scheme 6.4.1 Synthesis of EDOT-PCL macromonomer.

The Figure 6.4.1 show the ^{1}H NMR spectra signals of the new macromonomer EDOT-PCL in $CDCl_3$, the macromonomer structural formula and the peaks assignments. Carbon atoms in the thiophene ring are clearly discernible at 6.37 ppm (**a, b**) while for PCL oligomer structural units, the protons associated to the four carbon atoms placed in the proximity of carbonyl group (**f, g, h** and **i** in Figure 6.4.1), appeared in the range 1.36-2.42 ppm and the peak assignable to the two protons of aliphatic CH_2 nearest to the oxygen atom (type **j** in Figure 6.4.1) appeared, as expected, at 4.05-4.1 ppm. It is also worthy to mention that the peaks assignable to both the protons of CH_2 group in the vicinity of the hydroxyl chain end (protons k at 3.66-3.69 ppm) appeared separately from those of the other structural units.

The molecular weight (M_n) of the EDOT-PCL macromonomer was estimated with the Equation 5.3.1 (Chapter 5), comparing the integrals value of protons of type **c d** and **e** (originating from HMeEDOT) (or that of protons of type **k** belonging to the final structural unit of the new formed PCL chain) with the value of integral for the ($2n^{-2}$) protons of type **j** from the other (n^{-1}) structural units of PCL, the polymerization degree of n = 16.5 was obtained and a value of EDOT-PCL $M_{n\text{-}^{1}H\text{-}NMR}$ = 2055. The apparent molecular weight of the EDOT-PCL macromonomer was also evaluated by GPC

measurements, measurements led to M_n values of 3598 Da and polydispersity index of 1.49. The discrepancy between the values obtained by the two methods can be attributed to the significant difference between the hydrodynamic volume of linear PS standard used for the GPC columns calibration and those of PCL-ended by an aromatic moiety.

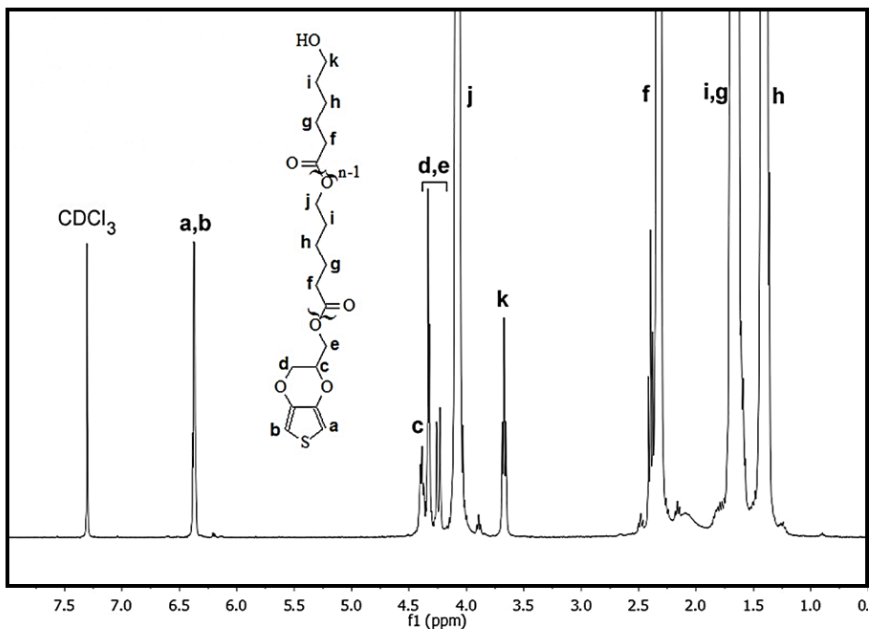

Figure 6.4.1 (a) ^{1}H-NMR spectrum of EDOT-PCL in $CDCl_3$.

The FTIR spectrum of EDOT-PCL is presented in Figure 6.4.2. In this spectrum characteristic bands associated with constitutive elements of the macromonomer, namely thiophene ring (Th) and ethylenedioxy ring in EDOT moiety, as well as bands and crystallization-sensitive bands of PCL oligomeric chains are all present. Absorption bands at 3530 cm^{-1} and 3439 cm^{-1} are due to the hydroxyl functional groups placed at the chain ends of PCL. The

distinctive band at 3115 cm^{-1} is assignable to =C-H stretching vibration of α-α' positions in Th. In the range 2946.39 cm^{-1} - 2866.58 cm^{-1} the absorption bands characteristic of -CH_2- asymmetric and symmetric stretching vibrations in PCL and EDOT are discernible. Crystalline-sensitive νC=O band from esteric groups of PCL appeared around 1725 cm^{-1}. Also for PCL are present the bands at 1471 cm^{-1} (-CH_2 bending), 1399 cm^{-1} (-CH_2 wagging), 1295 cm^{-1} (C-O-C asymmetric stretching), 1245 cm^{-1} (C-O-C symmetric stretching), and 962 cm^{-1} (-C-O- stretching of crystalline form). The band at 1192 cm^{-1} can be attributed to both PCL and ethylenedioxy group in EDOT for -CH_2 deformation and C-O-C bending vibration, respectively. Also for ethylenedioxy group in EDOT 1369 cm^{-1}, 1107 cm^{-1} and 1046 cm^{-1} are present, as well. The signals at 1487 cm^{-1} (C=C stretching), at 933 cm^{-1} and at 841 cm^{-1} (C-S-C stretching and deformation) are characteristic to the thiophene ring.

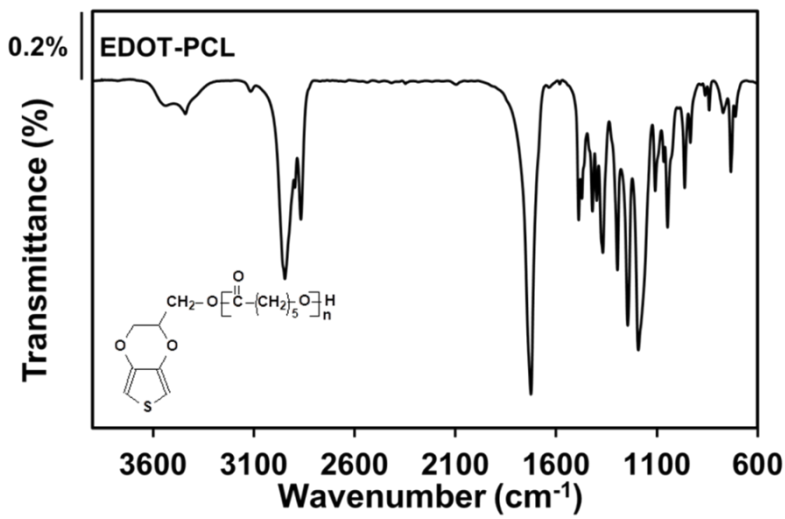

Figure 6.4.2 FTIR spectrum of EDOT-PCL macromonomer.

Bioplatforms characterization. The bioactive platform was prepared using a three-step process (Figure 6.4.3a), in a similar manner to that employed for section 6.3 of the present Chapter. First, the surface of i-PP films (0.5 × 1.5 cm^2) for biomedical implants, kindly supplied by Braun Surgical S.A. (Rubí, Barcelona, Spain), were functionalized with oxygen plasma (0.30 mbar) during 180 seconds using a power discharge of 250 W. [39] Each functionalized i-PP (i-PP_f) film was coated with PHMeEDOT NPs by immersing it in 5 mL of 0.2 HCl with 50 mM HMeEDOT monomer during 30 min and under agitation (250 rpm). Then, the oxidative chemical polymerization of the monomer was conducted by slowly dropping 1 mL of 0.2 M HCl with 60 mM of ammonium persulfate (APS). The reaction was kept at 37 °C and 80 rpm for 24 h. After this period, the resulting material (i-PP_f/NPs) was removed, washed with 0.2 M NaOH to balance the charge and dried.

In the last step, the EDOT-PCL macromononer and the EDOT monomer were electrocopolymerized on i-PP_f/NPs films. For this purpose, each film was introduced in a three-electrode cell filled with 20 mL of acetonitrile solution containing 0.1 M $LiClO_4$ as supporting electrolyte and both EDOT (7 mM) and EDOT-PCL (3 mM). Electrocopolymerization was conducted at a constant potential of +1.40 V and adjusting the polymerization charge to 1.0 C. It should be noted that, in this process PHMeEDOT NPs act as polymerization nuclei for the growing of PEDOT-*g*-PCL chains. For comparison, bioplatforms without PCL side groups were also prepared using only EDOT monomer (10 mM) in the electropolymerization step, which was conducted using identical experimental conditions. Hereafter,

flexible and free-standing bioplatforms formed by i-PP$_f$/NPs and coated with a PEDOT-*g*-PCL or PEDOT (control) layer are denoted i-PP$_f$/PEDOT-*g*-PCL or i-PP$_f$/PEDOT, respectively.

Figure 6.4.3b shows photographs of i-PP, i-PP$_f$/NPs, i-PP$_f$/PEDOT and i-PP$_f$/PEDOT-*g*-PCL. The translucent i-PP film becomes opaque and blueish after the incorporation of PHMeEDOT NPs, which turns to a dark blue when PEDOT and PEDOT-*g*-PCL layers are deposited by electro(co)polymerization. These visual transformations suggest that both the oxidative polymerization and the electro(co)polymerization occurred successfully.

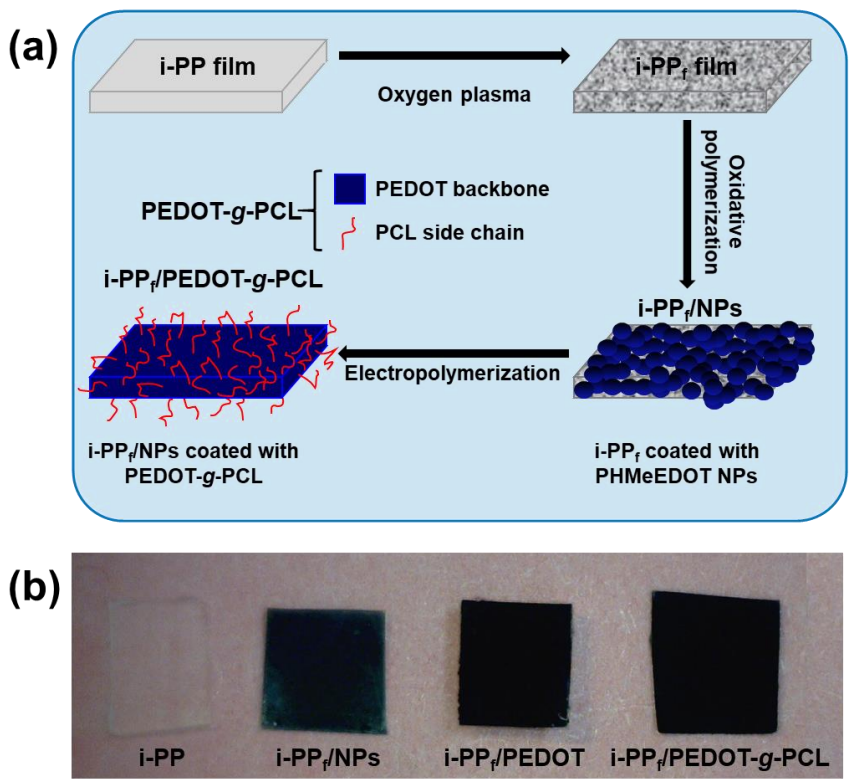

Figure 6.4.3 (a) Sketch representing the three steps used to prepare i-PP$_f$/PEDOT-*g*-PCL bioplatforms. (b) Photographs of i-PP, i-PP$_f$/NPs, i-PP$_f$/PEDOT and i-PP$_f$/PEDOT-*g*-PCL films.

Raman spectra of i-PP$_f$/PEDOT and i-PP$_f$/PEDOT-*g*-PCL are compared in Figure 6.4.4. The spectra of biomedical i-PP, i-PP$_f$ and i-PP$_f$/NPs were reported in the previous Section 6.3 with the corresponding discussion.

The characteristic peaks of PEDOT backbone predominate in the 785 nm laser Raman spectra recorded for two coated bioplatforms (Figure 6.4.4), even though some clear differences allowed us to identify the presence of PCL side chains in i-PP$_f$/PEDOT-*g*-PCL. More specifically, the following peaks were collected in the spectra of the two systems: the vibration mode of the thiophene C–S bond at 988 cm^{-1}; the stretching of the ethylenedioxy group at 1085 cm^{-1}; the C–C inter-ring stretching at 1258 cm^{-1}; the C–C stretching at 1365 cm^{-1}; and the C=C stretching at 1420 cm^{-1}. However, the C=O and C–C stretching peaks (1575 and 1137 cm^{-1}, respectively), which can be attributed to both i-PP$_f$ and PCL, are consistently more intense for i-PP$_f$/PEDOT-*g*-PCL than for i-PP$_f$/PEDOT.

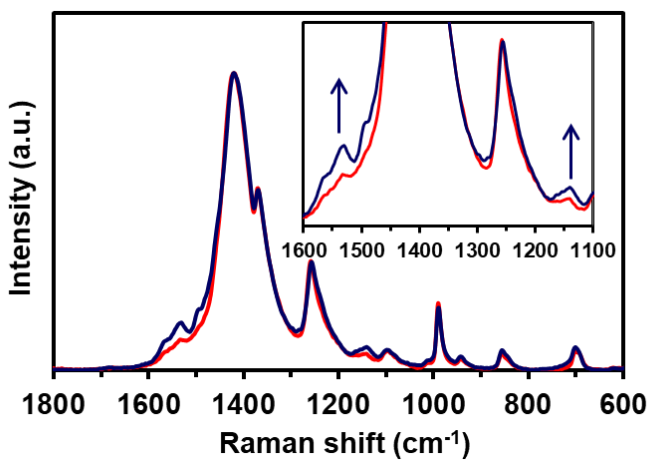

Figure 6.4.4 Raman spectra recorded for i-PP$_f$/PEDOT (red line) and i-PP$_f$/PEDOT-*g*-PCL (blue line) bioplatforms.

Evidence of the successful EDOT-PCL macromolecular incorporation in the i-PP$_f$/PEDOT-*g*-PCL bioplatform is also provided by the surface wettability. The contact angle (θ) for milli-Q water was θ = 102º ± 3º, 78º ± 5º, 82º ± 3º, < 20º and 84 ± 5º for i-PP, i-PP$_f$, i-PP$_f$/NPs, i-PP$_f$/PEDOT and i-PP$_f$/PEDOT-*g*-PCL films, respectively. After plasma treatment, hydrophobic i-PP transforms into slightly hydrophilic i-PP$_f$ due not only to the apparition of polar groups (*e.g.* C=O and C–O, as proved by FTIR [39,54]) but also by the creation of a superficial nano-patterning, as observed by SEM (Figure 6.3.3). However, the functionalization with PHMeEDOT NPs does not increase the wettability, which has been attributed to the combined action of two different factors (discussed in the next sub-sections): (*i*) PHMeEDOT NPs do completely cover the i-PP$_f$ surface; and (*ii*) the topographic changes experienced by i-PP$_f$/NPs occurred at the submicrometric length-scale-rather at the nanometric one.

On the other hand, the hydrophilicity of ICP PEDOT was attributed to the large amount dopant counterions. [55] Therefore, after coating with an homogenous PEDOT layer, the surface of the resulting bioplatform becomes very hydrophilic. Instead, i-PP$_f$/PEDOT-*g*-PCL is poorly hydrophilic due to effect of the PCL side chains. However, the copolymerization of EDOT-PCL with EDOT monomers prevents that i-PP$_f$/PEDOT-*g*-PCL behaves as a pure hydrophobic system (*i.e.* PCL typically exhibits water CA of ~120º [56]), which is expected to be beneficial for tissue engineering applications.

Thermal characterization. Thermal characterization and stability of the resulting bioactive platforms were analysed by differential scanning calorimetry (DSC) and thermogravimetric analysis (TGA),

respectively. Previously to the evaluation of i-PP$_f$/PEDOT and i-PP$_f$/PEDOT-*g*-PCL, the thermal properties of the EDOT-PCL macromonomer, i-PP, i-PP$_f$ and i-PP$_f$/NPs were examined. A three-step protocol consisting in heating-cooling-heating (described in the Chapter 4) was applied to all samples. Calorimetric results corresponding to the heating and cooling runs are summarized in Table 6.4.1.

DSC traces of both heating runs for EDOT-PCL macromonomer (Figure 6.4.5a), revealed a double-melting behaviour, that can be observed in the main endothermic peak which present a second shoulder. Such phenomenon was reported previously in the case of PCL blends [57] or for hyperbranched structures. [58] Thus, the behaviour of EDOT-PCL macromonomer can be associated to a morphological effect which implies the presence of two populations of crystals, differing in size and thickness. This has been noticed for the first time in the case of a PCL-containing electroactive macromonomer, the phenomenon could also be explained by the peculiar geometry and character of bicyclic EDOT moiety, which seems to interfere with PCL crystallization in both from: solution and melt state. The experimental values of melting and crystallization peaks for the EDOT-PCL macromonomer were found around 50 ºC and 27 ºC, respectively (Figure 6.4.5a), indicating the development of a well crystalline phase, besides, these values are consistent with those reported for PCL. [59] The degree of crystallinity, measured in the first and second heating runs, was high, close to 78% and 58%, respectively.

On the other hand, no significant differences were detected in DSC test between i-PP, i-PP$_f$ and i-PP$_f$/NPs formulations, as shown in

Figure 6.4.5b-d. In all cases a melting point around 158 ºC and a crystallization peak at 114 ºC were observed in the first and second runs, respectively. These data are consistent with those found in the literature, i-PP grades melt in the range of 100 – 180 °C, depending on their molecular structure. [60] The melting point observed in the i-PP grade used in this work seems to be related with the β-form of i-PP, since this form is less stable and shows a melting temperature (~155ºC) lower than α-form (~ 170ºC). [61] Heats of fusion were used to evaluate the crystallinity of polymers (see Eqn. 4.2), taking into account the heat of fusion for 100% crystalline i-PP (209 J/g). Crystallinities measured for solution-crystallized samples were sligthly lower than those measured for melt-crystallized samples (around 37% *vs.* 43%). The influence of PHMeEDOT NPs on the crystallization of i-PP was not significant due no appreciable variations were observed, neither in the crystallization temperature or in the crystallinity for i-PP_f/NPs.

Table 6.4.1 Calorimetric data derived from DSC scans of the studied samples.

Sample	1st heating			cooling		2nd heating		
	T_m (ºC)	ΔH_m (J/g)	$\chi^{\heartsuit}$ (%)	T_c (ºC)	ΔH_c (J/g)	T_m (ºC)	ΔH_m (J/g)	$\chi^{\heartsuit}$ (%)
i-PP	158.3	79.3	37.9	114.0	93.2	156.6	90.8	43.4
i-PP_f	157.9	78.7	37.6	113.9	93.6	156.3	91.3	43.7
i-PP_f/NPs	158.5	74.3	35.5	114.2	93.1	156.6	91.7	43.9
EDOT-PCL	50.1	106.9	78$^{\clubsuit}$	27.4	77	46.8	78.4	57.6$^{\clubsuit}$
i-PP_f/PEDOT	158.9	69.8	33.4	114.1	87.4	156.9	83.9	40.1
i-PP_f/PEDOT -*g*-PCL	158.9	63.1	27.9	112.4	74.9	157.0	72.7	34.8

♥χ calculated according to the Eqn. 4.2 and taking a value of 209 J/g. as ΔHm0 for a 100% crystalline i-PP

♣χ calculated according to a value of 136 J/g enthalpy for a 100% crystalline PCL

DSC thermograms of i-PP_f/PEDOT-*g*-PCL and i-PP_f/PEDOT are presented in Figure 6.4.5e-f while the evaluated values are also listed in Table 6.4.1. A similar thermal behavior, in relation to the fusion and crystallization of both, was observed. However, it should be noted that polymerization with EDOT or EDOT-PCL had significant effects on the crystal structure of i-PP. More specifically, a decrease in the crystallinity is observed (40% and 35% measured in the second heating for i-PP_f/PEDOT and i-PP_f/PEDOT-*g*-PCL, respectively). Nevertheless, in all the traces of i-PP_f/PEDOT-*g*-PCL in Figure 6.4.5e, the peaks characteristic to melting or crystallization of PCL side chains are missing. This phenomenon was noticed before for both linear [62] or ramified conjugated rod-coil systems. [63] It was explained either based on the value of PCL polymerization degree (in the case of the linear structure) or based on the value of the molar fraction of the incorporated PCL-macromonomer in the final copolymer (in case of graft copolymer). In the case of i-PP_f/PEDOT-*g*-PCL, based on our previous experience, [64] we assume that, due to well-recognized PCL lower crystallization rate [65] and also due to PEDOT-*g*-PCL copolymer architecture which drive its inter-chains interactions that could take place in the molten state (high π–π stacking between conjugated main chains and/or main chains and side chains interactions) delays, hinder and prevent the crystallization of PCL side chains.

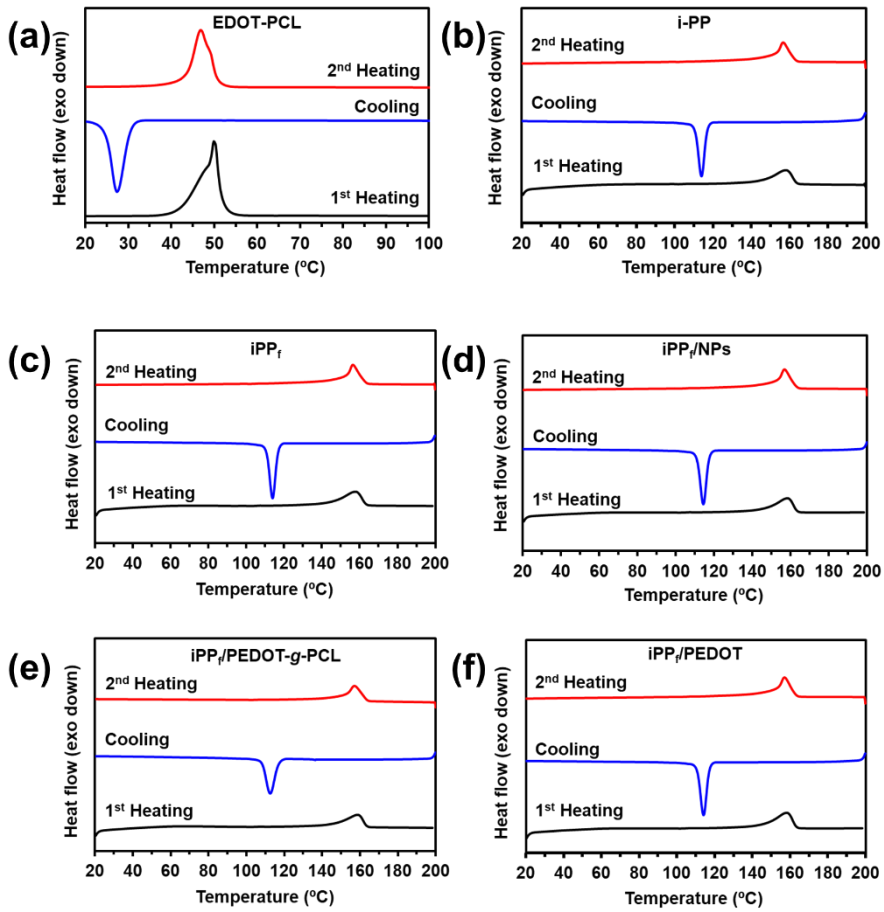

Figure 6.4.5 DSC thermograms for (a) EDOT-PCL macromonomer, (b) i-PP, (c) i-PP_f, (d) i-PP_f/NPs, (e) i-PP_f/PEDOT-*g*-PCL and (f) i-PP_f/PEDOT bioplatforms.

Thermogravimetric experiments of the studied bioplatforms are displayed in Figure 6.4.6. EDOT-PCL macromonomer (Figure 6.4.6a) showed a continuous mass loss from 250 to 350 ºC characterized by a single DTGA peak (*i.e.* the highest thermal degradation temperature) at 332 ºC with 3.4% of char yield. The macromonomer resulted to be less stable than neat PCL, whose T_{max} usually falls 100 degrees higher. [66,67] On the other hand, thermogravimetric analyses also demonstrated

that thermal stability increased as the functionalization of i-PP increases (*i.e.* i-PP$_f$ and i-PP$_f$/NPs, Figure 6.4.6b). Decomposition took place according to a single step, with a DTGA maximum degradation peak increasing from 416 ºC for i-PP to 453 ºC for i-PP$_f$/NPs. The onset degradation temperature (taken in the TGA curve as the temperature at which the weight loss is 5%) was high for all samples and also increased as i-PP was functionalized (338 ºC, 361 ºC and 413 ºC for i-PP, i-PP$_f$ and i-PP$_f$/NPs, respectively), reflecting that functionalization with plasma and posterior electro-activation with PHMeEDOT NPs enhanced the thermal stability of the polymer.

The thermal stability of the two bioactive platforms (Figure 6.4.6c) is higher than those showed for i-PP and i-PP$_f$ and slightly lower than i-PP$_f$/NPs (Figure 6.4.6b). Both platforms showed a similar TGA and DTGA curves (Figure 6.4.6c) with the same T_{max}, 450 ºC, which is the same value observed for i-PP$_f$/NPs. Also, both platforms reached the final degradation at the same temperature, 475 ºC, and left a char of 3% and 5% for i-PP$_f$/PEDOT and i-PP$_f$/PEDOT-*g*-PCL, respectively, which is related with the proportion of EDOT and EDOT-PCL in the final samples. However, there is a slight difference in the onset temperature, i-PP$_f$/PEDOT-*g*-PCL started to degrade 23 ºC later than i-PP$_f$/PEDOT, supporting the performance improvement of the bioactive platform when PCL side groups are grafted.

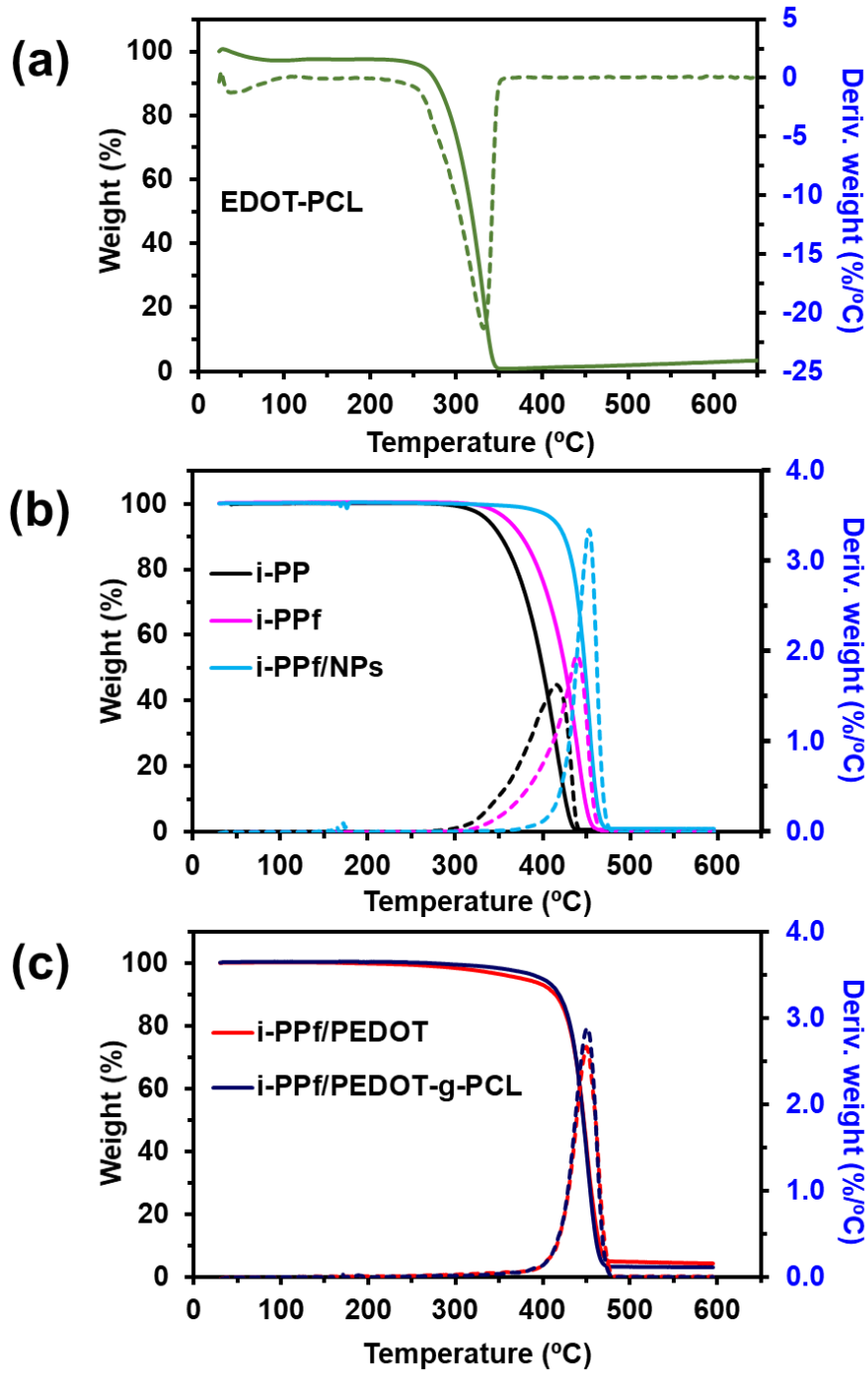

Figure 6.4.6 TGA and DTGA curves of (a) EDOT-PCL macromonomer, (b) i-PP, i-PP_f and i-PP_f/NPs; and (c) i-PP_f/PEDOT-*g*-PCL and (f) i-PP_f/PEDOT bioplatforms.

Electrochemical characterization. Electrochemical evaluation was performed by cyclic voltammetry, Figure 6.4.7a compares the cyclic voltammograms recorded for i-PP_f/NPs and i-PP_f/PEDOT in 0.1 M phosphate buffer saline (PBS, pH 7.4) solution. As is shown, the electrochemical activity of i-PP_f is practically inexistent, even after the functionalization with PHMeEDOT NPs. This reflects that the latter only nucleate the growing of PEDOT or PEDOT-*g*-PCL chains during the electrochemical polymerization and, therefore, no other active role can be attributed to PHMeEDOT NPs. Instead, the electrochemical activity increases considerably after the polymerization of the PEDOT layer, as is evidenced by the area of the voltammogram. After 50 consecutive oxidation-reduction cycles, the area of the voltammograms recorded for i-PP_f/PEDOT samples decreases very slightly (Figure 6.4.7a), indicating that this is an electrochemical stable bioplatform. More specifically, the loss of electroactivity (LEA) after 50 cycles was of 6 ± 1% only.

The electroactivity of i-PP_f/PEDOT-*g*-PCL is significantly higher than that of i-PP_f/PEDOT, as deduced from the comparison of the areas of the voltammograms (Figure 6.4.7b). Considering that the thickness of the two electroactive layers are very similar (9.0 ± 2.5 and 8.2 ± 2.4 μm for the PEDOT-*g*-PCL and PEDOT, respectively, as determined by profilometry), this observation suggests that PEDOT-*g*-PCL morphological and structural features could be responsible for this behaviour. Thus, a more porous morphology evidenced by SEM observations (see next sub-section), will allow the access and escape of dopant ions during the oxidation and reduction process, respectively, much easier for the graft copolymer than for the

homopolymer. On the other hand, the presence of PCL polar steric side chains in PEDOT-*g*-PCL, [68] due to their high ionic conductivity, [69] as well as to the high ion-solvating capability, [70] and also due to the presence of hydroxyl end groups [71] can facilitate and enhance the ionic transport in the bulk of mixed electronic-ionic PEDOT conjugated main chain during the redox process in an aqueous electrolyte.

However, the loss of electrochemical activity is much faster for i-PP$_f$/PEDOT-*g*-PCL, which experiences a LEA of 29 ± 5% after 50 redox cycles (Figure 6.4.7b). This has been attributed to the electrochemical degradation of PCL side chains, which are probably damaged by the successive potential scanning processes, being known the fact that the ester groups in PCL are redox active close to the lithium stripping and plating potential, forming degradation products. [72] The progressive degradation affects the structure of the grafted copolymer, reducing porosity and making more difficult the access and escape of dopant ions when oxidation and reduction potentials are applied.

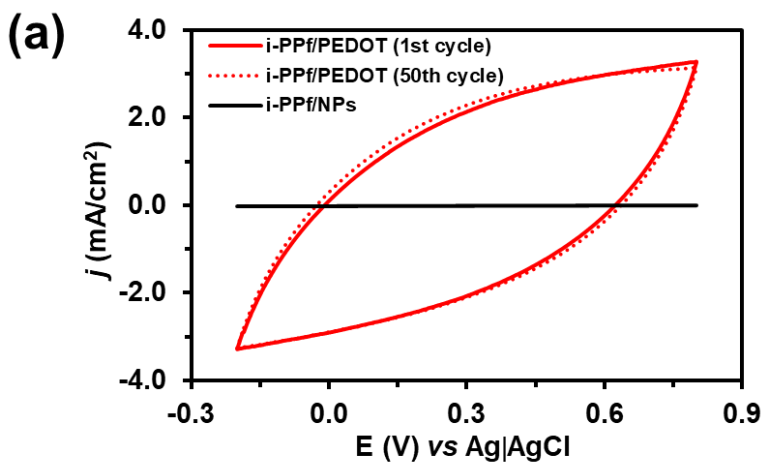

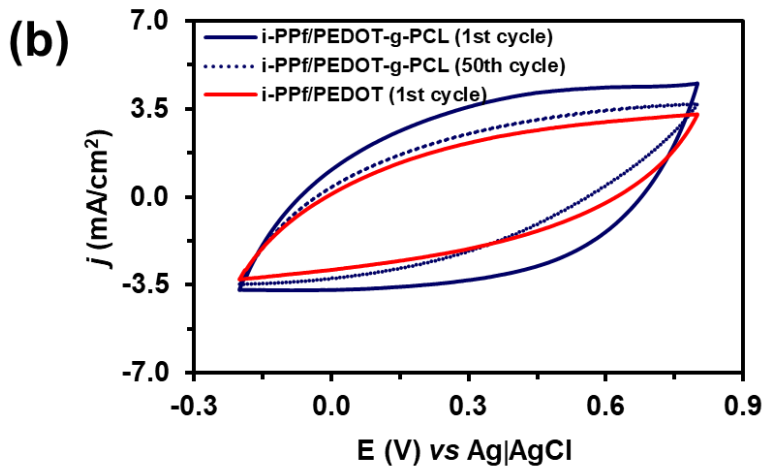

Figure 6.4.7 Comparison of the cyclic voltammograms recorded in PBS 0.1 M for (a) i-PP_f/NPs and i-PP_f/PEDOT; and (b) i-PP_f/PEDOT and i-PP_f/PEDOT-*g*-PCL. Voltammograms recorded for i-PP_f/PEDOT and i-PP_f/PEDOT-*g*-PCL after 50 consecutive redox cycles (dotted lines) are included in (a) and (b), respectively. CV assays were conducted using the following parameters: scan rate, 50 mV/s; initial and final potential, -0.20 V; reversal potential, +0.80 V.

Surface characterization. The morphology and topography of i-PP, i-PP_f and i-PP_f/NPs were discussed in the previous Section 6.3 (Figure 6.3.3). In summary, the i-PP surface becomes more complex after functionalization, the plasma treatment causes the appearing of a superficial and homogeneous nano-patterning on the whole surface (Figure 6.3.3a-b). This morphological change affects significantly the topography, showing a slight increase of the surface roughness (R_q) of 8 ± 6 nm due to the appearing of small and sharp peaks abundantly and homogeneously distributed. Besides, abundant PHMeEDOT NPs with capricious morphology are clearly detected in the surface of i-PP_f/NPs (Figure 6.3.3c), which experiences a drastic increment of the roughness (R_q = 312 ± 12 nm) with respect to i-PP_f. These NPs, which organize in a porous layer of 1.1 ± 0.1 μm in thickness, were

randomly distributed on the i-PP_f surface, forming a random contact network structure. However, the contact between such NPs was not large enough to ensure percolation and form conduction paths, which explains the inexistent electrochemical activity of i-PP_f/NPs films (Figure 6.4.7a).

Figure 6.4.8 shows significant morphological differences between i-PP_f/PEDOT and i-PP_f/PEDOT-*g*-PCL. In the latter, the PEDOT homopolymer completely covers the PHMeEDOT NPs, integrating them into a single conducting layer with continuous and well-defined conduction paths. This layer exhibits the typical heterogeneous morphology of electropolymerized PEDOT films, [44,73] which consists on the aggregation of dense clusters of packed molecules. Thus, the linear growing of PEDOT chains, which are exclusively formed by α-α linkages (*i.e.* the β-positions of the thiophene ring are occupied by the dioxane ring), favours the formation of compact spheroidal clusters that aggregate leaving a large number of submicrometric pores among them. This unique structure favours the access and scape of dopant ions during redox processes, explaining the excellent electrochemical behaviour reported for PEDOT. [44,73–75] Moreover, this morphological organization results in a rough surface with $R_q = 611 \pm 57$ nm, as is shown in the AFM images included in Figure 6.4.8a.

The microscopic texture of i-PP_f/PEDOT-*g*-PCL is smoother than that of i-PP_f/PEDOT, which has been attributed to the superficial location of the PCL side chains. This assumption is confirmed by the contrast in the AFM phase image included in Figure 6.4.8b, which allows distinguishing between two phases in i-PP_f/PEDOT-*g*-PCL.

Phase imaging is a powerful tool that is sensitive to surface stiffness/softness and adhesion between the tip and surface. The image recorded for i-PP_f/PEDOT-*g*-PCL shows bright and dark domains, which correspond to chemical-dependent phase shifts of up to 174º. The bright areas, which correspond to large phase angles, are associated with the PEDOT phase, whereas the dark areas represent the PCL phase. It is worth noting that the PCL phase occupies the main part of the surface, whereas the PEDOT phase only appears in regions largely dominated by the incorporation of EDOT monomers with respect to EDOT-PCL macromonomers. On the other hand, the roughness of i-PP_f/PEDOT-*g*-PCL (R_q = 448 ± 34 nm) is significantly lower than that of i-PP_f/PEDOT, even though the thickness of the PEDOT-*g*-PCL and PEDOT layers are very similar (9.0 ± 2.5 and 8.2 ± 2.4 μm, respectively).

Another important difference between i-PP_f/PEDOT-*g*-PCL and i-PP_f/PEDOT refers to the structure of the pores. Although both bioplatforms display a porous surface with a large number of submicrometric pores, i-PP_f/PEDOT-*g*-PCL shows a unique distribution of nanometric pores with sizes comprised between ~ 50 and ~ 100 nm. These additional nanopores, which have been attributed to the organization of the PCL side chains, are consistent with both the high electrochemical activity and the low electrochemical stability of i-PP_f/PEDOT-*g*-PCL in comparison to i-PP_f/PEDOT. Thus, PCL side chains are expected to be very sensitive to the electrochemical degradation, especially because of their small size, and nanometric pores probably collapse after a few consecutive redox cycles, reducing

drastically the electrochemical activity of the system with the number of redox cycles.

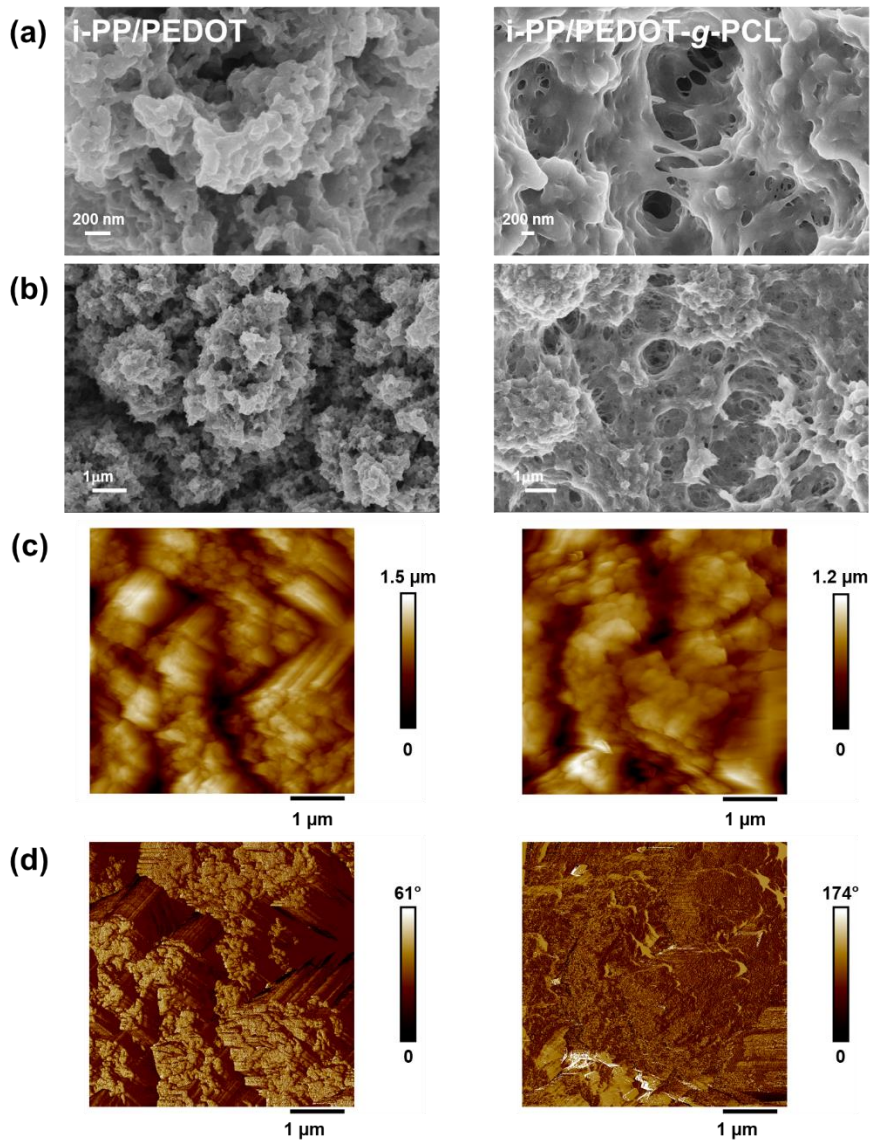

Figure 6.4.8 i-PP_f/PEDOT (left) and i-PP_f/PCL-*g*-PCL (right): High (a) and low (b) magnification SEM micrographs and 2D AFM height (c) and phase (d) contrast images.

Influence of PEDOT-g-PCL in cellular adhesion and proliferation.

The effect of the graft copolymer layer in cell adhesion and

proliferation was evaluated by considering two cell lines, HeLa and IMR-90, both extensively used in scientific research because of their fast growth. HeLa is a human immortal carcinogenic cell line with epithelial morphology, while IMR-90 primary cells are human Caucasian fetal lung fibroblasts (no-carcinogenic). Quantitative results for cell adhesion and proliferation assays (24 h and 7 days of cell culture, respectively) on tissue culture polystyrene (TCPS, control), i-PP, i-PP_f, i-PP_f/NPs, i-PP_f/PEDOT and i-PP_f/PEDOT-*g*-PCL are displayed in Figure 6.4.9. Results, which correspond to the average of three independent replicas for each system, are expressed in terms of cell viability (cv) relative to the TCPS control material.

The amount of cell adhered to the surface of biomedical i-PP is similar (HeLa) or slightly higher (IMR-90) than that of TCPS control, which is a well-known biocompatible material used for metal implants. [76] This behaviour is approximately maintained after plasma treatment of the i-PP_f, indicating that functionalization does not have a major impact on the interaction and attachment of the cells to the surface. However, the incorporation of the first ICP layer introduces important changes that, in addition, depend on the cell line. More specifically, PHMeEDOT NPs promotes IMR-90 cells adhesion by around 80% with respect to the control, while reduces the attachment of HeLa cells by the approximately 50%. However, the addition of the second ICP layer results in a significant increment of cell adhesion with respect to i-PP_f/NPs, this effect was especially remarkable for IMR-90 cells. Thus, the attachment of fibroblast cells is higher for i-PP_f/PEDOT and i-PP_f/PEDOT-*g*-PCL than for i-PP by ~ 70% and

~90%, respectively, while for HeLa cells the adhesion increment is negligible for i-PP_f/PEDOT and of ~ 60% for i-PP_f/PEDOT-*g*-PCL.

The different response of HeLa and IMR-90 cells towards ICPs can be interpreted on the basis of their contrasted fibronectin content. More specifically, PEDOT and, in general ICPs, have a great affinity towards fibronectin, its adsorption being an essential step for promoting cell-adhesion. [77] In cell lines derived from non-carcinogenic tissues fibronectin was found to be predominantly in the extracellular matrix, whereas carcinogenic cell lines display very little or no fibronectin. [78] The absence of extracellular fibronectin was specifically demonstrated for tumor HeLa cells that, instead, contain such protein in the cell nucleus. [79] This feature explains the significantly lower adhesion of HeLa cells to i-PP_f/PEDOT-*g*-PCL and, especially to i-PP_f/PEDOT, with respect to that found for IMPR-90 cells.

Covalent grafting of biocompatible side chains to ICPs backbone is a smart strategy to improve the biocompatibility of structures based on such class of polymers, which present chemical and physical properties that mimics the characteristic of natural extracellular matrix (*e.g.* ICP structures enable ions diffusion and exchange at the interface). [80] Analysis of cell viability through simple proliferation assays is a useful tool for assessing the impact of scaffolds in cell metabolism and, therefore, determine its potential applicability for tissue engineering applications. Results obtained in this work for examined materials (and the TCPS control) are shown in Figure 6.4.9b.

Not unexpectedly, results depend on the cell line. Proliferation of HeLa cells on i-PP and i-PP_f (cv = 116 ± 2% and 129 ± 19%, respectively) was slightly better than for the control TCPS, whereas that of i-PP_f/NPs was clearly worse (cv = 60 ± 24%). Instead, i-PP_f/PEDOT (cv = 144 ± 19%) shows a significant increase in cell number due to cell division (cytokinesis) with respect to both pristine and plasma-functionalized i-PP substrates. These results indicate that the doping level of chemically polymerized PHMeEDOT NPs is not high enough to facilitate the exchange of ions with adhered HeLa cells, which is turn is limited by the lack of fibronectin in the extracellular matrix carcinogenic cells (as discussed above). In contrast, PEDOT prepared using the experimental conditions described in this work is known to achieve a very high doping level, as generally occurs for ICPs synthesized by electropolymerization with respect to chemical oxidative polymerization, [81] and therefore, a very high content of counterions is contained inside the polymeric matrix. These unique electronic and chemical structures facilitate the exchange of ions at the PEDOT cell interface, promoting cell division. Indeed, this behaviour is so favourable that it overcomes the limitations associated to the lack of extracellular fibronectin in HeLa cells, improving the response of electrochemically inert surfaces (*i.e.* TCPS, i-PP, i-PP_f and i-PP_f/NPs). It is worth noting that these results are fully consistent with the cyclic voltammograms displayed in Figure 6.4.7.

i-PP_f/PEDOT-*g*-PCL exhibits an extraordinary capacity for promoting HeLa cells growth with cv = 268 ± 15%. The superior features of this bioplatform has been attributed to the synergy among the electrochemical activity of the PEDOT, the high biocompatibility

of PCL, which is frequently used for biomedical applications, and the ionic conductivity due to the dopant anions of PEDOT that, in turn, is enhanced by ion solvating polymer property of PCL chains. [69,70] The addition of the graft copolymer layer to biomedical i-PP results improves the cell viability by a factor of 2.3.

Results are more impressive for IMR-90 cells. In this case the viability for i-PP and i-PP_f surfaces (cv = 68 ± 9% and 72 ± 4%, respectively) is lower than for the control, which has attributed to the poor wettability of these substrates (*i.e.* growth of fibrin-containing cells is promoted on hydrophilic surfaces in comparison to hydrophobic ones). This situation is reversed for i-PP_f/NPs (cv = 98 ± 9%), even though its water contact angle is similar to that of i-PP_f. Again, this behaviour has been associated to the ability of ICPs to exchange ions with cells, as is supported by the results obtained when a relatively thick layer of PEDOT is deposited on PHMeEDOT NPs. Thus, the cv of i-PP_f/PEDOT (cv = 137 ± 11%) increased the double when compared to that of the i-PP substrate for biomedical applications.

For i-PP_f/PEDOT-*g*-PCL (cv = 196 ± 22%), the improvement represents an increase of almost a factor of 3 and 1.5 with respect to i-PP and i-PP_f/PEDOT, evidencing the benefits of the PCL grafting. These results prove the synergy between PEDOT and PCL effects at the bioplatform interface. Thus, the grafted copolymer approach presented in this study represents a smart strategy to functionalize currently used biomedical plastics, as i-PP, for matching of flexibility, biocompatibility and charge transport between the biointerface

material and living tissues, promoting considerably cell adhesion and growing.

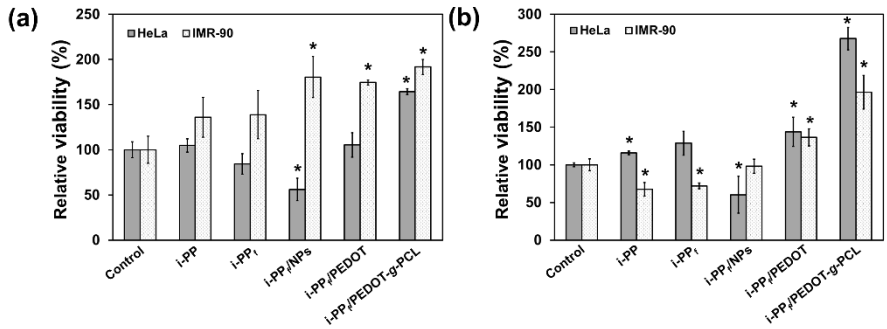

Figure 6.4.9 (a) Cellular adhesion and (b) cellular proliferation on the surface of i-PP, i-PP$_f$, i-PP$_f$/NPs, i-PP$_f$/PEDOT and i-PP$_f$/PEDOT-*g*-PCL. TCPS was used as a control substrate. Human HeLa and IMR-90 cells were cultured during (a) 24 h and (b) 7 days. Asterisk marks (*) represent significant difference among the samples at $p < 0.05$.

Conclusions

Improvement of well-stablished polymeric materials for biomedical applications is a current challenge. In this study, a graft copolymer is used as a molecular composite to coat previously functionalized and electroactivated i-PP for biomedical applications. The surface of i-PP functionalized with oxygen plasma treatment was covered with PHMeEDOT NPs prepared by chemical oxidative polymerization, which have been used as polymerization nuclei for *in situ* electrocopolymerization of EDOT-PCL macromonomer and EDOT monomer. The resulting bioplatform, is a flexible substrate coated with a graft copolymer that presents the advantages of PEDOT backbone and PCL side chains showing that i-PP$_f$/PEDOT-*g*-PCL has many favourable properties with respect to i-PP and i-PP$_f$/PEDOT for

tissue engineering applications. Besides, it has been confirmed by cell adhesion and proliferation assays of two human cell lines with very different characteristics, the i-PP_f/PEDOT-*g*-PCL improved the cell viability of i-PP by a factor of almost three.

Overall, this study has wide implications in plastic implants currently used, which can be improved facilitating their integration in tissues. In addition, future investigations will be oriented in this field, studying the impact of PEDOT-*g*-PCL in cell differentiation and the integration of i-PEDOT/PEDOT-*g*-PCL.

6.5 Conclusions

Mechanical properties of the conducting polymer PEDOT were improved thru its combination with a common plastic, isotactic polypropylene (i-PP). For that, two different methodologies were studied. In the first one, PEDOT NPs were supported into an i-PP matrix while, in the second one, a free-standing i-PP films were superficially modified with a 3-step electrochemical deposition of PEDOT.

Both composites, i-PP/PEDOT and i-PP$_f$/PEDOT, showed good electrochemical activity, which permitted to design a strategy for the electrochemical detection of bacteria and, distinguish its growth *versus* eukaryotic cells proliferation. The approach was based in the recognition of nicotinamide adenine dinucleotide (NADH) and its oxidized form (NAD+). This biomolecule is generated by both types of cells, *i.e.* prokaryote or eukaryotic cells, however, as prokaryote cellular membranes are permeable to NADH and NAD+, was possible the extracellular detection of this biomolecule during the growing of bacterial infections. Section 6.2 was dedicated to evaluate the capacity of i-PP/PEDOT to validate these differences and in Section 6.3, an improved i-PP$_f$/PEDOT, confirmed its ability to measure low concentrations of NADH in a culture medium.

Finally (Section 6.4), the biocompatibility of the electrochemical (bio)sensor i-PP$_f$/PEDOT was enhanced using the “grafting-through” technique. The excellent results from biological assays, indicated that the flexible and electroactive bioplatform i-PP$_f$/PEDOT-*g*-PCL can be also used for tissue engineering applications in the biomedical filed.

6.6 References

1 L. Hall-Stoodley, J. W. Costerton and P. Stoodley, *Nat. Rev. Microbiol.*, 2004, **2**, 95–108.

2 C. A. Fux, J. W. Costerton, P. S. Stewart and P. Stoodley, *Trends Microbiol.*, 2005, **13**, 34–40.

3 D. Lebeaux, A. Chauhan, O. Rendueles and C. Beloin, *Pathogens*, 2013, **2**, 288–356.

4 N. Høiby, T. Bjarnsholt, M. Givskov, S. Molin and O. Ciofu, *Int. J. Antimicrob. Agents*, 2010, **35**, 322–332.

5 A. L. Furst and M. B. Francis, *Chem. Rev.*, 2019, **119**, 700–726.

6 M. Amiri, A. Bezaatpour, H. Jafari, R. Boukherroub and S. Szunerits, *ACS Sensors*, 2018, **3**, 1069–1086.

7 O. Simoska and K. J. Stevenson, *Analyst*, 2019, **144**, 6461–6478.

8 L. Y. Zheng, R. B. Congdon, O. A. Sadik, C. N. H. Marques, D. G. Davies, B. G. Sammakia, L. M. Lesperance and J. N. Turner, *Sensors Actuators B Chem.*, 2013, **182**, 725–732.

9 A. C. Ward, A. J. Hannah, S. L. Kendrick, N. P. Tucker, G. MacGregor and P. Connolly, *Biosens. Bioelectron.*, 2018, **110**, 65–70.

10 J. B. J. H. van Duuren, M. Müsken, B. Karge, J. Tomasch, C. Wittmann, S. Häussler and M. Brönstrup, *Sci. Rep.*, 2017, **7**, 5223.

11 F. Ricci, A. Amine, D. Moscone and G. Palleschi, *Biosens. Bioelectron.*, 2007, **22**, 854–862.

12 M. L. Wos and P. C. Pollard, *Water Sci. Technol.*, 2009, **60**, 783–791.

13 W. Ying, *Antioxid. Redox Signal.*, 2008, **10**, 179–206.

14 L. R. Stein and S. Imai, *Trends Endocrinol. Metab.*, 2012, **23**, 420–428.

15 W. Ying, *Front. Biosci.*, 2007, **12**, 1863.

16 M. Pittelli, L. Formentini, G. Faraco, A. Lapucci, E. Rapizzi, F. Cialdai, G. Romano, G. Moneti, F. Moroni and A. Chiarugi, *J. Biol. Chem.*, 2010, **285**, 34106–34114.

17 A. Puiggalí-Jou, P. Micheletti, F. Estrany, L. J. del Valle and C. Alemán, *Adv. Healthc. Mater.*, 2017, **6**, 1700453.

18 Y. Hui, C. Bian, S. Xia, J. Tong and J. Wang, *Anal. Chim. Acta*, 2018, **1022**, 1–19.

19 A. Zykwinska, W. Domagala, B. Pilawa and M. Lapkowski, *Electrochim. Acta*, 2005, **50**, 1625–1633.

20 P. TEHRANI, A. KANCIURZEWSKA, X. CRISPIN, N.

ROBINSON, M. FAHLMAN and M. BERGGREN, *Solid State Ionics*, 2007, **177**, 3521–3527.

21 J.-M. Lin, Y.-L. Su, W.-T. Chang, W.-Y. Su and S.-H. Cheng, *Electrochim. Acta*, 2014, **149**, 65–75.

22 A. Özcan and S. İlkbaş, *Anal. Chim. Acta*, 2015, **891**, 312–320.

23 B. Wang, H.-R. Zhang, C. Huang, L. Xiong, J. Luo and X. Chen, *RSC Adv.*, 2017, **7**, 42113–42122.

24 M. Ahsani and R. Yegani, *Chem. Eng. Res. Des.*, 2015, **102**, 261–273.

25 A. . Nielsen, D. . Batchelder and R. Pyrz, *Polymer (Guildf).*, 2002, **43**, 2671–2676.

26 G. Zerbi, M. Gussoni and F. Ciampelli, *Spectrochim. Acta Part A Mol. Spectrosc.*, 1967, **23**, 301–311.

27 H. Tadokoro, M. Kobayashi, M. Ukita, K. Yasufuku, S. Murahashi and T. Torii, *J. Chem. Phys.*, 1965, **42**, 1432–1449.

28 S. Garreau, J. L. Duvail and G. Louarn, *Synth. Met.*, 2001, **125**, 325–329.

29 Y.-K. Han, M.-Y. Chang, W.-Y. Huang, H.-Y. Pan, K.-S. Ho, T.-H. Hsieh and S.-Y. Pan, *J. Electrochem. Soc.*, 2011, **158**, K88.

30 A. A. Farah, S. A. Rutledge, A. Schaarschmidt, R. Lai, J. P. Freedman and A. S. Helmy, *J. Appl. Phys.*, , DOI:10.1063/1.4768265.

31 M. M. Pérez-Madrigal, M. I. Giannotti, L. J. Del Valle, L. Franco, E. Armelin, J. Puiggalí, F. Sanz and C. Alemán, *ACS Appl. Mater. Interfaces*, 2014, **6**, 9719–9732.

32 S. Maione, A. M. Gil, G. Fabregat, L. J. Del Valle, J. Triguero, A. Laurent, D. Jacquemin, F. Estrany, A. I. Jiménez, D. Zanuy, C. Cativiela and C. Alemán, *Biomater. Sci.*, 2015, **3**, 1395–1405.

33 M. G. Saborío, O. Bertran, S. Lanzalaco, M. Häring, D. Díaz Díaz, F. Estrany and C. Alemán, *Phys. Chem. Chem. Phys.*, 2018, **20**, 9855–9864.

34 G. Fabregat, G. Ballano, E. Armelin, L. J. del Valle, C. Cativiela and C. Alemán, *Polym. Chem.*, 2013, **4**, 1412–1424.

35 L. Meng, A. P. F. Turner and W. C. Mak, *Biosens. Bioelectron.*, 2018, **120**, 115–121.

36 C. Sriprachuabwong, C. Karuwan, A. Wisitsorrat, D. Phokharatkul, T. Lomas, P. Sritongkham and A. Tuantranont, *J. Mater. Chem.*, 2012, **22**, 5478.

37 V. S. Vasantha and S.-M. Chen, *Electrochim. Acta*, 2006, **52**, 665–674.

38 Y. P. Hung, J. G. Albeck, M. Tantama and G. Yellen, *Cell Metab.*, 2011, **14**, 545–554.

39 S. Lanzalaco, P. Turon, C. Weis, C. Alemán and E. Armelin, *Soft Matter*, 2019, **15**, 3432–3442.

40 S. Garreau, G. Louarn, J. P. Buisson, G. Froyer and S. Lefrant, *Macromolecules*, 1999, **32**, 6807–6812.

41 M. Arruebarrena de Báez, P. . Hendra and M. Judkins, *Spectrochim. Acta Part A Mol. Biomol. Spectrosc.*, 1995, **51**, 2117–2124.

42 A. Shakoor and T. Z. Rizvi, *J. Raman Spectrosc.*, 2010, **41**, 237–240.

43 D. Aradilla, F. Estrany and C. Alemán, *J. Phys. Chem. C*, 2011, **115**, 8430–8438.

44 D. Aradilla, D. Azambuja, F. Estrany, M. T. Casas, C. A. Ferreira and C. Alemán, *J. Mater. Chem.*, 2012, **22**, 13110.

45 C. Ocampo, R. Oliver, E. Armelin, C. Alemán and F. Estrany, *J. Polym. Res.*, 2006, **13**, 193–200.

46 D. E. López-Pérez, D. Aradilla, L. J. Del Valle and C. Alemán, *J. Phys. Chem. C*, 2013, **117**, 6607–6619.

47 M. Marzocchi, I. Gualandi, M. Calienni, I. Zironi, E. Scavetta, G. Castellani and B. Fraboni, *ACS Appl. Mater. Interfaces*, 2015, **7**, 17993–18003.

48 S. Trasatti, *Pure Appl. Chem.*, 1986, **58**, 955–966.

49 L. Groenendaal, G. Zotti, P. H. Aubert, S. M. Waybright and J. R. Reynolds, *Adv. Mater.*, 2003, **15**, 855–879.

50 A. C. da Silva, T. Augusto, L. H. Andrade and S. I. Córdoba de Torresi, *Mater. Sci. Eng. C*, 2018, **83**, 35–43.

51 M. Kesik, H. Akbulut, S. Söylemez, Ş. C. Cevher, G. Hızalan, Y. Arslan Udum, T. Endo, S. Yamada, A. Çırpan, Y. Yağcı and L. Toppare, *Polym. Chem.*, 2014, **5**, 6295–6306.

52 T. Yilmaz, E. Guler, Z. P. Gumus, H. Akbulut, E. Aldemir, H. Coskunol, D. Goen Colak, I. Cianga, S. Yamada, S. Timur, T. Endo and Y. Yagci, *Polym. Chem.*, 2016, **7**, 7304–7315.

53 B. Demir, T. Yilmaz, E. Guler, Z. P. Gumus, H. Akbulut, E. Aldemir, H. Coskunol, D. G. Colak, I. Cianga, S. Yamada, S. Timur, T. Endo and Y. Yagci, *Talanta*, 2016, **161**, 789–796.

54 S. Lanzalaco, L. J. Del Valle, P. Turon, C. Weis, F. Estrany, C. Alemán and E. Armelin, *J. Mater. Chem. B*, 2020, **8**, 1049–1059.

55 M. N. Gueye, A. Carella, J. Faure-Vincent, R. Demadrille and J.-P. Simonato, *Prog. Mater. Sci.*, 2020, **108**, 100616.

56 V. Planz, S. Seif, J. S. Atchison, B. Vukosavljevic, L. Sparenberg, E.

Kroner and M. Windbergs, *Integr. Biol.*, 2016, **8**, 775–784.

57 H. Vázquez-Torres and C. A. Cruz-Ramos, *J. Appl. Polym. Sci.*, 1994, **54**, 1141–1159.

58 A. Díaz, A. Bacaicoa, M. T. Casas, L. Franco, A. Serra and J. Puiggalí, *Thermochim. Acta*, 2015, **607**, 39–52.

59 D. K. Platt, *Biodegradable Polymers*, Smithers Rapra Limited, Shawbury, UK, 2006.

60 J. Karger-Kocsis and T. Bárány, Eds., *Polypropylene Handbook*, Springer International Publishing, Cham, 2019.

61 G. Shi, B. Huang and J. Zhang, *Makromol. Chemie, Rapid Commun.*, 1984, **5**, 573–578.

62 M. Surin, O. Coulembier, K. Tran, J. De Winter, P. Leclère, P. Gerbaux, R. Lazzaroni and P. Dubois, *Org. Electron.*, 2010, **11**, 767–774.

63 D. Mecerreyes, R. Stevens, C. Nguyen, J. A. Pomposo, M. Bengoetxea and H. Grande, *Synth. Met.*, 2002, **126**, 173–178.

64 D. G. Colak, I. Cianga, L. Cianga and Y. Yagci, *Des. Monomers Polym.*, 2016, **19**, 508–534.

65 Z. Wei, G. Wang, P. Wang, L. Liu and M. Qi, *Polym. Eng. Sci.*, 2012, **52**, 1047–1057.

66 R. A. Ruseckaite and A. Jiménez, *Polym. Degrad. Stab.*, 2003, **81**, 353–358.

67 I. Keridou, L. Franco, P. Turon, L. J. del Valle and J. Puiggalí, *Macromol. Mater. Eng.*, 2018, **303**, 1800100.

68 G. S. Collier, I. Pelse and J. R. Reynolds, *ACS Macro Lett.*, 2018, **7**, 1208–1214.

69 E. Fresta, V. Fernández-Luna, P. B. Coto and R. D. Costa, *Adv. Funct. Mater.*, 2018, **28**, 1707011.

70 N. Jürgensen, J. Zimmermann, A. J. Morfa and G. Hernandez-Sosa, *Sci. Rep.*, 2016, **6**, 36643.

71 C. M. Pacheco-Moreno, M. Schreck, A. D. Scaccabarozzi, P. Bourgun, G. Wantz, M. M. Stevens, O. J. Dautel and N. Stingelin, *Adv. Mater.*, 2017, **29**, 1604446.

72 A. Bergfelt, M. J. Lacey, J. Hedman, C. Sångeland, D. Brandell and T. Bowden, *RSC Adv.*, 2018, **8**, 16716–16725.

73 D. Aradilla, F. Estrany, F. Casellas, J. I. Iribarren and C. Alemán, *Org. Electron.*, 2014, **15**, 40–46.

74 O. Bubnova, Z. U. Khan, H. Wang, S. Braun, D. R. Evans, M. Fabretto, P. Hojati-Talemi, D. Dagnelund, J.-B. Arlin, Y. H. Geerts,

S. Desbief, D. W. Breiby, J. W. Andreasen, R. Lazzaroni, W. M. Chen, I. Zozoulenko, M. Fahlman, P. J. Murphy, M. Berggren and X. Crispin, *Nat. Mater.*, 2014, **13**, 190–194.

75 L. V. Kayser and D. J. Lipomi, *Adv. Mater.*, 2019, **31**, 1806133.

76 N. R. Patel and P. P. Gohil, *Int. J. Emerg. Technol. Adv. Eng.*, 2012, **2**, 91–101.

77 P. J. Molino, M. J. Higgins, P. C. Innis, R. M. I. Kapsa and G. G. Wallace, *Langmuir*, 2012, **28**, 8433–8445.

78 H. S. Smith, J. L. Riggs and M. W. Mosesson, *Am. Assoc. Cancer Res.*, 1979, **39**, 4138–4144.

79 G. ZERLAUTH, J. WESIERSKA-GADEK and SAUERMANN. G, *J. Cell Sci.*, 1988, **89**, 415–421.

80 A.-D. Bendrea, L. Cianga and I. Cianga, *J. Biomater. Appl.*, 2011, **26**, 3–84.

81 G. Fabregat, C. Alemán, M. T. Casas and E. Armelin, *J. Phys. Chem. B*, 2012, **116**, 5064–5070.

CHAPTER 7

FREE-STANDING NANOMEMBRANE: BIOMIMETIC HYBRID AND FARADAIC MOTORS

European Polymer Journal, **2019**, 114, 213

Journal of Membrane Science, **2020**, 601, 117931

ACS Applied Materials & Interfaces, **2019**, 11, 29427

The seventh chapter is focused on the synthesis, characterization and application of electroactive free-standing nanomembrane, obtained by surface and structural modifications.

7.1 Introduction

In the last decade nanotechnology concepts and nanomaterials have been applied to obtain and improve devices with very different applications in biomedicine and biotechnology. [1–4] Within this context, there is a growing interest in the fabrication of nanomembranes (also known as ultra-thin films or nanosheets), their distinctive features make them suitable for their use as sensors, [5,6] biomotors, [7] biointerfaces for cellular matrices, [8–11] antimicrobial surfaces, [10,12] and drug release devices. [13]

The term nanomembrane typically refers to quasi-2D structures with macroscopic surface area and nanoscale thickness (*i.e.* from 10 to a few hundreds of nanometers). A decade ago Kunitake *et. al*., [14] one of the pioneers in the field, coined the term "*giant nanomembrane*" to denote self-supported, also named free-standing, nanomembranes with an aspect ratio of size and thickness greater than 10^6. This aspect ratio facilitates the macroscopic use of nanomembranes while the self-supporting property, which enables the nanomembrane to retain its mechanical integrity when it is removed from the substrate, is required to physically separate two spaces. Overall, these characteristics confer special properties to free-standing nanomenbranes (hereafter denoted FsNM), such as: low weight, high flexibility and robustness. [15] The seminal features and characteristics of FsNM technology, including fabrication methods, mechanical properties and health-care

applications (*e.g.* as wound dressings, tissue engineering materials and bioelectronic devices) have been recently reviewed. [16–18]

Although single-layered FsNM have been widely developed and employed during the last years, the utilization of polymeric multi-layered FsNM (hereafter ml-FsNM) has been much less explored despite the advantages of this approach. [16–18] The layer-by-layer (LbL) assembly, [19,20] which is based on the deposition alternating layers of oppositely charged materials onto a solid surface, is probably the simplest technique for the preparation of ml-FsNM. However, the thickness of the resulting free-standing polymeric films, which is 10-15 nm only, [21] represents an important limitation for their manipulation and, therefore, for their practical application. Spin-coating represents an interesting alternative to LbL technique since ml-FsNM with higher mechanical strength could be produced in a few steps. Optimization of the spin-coating parameters (*e.g.* spinning speed, spinning time and the polymer solution concentration) typically results in homogenous polymeric films with controlled thickness. In this approach, the liquid solution of the polymer is spin casted onto a solid substrate, which has been previously coated with a sacrificial layer. For the preparation of multi-layered films, the spin-coating process is repeated as many times as the number of desired accumulative layers and, finally, the sacrificial layer is dissolved in an appropriated solvent to achieve the detachment of the ml-FsNM.

In a recent but pioneering study, [22] the spin-coating multi-layering process was used to prepare multilayered films of poly(vinyl alcohol) (PVA) and poly(lactic acid) (PLA). These were transformed into suspended PLA nanomembranes, which subsequently patched into a

continuous film, by dissolving the sacrificial PVA layers between PLA layers. Since then, the spin-coating multi-layering process has been combined with other approaches, such as LbL and chemical cross-linking of assembled layers, to produce supported multi-layered polymeric films for biomedical applications (*e.g.* drug release and antimicrobial surfaces). [23–26] However, the preparation and application of polymeric ml-FsNM is a challenge yet, so, in this Section we explore the spin-coating technique combined with the *in situ* anodic polymerization of a ICP for the preparation of ml-FsNM, which will be studied as biomimetic hybrid or as Faradaic motors (artificial muscles).

Biomimetic hybrid materials

Biomimetics takes advantage of the natural structures found in biological systems, permitting a nanoscopic development of functional materials. Within this context, nanomaterials based on proteins offer countless potential for nano-sized devices such as nanoreactors, [27] filtration devices, [28] nanosensors [29,30] or drug delivery systems. [31] Many of these applications usually require channel shaped components, which provide nanoscopic pathways for the passage of ions and small molecules. Appropriately, a class of outer membrane proteins (OMPs) found in gram-negative bacteria and mitochondria, called porins, can naturally form β-barrel channels. [32] They act as gates of the cell membrane. The majority of the porins does not present any particular selectivity and allows the passive diffusion of hydrophilic solutes (*e.g.* ions, sugars, amino acids and ATP). [33]

The outside facing part of β-barrel channels is hydrophobic to match the alkyl chains of the membrane lipids, while the internal water-filled part contains charged and hydrophilic residues. The size of the pore, which usually ranges from 10 to 40 Å, prevents bulky molecules to diffused and the internal hydrophilic region defines the permeation mechanism of species crossing the channel. [34] In addition, β-barrels exhibit exceptional robustness and stability over time and temperature. [35,36] Those features make porins competitive for their insertion in non-biological synthetic environment such as polymers. From such perspective, the approaches used to modify polymeric membranes, which can be free-standing or tethered onto solid supports, with functional biomolecules are based on the utilization of amphiphilic copolymers and structured polymers. [29]

In a recent study, ion-responsive hybrid nanomembranes (NMs) were developed by combining poly(N-methylpyrrole) (PNMPy), a conducting polymer (ICP) that was electrochemically synthesized onto a rigid stainless steel electrode, with the Omp2a porin. [37] Electrochemical studies on the resulting system (PNMPy/Omp2a) showed the activity of the protein to promote the passive transport of K^+ through the ICP membrane. More recently, another hybrid NM was engineered by immobilizing the same protein onto nanoperforated poly(lactic acid) (pPLA) NMs, the resulting system being denoted pPLA/Omp2a. [38] Immobilization of the protein around and inside the nanoperforations, which exhibited an average diameter of 51 ± 22 nm and a depth of ~ 100 nm, greatly increased the material conductivity and selectivity against some ions. Despite the capacity of pPLA and pPLA/Omp2a NMs to be free-standing, the difficulties associated with

their handling limited ion diffusion and electrical measurements, which were conducted using NMs supported onto ITO substrates. [38] Under these conditions, the conductivity of npPLA/Omp2a membranes was comparable to that of the same protein supported onto lipid bilayers (LB/Omp2a). [39] However, the suppression of the solid support to have biomimetic and flexible platforms with conducting channels for the metabolite transport is highly desirable.

Faradaic motors or artificial muscles

Electro-chemo-mechanical artificial muscles made of electroactive polymeric films are motors driven by reversible electrochemical reactions (Faradaic motors).[40,41] Thus, electrons are extracted from or injected to polymeric chains during the reactions generating positive or negative chains, respectively, while hydrated counterions (*i.e.* anions or cations accompanied with water molecules) are exchanged between the polymeric matrix and the electrolyte to keep the charge balance inside the film. Such electronic and ionic charge transport processes cause the conformational movements of the polymer chains that, together with the compositional variation inside the polymeric matrix (*i.e.* entrance and scape of hydrated ions), guarantee the film volume variation during reversible oxidation and reduction reactions (swelling and shrinking, respectively). These physical and chemical events (*i.e.* electric pulse, chemical reaction, conformational movements, ions and water exchange, and volume variation) resemble those taking place in natural muscles during the contraction and, therefore, the electrochemically driven reversible variations of the film volume are used to construct Faradaic electrochemical devices. [42–44]

Bending artificial muscles based on electrochemical reactions have been mainly developed for intrinsically conducting polymers (ICPs),[43–45] carbon nanotubes [46,47] and graphenes. [48,49] Among them, the most studied are the bilayers made of ICP/tape,[42,43] ICP/metal, [50,51] ICP/plastic, [52] in which the second layer acts as a passive element transforming the volume variation induced by the electrochemical energy into mechanical energy through a bending movement. Besides, interpenetrated polymer networks, [53–55] with bending movements higher than ± 30º, and asymmetric bilayer made of two different conducting polymers [56–58] have been also successfully developed. Other approaches have been used to construct electromechanical actuators for specific applications. For example, in the field of elastic voltage controlled artificial muscles, ICPs have been grafted to soft block copolymers to produce elastomer-like materials capable of more than 150% actuation strain. [59,60] Agrawal *et al.* [61] dispersed carbon black nanoparticles in a liquid crystal elastomer network to produce conductive nanocomposites and promote cell viability by applying electromechanical stimuli. More recently, Lee *et al.* [62] reported on Micro-ElectroMechanical (MEM) 3D-printed switches using conductive poly(lactic acid) with excellent mechanical actuation characteristics. Excellent reviews summarizing all these advances have been recently reported. [40,63–66]

In this work we present a smart approach that synergistically combines the mechanical advantages of free-standing (also named self-supported) poly(lactic acid) (PLA) ultra-thin films and the electrochemical response of anodically polymerized ICP to produce effective multi-layered biomimetic hybrid or Faradaic motors

(artificial muscles). More specifically, free-standing 5-layered films consisting of three nanoperforated PLA (pPLA) ultra-thin films separated by two ICP nanolayers, fulfil the mechanical and electrochemical requirements of both bioapplications.

7.2 Perforated polyester nanomebranes as templates of electroactive and robust free-standing films

Abstract

Robust and flexible free-standing films made of spin-coated poly(lactic acid) (PLA) and poly(3,4-ethylenedioxythiophene) (PEDOT) nanolayers have been prepared. A steel sheet coated with a sacrificial layer of PEDOT:poly(styrenesulfonate) (PSS) and a spin-coated nanolayer of PLA was used as working electrode for the anodic polymerization of 3,4-ethylenedioxythiophene monomer. The latter was only successfully accomplished when rounded-shape nanoperforations of average diameter 49 ± 14 nm were introduced into PLA layers, which was achieved by combining the phase segregation processes undergone by immiscible PLA:poly(vinyl alcohol) (PVA) mixtures with selective solvent etching to remove PVA domains. Nanoperforations allowed the utilization of the semiconducting PEDOT:PSS sacrificial layer to immobilize the electropolymerized PEDOT chains. Morphological and topographical studies show the templating effect of PEDOT layers. In addition of flexibility and mechanical strength, free-standing 5-layered films present good electrochemical activity, evidencing their potential ability to reversibly exchange ions with the medium. These properties offer important advantages with respect to those of neat PLA and supported PEDOT films, as has been illustrated by cell culture and protein adsorption assays. Cell cultures evidenced the superior behaviour of 5-layered films as bioactive platforms for fibroblast and epithelial cells

proliferation, while adsorption assays reflected their potential as selective bioadhesive surfaces for protein separation.

Materials and methods

Materials. PEDOT:PSS 1.3 wt. % dispersion in H_2O, 3,4-ethylenedioxythiophene (EDOT), PVA 87-89% hydrolyzed and lithium perchlorate ($LiClO_4$) were purchased from Sigma-Aldrich (USA). PLA 2002D, a product of Natureworks, was kindly supplied by Nupik International (Polinyà, Spain). According to the manufacturer, this PLA has a D content of 4.25%, a residual monomer content of 0.3%, density of 1.24 g/cm^3, glass transition temperature (T_g) of 58 ºC, and melting temperature (T_m) of 153 ºC. Acetonitrile, chloroform and 1,1,1,3,3,3-hexafluoro-2-propanol (HFIP) were purchased from Panreac Quimica S.A.U. (Spain).

For cell culture experiments, Cos-1 fibroblast-like cells and Vero epithelial cells from African green monkey *(Cercopithecus aethiops)* were purchased from ATCC (USA). Dulbecco's phosphate buffered saline solution (PBS) without calcium chloride and magnesium chloride, Dulbecco's modified Eagle's medium (DMEM, with 4500 mg of glucose/L, 110 mg of sodium pyruvate/L and 2 mM L-lutamine), penicillin-streptomycin**,** *N*-(2-hydroxyethyl)piperazine-*N*′-(2-ethanesulfonic acid) (HEPES) solution (1 M, pH 7.0-7.6), 3-(4,5-dimethylthiazol-2-yl)-2,5-diphenyltetrazolium bromide (MTT, 97.5%) and trypsin-EDTA solution (0.05% trypsin, 0.02% EDTA) were all purchased from Sigma-Aldrich (USA). Fetal bovine serum (FBS) and trypan blue stain (0.4%) were purchased from Gibco, UK. Dimethyl sulfoxide (99.0%) was purchased from Panreac Química

S.A.U. (Spain) and sodium azide (NaN_3, ≥99.5%) from Sigma-Aldrich (USA).

For the protein adhesion assay, Bovine Serum Albumin (BSA) and Lysozyme (Lyz) from chicken egg white were obtained from Sigma-Aldrich. Besides, during the characterization the following reagents were provided by Sigma-Aldrich and used as received: Bradford reagent (Bio-Rad), TEMED (Amresco), coomassie blue, Tris base, sodium dodecyl sulfate and acrylamide/bisacrylamide (30%).

Synthesis of 5-pPLA/PEDOT nanomembrane. The nanofilms were obtained combining the spin-coating technique with an anodic polymerization. Nanoperforated PLA (pPLA) was obtained by blending PLA and PVA with a ratio of 90:10 v/v (PLA:PVA), prepared by mixing PLA (10 mg/mL) and PVA (10 mg/mL) HFIP solutions. Spin-coating was performed using 1200 rpm during 60 s with a spin-Coater (WS-400BZ-6NPP/A1/AR1 Laurell Technologies Corporation).

PEDOT was polymerized by chronoamperometry (CA) under a constant potential of +1.40 V adjusting the polymerization charge to 30 or 270 mC depending on the working area, 1 × 1 or 3 × 2 cm^2, respectively. Electrochemical experiments were conducted at room temperature in a three-electrode cell filled with 40 mL of a 10 mM EDOT solution in acetonitrile containing 0.1 M $LiClO_4$ as supporting electrolyte. Steel AISI 304 sheets, previously washed with water, ethanol and acetone, were employed as working and counter electrodes while Ag|AgCl was the reference electrode.

Five-layered films alternate pPLA and PEDOT ultrathin sheets, so, the composition of such five-layered films was

pPLA/PEDOT/pPLA/PEDOT/ pPLA, hereafter abbreviated as 5-pPLA/PEDOT.

Free-standing nanomembranes (FsNM) were separated from the steel substrate employing PEDOT:PSS as sacrificial layer, which was obtained by spin-coating at same conditions than pPLA. The detachment of the five-layered films from the steel substrate was achieved by selective elimination of the PEDOT:PSS sacrificial layer. Although PEDOT:PSS is not soluble in water, it forms a colloidal dispersion, thus, after immersion into milli-Q water for 12 h, the five-layered films were easily detached from the steel substrate with tweezers.

Characterization of 5-pPLA/PEDOT nanomembrane. Film thickness measurements were obtained by stylus profilometry and wettability by WCA. The morphology of systems without and with cells was analysed by SEM, using a microscope operating at 2 or 5 kV. The diameter of the perforations was measured with the Image J software. The topography was observed by AFM. The row scanning frequency was set to 0.87 or 0.68 Hz, depending on the sample response, and the physical tip sample motion speed was 10 mm/s. RMS roughness (Rq) and profile sections of the images were determined using the statistics application and tools of the NanoScope Analysis software version 1.20 (Bruker), which calculates the average considering all the values recorded in the topographic image with exception of the maximum and the minimum. The scan window sizes were $5 \times 5\ \mu m^2$.

The chemical composition was obtained by FTIR and Raman spectroscopy, while, the behaviour of the nanomembrane in a

biological system was studied by adhesion and proliferation of eukaryotic cells, proteins adsorption and electrophoresis.

Electrochemical characterization by CV were conducted in 0.1 M PBS (pH 7.4) at room temperature. The initial and final potentials were −0.20 V while the reversal potential was +0.60 V. FsNM were directly used as working electrodes in a three-electrodes cell, similar to CA. The electrochemical activity was determined through direct measurement of the anodic and cathodic areas in the control voltammograms using Nova software. Detailed description of all the characterization techniques was included in Chapter 4.

Results and discussion

Deposition of PEDOT layers by *in situ* polymerization of 3,4-ethylenedioxythiophene (EDOT) monomers was considered as an alternative for the modification PLA layers. Although it is an insulating polymer, the diffusion of small and medium size molecules across PLA nanostructures (*i.e.* nanofilms and nanofibers) has been reported, [67] therefore, the PEDOT nanolayer could be successfully obtained. Nevertheless, the thickness and aspect of the ICP film were not homogenous, which represented a significant drawback with respect to films generated directly onto bare steel electrodes. This fact was attributed to the influence of microstructure of the PLA layer interfering during the CA process.

In order to overcome this limitation, a physical modification was introduced in the spin-coated PLA layers. More specifically, PLA layers with nanopores crossing the entire thin-film thickness were prepared using spin-coating combined with phase segregation

processes in immiscible PLA:PVA mixtures and, subsequently, removing PVA domains via solvent etching. [11] This process, which is schematically illustrated in Scheme 7.2.1a, was achieved by spin-coating mixtures of PLA and PVA solutions in 1,1,1,3,3,3-hexafluoro-2-propanol (HFIP). Besides, 5-pPLA/PEDOT films were prepared by combining such process with the CA of EDOT, as is shown in Scheme 7.2.1b.

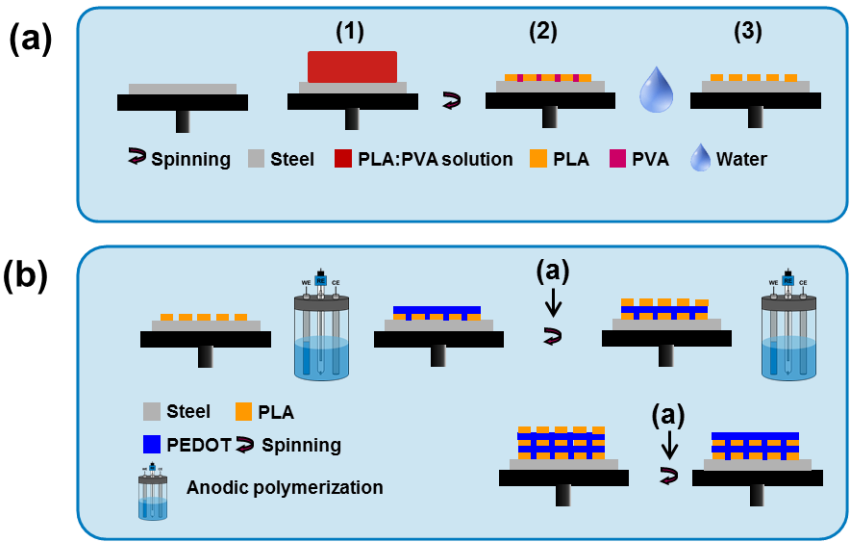

Scheme 7.2.1 (a) Diagram of the three-step procedure used to prepare the nanoperforated PLA films: (1) dropping of the 90:10 PLA-PVA mixture onto a steel substrate; (2) spin-coating of the PLA-PVA mixture; and (3) etching of PVA using milli-Q water. (b) Illustration of the preparation of 5-pPLA/PEDOT films. This consists in the alternation of perforated PLA layers, which were prepared as described in the three-step procedure of (a), and the deposition of PEDOT layers by CA.

5-pPLA/PEDOT characterization. Figure 7.2.1b displays a representative SEM micrograph and both 3D topographic and height AFM images of the nanoperforated PLA film spin-coated onto a steel

substrate. The average diameter of the nanoperforations, which are rounded-shape, is 49 ± 14 nm as determined from SEM micrographs. The root-mean-square roughness (Rq) increased from 1.7 ± 0.2 nm for non-perforated PLA (Figure 7.2.1a) to 6 ± 1 nm after removal of PVA domains via selective solvent etching, while the thickness increases from 110 ± 8 and 114 ± 11 nm.

The electropolymerized EDOT onto the first perforated PLA layer resulted in a cohesive bilayer with the ICP adhered to the polyester (Figure 7.2.1c). This is also evidenced in Figure 7.2.2a, which shows a micrograph of an intentionally scratched 2-layered film to observe both, the PLA and PEDOT sides. On the other hand, Figure 7.2.1c-f successively display the surface morphology and topography of the 2th (PEDOT), 3rd (perforated PLA), 4th (PEDOT) and 5th (perforated PLA) layers. As it can be seen, the shape and diameter of the nanoperforations are affected by the PEDOT intermediate layers. Specifically, nanoperforations becomes bigger (76 ± 27 and 103 ± 40 nm for the 3rd and 5th layer, respectively) and more irregular than in the 1st layer. These observations have been attributed to surface morphology of PEDOT layers, which affects the distribution of PLA:PVA phases during the spin-coating process. Thus, PEDOT presents a globular morphology in which the ICP chains grow forming small clusters that affect the size of PVA nanophases during the spin-coating of the PLA:PVA mixture. Obviously, the globular morphology of PEDOT, which presents a Rq substantially higher than that of spin-coated PLA, affects the 3rd and 5th layers (Figure 7.2.2b). Thus, the Rq of PLA layers increases from 6 ± 1 nm (1st) to 90 ± 14 and 103 ± 9 nm (3rd and 5th, respectively). The progressive enhancement of this

template effect correlates with the Rq of the 2nd and 4th PEDOT layers (138 ± 17 and 312 ± 14 nm, respectively).

Figure 7.2.2c displays the thickness of each layer in the 5-pPLA/PEDOT determined by scratching the films and measuring the step values with AFM and contact profilometry, respectively. As it can be seen, the two methodologies provide consistent results. The thickness of the whole 5-layered film is around 0.7 μm, which is distributed in ~ 0.4 μm and ~ 0.3 μm for the two PEDOT and three PLA layers, respectively. Interestingly, the thickness the 3rd and 5th PLA layers decrease by ~ 20% with respect to the 1st layer, which has been also attributed to the template effect exerted by PEDOT globules.

The water contact angle (WCA) was determined for each layer of 5-pPLA/PEDOT films supported onto steel (Figure 7.2.2d). Results indicate that the poor hydrophilicity of PLA, which exhibits WCA values relatively close to 90º (*i.e.* from 78º ± 4º to 84º ± 5º) and the very remarkable hydrophilicity of PEDOT (*i.e.* 46º ± 6º and 49º ± 8º for the 2nd and 4th layer, respectively) are practically independent of the layer. Besides, the effect of nanoperforations in the reduction of wettability is small, the WCA of non-perforated PLA films was found to be 72º ± 4º.

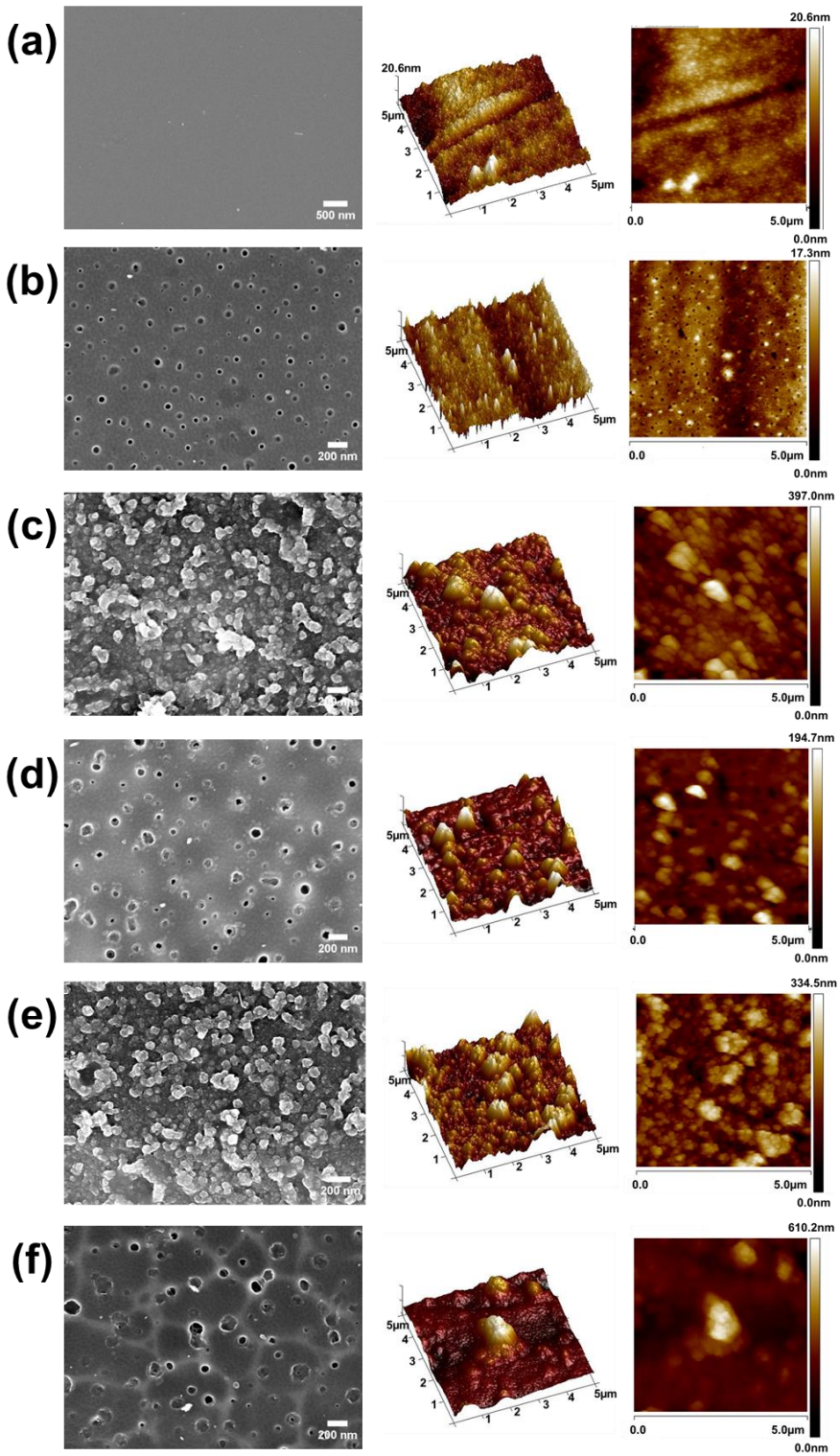
(a)
500 nm
20.6nm
5µm
5µm
20.6nm
0.0
5.0µm
0.0nm
(b)
200 nm
17.3nm
5µm
5µm
0.0
5.0µm
0.0nm
(c)
397.0nm
5µm
5µm
0.0
5.0µm
0.0nm
(d)
200 nm
194.7nm
5µm
5µm
0.0
5.0µm
0.0nm
(e)
200 nm
334.5nm
5µm
5µm
0.0
5.0µm
0.0nm
(f)
200 nm
610.2nm
5µm
5µm
0.0
5.0µm
0.0nm

Figure 7.2.1 High resolution SEM micrograph (left), 3D topographic and height AFM images (center and right, respectively) of (a) non-perforated PLA and each layer in 5-pPLA/PEDOT films: (b) 1st PLA layer; (b) 2nd PEDOT layer; (c) 3rd PLA layer; (d) 4th PEDOT layer; and (e) 5th PLA layer.

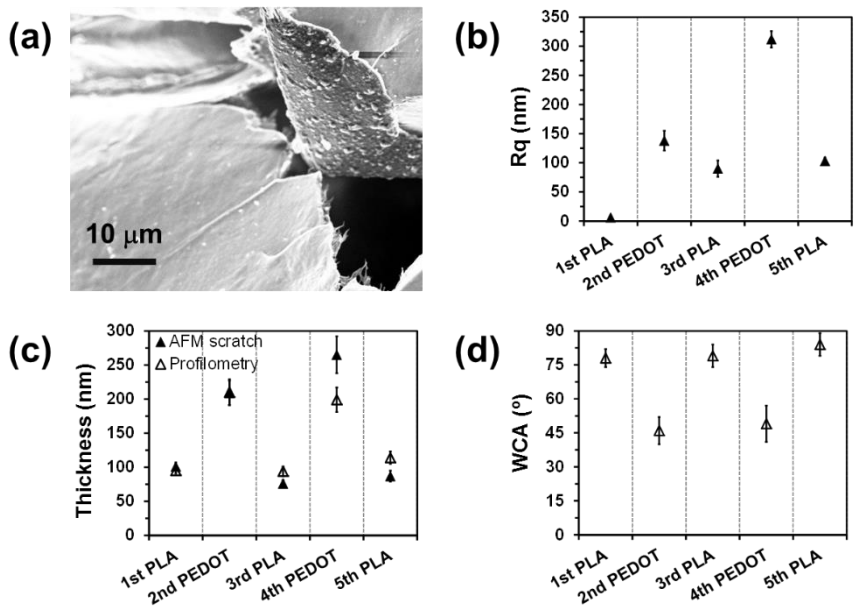

Figure 7.2.2 (a) SEM micrograph showing the two sides of an intentionally scratched 2-layered film made by EDOT electropolymerization onto a spin-coated PLA layer with nanoperforations. (b) Root-mean-square roughness (Rq), (c) thickness and (d) water contact angle (WCA) of each layer in 5-pPLA/PEDOT films. The thickness was determined by both profilometry and AFM scratching.

The preparation of FsNM required the utilization of a sacrificial layer onto the steel substrate, which will be subsequently dissolved to detach the 5-layered film as was explain in Scheme 7.2.2. Although PVA is typically used as sacrificial layer because of its solubility in water, in this case its utilization was not feasible. Insulating PVA precluded the CA of EDOT for the 2nd PEDOT layer, hindering the action of the steel working electrode in the CA process. In order to

overcome this drawback, a water dispersion of PEDOT:PSS was employed to prepare an electroactive sacrificial layer onto the steel sheet by spin-coating. The thickness and Rq of this sacrificial layer, which was obtained applying a spinning speed of 1200 rpm for 60 s, was 163 ± 3 and 7 ± 1 nm, respectively. Furthermore, it was not detected incompatibility between hydrophilic PEDOT:PSS (WCA: 36º ± 5º) and hydrophobic PLA when the 90:10 PLA:PVA v/v mixture was spin-coated onto the sacrificial layer due to the beneficial hydrophilicity of PVA.

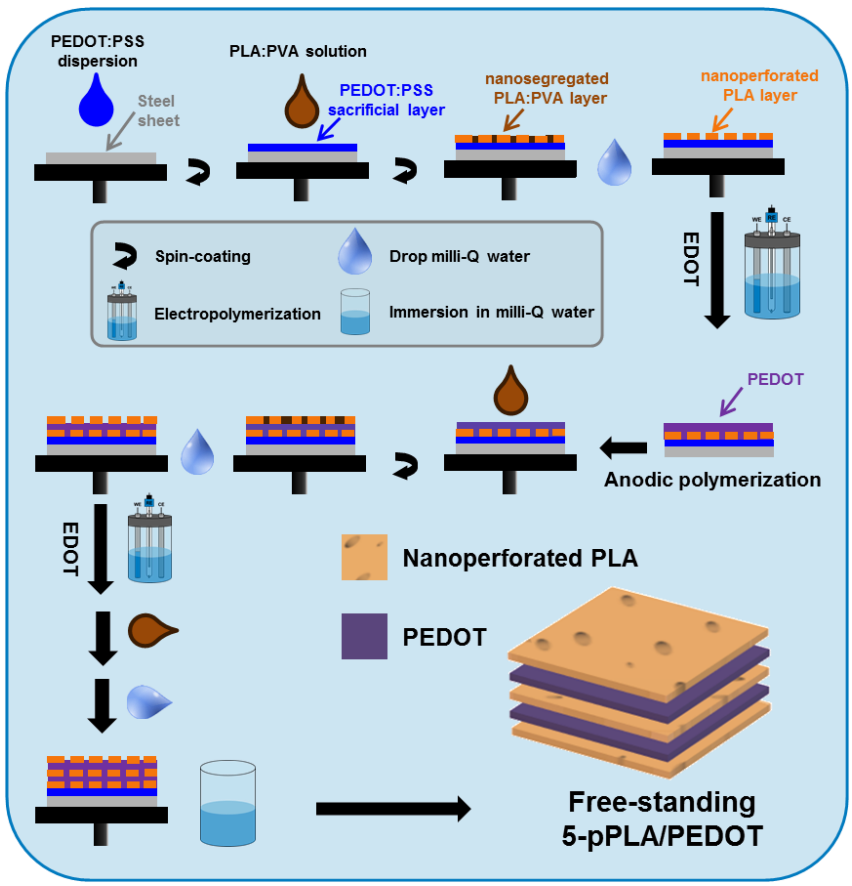

Scheme 7.2.2 Preparation route of 5-pPLA/PEDOT free-standing nanomembrane.

The deposition of the three nanoperforated PLA layers and the two PEDOT layers was performed as was illustrated previously (Scheme 7.2.1). PVA etching after spin-coating the PLA:PVA mixture was carried out by covering the surface of the layer with a drop of milli-Q water avoiding any undesired effect in the stability of the PEDOT:PSS sacrificial layer. Photographs displaying the aspect of the film after the deposition of each spin-coated or anodically polymerized layer are provided in Figure 7.2.3a, while a 5-pPLA/PEDOT of 1 cm^2 area is shown in Figure 7.2.3b. Detachment of the 5-pPLA/PEDOT film from the steel substrate was achieved by immersion into milli-Q water for 12 h. After this time, a pair of tweezers was used to completely detach the 5-layered film.

Free-standing 5-pPLA/PEDOT films are very flexible and robust, their folding into small shapes was an easy process. This is evidenced in Figure 7.2.3c, which show digital camera images of the aspiration of a film with an area of 1 cm^2 floating in water into a pipette with a tip diameter of 1 mm. As it can be seen, the film is completely introduced into the pipette due to its outstanding flexibility. After it release into a solvent, the film recovers its shape immediately, without need of any manipulation. This aspiration/shape recovery process can be repeated more than five times without producing any damage in the film.

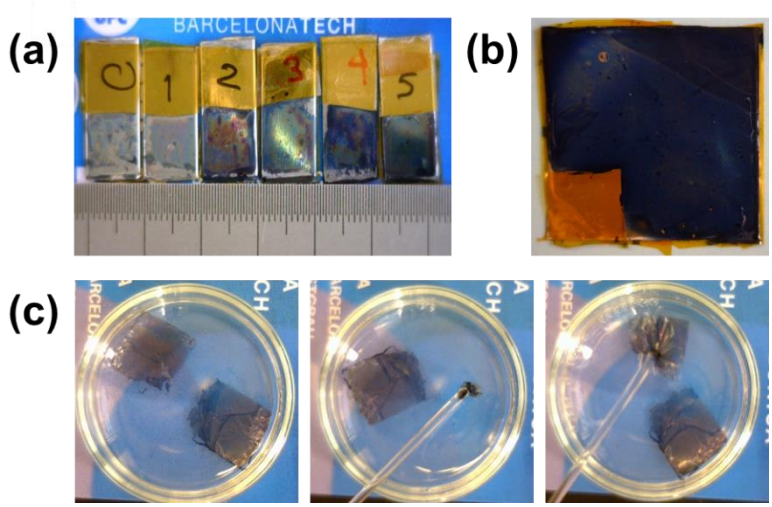

Figure 7.2.3 Digital camera images displaying: (a) a 5-pPLA/PEDOT film growing layer-by-layer (layer 0 refers to the sacrificial PEDOT:PSS layer); (b) a supported 5-pPLA/PEDOT film with area of 1 × 1 cm^2; (c) a free standing 5-pPLA/PEDOT film floating in water (left), its aspiration into a pipette (center) and the aspect of the film when it released from the pipette, recovering its initial shape.

The chemical composition was studied by FTIR and Raman spectroscopy. As it was expected, the FTIR spectra of PEDOT:PSS and anodically polymerized PEDOT are relatively similar, Figure 7.2.4a-b. Indeed, differences between them come from the dopant anions (PSS and ClO_4^-, respectively), which causes not only the apparition of their absorption bands but also a small shift in the ICP bands. However, in both cases characteristic bands from PEDOT are detected: the stretching modes of C=C in the thiophene ring at ~ 1527 cm^{-1}, the C–O–C vibrations at ~ 1230 and ~ 1040 cm^{-1}, and the stretching of the C–S bond in the thiophene ring at ~ 845 and ~ 680 cm^{-1}. On the other hand, the C=O stretching vibration at 1750 cm^{-1} and the asymmetric and symmetric C–O stretching at 1180 and 1085 $cm^{-1,}$ respectively, are the more intense bands of

nanoperforated PLA, Figure 7.2.4c. The spectrum recorded for multi-layered 5-pPLA/PEDOT film (Figure 7.2.4d) contains the characteristic bands of both PEDOT and PLA, corroborating the presence of both insulating and conducting layers.

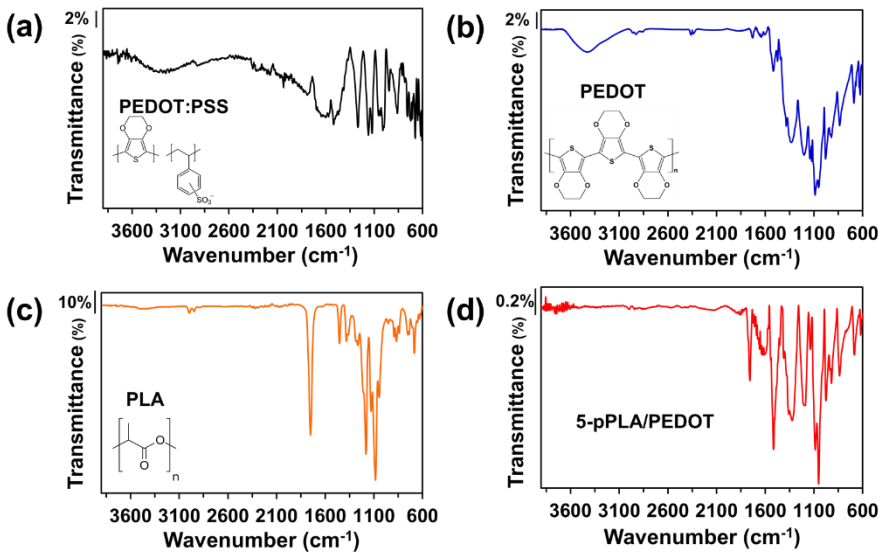

Figure 7.2.4 FTIR spectra of (a) neat PEDOT:PSS, (b) electropolymerized PEDOT, (c) nanoperforated PLA and (d) 5-pPLA/PEDOT.

Raman spectroscopy of the whole 5-pPLA/PEDOT system is provided in Figure 7.2.5, which displays the spectra of the film as it grows layer-by-layer from the sacrificial layer to the 5th PLA layer. The Raman fingerprints of PEDOT were reported in previous studies.[68,69] The main vibrational mode of PEDOT layers at 1424 cm^{-1}, the less intense band at 1364 cm^{-1}, and the shoulder at 1490 cm $^{-1}$ correspond to the symmetric $C_\alpha=C_\beta$ stretching, $C_\alpha–C_{\alpha'}$ inter-ring stretching vibrations, and asymmetric $C_\alpha=C_\beta$ stretching, respectively. Other important bands appear at 856 and 991 cm^{-1} which have been

attributed to the asymmetric C–S–C deformation (thiophene ring) and C–O–C ether ring deformation (ethylenedioxy group), respectively. Furthermore, the intensity of these fingerprint bands increases with the number of PEDOT layers, confirming the successful incorporation of electrochemically polymerized PEDOT.

Raman spectra of PLA layers are highly similar to those of PEDOT layers (Figure 7.2.5) due the lower content of the former polymer (*i.e.* the thickness of PLA layers was 2-3 times smaller than that of PEDOT layers, as shown in Figure 7.2.2c), and the superposition of the most characteristic bands was observed. Furthermore, the predominance of PEDOT bands in the 5-layered system can be also attributed to the resonance Raman effect, which increases the intensity of the bands of the material when the laser energy coincides with the frequency of the electronic transition of the sample. [70,71]

Adhesion and proliferation of cells. In order to examine the effects in the biocompatibility of the possible synergies between PLA and PEDOT layers, Cos-1 and Vero cells, which are green monkey kidney fibroblast and epithelial cells, respectively, were used for cell adhesion and cell proliferation studies conducted on PLA and PEDOT films supported on steel, 5-pPLA/PEDOT and bare steel sheets (control). Figure 7.2.6a shows that, in appearance, adhesion of cells preferably occurs onto PLA and 5-pPLA/PEDOT films, even though differences are statistically unmeaning (Student's T-test with $p < 0.05$). Figure 7.2.6b indicates that cell proliferation is slightly greater for supported PEDOT and 5-pPLA/PEDOT than for bare steel sheets and nanoperforated PLA films, even though significant differences with *p*-values lower than 0.05 were not detected when the Student's T-test

was applied. These results reflect that 5-pPLA/PEDOT films are able to capture the advantages of both PLA and PEDOT (*i.e.* mechanical strength and ability to exchange ions with cells, respectively).

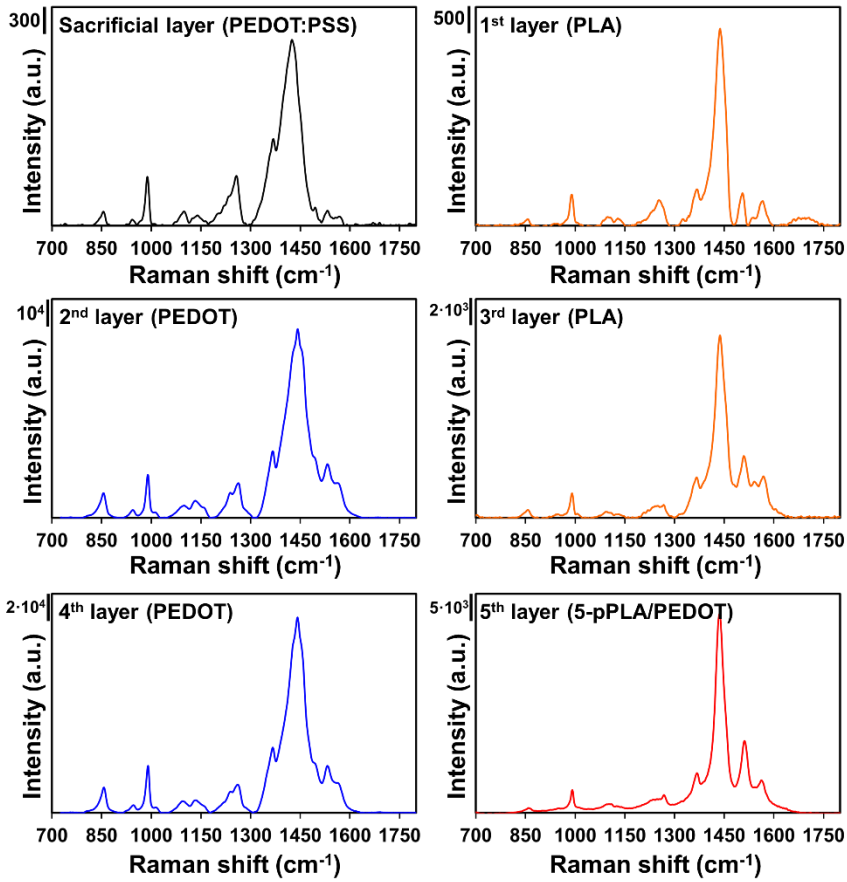

Figure 7.2.5 Raman spectra of the 5-pPLA/PEDOT films as it grows layer-by-layer.

On the other hand, micrographs of the films cultured for 24 hours and 7 days are displayed in Figure 7.2.6c. It is worth noting that in all cases cells exhibited a healthy morphology in terms of shape and appearance (*i.e.* no sign of detachment of the cells from the substrate was detected). Cos-1 cells display elongated shapes and are spindle-

shaped (bipolar) or stellate-shaped (multipolar), whereas Vero cells show more regular dimensions and grow attached to the substrate in discrete patches.

These *in vitro* cell assays evidence that PLA and PEDOT containing 5-layered favours the growth of fibroblast and epithelial cells by combining the best properties of each individual polymer in a single bioplatform.

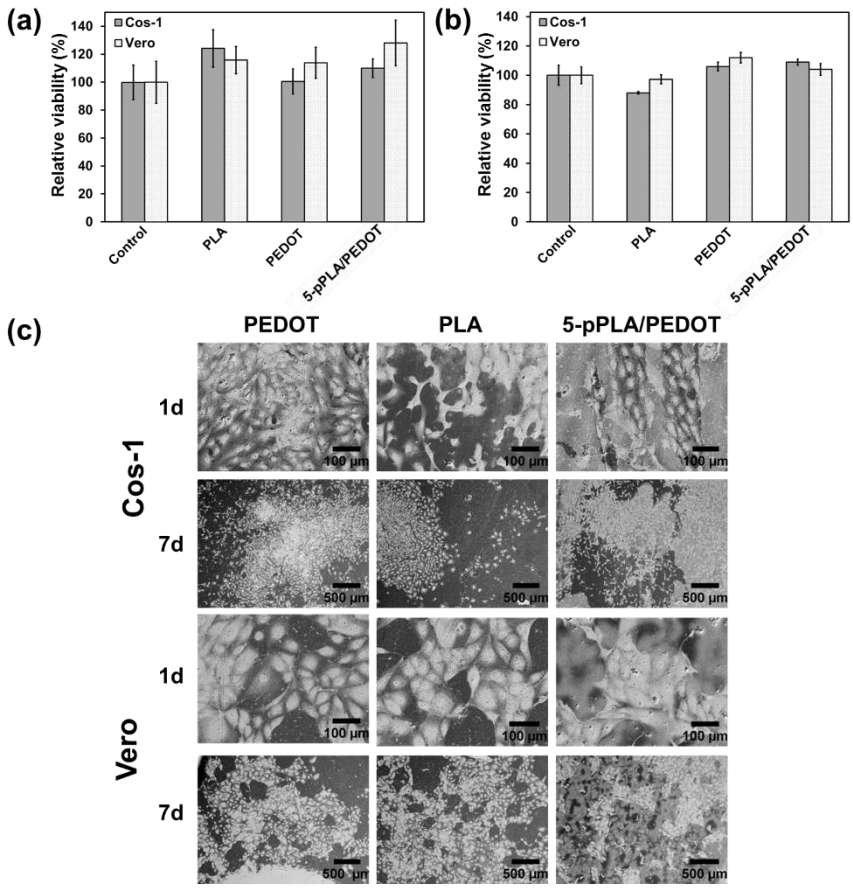

Figure 7.2.6 MTT evaluation of Cos-1 and Vero cells cultured on steel sheets (control), PLA, PEDOT and 5-pPLA/PEDOT films for (a) 24 h and (b) 7 days. Values are the mean and bars indicate their standard deviation. (c) Micrographs of the Cos-1 and Vero cells cultured on the different substrates after 24 h and 7 days.

Protein adsorption. In order to evaluate the ability of 5-pPLA/PEDOT to interact with different proteins, adsorption assays were conducted using bovine serum albumin (BSA) and lysozyme (Lyz) proteins, carefully chosen because of their different molecular weights and, especially, charges (BSA: M_w = 66.5 kDa, isoelectric point in water at 25 ºC = 4.7; Lyz: M_w = 14.3 kDa; isoelectric point = 11.3). Three replicates of bare steel sheets (used as control), PLA, PEDOT and 5-pPLA/PEDOT films supported on steel were immersed during 24 hours in a 0.5 mg/mL BSA or Lyz protein solution.

Figure 7.2.7a display the protein concentration onto the different surfaces measured by Bradford protein assay. As can be seen, the adsorption of both BSA and Lyz proteins was significantly higher on the membrane than on PLA and PEDOT films and the control. This has been attributed to the surface roughness (Rq = 103 ± 9, 6 ± 1, 376 ± 34 and 11 ± 2 nm for 5-pPLA/PEDOT, PLA, PEDOT and steel, respectively), which intrinsically favours the adherence of not only small proteins, like Lyz, but also of large biomolecules, such as BSA. Moreover, as it was expected, 5p-PLA/PEDOT are highly selective favouring the adsorption of the most charged protein, Lyz. Thus, oxidized PEDOT chains located at the nanoperforations prefer charge proteins while non-polar PLA tends to adsorb both BSA and Lyz. Consequently, the amount of Lyz is 56% higher than that of BSA. These results indicate that the combination of surface roughness and the controlled distribution of PEDOT chains, which can be regulated through the size of the nanoperforations (*i.e.* by the composition of the PLA:PVA mixture), [11] is a suitable strategy for the separation of charged proteins.

These results were corroborated using gel electrophoresis assays. The electrophoretogram of the proteins adhered onto the 5-pPLA/PEDOT is displayed in Figure 7.2.7b. Lane 2 and 3 shows a typical band corresponding to the a BSA control and the proteins adhered to 5-pPLA/PEDOT after 24 of incubation. Similar results were observed in Lane 4 and 5 which correspond to Lyz control and sample, meanwhile, the Lane 6 exhibit both bands (BSA and Lyz) as a result of the incubation in the presence of both proteins.

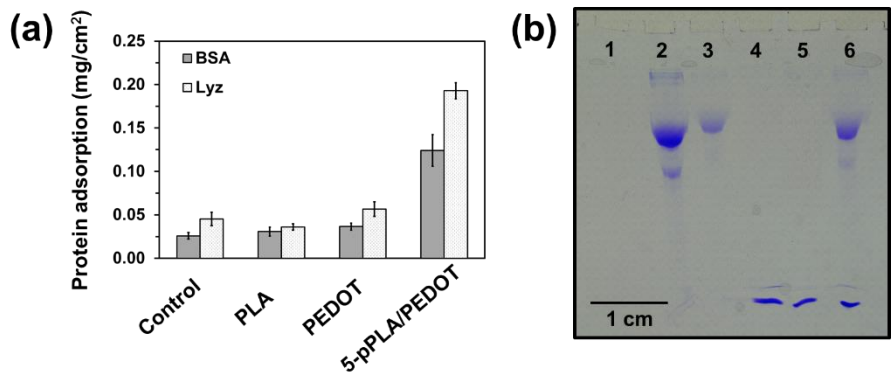

Figure 7.2.7 Adsorption (in %) of BSA and Lyz onto the surface of bare steel (control), PLA and PEDOT films supported on steel, and free standing 5-pPLA/PEDOT films after incubation for 24 h at room temperature. Values are the mean and bars indicate their standard deviation. The asterisk (*) indicates a significant difference with the control when the Student's T-test is applied ($p < 0.05$). (b) Electrophoretogram showing: the nanomembrane as a control (lane 1); BSA reference (lane2); BSA adsorption onto 5-pPLA/PEDOT (lane3); Lyz reference (lane 4); Lyz adsorption onto 5-pPLA/PEDOT (lane 5); BSA and Lyz adsorption onto 5-pPLA/PEDOT (lane 6).

Electroactivity of 5-pPLA/PEDOT FsNM. ICPs are considered smart materials in the world of biomedicine since they allow electrical and electrochemical stimulation for the detection of bioanalytes, the controlled release of drug or in the transport of signal through neural

implants, among others. [72] From a biotechnological point of view, ICPs are not only appropriate to stimulate nerve cells, which are specialized in receiving and transmit electrical stimuli, but also to enhance the viability of conventional cell types without the need of externally controlled stimuli. [9,72,73] This has been typically attributed to the intrinsic ability of CPs to exchange ions with the cell through its membrane, enhancing of the cell metabolism and promoting cell adhesion and proliferation. The ability of ICPs to exchange ions is measured by determining their electrochemical activity, which evaluates the facility of dopant ions to access and escape from the polymeric matrix upon oxidation and reduction processes, respectively.

Figure 7.2.8a displays the control cyclic voltammogram recorded for the 5-pPLA/PEDOT FsNM in a three-electrode cell with PBS 0.1M (pH 7.4) as electrolyte solution. The electroactivity, which is estimated from the area of the voltammogram, remains practically unaltered after 20 consecutive oxidation-reduction cycles, as is evidenced by the overlapping with the control voltammogram (Figure 7.2.8a). These results have been attributed to the conducting channels created by PEDOT layers, which can be appreciated as light shadows below PLA outer layer in the SEM micrographs shown in Figures 7.2.1d and 7.2.1f.

On the other hand, the effect produced by the adsorption of proteins in the electrochemical activity of the 5-pPLA/PEDOT FsNM is displayed in Figure 7.2.8b. As it was expected, the area of the voltammograms decreased significantly after the adsorption of BSA and, especially, Lyz. Moreover, the reduction of the cathodic current

density at the initial/final potentials is more pronounced when the adsorbed protein is Lyz than BSA, even though it noticeable for both proteins. These results are consistent with the higher affinity of the ICP phases, which are accessible through the nanoperforations of the outer PLA layer, towards Lyz, supporting the observations reported in Figure 7.2.7.

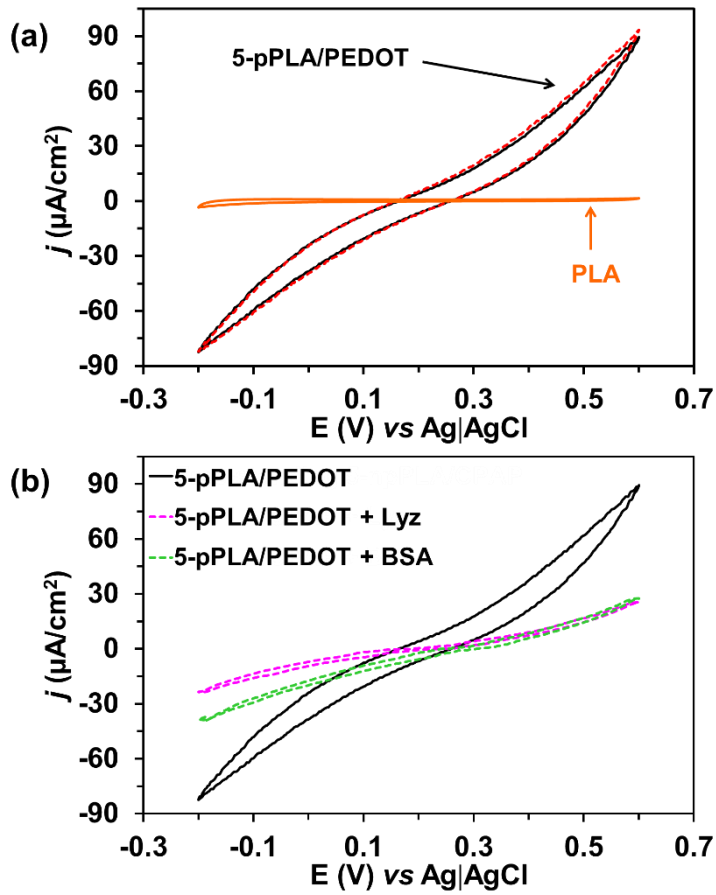

Figure 7.2.8 (a) First control voltammogram (solid black line) and voltammogram after 20 consecutive oxidation–reduction cycles (dashed red line) for 5-pPLA/PEDOT FsNM. (b) Cyclic voltammogram recorded for the 5-pPLA/PEDOT FsNM after 24 h incubation in 0.5 mg/mL BSA (dashed green line) or Lyz (dashed pink line) protein solution. In all cases, voltammograms were recorded in a 0.1M PBS solution (pH 7.4) using a scan rate of 100 mV/s. Initial and final potentials: −0.20 V; reversal potential: +0.60 V.

Conclusions

Although electropolymerized PEDOT presents excellent properties (*e.g.* high electrochemical activity and environmental stability), its mechanical consistency is null, disintegrating into powder when the film is detached from the support used as working electrode in a CA process. In this work we propose a new strategy to produce flexible, robust and electroactive free-standing multilayered films combining PLA, which provides mechanical strength, and *in situ* electropolymerized PEDOT. The novelty of this approach lies in: (*i*) the semiconducting nature of the PEDOT:PSS sacrificial layer, and (*ii*) the nanoperforations of the PLA layers, which enable the access of EDOT monomers to the semiconducting sacrificial layer or to the previously electropolymerized PEDOT layer. The synergistic interaction between the two polymers plays a pivotal role in 5-pPLA/PEDOT, which preserve the mechanical properties of PLA and the good electrochemical activity of PEDOT. Finally, cell culture and protein adsorption assays have shown that 5-pPLA/PEDOT behave as bioactive platforms for cell proliferation and as bioadhesive surfaces for protein separation, respectively. It is expected that, after further optimization, 5-pPLA/PEDOT FsNM will be suitable for many other promising technological applications due to the advantageous properties of their two components.

7.3 Free-standing flexible and biomimetic hybrid nanomembranes for ions and ATP transport

Abstract

The transport of metabolites across robust, flexible and free-standing biomimetic membranes made of three perforated poly(lactic acid) (pPLA) layers, separated by two anodically polymerized conducting layers of poly(3,4-ethylenedioxythiophene-*co*-3-dodecylthiophene), and functionalized on the external pPLA layers with a voltage dependent anion channel (VDAC) protein, has been demonstrated. The three pPLA layers offer robustness and flexibility to the bioactive platform and the possibility of obtaining conducting polymer layers by *in situ* anodic polymerization. The incorporation of dodecylthiophene units, which bear a 12 carbon atoms long linear alkyl chain, to the conducting layers allows to mimicking the amphiphilic environment offered by lipids in cells, increasing 32% the efficiency of the functionalization. Electrochemical impedance measurements in NaCl and adenosine triphosphate (ATP) solutions prove that the integration of the VDAC porin inside the PLA perforations considerably increases the membrane conductivity and is crucial for the electrolyte diffusion. Such results open the door for the development of advanced sensing devices for a broad panel of biomedical applications.

Materials and methods

Materials. Poly(3,4-ethylenedioxythiophene)–poly(styrene-sulfonate) (PEDOT:PSS) 1.3 wt. % dispersion in water, 3,4-

ethylenedioxythiophene (EDOT) and 3-dodecylthiophene (3DT) monomers, poly(vinyl alcohol) (PVA) 87-89% hydrolyzed and lithium perchlorate ($LiClO_4$) were purchased from Sigma-Aldrich (USA); $LiClO_4$ was stored at 80 °C before its use. PLA 2002D pellets were supplied by Nupik International (Polinyà, Spain). Acetonitrile and hexafluoroisopropanol (HFIP) were purchased from Panreac Quimica S.A.U. (Spain).

Synthesis of PEDOT and COP. Both poly(3,4-ethylenedioxythiophene) (PEDOT) and poly(3,4-ethylenedioxythiophene-*co*-3-dodecylthiophene) (COP) were prepared by anodic polymerization through a chronoamperometry (CA) in a three-electrode cell filled with a 0.1 M $LiClO_4$ acetonitrile solution containing 10 mM EDOT for PEDOT or 7 mM EDOT + 3 mM 3DT for COP. In both cases, a constant potential of +1.40 V was applied and the polymerization charge was adjusted to 30 mC for a working area of 1 cm^2. Polished steel AISI 304 sheets (1 × 1 cm^2) were employed as working and counter electrodes, while the reference electrode was an Ag|AgCl standard electrode (KCl 3 M).

Synthesis of 5-pPLA/PEDOT and 5-pPLA/COP FsNM. Films containing 3 layers of pPLA separated by 2 layers of PEDOT or COP were prepared by combining the spin-coating and the anodic polymerization (CA) techniques, following the procedure reported in Section 7.2. In brief, a steel sheet (AISI 304) of 3 × 3 cm^2 was coated with a sacrificial layer of PEDOT:PSS by spin-coating deposition (1200 rpm for 60 s). Then, a PLA:PVA layer was generated onto the sacrificial layer by spin-coating (1200 rpm for 60 s) a 80:20 v/v mixture of PLA (10 mg/mL) and PVA (10 mg/mL) HFIP solutions.

The perforated PLA layer (pPLA) was obtained by removing the PVA domains via water etching. The resulting PEDOT:PSS/pPLA bilayer was used as working electrode for the anodic polymerization of PEDOT or COP doped with ClO_4^-, as described before. Afterwards, the following pPLA, PEDOT or COP layers were obtained by iterating this procedure. Then, 5-layered films of composition pPLA/PEDOT/pPLA/PEDOT/pPLA (5-pPLA/PEDOT) and pPLA/COP/pPLA/COP/pPLA (5-pPLA/COP), still supported onto the PEDOT:PSS-coated steel substrate, were achieved. These supported membranes were easily detached from the metallic substrate by selective elimination of the PEDOT:PSS sacrificial layer. This was achieved by submerging the supported membranes into milli-Q water for 24 h. Finally, 5-layered membranes were completely detached from the steel substrate with the help of tweezers, and converted into self-supported multi-layered films.

Expression and purification of the VDAC protein. *Escherichia coli* BL21 (DE3) bacteria were transformed to produce 6 His-tagged VDAC36 proteins in inclusion bodies. Bacteria were then lysed and centrifuged to obtain the final pellet corresponding to the non-native proteins. VDAC36, solubilized in 20 mM phosphate pH 8, 1% (w/v) sodium dodecyl sulphate (SDS), was then purified by Ni^{2+} affinity column. VDAC36 was eluted and the buffer was exchanged to the refolded buffer (20 mM phosphate, 60 mM SDS and 1.5 M 2-methyl-2,4-pentanediol (MPD)) with a PD10 desalting column.

Functionalization of 5-pPLA/PEDOT and 5-pPLA/COP membranes. In order to integrate the porin, the VDAC36 protein was incubated with the free-standing 5-pPLA/PEDOT and 5-pPLA/COP

membranes. Films were placed in 1 mL of a protein solution, which contained 0.85 mg/mL VDAC36, 60 mM SDS and 1.5 M MPD, for 12 h at room temperature. The resulting 5-pPLA/PEDOT/VDAC and 5-pPLA/COP/VDAC functionalized membranes were rinsed three times with milli-Q water to remove residues. Blank (non-functionalized) 5-pPLA/PEDOT and 5-pPLA/COP membranes were obtained using the same solution (*i.e.* 60 mM SDS and 1.5 M MPD) but without VDAC36.

The concentration of immobilized protein was determined using a UV–vis Cary 100 Bio spectrophotometer (Agilent, USA) and a 1 cm length quartz cuvette. The absorbance from 250 to 300 nm was recorded for the protein solutions before and after incubation with the polymeric membranes. The spectra for the solutions after incubation were corrected by subtracting the spectra of the rinsing solutions.

Characterization of FsNM and FsNM functionalized with VDAC.

In order to evaluate the effect of the alterations made in the membranes of Section 7. 2, was necessary to observe the morphology by SEM, study the wettability thru WCA and measure the film thickness and roughness by stylus profilometry. Besides, FTIR (KBr pellets) and XPS of the functionalized films were performed. More information about the characterization techniques and instruments used can be found in Chapter 4.

Electrochemical measurements. The electroactivity and electrostability of the new platforms were studied by cyclic voltammetry (CV) through direct measure of the anodic and cathodic areas in the control voltammograms. A three-electrode cell composed by the free-standing NM as working electrode (WE), platinum wire as

counter-electrode, and a reference electrode of Ag|AgCl (KCl, 3M), was used. More specifically, the free-standing film was hold by an alligator pinch electrode clip and immersed in the electrolyte solution. The surface of film immersed in the solution was 1 cm^2, while the pinch was not in contact with the solution. The electrolyte solution was composed of 0.1 M phosphate buffer saline (PBS) solution (pH 7.4). The initial and final potential was –0.20 V, while the reversal potential was 1.00 V. A scan rate of 50 mV/s was used in all cases. All experiments were repeated three times.

Electrochemical impedance spectroscopy (EIS) measurements were performed using a conventional three-electrode cell and an AUTOLAB-302N potentiostat/galvanostat operating between the frequency range of 10^5 Hz and 10^{-2} Hz and 10 mV of amplitude for the sinusoidal voltage. All experiments were performed at room temperature with 5-layered free-standing membranes. For the EIS assays the electrolyte solutions were: 0.5 M NaCl, 0.05 M ATP and 0.1 M ATP. Platinum wire was used as counter-electrode, whereas Ag|AgCl saturated (KCl 3M) was employed as reference electrode.

Results and discussion

The previous section reported a strategy to produce flexible, robust and electroactive free-standing 5-layer films combining PLA and, the ICP, PEDOT. The combination of surface roughness and the affinity of the ICP phases, which are accessible through the nanoperforations of the outer PLA layer, towards charged protein exhibited an interesting ability as bioadhesive surface for proteins. Thus, this work proposes to improve this ability altering the membrane with bigger

perforation sizes in the outer PLA layer and incorporating dodecylthiophene units, which mimick the amphiphilic environment offered by lipids in cells.

PLA was chosen because of the suitability of this material to prepare perforated layers. [11] Indeed, perforated layers are obtained by selecting two polymers, which are used to induce phase-segregation processes, and by removing the less abundant one by solvent etching. In order to be successful, the two selected polymers should satisfy the following conditions: (*i*) the two polymers must be immiscible to induce phase segregation processes; (*ii*) the molecular weight should be similar to promote the formation of nano/micro-features (*i.e.* avoiding that the less abundant polymer acts in another way, for example as plasticizer); (*iii*) the polymer used to remain in the layer must be insoluble in water, which is the solvent used in this work to remove the less abundant polymer and the sacrificial layer, and to immobilize the VDAC protein at the perforations of the external layers (*e.g.* the utilization of PVA as the most abundant polymer is precluded because of its solubility in water); and (*iv*) the two polymers used to fabricate the perforated layer must be soluble in a common solvent to facilitate the spin-coating process. Previous studies showed that PLA satisfies all the conditions while other polymers, like poly(ethylene glycol) (PEG), fails in some of them (*e.g.* PEG does not favour phase segregation processes because it does not produce enough instabilities at the polymer–polymer interfaces). [11]

Supported 5-pPLA/PEDOT and 5-pPLA/COP free-standing membranes were prepared by alternating spin-coated pPLA and electropolymerized conducting PEDOT or COP layers, as described in

the above. When spin-coating the 1st pPLA layer of pPLA onto the PEDOT:PSS sacrificial layer (thickness: 302 ± 3 nm), the strategy of using two immiscible polymers (PLA:PVA, 80:20 v/v) resulted in the formation of segregated pseudo-spherical domains, as shown in Figure 7.3.1a. Afterwards, PVA domains were successfully removed by solubilizing them in water, perforations of 462 ± 219 nm in diameter were achieve (Figure 7.3.1b). It is worth noting that the formation of biggest perforations was designed to facilitate the electropolymerization of the 2nd conducting layer (*i.e.* the access of the EDOT and 3DT monomers to the conducting PEDOT:PSS sacrificial layer, which acts as working electrode in the electropolymerization) and to increase the adhesion of VDAC protein.

The surface morphologies of PEDOT and COP films are compared in Figures 7.3.1c-d, respectively. As shown in SEM micrographs, both materials exhibit a typical coral-like morphology suggesting that the distribution of EDOT and 3DT units in COP chains is very homogeneous. The surface morphology of PEDOT and COP in the 2nd layers (Insert on Figures 7.3.1c-d, respectively), is very similar to that displayed by the CPs directly generated onto steel substrates (Figures 7.3.1c-d). This demonstrates that perforations were successfully formed by phase segregation in the 1st pPLA layer, allowing a homogeneous electropolymerization.

SEM micrographs of the 3rd pPLA layer deposited onto the 2nd PEDOT and COP layers (not included), showed rounded-shape perforations with an average diameter of 232 ± 127 nm and 245 ± 96 nm, respectively. The 4th PEDOT and COP layers were successfully generated onto the 3rd PLA layer, resulting in a similar morphology

that the one displayed in the inserts of Figures 7.3.1c-d. This was the evidence that EDOT and/or 3DT monomers were able to access the ICP chains deposited in the 2nd layer through the perforations of the 3rd pPLA layer.

Figures 7.3.1e-f show the morphology of the outer pPLA layer (*i.e.* the fifth layer of the 5-pPLA/PEDOT and 5-pPLA/COP bioactive membranes). In this case the average diameter of the perforations increased to 403 ± 294 nm and 321 ± 150 nm, respectively. The diameter of the perforations in the 3rd and 5th pPLA layers is affected by the morphology and topography of the previous ICP layers. Indeed, the diameter of the perforations is smaller in 5-pPLA/COP than in 5-pPLA/PEDOT since the surface roughness is lower for COP layers than for PEDOT layers. Besides, the 4th COP or PEDOT layer can be observed through the perforations of the outer pPLA layer in Figures 7.3.1e-f.

The incorporation of the long alkyl chains to the polythiophene backbone affects the thickness, the surface topography and the water wettability of the films. Although COP and PEDOT films were prepared using identical conditions, the average thickness of the former is more than twice that of the latter (*i.e.* 381 ± 59 and 171 ± 26 nm, respectively). Similarly, the root-mean-square roughness (Rq) values reflect a smoother surface for COP than for PEDOT (*i.e.* Rq= 235 ± 68 and 311 ± 31 nm, respectively). Moreover, the water contact angle (WCA) increased from 57° ± 5º for PEDOT to 64° ± 7º for COP.

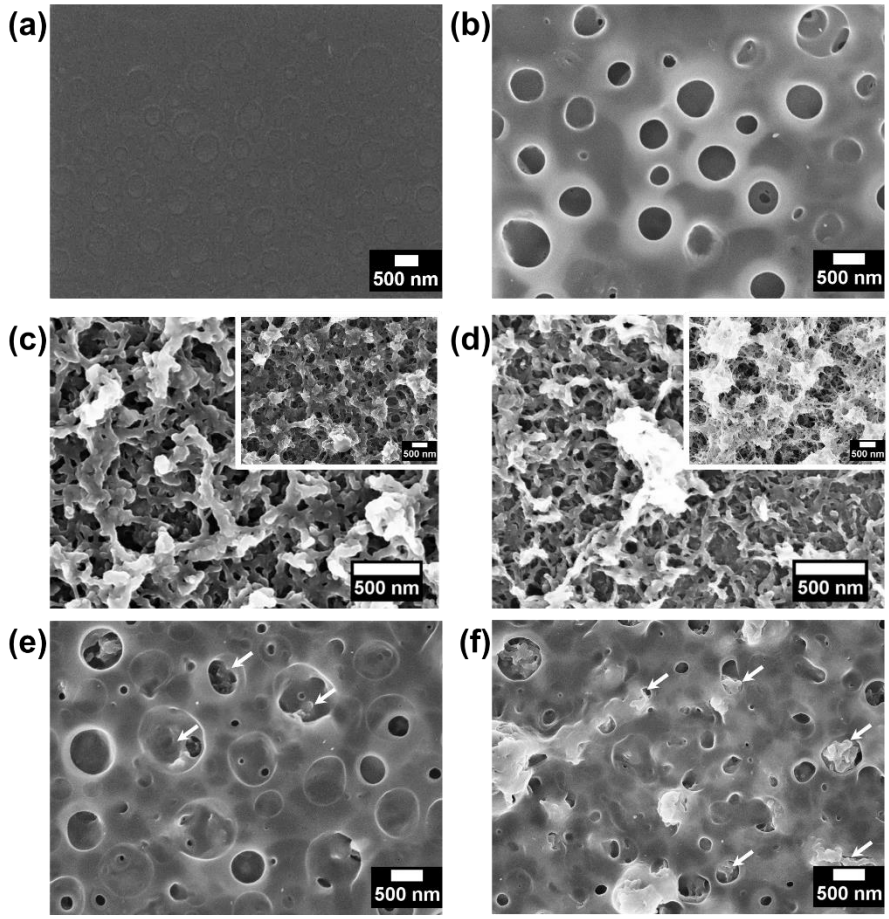

Figure 7.3.1 SEM images of (a) spin-coated 80:20 PLA:PVA layer. (b) 1st pPLA layer after elimination of PVA by water etching. PEDOT and COP electrodeposit on steel, insert 2nd PEDOT and COP and layer electropolymerized onto the 1st pPLA layer. (e-f) 5th pPLA layer of the systems 5-pPLA/PEDOT and 5-pPLA/COP. Arrows in (e) and (f) indicate the ICP layer observed under the outer pPLA layer. pPLA refers to the perforated poly (lactic acid) layer, PEDOT is poly (3,4-ethylenedioxythiophene) and COP is the copolymer of 3,4-ethylenedioxythiophene and 3-dodecylthiophene.

The total thickness of 5-pPLA/COP films is 998 nm ± 57nm, while that of 5-pPLA/PEDOT is 741 nm ± 23 nm, as measured by profilometry. These values are consistent with the sum of the thicknesses obtained for single-layered films: COP and PEDOT

supported onto steel and pPLA spin-coated using a 80:20 v/v PLA:PVA mixture (*i.e.* 170 ± 14 nm). [11] Similarly, the surface roughness is significantly higher for 5-pPLA/COP (Rq = 418 nm ± 76 nm) than for 5-pPLA/PEDOT (Rq = 185 nm ± 50 nm), which differs from the results discussed for the ICPs directly generated onto steel. This has been attributed to the templating effect induced by the alkyl chains of the COP when it grows onto elastic pPLA membranes. On the other hand, the water wettability, which is mainly controlled by the outer pPLA layer, is pretty similar for the two 5-layered systems (θ = 88º ± 6º and 85º ± 8º for 5-pPLA/PEDOT and 5-pPLA/COP, respectively).

Control voltammograms of PEDOT and COP films deposited onto steel sheets were conducted in 0.1 M PBS to study the effect of the 3DT units on the electroactivity and electrostability of the samples. As is shown in Figure 7.3.2a, the charge stored in both samples is similar, indicating that the incorporation of thiophene monomers bearing alkyl chain does not significantly affect the electroactivity of the film. After 25 consecutive oxidation - reduction cycles (solid lines) the loss of electrochemical activity is 28% ± 13% and 31% ± 3% for PEDOT and COP, respectively.

The electroactivity and electrostability of the two 5-layered membranes have been examined to confirm the efficiency of the oxidation - reduction processes when insulating PLA sheets separate the ICP layers. Figure 7.3.2b compares the cyclic voltammograms recorded in PBS 0.1 M for free-standing 5-layered membranes. As expected, the electrochemical activity is lower for free-standing membranes than for CP films supported on steel substrate (Figure

7.3.2a) due to the presence of pPLA layers. The loss of electrochemical activity (LEA) after 25 consecutive redox cycles is lower for 5-pPLA/PEDOT than for 5-pPLA/COP (LEA = 1% and 17%, respectively).

Additionally, the robustness and flexibility of the free-standing membranes were observed by the manipulation of the films. Then, Figure 7.3.2c shows digital camera images of a 5-pPLA/COP membrane, which was fabricated and detached using the procedure described in the Methods section. The sequence of images (Figure 7.3.2c1-4) reveals that the free-standing films are not only manageable and robust but they are also very flexible. Figure 7.3.2c-2 shows the aspiration process of a film, with an area of 0.5 cm^2, floating in water into a pipette with a tip diameter of 1.5 mm. Due to its outstanding flexibility, the 5-layered membrane does not obstruct the pipette tip but, instead, is completely introduced and delivered from it without damage (Figure 7.3.2c-3). After release into the solvent, the film slowly tends to recover its original shape (Figure 7.3.2c-4). Then, the film can be dried for manipulation without damaging its structure.

The aspiration-release-shape recovery-drying process can be repeated at least five times without any damage to the membrane. The same behaviour was obtained for 5-pPLA/PEDOT films (not shown). The mechanical stability of the 5-pPLA/COP and 5-pPLA/PEDOT membrane is demonstrated in Figure 7.3.2d, which shows representative low magnification SEM micrographs recorded after two consecutive aspiration-release-shape recovery-drying cycles. As is shown, no structural fail was detected at the surface of the films in these or any of the recorded micrographs.

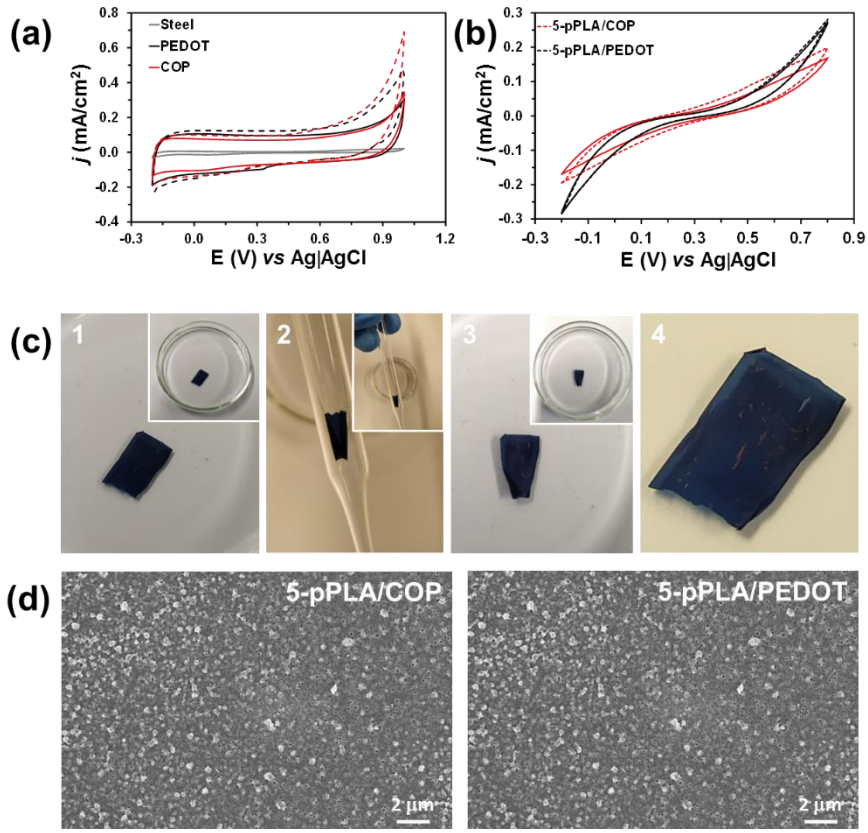

Figure 7.3.2 (a) First control voltammogram (dashed lines) and voltammogram after 25 consecutive oxidation - reduction cycles (solid lines) in 0.1 M PBS for steel, COP and PEDOT. (b) First control voltammogram (dashed lines) and voltammogram curve after 25 consecutive oxidation - reduction cycles (solid lines) in PBS 0.1 M for free-standing 5-pPLA/PEDOT and 5-pPLA/COP films. (c) Digital camera images of a 5-pPLA/COP free-standing film immersed in water (c1); aspired film floating in water into a pipette (c2); aspect of the film while it recovers the shape once it has been released into the water solution (c3); and film after having completely recovered the shape (c4). (d) Representative SEM micrographs of 5-pPLA/COP and 5-pPLA/PEDOT free-standing membranes showing that, after two aspiration-release-shape recovery-drying cycles, no structural damage is detected at the surface.

Bioactivation of the free-standing nanomembranes with porin. The novelty of the present work relies on the design of an advanced functional platform by immobilizing porin proteins onto a smart free-standing biomimetic membrane. This biomimetic membrane consists of three PLA layers with sub-micrometric perforations (pPLA layers) separated by two layers of an ICP. In this work two conducting layers were studied: PEDOT and the copolymer (COP) of 3,4-ethylenedioxythiophene (EDOT; Scheme 7.3.1a) and 3-dodecylthiophene (3DT; Scheme 7.3.1b). The incorporation of 3DT units, which bear a 12 carbon atoms long linear alkyl chain, is aimed to mimic the natural amphiphilic environment required by OMPs (*i.e.* like that offered by lipids), without losing the excellent conducting properties of PEDOT.

The resulting free-standing 5-layered membrane, hereafter named 5-pPLA/COP, has been transformed into 5-pPLA/COP/VDAC by immobilizing a Voltage Dependent Anion Channel (VDAC) protein (Scheme 7.3.1c) at the external pPLA layers. VDACs are porins found in the outer mitochondrial membrane of all eukaryotic cells, which are associated with the permeability of the mitochondria [74] and regulate the diffusion of ions and metabolites, such as nicotinamide adenine dinucleotide hydrogen (NADH) or adenosine triphosphate (ATP). [75] The protein used to prepare 5-pPLA/COP/VDAC is VDAC36 from *Solanum tuberosum*, a plant model organism. [76] Although the molecular weight of this voltage-dependent anion selective porin is similar to that of Omp2a (36 and 39 kDa, respectively), these two proteins highly differ in the diameter of their channels. The effective diameter of the protein channel of VDAC36 and Omp2a is about 2.0

and 1.2 nm, respectively, and, therefore, the former is expected to allow the diffusion of larger solutes than the latter. [77]

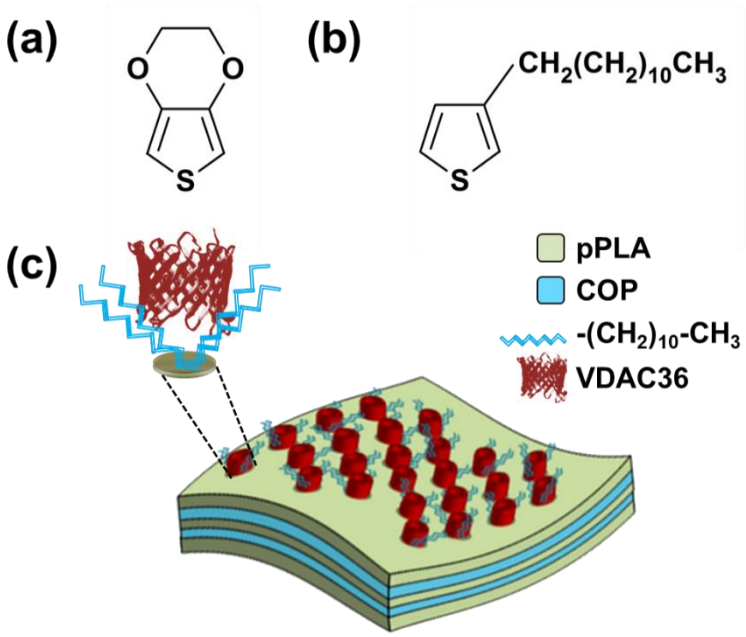

Scheme 7.3.1 Chemical structure of (a) 3,4-ethylenedioxythiophene (EDOT) and (b) 3-dodecylthiophene (3DT) repeat units. (c) Structure of 5-pPLA/COP/VDAC, *i.e.*, 5-pPLA/COP functionalized with Voltage Dependent Anion Channel (VDAC) protein.

In order to ascertain the influence of the dodecyl side groups in the functionalized device, the performance of 5-pPLA/PEDOT/VDAC and 5-pPLA/COP/VDAC (Scheme 7.3.1c), in which the two COP layers have been substituted by the PEDOT homopolymer, has been compared by FTIR and XPS.

Figure 7.3.3a compares the FTIR spectra recorded for COP and PEDOT, both showing the polythiophene characteristic bands. COP and PEDOT spectra show the asymmetric and symmetric stretching

vibrations of the methylene groups at 2916-2864 cm^{-1}, even though these are more intense for the former than for the latter due to the long alkyl chain of 3DT monomer. Moreover, the COP also presents a small band at 729 cm^{-1}, which has been attributed to the rocking of the methylene groups. [78,79] Besides, the absorption bands at 1648 cm^{-1} and 1520 cm^{-1} correspond to the vibrations of the aromatic thiophene ring, whereas the bands at 991 cm^{-1} and 856 cm^{-1} have been attributed to the ethylenedioxy group (C–O–C stretching) and the C–S characteristic peak of the thiophene ring, respectively. [80]

FTIR spectra of free-standing 5-layered films before and after incorporation of the VDAC36 protein are displayed in Figure 7.3.3b. The amide II and amide III protein bands are highlighted. Unfortunately, the bands associated to the amide I, which mainly corresponds to the C=O stretching and side chain bands of charged amino residues (all them between 1600 and 1750 cm^{-1}) cannot be used for protein identification due to the overlapping with the bands associated to the aromatic thiophene ring (C=C and C–C stretching) of COP or PEDOT (Figure 7.3.3a). However, both the amide II, which results from the N–H bending and the C–N stretching vibrations, and the amide III which is a very complex band that comes from a mixture of several displacements (for instance, N–H in plane bending coupled to C–N stretching) are clearly identified at 1517 and 1200-1300 cm^{-1}, respectively. The latter bands, which do not appear in the free-protein samples, are indicators of the VDAC36 presence at the surface of 5-pPLA/COP/VDAC and 5-pPLA/PEDOT/VDAC films.

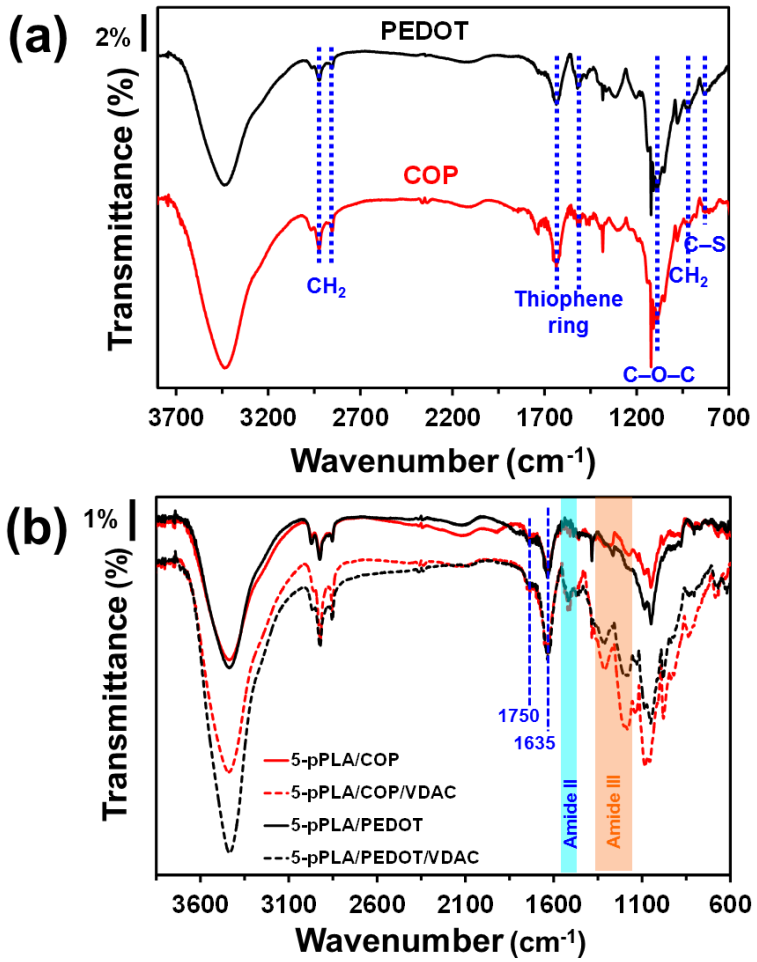

Figure 7.3.3 FTIR spectra of (a) PEDOT and COP films electrodeposit on steel and (b) free-standing 5-layered films before and after incorporation of the VDAC protein.

On the other hand, the successful incorporation of 3DT units to COP chains was also corroborated by XPS analyses (Table 7.3.1). For PEDOT, the S 2p / C 1s ratio is 0.15, which almost matches the theoretical value of 0.16. For COP, the experimental and theoretical S 2p / C 1s ratios decrease to 0.11 and 0.09, respectively, the difference between them has been attributed to: (*i*) the overoxidation of 3DT units (*i.e.* the β or β' position of the thiophene ring are free in 3DT units,

while they are blocked in EDOT units), which also affects the O 1s content; and/or (*ii*) the content of EDOT units in COP chains is slightly higher than the content of 3DT units (*i.e.* 1.2 times, if the influence of factor (*i*) is neglected). Comparison of the theoretical and experimental O 1s / C 1s ratios for PEDOT (Table 7.3.1) indicates that the content of O 1s is higher than expected, evidencing the adsorption of CO_2 and water molecules (*i.e.* PEDOT is a hydrophilic polymer) from the atmosphere. Considering that the adsorption of CO_2 and water is similar for PEDOT and COP, the experimental value of the O 1s / C 1s ratio obtained for the latter, which is significantly higher than the theoretical one, confirms the overoxidation of the 3DT units.

Table 7.3.1 Atomic percent composition (C 1s, S 2p and O 1s) obtained by XPS for PEDOT and COP films. Theoretical and experimental S 2p / C 1s and O 1s / C 1s ratios are displayed for comparison.

Sample	C 1s	S 2p	O 1s	S / C♣	S / C♦	O / C♣	O / C♦
PEDOT	62.74	9.24	28.02	0.16	0.15	0.33	0.45
COP	65.47	7.37	27.16	0.09	0.11	0.18♠	0.41

♣ Theoretical ratio; ♦ Experimental ratio; ♠ Calculated considering that the amount of EDOT units is higher than the amount of 3DT units by 1.2

Table 7.3.2 compares the surface atomic compositions of 5-pPLA/COP/VDAC and 5-pPLA/PEDOT/VDAC with the corresponding controls, which were prepared incubating the free-standing membranes in a 60 mM SDS and 1.5 M MPD solution without protein. Whilst the penetration of X-ray radiation using the conditions described in Chapter 4 is expected to be ~10 nm, here the penetration is unknown due to both the nanometric thickness of the layers and the filling of the perforations of the outer pPLA layers (see below). The N 1s detected in the composition of 5-pPLA/COP and 5-

pPLA/PEDOT controls has been attributed to the usual N_2 contamination from air. However, the N 1s increases from 0.63 - 0.64% in the control samples to 0.89% and 0.85% in 5-pPLA/COP/VDAC and 5-pPLA/PEDOT/VDAC, respectively, supporting the successful integration of the VDAC36 onto the surface of the films.

Table 7.3.2 Atomic percent composition (C 1s, O 1s, S 2p and N 1s) obtained by X-ray photoelectron spectroscopy (XPS) for control and functionalized free-standing films.

Sample	C 1s (%)	O 1s (%)	S 2p (%)	N 1s (%)
5-pPLA/COP (control)	57.71	35.24	6.42	0.63
5-pPLA/COP/VDAC	69.66	22.30	7.48	0.89
5-pPLA/PEDOT (control)	66.05	27.27	6.05	0.64
5-pPLA/PEDOT/VDAC	63.30	30.03	5.62	0.85

In order to quantify the amount of VDAC retained by the films, the solutions containing the protein were analysed by UV absorbance. More specifically, the absorbance at 280 nm was determined for the protein solution before and after films incubation, correction of the rinsing solutions being applied to the latter. The VDAC36 molar extinction coefficient, calculated by the ProtParam software, is 20400 $M^{-1}cm^{-1}$. [81] The original concentration was 0.847 mg/mL. After incubation, the concentrations were 0.825 and 0.830 mg/mL for the 5-pPLA/COP and 5-pPLA/PEDOT, respectively. Accordingly, the quantity of protein retained by the 5-pPLA/COP/VDAC and 5-pPLA/PEDOT/VDAC films is 2.704 and 2.043 $\mu g/cm^2$, respectively. This result indicates that the retention of protein increased by 32% when 3DT units were incorporated to the ICP layers,

demonstrating the importance of the lipid-like environment for the incorporation of the porins in artificial membranes.

This biomimetic effect has been attributed to the very different hydrophobic degrees co-existing in COP chains. Thus, the water contact angles measured for PEDOT [82] and unsubstituted polythiophene [83] films, both prepared by anodic polymerization, are 82º ± 2º and 89º ± 2º, respectively, these values are at the interface of hydrophilic and hydrophobic behaviors. In contrast, the water contact angle for dodecyl chains grafted to silane is near to 165 ºC, [84] close to the superhydrophobicity. Thus, hydrophobicity was found to increase very rapidly when the grafted alkyl groups involve at least 12 carbon atoms, which is fulfilled in COP, and the density of dodecyl groups (*i.e.* amount by surface unit) is high enough. [84] Obviously, in the case of COP the density of 3DT units is not sufficient to produce superhydrophobicity but it is enough to facilitate the formation of two distinct environments, mimicking lipids and increasing the retention of protein by 32%.

Effectiveness of ion transport across 5-pPLA/COP/VDAC by electrochemical impedance spectroscopy measurements. EIS measurements were performed to study the effectiveness of the protein activity on the ion transport across the bioactivated free-standing membranes. Both functionalized and control free-standing membranes were considered in this step by using three different electrolyte solutions: NaCl 0.5 M, ATP 0.05 M and ATP 0.1 M. The NaCl 0.5 M solution was selected as the standard to assess the membrane resistance and for further comparison to the results from previous works involving biomimetic membranes made of polymers and porins.

Instead, the ATP electrolyte was examined to take profit of the main VDAC function in vivo, which is the transport of this metabolite across the mitochondrial membranes. Accordingly, 5-pPLA/COP/VDAC and, especially, 5-pPLA/PEDOT/VDAC films are expected to behave as biosensors of relevant cellular compounds. The results were expressed as solution resistance (R_S), membrane resistance (R_M) and membrane capacitance, *i.e.* the capacitance of real systems (CPE, constant phase element), by using the simple Randles electrical circuit.

Figure 7.3.4 displays the collected impedance (Z) data as a Nyquist plot for the three studied electrolyte solutions. The corresponding Nyquist plots for bioactivated membranes obtained using 0.5 M NaCl (Figure 7.3.4a) and 0.1 M ATP solutions (Figure 7.3.4c) show a low capacitive semicircle in the high-frequency range and a straight ascending vertical line (almost 90º to the real axis and overlapping the semicircle) in the low-frequency range. This vertical line combines the effects of mass capacitance, which is ascribed to PEDOT layers, and the diffusion of electrolytes. [85] On the other hand, Nyquist plots for control 5-pPLA/COP and 5-pPLA/PEDOT membranes consist of a large semicircle (*i.e.* high capacitance), which extends from the high frequency to the low frequency range. A similar behaviour is observed for functionalized membranes when a 0.05 M ATP solution is employed (Figure 7.3.4b), reflecting a concentration-dependent behaviour.

The diameter of the semicircle, which is very sensitive to the microstructure of the membrane, is directly proportional to the membrane resistance. Accordingly, the results displayed in Figure

7.3.4 indicate that the incorporation of the VDAC36 protein inside the pores considerably increases the membrane conductivity. Besides, the Nyquist plots obtained for non-functionalized membranes in 0.5 M NaCl and 0.05 M ATP do not show any straight line ascending in the low frequency range, indicating that diffusion is hindered in these systems.

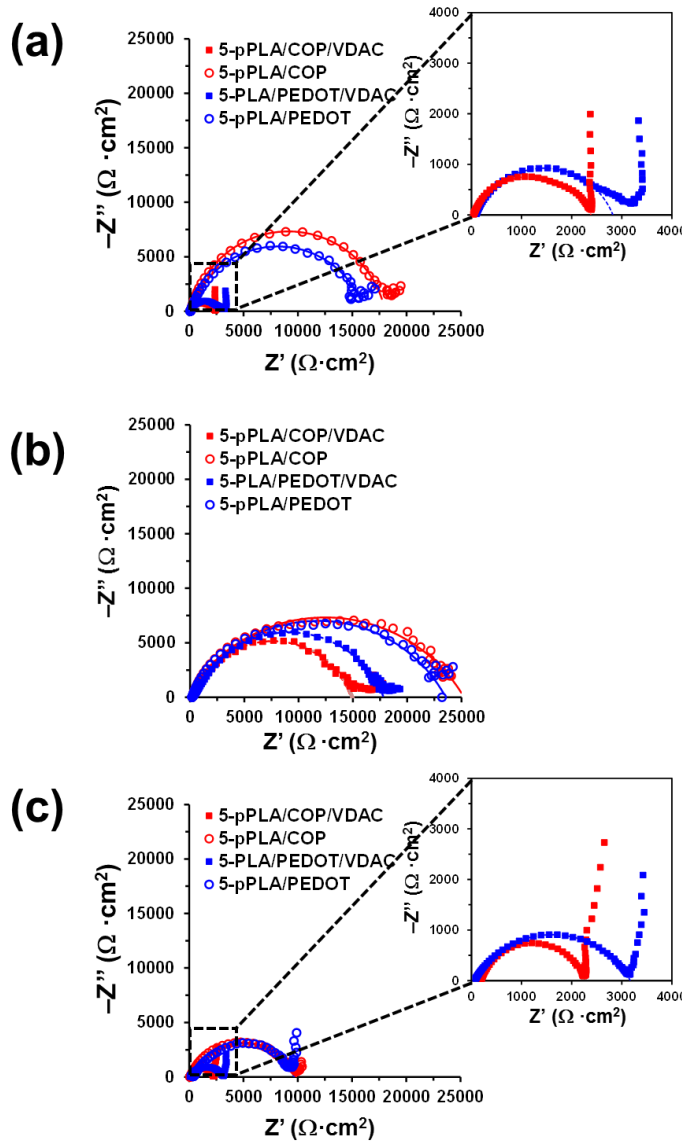

Figure 7.3.4 Nyquist plots for non-functionalized (control) and VDAC-functionalized free-standing 5-layered membranes in (a) NaCl 0.5 M, (b) ATP 0.05 M and (c) ATP 0.1 M aqueous solutions. VDAC is Voltage Dependent Anion Channel protein used in this work.

The noisy points that appear in the low frequency range of Nyquist plots, especially for the ATP 0.05 M solution in the low-frequency range, have been associated to the free-standing nature of the membrane. This makes difficult the fitting of the experimental data to a proposed electric equivalent circuit (EEC) for explaining the whole EIS profiles. In order to overcome this drawback, the simplified Randles EEC (Figure 7.3.5a) has been used to obtain the electrolyte resistance (R_s), the membrane resistance (R_M), which represents the ability of the membrane to impede ion transport at the interface, and the double layer capacitance (C_{dl}) in parallel with R_M, which can store only charge and ion movement. The role played by the C_{dl} in ion-exchange membrane systems constituted by the membrane and two diffusion boundary layers adjacent to the membrane was recently analysed by Moya. [86] At high frequencies, C_{dl} has very low impedance values and the main contribution comes from R_s (*i.e.* the solution acts as an Ohmic resistor). Accordingly, the semicircles start at R_s (Figure 7.3.4). At low frequencies, C_{dl} has very high impedance values and all the current goes through R_M. Therefore, the impedance contribution at the point where the right end of the semi-circle intercepts the y-axis is $R_s + R_M$. C_{dl} has been modelled as a constant phase element (CPE_{dl}), which represents the capacitance of real systems, as explained above. Thus, CPE_{dl} represents the selective ability of the system to impede ion transport, taking into account the contribution of all membrane components. In addition to the heterogeneity of the surface (*i.e.* roughness, porosity, reactivity), the CPE impedance (Z_{CPE}) is related

to non-uniform diffusion across the interface. Mathematically, Z_{CPE} is expressed as $[Q\cdot(i\cdot\omega)^n]^{-1}$, where Q is the CPE parameter, *i* the imaginary unit, ω the angular frequency, and *n* the CPE exponent representing a pure capacitor (n = 1), a pure resistor (n = 0) or a diffusion process (n = 0.5). [87] Both R_M and CPE_{dl} are expected to include the contribution of the VDAC36-integrated protein for 5-pPLA/COP/VDAC and 5-pPLA/PEDOT/VDAC membranes.

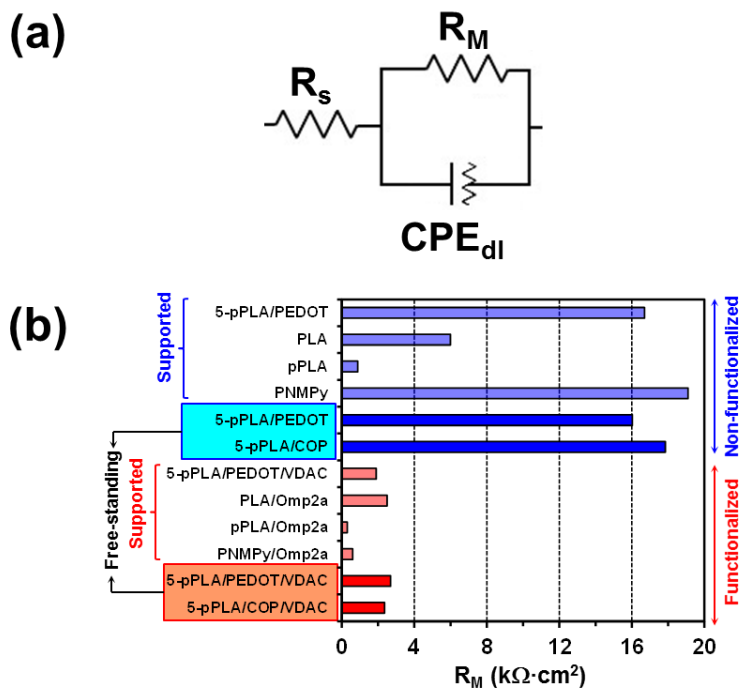

Figure 7.3.5 Randles EEC used to fit the experimental data in the semicircle of the Nyquist plots. (b) Comparison of the R_M values obtained in this work for free-standing 5-pPLA/COP/VDAC and 5-pPLA/PEDOT/VDAC, 5-pPLA/COP and 5-pPLA/PEDOT membranes with those obtained for supported functionalized and non-functionalized organic membranes. R_M values were determined by EIS using a NaCl 0.5 M electrolyte solution in all cases with exception of the supported PNMPy and PNMPy/Omp2a membranes, for which a NaCl 0.14 M electrolyte solution was used and the data were taken from previously reported works.[37,38]

The parameters obtained from the fitting of the experimental data in the semicircle to the Randles EEC are listed in Table 7.3.3. The presence of COP in membranes slightly increases the resistance of non-functionalized membranes, as R_M is higher for 5-pPLA/COP than for 5-pPLA/PEDOT by 11%, 7% and 4% in NaCl 0.5 M, ATP 0.05 M and ATP 0.1 M, respectively. This has been attributed to differences in the electrical conductivity of the ICP matrices (*i.e.* the electrical conductivity is lower for COP than for PEDOT). The low conductivity of poly(3-alkylthiophene)s in comparison to PEDOT was previously studied, being attributed to the self-rigidification of the thiophene ring in the latter. [88] More specifically, in PEDOT the π-conjugation induced by the geometric restrictions imposed by the cyclic substituent and the electron-donating effects of the oxygen atoms produce a gain in aromaticity and favour electrostatic interactions when planarity is reached. This gain is not achieved in poly(3-alkylthiophene)s, which reduces the aromaticity and the effective conduction pathways. On the other hand, the capacitive behaviour of the non-functionalized films is very similar, independently of the ICP used for the 2nd and 4th layer.

After the incorporation of the VDAC porin, the diameter of the semi-circle decreases drastically. This reflects an enhanced flow of charges at the electrolyte–membrane interface, as well as an increment of current crossing the nanomaterial, both phenomena leading to a great reduction of R_M when compared to the non-functionalized systems. The membrane resistance decay increases with the conductivity of the electrolyte solution. Moreover, the initial hypothesis that the incorporation of 3DT units would help to retain a

higher amount of protein and to keep it in its active form is fully supported by the EIS results. Indeed, the combination of VDAC36 with COP leads to a greater resistance reduction than when is combined with PEDOT. Despite these benefits, it should be noted that the reduction in resistance could be even greater by controlling the orientation of the protein immobilized in the pores. However, this is a challenge that is not easy to tackle.

Table 7.3.3 Resistance of the electrolytic solution (R_s), resistance of the membrane (R_M) and constant phase element (CPE) with the exponent parameter *n* for the different functionalized and non-functionalized (control) free-standing 5-layered membranes.

Sample	R_s ($\Omega \cdot cm^2$)	R_M ($k\Omega \cdot cm^2$)♥	CPE ($\mu F \cdot cm^{-2} s^{n-1}$)	*n*
		NaCl (0.5 M)		
5-pPLA/COP/VDAC	102	2.36 (87%)	1.07	0.732
5-pPLA/COP	102	17.85	4.61	0.876
5-pPLA/PEDOT/VDAC	102	2.69 (83%)	0.53	0.768
5-pPLA/PEDOT	102	16.03	4.50	0.814
		ATP (0.05 M)		
5-pPLA/COP/VDAC	431	14.40 (43%)	0.12	0.790
5-pPLA/COP	431	25.12	5.00	0.689
5-pPLA/PEDOT/VDAC	431	17.40 (26%)	0.16	0.766
5-pPLA/PEDOT	431	23.52	4.64	0.679
		ATP (0.1 M)		
5-pPLA/COP/VDAC	202	2.07 (78%)	0.53	0.794
5-pPLA/COP	202	9.53	4.72	0.674
5-pPLA/PEDOT/VDAC	202	3.11 (66%)	0.35	0.751
5-pPLA/PEDOT	202	9.18	4.60	0.653

Data were obtained by fitting the semicircle of the Nyquist plots fom EIS measurements to a simple Randles circuit.

♥ The percentages in parenthesis indicates the resistance reduction for the membranes with the same ICP after incorporation of the VDAC36 protein.

Figure 7.3.5b compares the resistance of free-standing membranes studied in this work with the supported membranes reported in literature, before and after functionalization with porins. In all cases, R_M was determined by EIS using NaCl as electrolyte (*i.e.* a NaCl 0.5 M solution was selected for all studies with exception of PNMPy and PNMPy/Omp2a, in which a NaCl 0.14 M solution was used). The resistance of the free-standing 5-layered membranes functionalized with VDAC36 is slightly higher than that previously obtained for supported PNMPy/Omp2a [37] and npPLA/Omp2a [38] membranes (R_M = 0.6 and 0.3 kΩ·cm^2, respectively). The latter were built by immobilizing the pore-forming Omp2a protein over a PNMPy film electropolymerized onto a rigid steel electrode and over a npPLA film spin-coated onto a ITO substrate, respectively. The thickness of the PNMPy and npPLA films (~300 and 110 ± 7 nm, respectively) was reported to be similar to those of the ICP and pPLA layers in the 5-layered membrane developed in this work. Hence, the higher resistance of the free-standing films has been essentially attributed to the fact that supported membranes do not suffer drawbacks associated to the manipulation of thin free-standing films, like the folds inducing local changes in the resistance. In order to confirm this assumption, the R_M of supported 5-pPLA/PEDOT/VDAC and 5-pPLA/PEDOT membranes were determined by EIS in NaCl 0.5 M solution. As shown in Figure 7.3.5b, the resistances measured for supported 5-pPLA/PEDOT/VDAC (R_M = 1.9 kΩ·cm^2) and 5-pPLA/PEDOT (R_M = 16.7 kΩ·cm^2) were slightly lower and higher, respectively, than those obtained for the corresponding free-standing film. This indicates that the self-supporting capacity of 5-layered membranes only produces a small change in the resistance.

On the other hand, Table 7.3.3 shows that, independently of the electrolyte solutions, CPE_{dl} decreases after the integration of VDAC36, indicating that protein-promoted ion diffusion causes a loss of capacitance. For the study in 0.5 M NaCl, the increasing contribution of the diffusion process is also reflected by the reduction of the *n* exponent (see Z_{CPE} expression). The opposite behaviour is observed in the ATP solutions for which the *n* value is higher for the functionalized membranes than for the control ones. This difference has been attributed not only to the ATP diffusion coefficient, which is much lower than that of Cl^- (3.10-6 and 2.03 10-5 cm^2/s for ATP and Cl^-, respectively) but also to the binding affinity of ATP with VDAC proteins. [89–91]

It is worth noting that the working conditions of 5-layered membranes functionalized with VDAC36 are restricted by the stability of the β-barrel structure, which is responsible of the channel activity. In general, the stability of β-barrel channels is pH and temperature dependent. Thus, it has been observed that the stability of VDAC's β-barrel and, therefore, the transport of metabolites across the pore decrease at low pH and is restored at pH 7. [92] Besides, it has been proved that the structure of OMPs used for biomimetic membranes remains stable up to temperatures higher than 100 ºC without losing properties. [36]

On the other hand, the economic viability of producing polymeric flexible devices functionalized membrane proteins is limited by the cost of the latter. This drawback can be drastically mitigated utilizing optimized expression bacterial systems for the production of membrane proteins. In last years, membrane proteins have been often

overexpressed in *Escherichia coli* bacteria, [93,94] which were selected because of the following advantages: (*i*) easy DNA transformation; (*ii*) fast growth and high cell density cultures; (*iii*) inexpensive culture costs and (*iv*) high yield of overexpression. These biotechnological techniques are expected to contribute the implementation of biomimetic membranes as routine devices in technological and biomedical applications.

Permselectivity measurements. The influence of the VDAC porin on the ion permselectivity was examined considering the 5-pPLA/COP/VDAC and 5-pPLA/COP membranes fixed to porous support (glass frit discs of 25 mm in diameter having a non-porous peripheral adage of 6 mm, 3.65 in thickness and average pore size of 10-16 µm) in a two-compartment cell with a circular exposed area of 4.5 cm^2. A 0.1 M NaCl solution was used for this study, as is usual in this kind of assays, since the transport number and the diffusion coefficient of ATP are unknown. Complete description of the set-up, the cell and the porous support is provided in previous work. [95] Both compartments were filled with a 0.1 M NaCl solution and, after fix the membrane to the porous support, chronoamperometric measurements were performed using steel AISI 316L sheets as working and counter electrodes while an Ag|AgCl electrode was used as reference electrode.

The transition time for an ideally permselective membrane was calculated using the Equation 7.3.1: [96]

$$P = \frac{|z|\mathrm{F}D^{0.5}\pi^{0.5}C}{2(1-t_i)\frac{I}{A}\sigma^{0.5}} \qquad \textbf{Eqn. 7.3.1}$$

where P is the permselectivity, z is the absolute charge of the chloride ion, F is the Faraday constant (96485 A·s/mol), D is the diffusion coefficient ($1.48 \cdot 10^5$ cm^2/s), t_i is the transport number (0.604) of the chloride ion in 0.1 M NaCl, C is the concentration of chloride ions (0.1 M), I is the applied current (10 mA in this case), A is the exposed membrane area, and σ is the transition time for the real membrane, which was measured as the inflection point of the chronopentiometric curve.

The permselectivity, normalized with respect to the porous support (*i.e.* P = 100% for the porous support), is 62% ± 6% and 89% ± 7% for 5-pPLA/COP and 5-pPLA/COP/VDAC, respectively. A membrane with permselectivity of 0% shows no ion selectivity compared to the solution phase, while a permselectivity of 100% means the co-ion flux through the membrane is 0. Our results clearly show that the incorporation of the VDAC36 protein has a positive effect in the permselectivity of biomimetic hybrid nanomembranes.

Conclusions

In the present study, a free standing and conducting polymeric membrane with porin protein immobilized has been developed and proved to be efficient for transport of ATP and NaCl, for first time. The VDAC36 protein has been immobilized at the external layers of free-standing 5-pPLA/COP membranes. The retention of such protein has been found to be higher for COP- than for PEDOT-containing membranes, indicating that the dodecyl alkyl chains successfully mimic the lipophilic environment of cell membranes. The

incorporation of the porin, which retains its function, has induced important electrochemical changes in the membrane resistance and capacitance, promoting the diffusion of ions, especially of ATP. In conclusion, the hybrid system obtained by combining synthetic polymers (ICP and biodegradable PLA) and porin proteins is well-suited for the development of flexible membrane biosensors with fully functional transmembrane ion channels. The new platform is fully free-standing and flexible and can be applied in many biomedical technologies, opening new frontiers for the future development of high-throughput screening assays.

7.4 Free-standing Faradaic motors based on biocompatible nanoperforated poly(lactic acid) layers and electropolymerized poly(3,4-ethylenedioxythiophene)

Abstract

The electro-chemo-mechanical response of robust and flexible free-standing films made of three nanoperforated poly(lactic acid) (pPLA) layers separated by two anodically polymerized poly(3,4-ethylenedioxythiophene) (PEDOT) layers, has been demonstrated. The mechanical and electrochemical properties of these films, which are provided by pPLA and PEDOT, respectively, have been studied by nanoindentation, cyclic voltammetry and galvanostatic charge-discharge assays. The unprecedented combination of properties obtained for this system is appropriate for its utilization as a Faradaic motor, also named artificial muscle. Application of square potential waves lead to important bending movements in the films, which can be repeated for more than 500 cycles without damaging its mechanical integrity. Furthermore, the actuator is able to push a huge amount of mass, as it has been proved by increasing the mass of the passive pPLA up to 328% while keeping unaltered the mass of electroactive PEDOT.

Materials and methods

Materials and synthesis of 5-pPLA/PEDOT FsNM. The combination of spin-coating and electropolymerization techniques was used to prepare self-supported 5-layered films, which alternate pPLA and PEDOT ultra-thin sheets, separated from the steel substrate

by PEDOT:PSS sacrificial layer. Materials and procedure have been already reported in Section 7.2.

In brief, a PEDOT:PSS layer followed by a nanoperforated PLA (pPLA) layer, both spin-coated onto steel substrate (AISI 304 sheet of 3 × 3 cm^2), were used as working electrode for the anodic polymerization of EDOT. pPLA layers were obtained by blending PLA and PVA with a ratio of 90:10 v/v (PLA:PVA), prepared by mixing PLA (10 mg/mL) and PVA (10 mg/mL) HFIP solutions, and removing PVA domains via solvent etching. The detachment of the 5-layered films from the steel substrate was achieved after immersion into milli-Q water for 12 h when the PEDOT:PSS forms a colloidal dispersion in the medium.

Characterization of 5-pPLA/PEDOT FsNM. In order to continue the study of 5-pPLA/PEDOT FsNM SEM (operating at 5 kV), nanoindentation and different electrochemical assays were performed. A more detailed information was included in Chapter 4.

All the electrochemical assays (CV, GDC and electro-chemo-mechanical assays) were done in a three-electrodes cell containing $LiClO_4$ 0.1 M aqueous solution at room temperature. A conventional Ag|AgCl electrode and a platinum wire were used as reference electrode and counter electrode, respectively. Cyclic voltammograms were recorded with an initial and final potential of − 0.20 V and + 0.60 V.

Results and discussion

Self-standing 5-pPLA/PEDOT membranes were prepared from the procedure reported in Section 7.2, which was sketched in Scheme

7.2.2. In brief, a sacrificial layer of 302 ± 3 nm thickness was obtained onto a steel AISI 304 sheet of 3 × 3 cm^2 by spin-coating using a commercial aqueous solution of PEDOT doped with polystyrene sulfonate (PEDOT:PSS). Then, a pPLA layer was spin-coated onto the sacrificial layer. This was achieved by spin-coating a mixture of PLA and PVA. Since these are immiscible polymers, the formation of spherical nanofeatures was induced by phase segregation (*i.e.* segregated nanodomains). The diameter of such nanofeatures was adjusted to the entire film thickness by regulating the operational conditions of the spin-coating process (*i.e.* time and angular speed) and the concentration of the less abundant polymer (PVA) in the feeding mixture. After this, selective water etching was applied to dissolve the less abundant PVA, transforming the formed nanofeatures into nanoperforations while PLA remained unaltered.

The resulting PEDOT:PSS/pPLA bilayer was used as working electrode for the anodic polymerization of PEDOT doped with ClO_4^-. In all cases, pPLA layers were obtained by blending PLA and polyvinyl alcohol (PVA) with a ratio of 90:10 v/v, and removing PVA domains via water etching. PEDOT was anodically polymerized using a constant potential of +1.40 V and adjusting the polymerization charge to 270 mC. As it was proved in Section 7.2, the anodic polymerization was successful due to the nanoperforations of the PLA layer, which allow the 3,4-ethylenedioxythiophene (EDOT) monomer to reach the internal semiconducting layer (*i.e.* PEDOT:PSS sacrificial layer or the previously electropolymerized PEDOT layer). This process was repeated until the 5-layered film made of three pPLA

layers separated by two anodically polymerized PEDOT layers was obtained.

As determined by contact profilometry, the thickness of pPLA layers was approximately half of the thickness of PEDOT layers. More specifically, the thickness of the 1st (adhered to the sacrificial layer), 3rd (intermediate) and 5th (external) pPLA layer was 95 ± 4, 94 ± 7 and 114 ± 9 nm, respectively, while the 2th an 4th PEDOT layer exhibited a thickness of 210 ± 19 and 199 ± 18 nm, respectively. Accordingly, the thickness of the whole 5-layered film is around 0.7 μm, which is distributed in ~0.3 μm and ~0.4 μm for the pPLA and PEDOT layers, respectively. Finally, the 5-pPLA/PEDOT film was detached from the steel substrate by immersion into milli-Q water for 12 h.

5-pPLA/PEDOT FsNM characterization. Figure 7.4.1a shows a representative supported 5-pPLA/PEDOT membrane with area of 3 × 2 cm^2 prepared for this work. This membrane is cut and converted into six self-standing membranes with area of 2 × 0.5 cm^2 by elimination of the sacrificial layer. Figure 7.4.1a also displays three of the resulting self-standing membranes floating in water. An average film thickness of 725 ± 60 nm was obtained by profilometry scratching. Membranes were stable on air and in water solution for their manipulation, stability that remained after months from their preparation. Rounded-shape nanoperforations at the surface of the supported 5-pPLA/PEDOT membrane are shown in the Figure 7.4.1b, which exhibits a representative SEM micrograph. The diameter of the nanoperforations, which allow to intuit the globular aspect of the internal PEDOT layer appearing inside them, is 109 ± 34 nm. The internal PEDOT layers are more clearly identified in Figure 7.4.1c,

which displays the transversal view of a self-standing membrane, as well as, a representative energy dispersive X-ray (EDX) spectra from both surface and the internal regions (Figure 7.4.1d). As it can be seen, the only elements detected at the surface were carbon and oxygen, which is consistent with the PLA composition, while the peak of sulfur corresponding to PEDOT is clearly identified at the spectrum of the internal region. Detailed structural (*i.e.* layer-by-layer SEM and AFM studies) and spectroscopic (*i.e.* FTIR and layer-by-layer Raman studies) characterization of 5-pPLA/PEDOT membranes was provided in the previous Section 7.2 and, therefore, in the rest of this study we have focused on the mechanical, electrochemical and chemo-electro-mechanical response of the self-standing membrane.

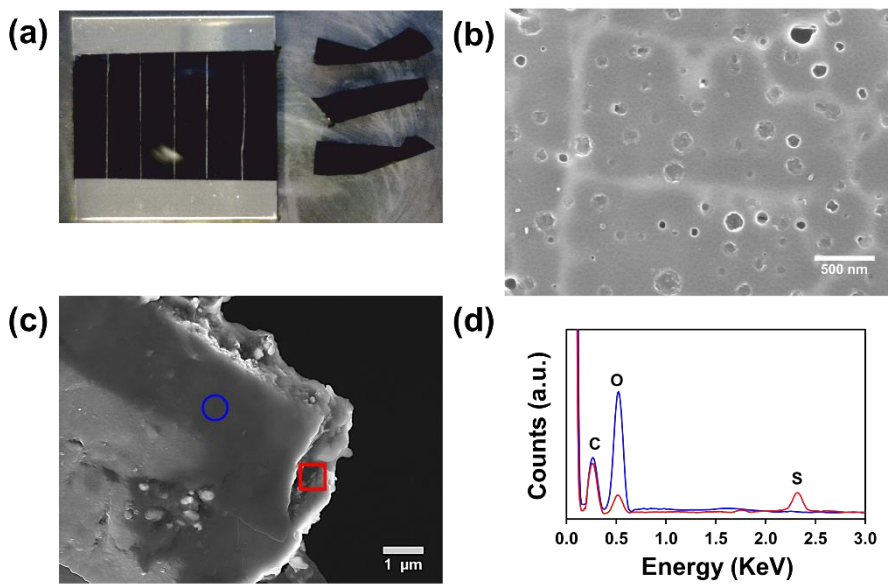

Figure 7.4.1 (a) Digital camera images displaying a scratched 5-pPLA/PEDOT membrane with an area of 3 × 2 cm^2 supported onto the steel substrate and three free-standing 5-pPLA/PEDOT films (2.0 × 0.5 cm^2) floating in water. (b) Representative SEM micrograph of the surface of a supported 5-pPLA/PEDOT membrane. (c) SEM micrograph showing

the transversal view of the self-standing membrane and (d) representative EDX analyses of the external PLA layer (blue circle) and the internal PEDOT-containing regions (red square).

The variation of the micromechanical properties, hardness and elastic modulus, as a function of the indentation depth for the 5-pPLA/PEDOT membrane deposited over commercial steel is presented in Figure 7.4.2. In order to evaluate the effect of the substrate, the micromechanical properties for the substrate steel were determined at the same conditions. Hardness and elastic modulus for the substrate steel employed were found to be 7.05 ± 0.74 GPa and 216 ± 13 GPa, respectively, at the sub-micrometric length scale. Hardness values are higher than those expected for TRIP steels as reported by Roa *et al.*, [97] whereas elastic modulus values are in satisfactory agreement with those determined by other authors in steels. [98,99]

A clear influence of the substrate for displacement into surface of around 80 and 50 nm for the hardness and elastic modulus, respectively, was found. Furthermore, the hardness and the elastic modulus data present a relatively large scatter due to the heterogeneity of the membrane in terms of local variations and porosity. Three different regions can be clearly observed in Figure 7.4.2a: (*i*) for indents shallower than 30 nm the values are strongly affected by length scale or indentation size effect; (*ii*) penetration depth ranged between 30 to 80 nm, the hardness remains stable and equals to 0.18 ± 0.08 GPa, which may be related with the coating hardness; and (*iii*) for penetration depths higher than 80 nm, the plastic field slightly interacts with the metallic substrate and starts to increase.

As it is shown in Figure 7.4.2b, the elastic modulus for the 5-pPLA/PEDOT membrane linearly increases for penetration depths higher than 15 nm due to the elastic field directly interacts with the employed substrate. Within this context, an appropriate model was required in order to deconvolute the substrate effect and be able to determine the elastic modulus for the membrane alone. The Bec *et al.*[100] equation (Eqn. 7.4.1) was employed to determine the intrinsic elastic modulus for the membrane:

$$\frac{1}{E_{eff}} = \frac{2a}{1+\frac{2t}{\pi a}}\left(\frac{t}{\pi a^2 E_m} + \frac{1}{2aE_s}\right) \qquad \textbf{Eqn. 7.4.1}$$

where E_{eff} is the effective elastic modulus determined through the equation proposed by Oliver and Pharr,[98] the subindex *m* and *s* refer to membrane and substrate, respectively, *a* is the contact radius, and *t* is the coating thickness. As a result, the membrane elastic modulus was calculated to be 3.4 GPa. This value is about 30 % lower than those presented in the plateau labelled as * in Figure 7.4.2b, sustaining then the strong interaction of the elastic field with the substrate.

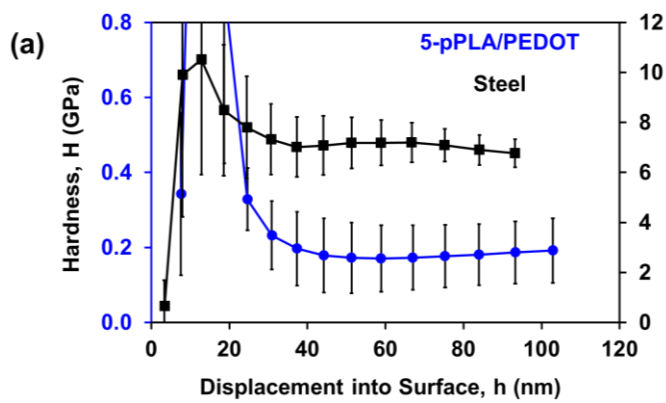

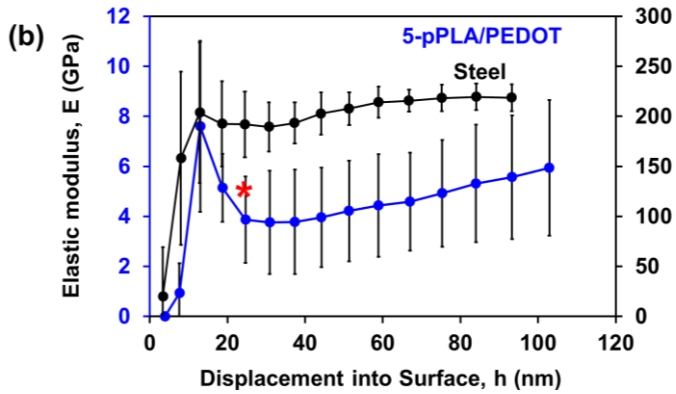

Figure 7.4.2 Mechanical properties, obtained by nanoindentation, for both a 5-pPLA/PEDOT membrane supported onto a steel substrate and the used steel, as a function of the displacement into surface: (a) hardness and (b) elastic modulus.

Electrochemical characterization of 5-pPLA/PEDOT FsNM. Figure 7.4.3a displays the cyclic voltammograms recorded in 0.1 M $LiClO_4$ aqueous solution for 5-pPLA/PEDOT films supported onto steel as they grow layer-by-layer. As it can be seen, the electroactivity, which is estimated from the cathodic and anodic areas of the voltammograms, is significantly higher for PEDOT layers than for pPLA layers. Obviously, this difference is more pronounced when the 1st pPLA and the 2nd PEDOT layers are compared. Besides, the 3rd pPLA layer exhibits a high electroactivity in comparison with the 1st one, since the nanoperforations of the former allow the mobility of dopant ions from the 2nd PEDOT layer. In addition, the electroactivity is higher for the 4th PEDOT layer than for the 2nd one due to nanoperforations in the 3rd pPLA layer.

Figure 7.4.3b displays the cyclic voltammogram recorded for a free-standing 5-pPLA/PEDOT film in 0.1 M $LiClO_4$ aqueous solution. The electroactivity is smaller for the free-standing film than for the

one supported onto steel. This expected result has been attributed to the difficulties associated with the immobilization of the free-standing membrane onto the electrode, making very difficult the contact between them to be complete once the sacrificial layer has been removed. In spite of this limitation, the electrochemical activity of free-standing 5-pPLA/PEDOT is noticeably high, especially when compared with that of a supported pPLA film (Figure 7.4.3b). This electroactivity remains practically unaltered after 25 consecutive oxidation-reduction cycles (*i.e.* reduction of only 4.8%), as is evidenced by the similarity between the two voltammograms (Figure 7.4.3b). These results have been attributed to the conducting channels created by PEDOT layers, which can be appreciated in pPLA outer layer (Figure 7.4.1b). Although the electroactivity of free-standing 5-pPLA/PEDOT films remains practically intact and the mechanical integrity is apparently preserved after 25 consecutive redox cycles, morphological inspection reveals significant changes in the nanoperforations of the external pPLA layer (Figure 7.4.3c). The spherical form of the nanoperforations is preserved while their average diameter (237 ± 77 nm) increases more than twice with respect to that of as prepared membranes (109 ± 34 nm). This has been attributed to electro-chemo-mechanical effects underwent by the internal PEDOT layers when they are submitted to oxidation and reduction processes. PEDOT layers swells during oxidation by the entrance of hydrated perchlorate anions and shrink during reduction by the expulsion of the same hydrated counter-anions (Scheme7.4.1) The continued swelling-shrinking processes experienced by PEDOT layers during the potential scan affect the structure of the flexible upper pPLA layer, increasing the area of pores.

In order to ascertain if the studied free-standing films retain the structure when they are submitted to prolonged electrochemical stress, 1500 galvanostatic charge-discharge (GCD) cycles were run at a current density of 1.05 mA/g in the two-electrode configuration. The cell voltage varied approximately from –0.25 to 0.65 V through each cycle, which corresponds to charge-discharge time of 7.7 seconds. Figure 7.4.3d shows the first GCD curves, which apparently present a pseudo-triangular shape with a voltage drop (V_{drop}) of ~0.25 V at the beginning of the discharging step, which is due to internal resistance of the electrode. Detailed inspection of the second GCD cycle in Figure 7.4.3e allows appreciating the deviation from the ideal triangle with a voltage drop at a time close to 5 s. However, such shape clearly corresponds to that expected for a real electrochemically active conducting polymer, as it is PEDOT. [101,102] After 1500 GCD cycles both the value of V_{drop} and the shape of the curve remained practically unaltered (Figure 7.4.3e), evidencing the lifetime stability of 5-pPLA/PEDOT.

As observed above for cyclic voltammetry, consecutive charge-discharge cycles induce structural changes in PEDOT electrodes, which evolve from a compact morphology to a more porous one and vice-versa. This affects the shape and size of the nanoperforations of the external pPLA layer, which become less rounded and much bigger after 1500 GCD cycles (Figure 7.4.3f). More specifically, the average diameter increases to 491 ± 215 nm, which represents an increment of around four times with respect to those of as prepared films, and become very heterogeneous, as is proved by the large standard deviation. In spite of this, it is worth noting that the mechanical

integrity of the PEDOT layer was apparently maintained in all cases, since no fracture or crack was detected in the surface of the film. Note also that the remarkable influence of the charge (swelling) and discharge (shrinkage) processes experienced by the PEDOT layers on the structure of the external PLA layer is fully consistent with an actuation mechanism.

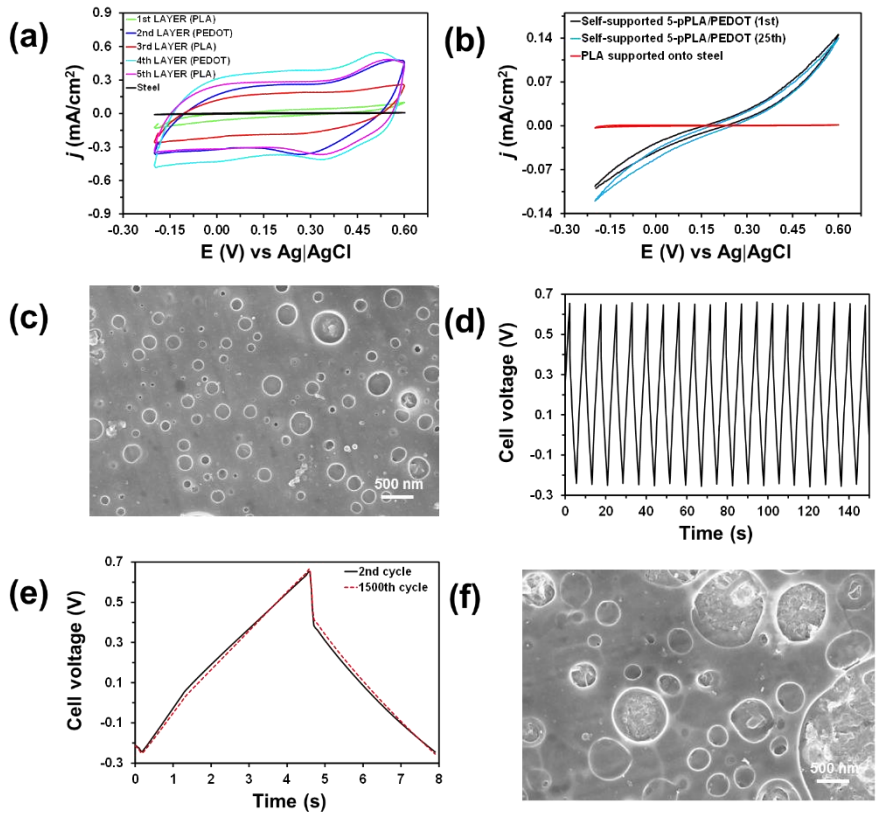

Figure 7.4.3 (a) Cyclic voltammograms recorded for a 5-pPLA/PEDOT film supported onto a steel substrate as it grows layer by layer. Scan rate: 100 mV/s. (b) First control voltammogram (black line) and voltammogram after 25 consecutive oxidation-reduction cycles (blue line) for a freestanding 5-pPLA/PEDOT film. The first control voltammogram recorded for a supported pPLA film is included for comparison (red line). (c) SEM micrograph of a 5-pPLA/PEDOT film after 25 consecutive oxidation-reduction cycles. (d) Curves for the first GCD cycles recorded at

0.75 mA for a free-standing 5-pPLA/PEDOT film. (e) Comparison of the 2nd and 1500th GCD cycles. (f) SEM micrograph of a free-standing 5-pPLA/ PEDOT film after 1500 consecutive GCD cycles.

Once the mechanical and electrochemical properties of free-standing 5-pPLA/PEDOT membranes were proved, the electro-chemo-mechanical response was analysed applying square potential waves from ± 0.6 to ± 4.0 V during a period of time *t*, where *t* = 2, 4, 8 or 10 s. The positive voltage was held half of the time to oxidize the PEDOT layers, while the negative voltage was kept the same time to reduce them. Such electronic and ionic charge transport processes cause the conformational movements of the polymer chains that, together with the compositional variation inside the polymeric matrix (*i.e.* entrance and scape of hydrated ions), guarantee the film volume variation during reversible oxidation and reduction reactions (swelling and shrinking, respectively), the reaction is illustrated in Scheme 7.4.1. Although reversible bending displacements were successfully obtained for swelling-shrinking times examined, results discussed in this work have been focused on assays conducted using 10 s (*i.e.* 5 s for oxidation and 5s for reduction), since their monitoring was easier.

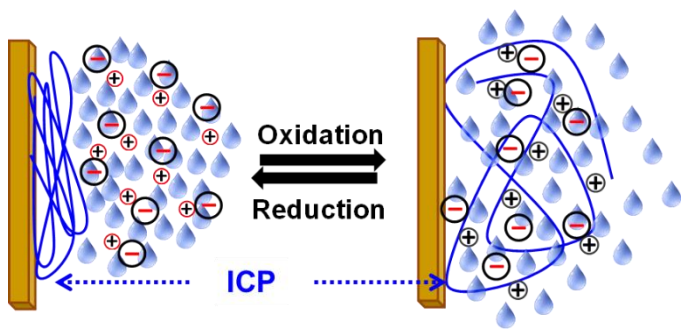

Scheme 7.4.1 Reaction-induced swelling-shrinking of a ICP film.

Figure 7.4.4a displays the experimental set up used to follow the movements of the free-standing 5-pPLA/PEDOT films. It is worth noting that the structural asymmetries caused by the templating effect exerted by PEDOT on pPLA layers, which essentially affects the roughness of the layer (*i.e.* 6 ± 1, 90 ± 14 and 103 ± 9 nm for the 1st, 3rd and 5th pPLA layer, respectively) and the size of the nanoperforations (*i.e.* 49 ± 14, 76 ± 27 and 103 ± 40 nm), facilitate the observed bending movements. The separate quantification of the angular displacement and the length variation, which are typically observed in self-standing and supported (*i.e.* thick bilayers) ICP-containing actuators, respectively, is hindered by the co-existence of both kind of movements in 5-pPLA/PEDOT actuators. In addition, 5-pPLA/PEDOT films fold over themselves due to their sub-micrometric thickness and flexibility. In order to overcome these limitations, the global movement was quantified by photographing the film and comparing the variation in the film surface area (ΔA) from the recorded images.

Figure 7.4.4b displays the variation of ΔA with the potential. As it was expected, ΔA grows with the potential, increasing from 3.8% ± 0.9% for ± 0.6 V to 28.0% ± 4.2% for ± 4.0 V. The significant change described by the film is shown in Figure 7.4.4c, which present photographs on its voltammetric response to the studied potentials. The angle (Δα) associated to bending movement at the different potentials is included in Figure 7.4.4c. The mechanical response of the 5-layered film upon consecutive swelling-shrinking processes was evaluated by applying consecutive square potential waves (up to 500) at the above mentioned potentials. Cyclability results, which are

displayed in Figure 7.4.4d, indicate that the free-standing films remained intact when the square wave was ± 0.6, ± 1.0 and ± 2.0 V. In contrast, films failed after 220 ± 16 and 80 ± 12 cycles when the potential was ± 3.0 and ± 4.0 V, respectively. Accordingly, next assays were conducted using a voltage ± 2 V.

In order to evaluate the actuation force of the 5-pPLA/PEDOT film, the mass of the outer PLA layer was increased during the preparation process. More specifically, the spin-coating rate was decreased from 1200 rpm to 900, 600, 300 or 100 rpm. This represented an increment in the total mass of the films (Δm) comprised between 21% ± 8% (900 rpm) and 328% ± 35% (100 rpm) with respect to the film with the outer PLA layer prepared at 1200 rpm. Figure 7.4.4e, which represents the variation of ΔA against Δm when square voltage waves of ± 2.0 V were applied for 10 s, shows that ΔA decreases with increasing Δm. However, such reduction is not pronounced when Δm < 120% and the bending movement is still appreciable when Δm is as high as 328% ± 35%. Overall, these results indicate that the 5-pPLA/PEDOT actuator is able to push a huge amount of mass.

Multimedia files of the electro-chemo-mechanical assays are available in the Supporting Information of ACS Publications website at DOI: 10.1021/acsami.9b08678.

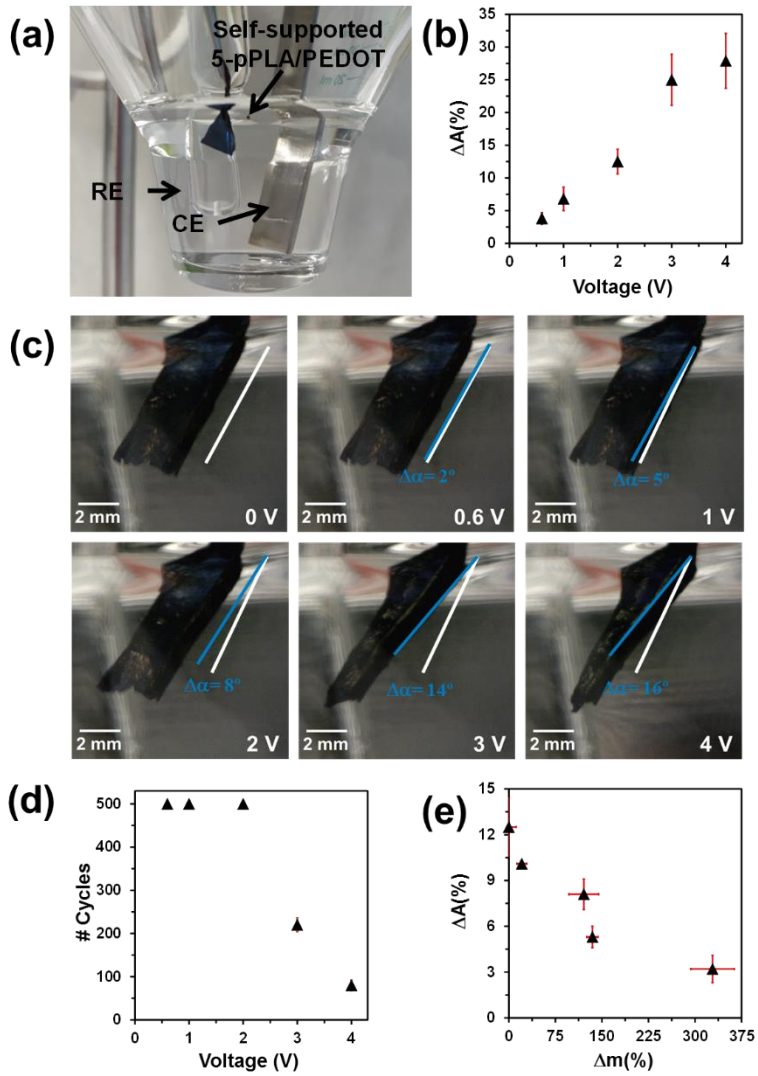

Figure 7.4.4 (a) Experimental set up used to follow the movements of the free-standing 5-pPLA/PEDOT films. (b) Variation of the surface area (ΔA) against the voltage used for square potential waves. (c) Photographs displaying the response of free-standing 5-pPLA/PEDOT films against different voltages. The bending angle (Δα) at different potentials, which was measured from to the initial position at 0 V (white line) the position reached by the film at the desired potential (blue line), is also displayed. (d) Number of cycles that retain the mechanical integrity of the 5-pPLA/PEDOT film after apply up to 500 consecutive square potential waves using different voltages. (e) Variation of the surface area (ΔA) against the increment of mass for the outer pPLA layer (Δm) when square voltage waves of ± 2.0 V were applied for 10 s.

In summary, ICPs, especially PPy, have largely been studied as adequate materials for constructing actuators due to their property of oxidize and reduce in a reversible way. Such electrochemical reactions typically result into large angular displacements (up to 300º) when the actuator involves bilayer structures consisting of a thick tape or a plastic film with a thick ICP layer on the right or the left side. [42,43,52] Alternatively, approaches based on thick self-supported ICP films forming interpenetrated polymer networks [56–58,103] have been used as macroscopic tools able to translate the electrochemical reactions into film length variations. In both approaches, ICP films required to be thick enough to reach the working conditions without breaking. In contrast, the strategy presented in this work avoids mechanical failure by intercalating ICP layers of ultra-thin thickness (*i.e.* the charge consumed during the electropolymerization was adjusted to 270 mC only, whereas thick ICP films forming interpenetrated networks consumed > 25 C during the electropolymerization [56–58,103]) between robust and elastic pPLA nanofilms. Moreover, self-supported 5-pPLA/PEDOT films exhibit bending movement without the assistance of any tape or thick plastic film adhered to it.

Although, direct comparison of angular displacement between thick bilayer structures and 5-pPLA/PEDOT membranes is precluded because of the thickness of the latter (*i.e.* ultra-thin 5-pPLA/PEDOT membranes tend to fold over themselves during the bending), the bending of this self-supported nanodevice instead of the classical length variations represents a significant improvement with respect to thick self-supported films forming interpenetrated polymer networks. Moreover, this bending is preserved after a very large number of

cycles. In addition, a triple PPy layer artificial muscles have been found to trail weights of up 180% the mass of ICP, [104,105] while 5-pPLA/PEDOT films still exhibit appreciable bending when the mass of PLA, which is the most abundant component in the film, increases up to 328% ± 35%.

Conclusions

A novel actuator based on free-standing 5-layered films of submicrometric thickness (~ 0.7 μm) has been fabricated. The preparation process involves three spin-coated pPLA layers, which bring mechanical strength and flexibility, separated by two anodically polymerized PEDOT layers that provide the electrochemically response. These films were exposed to square potential waves to induce volumetric expansion and contraction of the PEDOT layers, causing reversible bending movements. The excellent performance of the developed Faradaic motor has been proved by observing movement when the total mass of the film increased up to 328% while the mass of conducting polymer is maintained. The utilization of two well-known biocompatible polymers, PLA and PEDOT, as unique components of the artificial muscle opens new possibilities in the biomedical field in which both are currently employed for a huge number of biomedical applications.

7.5 Conclusions

Taking advantage of the acquired knowledge in polymer modifications (structural and surface design), a smart methodology was proposed to produce flexible, robust and electroactive free-standing multilayered ultra-thin films.

This new strategy involved a layer-by-layer (LbL) assembly, which combined the spin-coating technique and the electrochemical polymerization of an ICP (in this case, by CA). For that, the following strategies were crucial (*i*) the use of PEDOT:PSS as semiconductive sacrificial layer; (*ii*) the used and suitability of PLA to prepare nanoperforated layers that enabled the access of monomers (in this Thesis: EDOT or 3DT) to the nearest semiconductive layer; and (*iii*) the *in situ* electropolymerization of a ICP layer.

In a first step, the general behavior of the membrane was evaluated. Interaction between the two polymers resulted in a system that preserve the mechanical properties of PLA and the good electrochemical activity of the ICP (PEDOT), besides, cell culture and protein adsorption assays showed that it behaves as bioactive platforms for cell proliferation and as bioadhesive surfaces for protein separation, respectively. So, after minimal optimization, the FsNM was biological functionalized with a porin protein resulting in a biomimetic hybrid for the efficient transport of ATP and NaCl molecules. Finally, the original FsNM was also evaluated as a novel actuator, exposing to square potential waves to induce volumetric expansion and contraction of the PEDOT layers, causing reversible bending movements even when the total mass of the film increased up to 328% and ICP mass was maintained.

The nanomechanical properties, electrochemical activity and the biocompatibility evidenced by the fashioned FsNM new hybrid materials, make them not only ideal platforms for the obtaining of biomimetic hybrid and Faradaic motors (artificial muscles), but also open huge number of applications with special emphasis in the biomedical field.

7.6 References

1 S. Mitragotri, D. G. Anderson, X. Chen, E. K. Chow, D. Ho, A. V. Kabanov, J. M. Karp, K. Kataoka, C. A. Mirkin, S. H. Petrosko, J. Shi, M. M. Stevens, S. Sun, S. Teoh, S. S. Venkatraman, Y. Xia, S. Wang, Z. Gu and C. Xu, *ACS Nano*, 2015, **9**, 6644–6654.

2 N. L. Teradal and R. Jelinek, *Adv. Healthc. Mater.*, 2017, **6**, 1–36.

3 S. Fleischer and T. Dvir, *Curr. Opin. Biotechnol.*, 2013, **24**, 664–671.

4 T. Cohen-Karni, R. Langer and D. S. Kohane, *ACS Nano*, 2012, **6**, 6541–6545.

5 J. D. Kittle, C. Wang, C. Qian, Y. Zhang, M. Zhang, M. Roman, J. R. Morris, R. B. Moore and A. R. Esker, *Biomacromolecules*, 2012, **13**, 714–718.

6 R. T. ElAfandy, A. F. AbuElela, P. Mishra, B. Janjua, H. M. Oubei, U. Büttner, M. A. Majid, T. K. Ng, J. S. Merzaban and B. S. Ooi, *Small*, 2017, **13**, 1–7.

7 D. Son, J. Lee, S. Qiao, R. Ghaffari, J. Kim, J. E. Lee, C. Song, S. J. Kim, D. J. Lee, S. W. Jun, S. Yang, M. Park, J. Shin, K. Do, M. Lee, K. Kang, C. S. Hwang, N. Lu, T. Hyeon and D. H. Kim, *Nat. Nanotechnol.*, 2014, **9**, 397–404.

8 C. S. Hajicharalambous, J. Lichter, W. T. Hix, M. Swierczewska, M. F. Rubner and P. Rajagopalan, *Biomaterials*, 2009, **30**, 4029–4036.

9 M. M. Pérez-Madrigal, M. I. Giannotti, L. J. Del Valle, L. Franco, E. Armelin, J. Puiggalí, F. Sanz and C. Alemán, *ACS Appl. Mater. Interfaces*, 2014, **6**, 9719–9732.

10 Z. Tai, H. Ma, B. Liu, X. Yan and Q. Xue, *Colloids Surfaces B Biointerfaces*, 2012, **89**, 147–151.

11 A. Puiggalí-Jou, J. Medina, L. J. Del Valle and C. Alemán, *Eur. Polym. J.*, 2016, **75**, 552–564.

12 S. Y. Wong, Q. Li, J. Veselinovic, B. S. Kim, A. M. Klibanov and P. T. Hammond, *Biomaterials*, 2010, **31**, 4079–4087.

13 M. M. Pérez-Madrigal, E. Llorens, L. J. Del Valle, J. Puiggalí, E. Armelin and C. Alemán, *Express Polym. Lett.*, 2016, **10**, 628–646.

14 H. Watanabe, E. Muto, T. Ohzono, A. Nakao and T. Kunitake, *J. Mater. Chem.*, 2009, **19**, 2425–2431.

15 K. D. Sattler, Ed., *Handbook of Nanophysics*, CRC Press, 2010.

16 T. Fujie, *Polym. J.*, 2016, **48**, 773–780.

17 M. M. Pérez-Madrigal, E. Armelin, J. Puiggalí and C. Alemán, *J. Mater. Chem. B*, 2015, **3**, 5904–5932.

18 S. Zhang, Y. Sunami and H. Hashimoto, *Nanomaterials*, 2017, **7**, 1–7.

19 G. Decher, Y. Lvov and J. Schmitt, *Thin Solid Films*, 1994, **244**, 772–777.

20 G. Decher, *Science (80-.).*, 1997, **277**, 1232–1237.

21 A. D. Stroock, R. S. Kane, M. Weck, S. J. Metallo and G. M.

Whitesides, *Langmuir*, 2003, **19**, 2466–2472.
22 Y. Okamura, K. Kabata, M. Kinoshita, H. Miyazaki, A. Saito, T. Fujie, S. Ohtsubo, D. Saitoh and S. Takeoka, *Adv. Mater.*, 2013, **25**, 545–551.
23 J. Stana, J. Stergar, L. Gradišnik, V. Flis, R. Kargl, E. Fröhlich, K. Stana Kleinschek, T. Mohan and U. Maver, *Biomacromolecules*, 2017, **18**, 2732–2746.
24 S. Kim, J. M. Moon, J. S. Choi, W. K. Cho and S. M. Kang, *Adv. Funct. Mater.*, 2016, **26**, 4099–4105.
25 C. Ferris, M. V. De Paz, Á. Aguilar-De-Leyva, I. Caraballo and J. A. Galbis, *Polym. Chem.*, 2014, **5**, 2370–2381.
26 W. Liu, H. Pan, L. Li, H. Lv, Z. Wu, F. Cao and J. Zhu, *J. Manuf. Process.*, 2017, **25**, 418–425.
27 D. M. Vriezema, M. C. Aragonès, J. A. A. W. Elemans, J. J. L. M. Cornelissen, A. E. Rowan and R. J. M. Nolte, *Chem. Rev.*, 2005, **105**, 1445–1489.
28 J. R. Werber, C. O. Osuji and M. Elimelech, *Nat. Rev. Mater.*, 2016, **1**, 1-16.
29 A. Puiggalí-Jou, L. J. del Valle and C. Alemán, *Soft Matter*, 2019, **15**, 2722–2736.
30 Y. R. Kim, S. Jung, H. Ryu, Y. E. Yoo, S. M. Kim and T. J. Jeon, *Sensors (Switzerland)*, 2012, **12**, 9530–9550.
31 S. Mura, J. Nicolas and P. Couvreur, *Nat. Mater.*, 2013, **12**, 991–1003.
32 R. Koebnik, K. P. Locher and P. Van Gelder, *Mol. Microbiol.*, 2000, **37**, 239–253.
33 S. Galdiero, A. Falanga, M. Cantisani, R. Tarallo, M. Elena Della Pepa, V. D'Oriano and M. Galdiero, *Curr. Protein Pept. Sci.*, 2013, **13**, 843–854.
34 J. C. Ahumada, C. Alemán, J. Soto-Delgado and J. Torras, *J. Phys. Chem. B*, 2019, **123**, 86–94.
35 J. H. Kleinschmidt, *Protein-Lipid Interact. From Membr. Domains to Cell. Networks*, 2006, 27–56.
36 M. Lopes-Rodrigues, A. Puiggalí-Jou, D. Martí-Balleste, L. J. Del Valle, C. Michaux, E. A. Perpète and C. Alemán, *ACS Omega*, 2018, **3**, 7856–7867.
37 M. M. Pérez-Madrigal, L. J. Del Valle, E. Armelin, C. Michaux, G. Roussel, E. A. Perpète and C. Alemán, *ACS Appl. Mater. Interfaces*, 2015, **7**, 1632–1643.
38 A. Puiggalí-Jou, M. M. Pérez-Madrigal, L. J. Del Valle, E. Armelin, M. T. Casas, C. Michaux, E. A. Perpète, F. Estrany and C. Alemán, *Nanoscale*, 2016, **8**, 16922–16935.
39 A. Puiggalí-Jou, J. Pawlowski, L. J. Del Valle, C. Michaux, E. A. Perpète, S. Sek and C. Alemán, *ACS Omega*, 2018, **3**, 9003–9019.
40 T. F. Otero, J. G. Martinez and J. Arias-Pardilla, *Electrochim. Acta*,

2012, **84**, 112–128.
41 T. F. Otero, *Electrochim. Acta*, 2016, **212**, 440–457.
42 Q. Pei and O. Inganläs, *Adv. Mater.*, 1992, **4**, 277–278.
43 T. F. Otero and E. Angulo, *J. Appl. Electrochem.*, 1992, **22**, 369–375.
44 L. Valero, J. Arias-Pardilla, J. Cauich-Rodríguez, M. A. Smit and T. F. Otero, *Electrochim. Acta*, 2011, **56**, 3721–3726.
45 M. Beregoi, A. Evanghelidis, V. C. Diculescu, H. Iovu and I. Enculescu, *ACS Appl. Mater. Interfaces*, 2017, **9**, 38068–38075.
46 G. M. Spinks, V. Mottaghitalab, M. Bahrami-Samani, P. G. Whitten and G. G. Wallace, *Adv. Mater.*, 2006, **18**, 637–640.
47 K. Mukai, K. Asaka, K. Hata, T. Fernández Otero and H. Oike, *Chem. - A Eur. J.*, 2011, **17**, 10965–10971.
48 X. Xie, L. Qu, C. Zhou, Y. Li, J. Zhu, H. Bai, G. Shi and L. Dai, *ACS Nano*, 2010, **4**, 6050–6054.
49 J. Liang, Y. Huang, J. Oh, M. Kozlov, D. Sui, S. Fang, R. H. Baughman, Y. Ma and Y. Chen, *Adv. Funct. Mater.*, 2011, **21**, 3778–3784.
50 E. W. H. Jager, O. Inganäs and I. Lundström, *Science (80-.).*, 2000, **288**, 2335–2338.
51 E. W. H. Jager, E. Smela and O. Inganas, *Science (80-.).*, 2000, **290**, 1540–1545.
52 S. J. Higgins, K. V. Lovell, R. M. G. Rajapakse and N. M. Walsby, *J. Mater. Chem.*, 2003, **13**, 2485–2489.
53 N. Festin, C. Plesse, P. Pirim, C. Chevrot and F. Vidal, *Sensors Actuators, B Chem.*, 2014, **193**, 82–88.
54 F. Vidal, J. F. Popp, C. Plesse, C. Chevrot and D. Teyssié, *J. Appl. Polym. Sci.*, 2003, **90**, 3569–3577.
55 C. Plesse, F. Vidal, D. Teyssié and C. Chevrot, *Chem. Commun.*, 2010, **46**, 2910–2912.
56 M. Fuchiwaki and T. F. Otero, *J. Mater. Chem. B*, 2014, **2**, 1954–1965.
57 M. Fuchiwaki, K. Tanaka and K. Kaneto, *Sensors Actuators, A Phys.*, 2009, **150**, 272–276.
58 M. Fuchiwaki, J. G. Martinez and T. F. Otero, *Adv. Funct. Mater.*, 2015, **25**, 1535–1541.
59 H. Stoyanov, M. Kollosche, D. N. McCarthy and G. Kofod, *J. Mater. Chem.*, 2010, **20**, 7558–7564.
60 H. Stoyanov, M. Kollosche, S. Risse, R. Waché and G. Kofod, *Adv. Mater.*, 2013, **25**, 578–583.
61 A. Agrawal, H. Chen, H. Kim, B. Zhu, O. Adetiba, A. Miranda, A. Cristian Chipara, P. M. Ajayan, J. G. Jacot and R. Verduzco, *ACS Macro Lett.*, 2016, **5**, 1386–1390.
62 Y. Lee, J. Han, B. Choi, J. Yoon, J. Park, Y. Kim, J. Lee, D. H. Kim, D. M. Kim, M. Lim, M. H. Kang, S. Kim and S. J. Choi, *ACS Appl. Mater. Interfaces*, 2018, **10**, 15841–15846.

63 T. F. Otero and J. G. Martinez, *Prog. Polym. Sci.*, 2015, **44**, 62–78.
64 B. Yan, Y. Wu and L. Guo, *Polymers (Basel).*, 2017, **9**, 1–20.
65 Q. M. Zhang and M. J. Serpe, *ChemPhysChem*, 2017, **18**, 1451–1465.
66 S. M. Mirvakili and I. W. Hunter, *Adv. Mater.*, 2018, **30**, 1–28.
67 Y.-K. Han, M.-Y. Chang, W.-Y. Huang, H.-Y. Pan, K.-S. Ho, T.-H. Hsieh and S.-Y. Pan, *J. Electrochem. Soc.*, 2011, **158**, K88.
68 A. A. Farah, S. A. Rutledge, A. Schaarschmidt, R. Lai, J. P. Freedman and A. S. Helmy, *J. Appl. Phys.*, 2012, **112**, 113709-8.
69 A. Shakoor and T. Z. Rizvi, *J. Raman Spectrosc.*, 2010, **41**, 237–240.
70 R. V. Salvatierra, L. G. Moura, M. M. Oliveira, M. A. Pimenta and A. J. G. Zarbin, *J. Raman Spectrosc.*, 2012, **43**, 1094–1100.
71 R. Balint, N. J. Cassidy and S. H. Cartmell, *Acta Biomater.*, 2014, **10**, 2341–2353.
72 K. J. Gilmore, M. Kita, Y. Han, A. Gelmi, M. J. Higgins, S. E. Moulton, G. M. Clark, R. Kapsa and G. G. Wallace, *Biomaterials*, 2009, **30**, 5292–5304.
73 L. Groenendaal, G. Zotti, P. H. Aubert, S. M. Waybright and J. R. Reynolds, *Adv. Mater.*, 2003, **15**, 855–879.
74 B. W. Hoogenboom, K. Suda, A. Engel and D. Fotiadis, *J. Mol. Biol.*, 2007, **370**, 246–255.
75 K. Zeth, *Biochim. Biophys. Acta - Bioenerg.*, 2010, **1797**, 1292–1299.
76 L. Groenendaal, F. Jonas, D. Freitag, H. Pielartzik and J. R. Reynolds, *Adv. Mater.*, 2000, **12**, 481–494.
77 D. Aradilla, F. Estrany and C. Alemán, *J. Phys. Chem. C*, 2011, **115**, 8430–8438.
78 L. De Lazari Ferreira and H. D. R. Calado, *J. Solid State Electrochem.*, 2018, **22**, 1507–1515.
79 R. Singhal, W. Takashima, K. Kaneto and S. B. Samanta, 2002, **86**, 42–48.
80 J. Zhang, Z. Han, M. Chen, X. Yang and W. Cao, *J. Phys. Chem. Solids*, 2010, **71**, 1316–1323.
81 V. K. Garg, H. Avashthi, A. Tiwari, P. A. Jain, P. W. R. Ramkete, A. M. Kayastha and V. K. Singh, *Bioinformation*, 2016, **12**, 74–77.
82 S. Maione, A. M. Gil, G. Fabregat, L. J. Del Valle, J. Triguero, A. Laurent, D. Jacquemin, F. Estrany, A. I. Jiménez, D. Zanuy, C. Cativiela and C. Alemán, *Biomater. Sci.*, 2015, **3**, 1395–1405.
83 S. Maione, G. Fabregat, L. J. Del Valle, A. D. Bendrea, L. Cianga, I. Cianga, F. Estrany and C. Alemán, *J. Polym. Sci. Part B Polym. Phys.*, 2015, **53**, 239–252.
84 H. J. Perera, H. Mortazavian and F. D. Blum, *Langmuir*, 2017, **33**, 2799–2809.
85 A. A. Moya, *J. Power Sources*, 2018, **397**, 124–133.
86 A. A. Moya, *J. Phys. Chem. C*, 2016, **120**, 6543–6552.
87 P. Córdoba-Torres, *Electrochim. Acta*, 2017, **225**, 592–604.
88 J. Poater, J. Casanovas, M. Solà and C. Alemán, *J. Phys. Chem. A*,

2010, **114**, 1023–1028.
89 T. Rostovtseva and M. Colombini, *Biophys. J.*, 1997, **72**, 1954–1962.
90 G. R. Smith and M. S. P. Sansom, *Biophys. Chem.*, 1999, **79**, 129–151.
91 A. K. S. Camara, Y. F. Zhou, P. C. Wen, E. Tajkhorshid and W. M. Kwok, *Front. Physiol.*, 2017, **8**, 1–18.
92 L. Shao, K. W. Kinnally and C. A. Mannella, *Biophys. J.*, 1996, **71**, 778–786.
93 G. L. Rosano and E. A. Ceccarelli, *Front. Microbiol.*, 2014, **5**, 1–17.
94 S. Schlegel, A. Hjelm, T. Baumgarten, D. Vikström and J. W. De Gier, *Biochim. Biophys. Acta - Mol. Cell Res.*, 2014, **1843**, 1739–1749.
95 M. Fernández de Labastida and A. Yaroshchuk, *J. Memb. Sci.*, 2019, **585**, 271–281.
96 N. Pismenskaia, P. Sistat, P. Huguet, V. Nikonenko and G. Pourcelly, *J. Memb. Sci.*, 2004, **228**, 65–76.
97 J. J. Roa, G. Fargas, A. Mateo and E. Jiménez-Piqué, *Mater. Sci. Eng. A*, 2015, **645**, 188–195.
98 W. C. Oliver and G. M. Pharr, *J. Mater. Res.*, 1992, **7**, 1564-1583.
99 C. Tromas, J. C. Stinville, C. Templier and P. Villechaise, *Acta Mater.*, 2012, **60**, 1965–1973.
100 S. Bec, A. Tonck and J. L. Loubet, *Philos. Mag.*, 2006, **86**, 5347–5358.
101 M. M. Pérez-Madrigal, M. G. Edo, A. Díaz, J. Puiggalí and C. Alemán, *J. Phys. Chem. C*, 2017, **121**, 3182–3193.
102 M. M. Pérez-Madrigal, F. Estrany, E. Armelin, D. D. Díaz and C. Alemán, *J. Mater. Chem. A*, 2016, **4**, 1792–1805.
103 T. F. Otero, L. X. Martinez-Soria, J. Schumacher, L. Valero and V. H. Pascual, *ChemistryOpen*, 2017, **6**, 25–32.
104 L. V. Conzuelo, J. Arias-Pardilla, J. V. Cauich-Rodríguez, M. A. Smit and T. F. Otero, *Sensors*, 2010, **10**, 2638–2674.
105 T. F. Otero and M. T. Cortes, *Smart Struct. Mater. 2001 Electroact. Polym. Actuators Devices*, 2001, **4329**, 93.

CONCLUSIONS

This chapter recapitulates the main goals achieved this Thesis.

In summary, four intrinsically conducting polymers (ICPs) were structurally or superficially modified to take advantage of their electrochemical and electrical behavior, to enhance their biocompatibility and to improve their mechanical stability. After careful characterization, the enhanced composites were established as promising biomaterials for several biomedical applications, mainly focused on the biosensing field.

The state-of-the-art revealed several routes to optimize ICPs capacities for the electrochemical recognition of a wide range of biomolecules. However, just a few works have been focused on approaches based on the assembly between ICPs and conventional insulating polymers or biopolymers. The main characteristic of those assembly-based approaches, which are opposite to the blending or mixing of polymers, is the independent organization of the individual polymeric constituents, while at the same time the properties of all them are maintained, or even improved, in the whole assembly. Within this context, in the present Thesis, three engineering strategies were successfully designed, developed and evaluated.

The first strategy studied employed the "grafting-through" technique to transform ICPs backbones by attaching conventional polymers as side chains, the resulting materials being considered as "molecular composites". Results reflected an improvement in the biocompatibility and an efficient performance as electrochemical sensors for biomolecules.

- Three conjugated biomaterials were synthesized by applying the "grafting-through" approach. For this purpose, macromonomers

incorporating PEG or PCL side chains were copolymerized with unsubstituted monomers. The chemical structure of those materials consists on: (*i*) PPy backbone grafted with PEG side chains; (*ii*) PEDOT backbone with PCL side chains; and (*iii*) PTh backbone grafted with both PEG and PCL side chains.

- Electrocopolymerization results indicate that macromonomers have low mobility towards the working electrodes and, therefore, effective films were only obtained using long reaction times and low percentages of macromonomers in the feeding solution.
- In all cases, the grafting of PCL and PEG side chains was beneficious in terms of biocompatibility, as proved by *in vitro* biological assays. The incorporation of those side chains reduced the cytotoxicity by *ca.* 15 - 20 % with respect to the conjugated non-grafted analogue. This observation suggests that conjugated grafted copolymers can be implanted in living systems.
- The electrochemical response of the prepared copolymers allowed their use as electrochemical (bio)sensors for the detection of low concentrations of dopamine (0.5 µM), serotonin (0.5 µM) or nicotinamide adenine dinucleotide (0.2 µM), even in the presence of interfering substances.

The second approach was focused on the preparation of free-standing, flexible and electroactive polymeric films able to distinguish between eukaryotic and prokaryotic cells. Methodologies based on mechanical and chemical activation treatments were developed for the integration of ICPs into a conventional insulating polymer for biomedical applications. The resulting bioplatforms have

been used to detect bacterial infections as well as to improve the tissues engineering capacity of the polymer used as substrate.

- The mechanical handling of PEDOT was improved through its combination with i-PP, embedding ICP NPs into the i-PP matrix (i-PP/PEDOT), or following a layer by layer assembly approach (i-PP_f/PEDOT).
- Highly sensitive and selective electrochemical sensors were successfully designed for the detection of bacterial infections. The detection process was based on the oxidation of NADH, which has been proved to be related with the bacterial metabolism.
- The biocompatibility of the electrochemical (bio)sensor was enhanced ~ 50 - 100 % replacing the PEDOT homopolymer by a graft copolymer having PEDOT as backbone and PCL as side group.

The final project fashioned electroactive and flexible multi-functional nanomembranes. A layer-by-layer assembly was used to connect an ICP with a biopolymer. Self-supported nanomembranes of 5 layers showed benefits as biomimetic platforms and as artificial muscle.

- Spin-coating technique and electrochemical polymerization were combined to fabricate a novel class of free standing nanomembrane, which displayed biocompatibility and good electroactivity.
- Bioinspired FsNM was optimized with the incorporation of VDAC protein and a graft copolymer, having a PEDOT

backbone and a short lipophilic side chain. The biomimetic hybrid material was used as sensor for the efficient transport of ATP and NaCl.

- In a secondary application, the mechanical integrity and the electrochemical properties of the FsNM were used as a Faradaic motor able to raise and push a weight. More specifically, those membranes exhibited a swelling-shrinking ability of *ca*. 28 % with respect to their initial state, even with a weight increase up to 328%.

In general, the designed strategies for the modifications of ICPs and its resultant composites, open a wide range of possibilities to the development of new and functional polymeric biomaterials to fulfill the necessities of medical devices.

A

ANNEXES

Publication in international peer-reviewed journals

- **Molina, B. G.;** Bendrea, A.; Cianga, L.; Armelin, E.; del Valle, LJ.; Cianga, Ioan; Aleman, C. *The biocompatible polythiophene-: G-polycaprolactone copolymer as an efficient dopamine sensor platform.* Polymer chemistry (2017), Vol. 8, num. 39, p. 6112-6122. DOI: 10.1039/c7py01326d.
- **Molina, B. G.;** Cianga, L.; Bendrea, A.; Cianga, Ioan; del Valle, LJ.; Estrany, F.; Aleman, C.; Armelin, E. *Amphiphilic polypyrrole-poly (Schiff base) copolymers with poly(ethylene glycol) side chains: synthesis, properties and applications.* Polymer chemistry (2018), Vol. 9, num. 31, p. 4218- 4232. DOI:10.1039/c8py00762d.
- **Molina, B. G.;** Dominguez E.; Armelin, E.; Aleman, C. *Assembly of Conducting Polymer and Biohydrogel for the Release and Real-Time Monitoring of Vitamin K3.* Gels (2018), Vol. 4, num. 4, p. 86. DOI: 10.3390/gels4040086. (Gels, Volume 4, Issue 4 Cover). DOI:10.3390/gels4040086.
- **Molina, B. G.**; Cuesta, S.; Puiggalí, A.; del Valle L J.; Armelin, E.; Aleman, C. *Perforated polyester nanomebranes as templates of electroactive and robust free-standing films*. European Polymer Journal (2019), Vol. 114, p. 213-222. DOI: 10.1016/j.eurpolymj.2019.02.038.
- Enshae H;, **Molina, B. G.**; del Valle, LJ.; Estrany, F.; Arnan, C.; Puiggalí, J; Saperas, N; Aleman, C . *Scaffolds for Sustained Release of Ambroxol, a Pharmacological Chaperone that Increases the Activity of Misfolded β-Glucocerebrosidase*. Macromol. Biosci (2019) Vol 19, p.1900130. DOI: 10.1002/mabi.201900130.
- **Molina, B. G.**; Cuesta, S.; Besharatloo, H.; Roa, J.J.; Armelin, E.; Aleman, C. *Free-Standing Faradaic Motors Based on Biocompatible Nanoperforated Poly(lactic Acid) Layers and Electropolymerized Poly(3,4-ethylenedioxythiophene).* ACS Appl. Mater. Interfaces (2019), Vol. 11, p. 29427−29435. DOI: 10.1021/acsami.9b08678.
- **Molina, B. G.**; del Valle, LJ.; Turon, P. Armelin, E.; Aleman, C. *Electrochemical Sensor for Bacterial Metabolism Based on the Detection of NADH by Polythiophene Nanoparticles*. J. Phys. Chem. C (2019), Vol. 123, p. 22181−22190. DOI: 10.1021/acs.jpcc.9b03982.
- **Molina, B. G.;** Bendrea, A.; Cianga, L.; Armelin, E.; Cianga, Ioan; Aleman, C. *An amphiphilic, heterografted polythiophene copolymer containing biocompatible/biodegradable side chains for use as an (electro) active surface in biomedical applications*. Polym. Chem. (2019), Vol. 10, p. 5010-5022. DOI: 10.1039/c9py00926d.
- Bayat, M; Izadan, H; **Molina, B. G.;** Sánchez, M; Santiago, S; Semnani, D; Dinari, M; Guirado, G; Estrany, F; Alemán, C. *Electrochromic Self-Electrostabilized Polypyrrole Films Doped with*

Surfactant and Azo Dye. Polymers (2019), Vol. 11, p. 1757. DOI:10.3390/polym11111757.

- **Molina, B. G.;** Lopes-Rodrigues, M.; Estrany, F.; Michaux, C.; Perpète, E. A.; Armelin, E.; Aleman, C. *Free-standing flexible and biomimetic hybrid membranes for ions and ATP transport.* Journal of Membrane Science (2020), Vol. 601, p. 117931. DOI: 10.1016/j.memsci.2020.117931.

Communications in international scientific congresses

- **Molina, B. G.**; del Valle, L J.; Armelin, E.; Aleman, C. Electrochemical sensor for bacterial biofilm detection. 11° Congreso Internacional de Investigación Científica Multidisciplinaria, Chihuahua, Chih. México: November 14-15, 2019.
- **Molina, B. G.**; Cuesta, S.; Armelin, E.; Aleman, C. Free-standing, electroactive and biocompatible nanomembranes prepared with porous PLA films and conducting polymer layers. 11° Congreso Internacional de Investigación Científica Multidisciplinaria, Chihuahua, Chih. México: November 14-15, 2019.
- **Molina, B. G.**; Domínguez, E.; Puiggali, J.; Armelin, E.; Aleman, C. A rational design of hydrogel with electroactive properties. Polymers 2018: Polymers: Design, Function and Application, Barcelona, Spain: March 21-23, 2018, p118.
- **Molina, B. G.**; Cianga, L.; Cianga, Ioan; del Valle, LJ.; Estrany, F.; Armelin, E.; Aleman, C. Biosensor platform for selective neurotransmitter detection. Polymers 2018: Polymers: Design, Function and Application, Barcelona, Spain: March 21-23, 2018, p125.

Research stay

- Monash University, Monash Institute of Pharmaceutical Science and Melbourne center for nanofabrication. Victoria, Australia. (April-July 2019) *Novel dual-responsive, pH and electro-sensitive, drug delivery system.*

Abbreviations	
AA	Ascorbic acid
ACh	Acetylcholine
ACN	Acetonitrile
AFM	Atomic force microscopy
AFP	α- fetoprotein antibody
AgNPs	Silver nanoparticles
APS	Ammonium persulfate
ASH	Average step height
ATCC	American type culture collection
ATP	Adenosine triphosphate
ATR	Attenuated total reflectance
AuNPs	Gold nanoparticles
AZBPy	Azomethine-containing bis-pyrrole moieties
AZBPyBA	3,5-bis(((e)-(1h-pyrrol-2-yl) methylene) amino) benzoic acid
BME	β-mercaptoethanol (2-mercaptoethanol)
BSA	Bovine serum albumin
CA	Chronoamperometry
CE	Counter electrode
CFU	Colony-forming units
CHO	Cholineoxidase
cMWCNTs	Carboxylated multiwalled carbon nanotubes
CNTs	Carbon nanotubes
COP	Poly(3,4-ethylenedioxythiophene-*co*-3-dodecylthiophene)
COPCTS	Cobalt(ii) phthalocyanine tetrasulfonate
CPE	Constant phase element
CV	Cyclic voltammetry
cv	Cell viability
DA	Dopamine (3,4-dihydroxyphenethylamine)
DABA	3,5-diaminobenzoic acid
DBSA	4-dodecylbenzenesulfonic acid
DCCI	N,N'-dicyclohexylcarbodiimide
DDPPy	Polypyrrole with the attachmentment of DNA-dendrimer
DLS	Dynamic light scattering
DMAP	4-dimethylamino pyridine

DMEM	Dulbecco's modified eagle medium
DMSO	Dimethyl sulfoxide
DNA	Deoxyribonucleic acid
DPV	Differential pulse voltammetry
DSC	Differential scanning calorimetry
E. Coli	*Escherichia coli*
EDOT	3,4-ethylenedioxythiophene
EDTA	Ethylenediaminetetraacetic acid
EDX	Energy-dispersive x-ray spectroscopy
EEC	Electric equivalent circuit
EIS	Electrochemical impedance spectroscopy
EP	Epinephrine
FA	Facially amphiphilic structure
FBS	Fetal bovine serum
FDA	Food and drug administration
FsNM	Free-standing nanomenbranes
FTIR	Fourier-transform infrared spectroscopy
GA	Gluteraldehyde
GC	Glassy carbon
GCD	Galvanostatic charge/discharge
GO	Graphene oxide
GOD	Enzyme glucose oxidase
GPC	Gel permeation chromatography
Gr	Graphene
HEPES	N-(2-hydroxyethyl)piperazine-n′-(2-ethanesulfonic acid)
ICP	Intrinsically conducting polymer
ICPs	Intrinsically conducting polymers
i-PP	Isotactic polypropylene
ITO-glass	Indium tin oxide coated
IUPAC	International union of pure and applied chemistry
LB broth	Luria-bertani medium
LbL	Layer-by-layer
LEA	Loss of electroactivity
LOD	Limit of detection
Lyz	Lysozyme from chicken egg white
MB	Methylene blue

MEM	Micro-electromechanical
MIP	Molecularly imprinted polymer
MIT	Molecular imprinting technique
ml-FSNM	Multi-layered free-standing nanomenbranes
M_n	Molecular weight
MPD	2-methyl-2,4-pentanediol
MTT	[3-(4,5-dimethylthiazol-2-yl)-2,5-diphenyltetrazolium bromide]
NAD+	Nicotinamide adenine dinucleotide oxidative form
NADH	Nicotinamide adenine dinucleotide
$NI(OH)_2NF$	Nickel hydroxide nanoflakes
NMR	Nuclear magnetic resonance
NMs	Nanomembranes
NPs	Nanoparticle
OMPS	Outer membrane proteins
oPPyNFs	Over-oxidized polypyrrole nanofibers
oPPyNW	Over-oxidized polypyrrole nanowires
PAB	Poly(aniline blue)
PAni	Polyaniline
PBS	Phosphate buffered saline solution
PCL	Polycaprolactone
PCNCPy	Poly[n-(2-cyanoethyl)pyrrole]
PDA	Polydopamine
PDMS	Polydimethylsiloxane
PE	Polyethylene
PEDOT	Poly(3,4-ethylenedioxythiophene)
PEDOT NPs	Poly(3,4-ethylenedioxythiophene) nanoparticles
PEDOT:PSS	Poly(3,4-ethylenedioxythiophene)-poly(styrenesulfonate)
PEDOTNTs	Poly (3,4-ethylenedioxythiophene) nanotubes
PEG	Poly(ethylene glycol)
PGA	Polyglycolic acid
PGS	Poly(glycerol-*co*-sebacate)
PHMeEDOT	Poly(hydroxymethyl-3,4-ethylenedioxythiophene)
PILS	Poly(ionic liquids)
PLA	Polylactic acid
PLGA	Poly(lactic-*co*-glycolic acid)

PMEA	Planar microelectrode array
PMMA	Poly (methyl methacrylate)
PNMPy	Poly(n-methylpyrrole)
POA	Poly(o-anisidine)
pPLA	Nanoperforated poly(lactic acid)
PPy	Polypyrrole
PPyNTs	Polypyrrole nanotubes
PSB	Poly(schiff base)
PSSA	Poly(styrenesulfonic acid)
PTFE	Poly(tetrafluoroethylene)
PTH	Polythiophene
PTSA	P-toluene sulfonic acid
PVA	Poly(vinyl alcohol)
PVC	Poly(vinylchloride)
Py	Pyrrole
RCS	Refrigerated cooling system
RE	Reference electrode
rGO	Reduced graphene oxide
S. Aureus	*Staphylococcus aureus*
SA	Self-assembling
SDS	Sodium dodecyl sulfate
SEM	Scanning electron microscopy
SPE	Carbon screen-printed electrode
ssDNA	Single strand DNA
TBATFB	Tetrabutylammonium tetrafluoroborate
TCPS	Tissue culture poly styrene
TEM	Transmission electron microscopy
TGA	Thermogravimetric analysis
THF	Tetrahydrofuran
UA	Uric acid
UV-vis	Ultraviolet visible spectroscopy
VD	Vertical distance
VDAC	Voltage dependent anion channel
WCA	Water contact angle
WE	Working electrode
WOS	Web of science
XPS	X-ray photoelectron spectroscopy

^{13}C-NMR	Carbon-13 nuclear magnetic resonance
^{1}H-NMR	Proton nuclear magnetic resonance
3DT	3-dodecylthiophene

Symbols	
E_k	Kinetic energy
ΔQ	Difference in voltammetric charges between the second and the last cycles
ΔH_m^0	Heat of fusion for 100% crystalline material
z	Absolute charge of the chloride ion
$\Delta\alpha$	Angle associated to bending movement
E_g	Band gap energy
t	Coating thickness
C	Concentration of chloride ions
θ	Contact angle
a	Contact radius
I	Current
X_c	Degree of crystallinity
D	Diffusion coefficient
C_{dl}	Double layer capacitance
E_{eff}	Effective elastic modulus
F	Faraday constant
ΔH_m	Heat of fusion of the measured sample
R_h	Hydrodynamic radius
Z	Impedance
ΔA	Increment in the surface area
Δm	Increment in the total mass
λ_{max}	Maxim absorbance in wavelength (nm)
A	Membrane area
Em	Membrane elastic modulus
λ_{min}	Minim absorbance in wavelength (nm)
P	Permselectivity
τ	Polymerization time
R_q	Root-mean-square roughness
R_s	Resistance of the electrolytic solution
R_M	Resistance of the membrane

±	Standard deviation
E^o	Standard reduction potential
p	Statistical confidence level
Es	Substrate elastic modulus
L	Thickness
σ	Transition time
t_i	Transport number
Q	Voltammetric charge
Q_i	Voltammetric charge corresponding to the second cycle.
% v/v	Volume concentration of a solution express, volume per volume
λ	Wavelength (nm)
% w/w	Weight concentration of a solution express, weight per weight